REPORT DOCUMENTATION PAGE

Form Approved OMB No. 0704-0188

1. AGENCY USE ONLY (Leave blank)	2. REPORT DATE September 1995	3. REPORT TYPE AND DATES COVERED Final Report

4. TITLE AND SUBTITLE

Gas Flow and Heat Protection by Strong Injection in the Shock Wave Interference Region Near the Blunt Body Front Surface

5. FUNDING NUMBERS

F6170894W0912

6. AUTHOR(S)

V. Ya. Bezmenov, S.M. Boldyrev, V. Ya. Borovoy, A. Yu. Chinilov, R. A. Kazansky, S.N. Krutiy, V.P. Kulesh, I.V.Struminskaya, Ad.B. Vasilevsky, L.V. Yakovleva

7. PERFORMING ORGANIZATION NAME(S) AND ADDRESS(ES)

TsAGI
Zhukovsky
Moscow, Russia 140160

8. PERFORMING ORGANIZATION REPORT NUMBER

SPC-94-4061

9. SPONSORING/MONITORING AGENCY NAME(S) AND ADDRESS(ES)

EOARD
PSC 802 BOX 14
FPO 09499-0200

10. SPONSORING/MONITORING AGENCY REPORT NUMBER

SPC-94-4061

11. SUPPLEMENTARY NOTES

12a. DISTRIBUTION/AVAILABILITY STATEMENT

Dist "A"

Unlimited

12b. DISTRIBUTION CODE

13. ABSTRACT (Maximum 200 words)

Results of the experimental study of the influence of tangential gas injection on the flow and heat transfer in the region of interaction of the impinging planar shock generated by a sharp wedge and a bow shock wave generated upstream of the cylindrical blunted body are presented. The experimental study was conducted in the TsAGI UT -1 wind tunnel at a free stream Mach number of 6, total pressure $P_0 = 20$ bar, stagnation temperature $T_0 = 570$ K, Reynolds number based on the free stream flow parameters and bluntness radius $Re_\infty = 0.19 \times 10^6$. A sharp wedge having $\theta = 15°$ was used as a shock generator. Gas (air and helium) was injected through a tangential slot located either in the symmetry line of the blunted body or at a distance of $\varphi_j = -33°$ from the symmetry line. In the second case gas was injected in the direction of the symmetry line. In both cases gas was injected into the region of the shock wave interference. The shock generator location, the slot sizes, the mass flow rate and pressure of the injected gas were varied. Results of numerical calculations of an inviscid gas flow are also presented.

14. SUBJECT TERMS

15. NUMBER OF PAGES 145

16. PRICE CODE

17. SECURITY CLASSIFICATION OF REPORT	18. SECURITY CLASSIFICATION OF THIS PAGE	19. SECURITY CLASSIFICATION OF ABSTRACT	20. LIMITATION OF ABSTRACT
UNCLASSIFIED	UNCLASSIFIED	UNCLASSIFIED	UL

NSN 7540-01-280-5500

Standard Form 298 (Rev. 2-89)
Prescribed by ANSI Std. 239-18
298-102

Gas Flow and Heat Protection by Strong Injection in the Shock Wave Interference Region Near the Blunt Body Front Surface
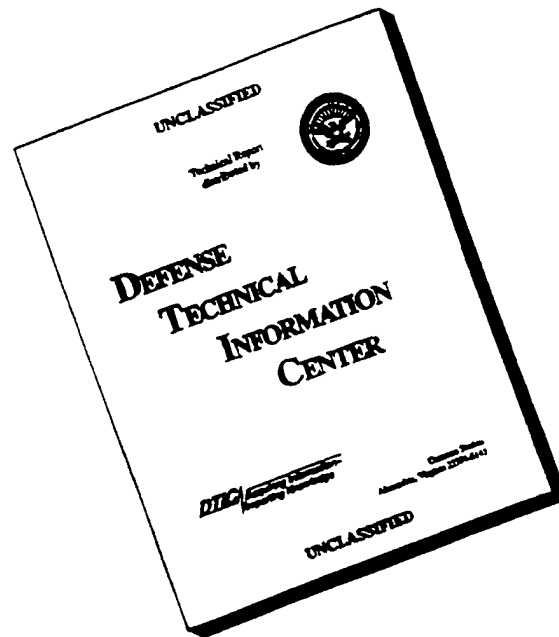
SPC-94-4061

Final Report

EXECUTERS:

V.Ya.Bezmenov
S.M.Boldyrev
V.Ya.Borovoy
A.Yu.Chinilov
R.A.Kazansky
S.N.Krutiy
V.P.Kulesh
I.V.Struminskaya
Ad.B.Vasilevsky
L.V.Yakovleva

19970113 015

Sept. 1995

DISCLAIMER NOTICE

THIS DOCUMENT IS BEST
QUALITY AVAILABLE. THE
COPY FURNISHED TO DTIC
CONTAINED A SIGNIFICANT
NUMBER OF PAGES WHICH DO
NOT REPRODUCE LEGIBLY.

Abstract

Results of the experimental study of the influence of tangential gas injection on the flow and heat transfer in the region of interaction of the impinging planar shock generated by a sharp wedge and a bow shock wave generated upstream of the cylindrical blunted body are presented.

The experimental study was conducted in the TsAGI UT-1 wind tunnel at a free stream Mach number of 6, total pressure $P_o = 20$ bar, stagnation temperature $T_o = 570$ K, Reynolds number based on the free stream flow parameters and bluntness radius $Re_\infty = 0.19 \times 10^6$. A sharp wedge having $\theta = 15^o$ was used as a shock generator.

Gas (air and helium) was injected through a tangential slot located either in the symmetry line of the blunted body or at a distance of $\varphi_j = -33^o$ from the symmetry line. In the second case gas was injected in the direction to the symmetry line. In both cases gas with injected into the region of the shock wave interference.

The shock generator location, the slot sizes, the mass flow rate and pressure of the injected gas were varied. Results of numerical calculations of an inviscid gas flow are also presented.

Content

NOMENCLATURE

b — slot length, m

G — mass flow rate, kg/s

$G_j^* = G_j/\rho_\infty u_\infty Rb$ — normalized mass flow rate of injected gas

H — high dynamic pressure jet, Fig. 1

h_j — slot height, Fig. 6

h_v — distance from bluntness surface to slot, Fig. 6

h_w — step height, Fig. 6

$h_{j*} = G_j/\rho_{j*} u_{j*} b$ — effective slot height, mm

$I_j^* = \rho_{je} u_{je} h^2/\rho_\infty u_\infty^2 R$ — normalized momentum of injected gas

L_1 — ratio of length of transmitted shock to bluntness radius, Fig. 1

M — Mach number

M_∞ — free stream Mach number

P — pressure, bar

P_j — total pressure of injected gas, bar

q — heat flux, W/cm^2

q_m — maximum heat flux, W/cm^2

q_o — heat flux in given point without injection, W/cm^2

q_{so} — heat flux in symmetry line of cylinder alone without injection, W/cm^2

R — radius, m

Re — Reynolds number

$Re_\infty = \rho_\infty u_\infty R/\mu_\infty$ — free stream Reynolds number

T — temperature, K

T_b — temperature of the wall, K

T_{wb} — initial temperature of the wall, K

u — full velocity, m/s

u_x — velocity component along x−axis, m/s

v_y — velocity component along y−axis, m/s

$V_j^* = G_j/\rho_{je} u_e Rb$ — normalized volume of injected gas

X — axis parallel to free stream direction

X_w — ratio of bow wave detachment to bluntness radius, Fig. 1

X_1 — ratio of transmitted shock detachment to bluntness radius, Fig. 1

X^* — distance from bluntness surface to intersection point of impinging shock with symmetry line normalized by bluntness radius, Fig. 1

Y — axis normal to free stream

β — impinging shock angle, degrees, Fig. 1

β_1 — transmitted shock angle, degrees, Fig. 1

θ — shock generator angle, degrees

μ — viscosity, kg/(m*s)

ρ — density, kg/m^3

τ — time, s

ζ — angle between tangent to blunted surface and axis of injected jet, degrees, Fig. 1

φ — distance from symmetry line, degrees

φ_j — distance from symmetry line to slot, degrees

Indices

j — injectant

je — isentropic expended jet

o — isentropic stagnation parameters; without injection (for q)

s — symmetry line of bluntness

so — in symmetry line without injector

w — outer surface

∞ — free stream condition

$*$ — sound speed condition

Introduction

Shock wave interference is one of the most challenging problems of gasdynamics. Interference results in qualitative change of the heat flux and pressure distributions over a streamlined body surface.

For many years shock wave interference has been studied mainly in connection with the problem of flows over leading edges of wings and empennage. In this case a planar impinging shock is inclined to the cylindrical surface generatrices. A great number of works devoted to this problem has been carried out in the Soviet Union and USA. It was shown that due to the shock/shock interference narrow regions are formed, where heat flux and pressure is many times greater than in case of absence of the impinging shock [1]. On the basis of experimental study of the flow in the incidence region of a two−dimensional shock upon a sphere, a phenomenological classification was carried out by Edney [2] and 6 basic types of interference flows were pointed out.

During the last decade an intensive study of two−dimensional shock wave interference was performed in the context of the problem of the flow over the cowl of the hypersonic aircraft inlet [3]. In this case severe two−dimensional local increase both in heat flux and pressure was observed too. Cooling of the leading edge of the cowl is a more complicated problem than cooling of the wing leading edge. This is due to the fact that the cowl must have a small bluntness radius.

From [3], it follows that the maximum heat flux is located on the cylindrical surface in the vicinity of the generatrix with a central angle of about 20°. However, the preliminary investigations performed at TsAGI in 1994 have shown that in some cases the heat flux can reach greater values at farther distances from the symmetry line, on generatrices with the central angle of $36-42^\circ$. Hence, an intensive cooling is needed for a greater region than it was assumed earlier.

The heat flux in the interference region on the cylindrical bluntness with a small radius is so high that it exceeds the heat flux which can be taked off from the inner wall surface by pumping a coolant. Apparently, this explains that Holden at all [4] investigated the interference region cooling by means of gas injection. Gas was injected through the perforating holes located on the front cylinder surface facing a free stream flow. It was shown that even at a large intensity of injection a substantial decrease in the heat flux in the presence of interference takes no place. Partly, this is due to a deep penetration of injectant into a free stream and its moving away from the protected surface. It is also of great importance that fact that a pressure peak is formed in the interference region. Due to this, the inflow of the cooling gas into this region is less than into the near located regions where as there is a need for the active cooling of the interference region. That is why it is not reasonable to expect a substantial positive effect due to gas injection normal to the surface even at low injectant velocities.

In this work, a tangential injection of the cooling gas on the nose surface of the cylindricaly blunted body is investigated. It can be assumed that at rather large injectant momentum it can penetrate into the interference region.

There are many articles devoted to study tangential gas injection at subsonic and supersonic speeds. Almost in all papers, a gradient−free flow on the plate or cone surface is studied [5, 6]. There is only one article which studies the effect of a tangential injection on the heat transfer in the shock wave interference region [7]. The type VI interaction on a plate was investigated. But it is known, that this case

does not lead to an essential increase in pressure and heat flux. An essential decrease in heat flux was not attained because the injectant did not penetrate into the interference region even at a moderate strength of the planar impinging shock wave $\beta > 7.5°$, Fig. 1.

The given work is devoted to the problem of cooling a cylindrical surface by means of tangential injection in regions of types III and IV interference which are characterized by maximum increase in pressure and heat flux. Such a study is performed for the first time.

The experimental study was performed in the TsAGI UT−1 shock wind tunnel at a free stream Mach number of 6 and Reynolds number of $Re_\infty = 0.19 \times 10^6$. The experiments were conducted at two injection slot locations: in the symmetry line and at a rather far distance from the symmetry line. The impinging shock wave location with respect to the cylindrical surface, the coolant mass flow rate and other parameters were varying. The experiments have shown that the tangential gas injection can provide cooling of the interference region. A correlation parameter which permits evaluation of the required coolant mass flow rate was found.

The experience of studying the shock wave interference flow without injection has shown that calculations of the inviscid gas flow qualitatively and correctly describe a lot of the flow singularities and facilitate the experimental result interpretation. For this reason a numerical simulation of the interference flow with tangential gas injection was performed in this work. It has shown the effect of gas injection on the shock wave structure at the front body surface and revealed the region where the cooling gas penetrates.

1. Experimental equipment

1.1. UT−1 wind tunnel. Flow parameters

The tests were conducted when the tunnel was operating in a Ludwieg tunnel version. The main elements this version of the UT−1 wind tunnel are (Fig. 2): 1 − chamber equipped with the external resistance heater for heating a working gas up to $T_0 \leq 870$ K, 2 − diaphragm, 3 − set of contoured nozzles, 4 − test section (D=0.5 m), 5 − exhaust passage, 6 − window .

The tests were performed under following parameters: air was used as a working gas, the free stream Mach number of 6.03, the total pressure $P_0 = 20$ bar, the stagnation temperature $T_0 = 570$ K, the nozzle exit section diameter D=0.3 m.

During the tunnel running, the gas pressure and temperature upstream of the nozzle throat before the rupture of diaphragm were measured. The initial model temperature and its change during the experiment were measured too.

1.2. Flow visualization system

The UT−1 wind tunnel is equipped with several flow visualization systems. There is an optical system designed for taking a shadow photograph of the flow pattern over models. The maximum exposure dimension in single photographing is 180 x 140 mm. When photographing 1000 frames per second, the exposure diameter is equal to 15.5 mm. The exposure time is 10^{-6} s.

At the above parameters the flow is characterized by the high gas density gradients, that leads to essential deflections of the light rays. That is why there is no need for a high sensitivity for the flow visualization. The most suitable method for this case is a direct shadow method. The preliminary tests with application of the direct shadow visualization method have shown that at the chosen high air pressure sensitivity of the shadow method appeared to be excessively high. This manifested itself in an excessive image width of shock waves and image distortion of the model shape.

For providing the necessary sensitivity the direct shadow method was improved (Fig. 3) by introducing the lens 5 with the focal distance f=500 mm and light beam diameter of 110 mm. This lens was installed so that the focal plane optically conjugated with the film plane was inside the tunnel. In testing of the improved direct shadow method an optimal location of the focal plane was chosen.

During these tests the beam of the parallel light rays was create by the lighting part of the shadow device with the full light field diameter of 210 mm. A pulse lamp with a burst time of the order of 10^{-6} s was used as a light source. A round diaphragm with diameter of 2 mm was used in the illuminator.

1.3. Gas supply system

The main system elements for supplying gas to the model are (Fig. 4): cylinder 19 with capacity of 40 , valve 17 for filling the cylinder, pressure−relief valve 18 (into atmosphere), quick−action electropneumatic valve 13.

The cross−sections of all system elements essentially exceeds the minimum slot section of the basic model 1 $f_j = 98$ mm^2; other models had a smaller area f_j. Because of this the gas velocity in the system ducts was essentially lower than the sonic velocity (sonic velocity is attained only at the slot exit section). Testing of the system and model with the slot cross−section of 98 mm^2 has shown that the hydraulic resistance of the supplying system constitutes only several percents of the hydraulic resistance of the model.

The maximum gas pressure in the system is 150 bar. The valve (13) turn on/off is synchronized with the wind tunnel operation and data acquisition and measuring system. The time of achieving the pressure in the model was about 0.02 s.

The gas pressure P_j and temperature T_j in the supplying system (transducers 15 and 16 respectively) and at the model entrance (transducers 8 and 9) were measured. Pressure transducer 8 has a low response time ($\tau = 2$ ms).

1.4. Models and shock generator

The model scheme and basic dimensions are shown in Figs. 5 and 6. The model is fixed on the pylon 7 (Fig. 4) by means of a cylindrical holder 6. The pylon can move along the rails .

The planar impinging shock wave generator (wedge) 1 is fixed in the slide 21 by means of pylon 22. The slide can be moved along the rails in the direction of the x − axis. In addition, the wedge can be moved in the y−direction. The setting accuracy of the dimensions x, y between the wedge and the plate is equal to 0.05 mm.

The flow deflection angle (the wedge surface angle) was equal to 15° in this experiment. The maximum heat flux complification in the interference region corresponds approximately to this flow deflection angle. The model and shock wave generator dimensions were chosen as large as possible provided that a flow choking does not occur in the UT−1 tunnel.

The model consists of the plate with cylindrical bluntness 2, removable injection device 1 and compensator 3 (Fig. 5). The compensator is designed for decreasing the lift force acting on the model and pylon.

The injection device was manufactured in 4 versions, Table 1. The first version of the injection device (model 1) is the basic one (Fig. 6a) and provides gas injection in the direction to the lower plate surface (to the model stern). The slot exit section was located near the symmetry line of bluntness, $\varphi_j = +4°$. The slot height was $h_j = 0.63$ mm. The slot was at the distance $h_v = 1$ mm from the model surface. The outer surface of the injection device (model 1) is at the distance $h_w = 2.1$ mm from the model surface in the slot exit section. When selecting the dimensions of the injection device the essential jet expansion at a high injectant pressure was taken into account.

Models 2 and 3 differed from model 1 mainly in the slot height: $h_j = 0.23$ and 0.15 mm, respectively. For models 2 and 3 the distance from the outer injection device surface to the model surface is equal to 1.6 mm and the angle $\varphi_j = +6°$.

Since the angle φ_j for models 1÷3 angle is small, further their angle is taken as $\varphi_j = 0$.

Model 4 was designed to study injection in direction to the symmetry line. In this case the injection device was installed on the lower surface of the plate (Fig.6b). The slot exit section was at the angle $\varphi_j = -33°$. That is why the compensator was installed on the upper surface of the plate. The slot height for this model was 0.25 mm and the distance from the outer injection device surface to the model surface was 1.6 mm.

Change of gas mass flow rate with the total injectant pressure (pressure in the supply system cylinder) is approximately of a linear character (Fig.7). It should be noted that while constructing these functions much more amount of experimental data was used as it can be seen from the figure because many of these data practically coincide in their absolute value. The deviation from a linear function is associated with the presence of a thick boundary layer in the slot throat section. This experimental result is confirmed by the performed evaluations of the boundary layer detachment thickness.

The presence of a thick boundary layer in the injection slot duct led to a substantial decrease in a mass flow rate through the slot as compared to the design inviscid gas mass flow rate. For this reason, for data analysis we use a notion of the effective slot height $h_j* = G_j/\rho_j* u_j* b$, where G_j, ρ_j*, u_j*, are the mass flow rate, density, velocity of injected gas in the slot throat section (by sound velocity), b is slot length along the bluntness generatrix.

With increasing the injectant pressure P_j the boundary layer thickness decreases, this result in increase of the effective slot height h_j*. Figure 8 shows the effect of the ratio of the effective slot height to the geometric height h_j*/h_j. It is seen that the effective slot height at a rather high injectant pressure $P_j \geq 3.5$ bar is approximately constant. In further analysis we use experimental values of the effective slot height.

1.5. Model instrumentation

For heat flux measuring the "thin wall" technique was used. This method was implemented in the following way: to the cylindrical model surface in the vicinity of the plane of symmetry a foil strip of 21 mm width was soldered. A foil of 0.2 mm thickness made of stainless steel was used. At the sections 1 and 2 located at the distance of 4 mm from the symmetry plane the thermocouple wires 0.1 mm diameter were soldered to the internal foil side, Fig. 5. The wires were fabricated from the copel alloy. In the vicinity of the welding place, the wires were rolled off with the special rolls up to the thickness of $0.03-0.04$ mm. The coordinates of the wire welding are given in Table 2. In the places of welding the nonconventional thermocouple "copel−stainless steel" was formed.

Each thermocouple after its installation on the thin wall was calibrated. For this purpose a special impulse heat calibration installation developed at TsAGI was used. The installation allows the convective heat flux pulses to be produced onto the calibrated sensors with the increment period of $1-2$ ms. By means of this installation, the sensitivity coefficient $K = q/(du/d\tau)$ for each sensor was determined, where q is the density of the convective heat flux influencing the sensor, $du/d\tau$ is the derivative of the time history value of the output sensor signal. Such a calibration method for sensors allows all the factors influencing their sensitivity : real values of the thermo−emf, wire−heat leakage and heat leakage through the surrounding walls, intrinsic heat capacity of the sensor and so on to be taken into account. Calibration of the thermocouples on the thin wall has shown that the individual sensitivity coefficients from point to point on the thin wall change within the range of $\pm 5\%$, that provided in processing experimental results to use a common sensitivity coefficient averaged for the model.

1.6. Measurement recording system

Measurements, data recording and processing were performed by measuring computer complex (MCC).

The MCC consists of primary converters (pressure transducers, microthermocouples), multichannel amplifiers, data acquisition and distribution system on the basis of high−speed analog−to−digital converters and personal computer. The MCC also comprises means for calibration of rapid metrological inspection and measurement/ conversion channel.

Before the wind tunnel run the MCC provides measurement of the initial parameters which determine the wind tunnel regime. During run the MCC provides acquisition of data from sensors located in the model, wind tunnel systems and gas supplying system. During 10 minutes directly after the run, analysis of the primary results obtained on the computer display, data processing in the form suitable for the user and printout (hard copy) of curves and tables are made.

Main features of MCC

— measurement channels 128
— maximum sampling frequency .... 3000 per second *for each channel*
— maximum channel sampling rate .... 200000 channels/s
— input signal range (with amplifier)

.... from $\pm 0.....150*10^{-6}$ B to $\pm 0.....100*10^{-3}$B

— input signal range (without amplifier)

.........., 1.28 B, 2.5 B, 5.5 B, 10.0 B

— amplifier bandwidth .... 1000 Hz

— accuracy (depending on range of response)... $0.2 \div 0.5$ %

2. Processing techniques

A thin wall technique assumes that the process of the wall heating is governed by the heat balance equation in the form:

$$\rho c \delta (dT_w/d\tau) = h(T_o - T_w),$$

where ρ, c and δ are the density, the heat capacity and the wall material thickness, T_w is the wall temperature, T_o is the recovery temperature (i.e., the stagnation temperature in the present report), h is the heat transfer coefficient, τ is the time.

If we assume that the heat transfer coefficient does not depend on the wall temperature than the equation can be reduced to the form :

$$d\{\ln[(T_o - T_w)/ (T_o - T_{wb})]\}/d\tau = -h/\rho c \delta,$$

where T_{wb} is the initial temperature of the wall and having made integration we have a solution:

$$(T_w - T_{wb})/ (T_o - T_{wb}) = 1 - e^{-h\tau/\rho c \delta}.$$

Using in calculations the experimental temperature values recorded at different moments the results can be greatly influenced by the interference caused by various random processes.

For smoothing the curves of heating k — spline approximation by means of the least squares method was used [8]. For this purpose, from the results of measurements of the wall temperature a sequence of the values:

$$J_k = \ln\{[T_o - T_w(\tau_k)]/ (T_o - T_{wb})\},$$

was calculated, which then was approximated by spline as the time function $f(\tau)$. Then at the moment τ we have:

$$h = -\rho c \delta [df(\tau)/d\tau],$$
$$q = h(T_o - T_w).$$

As a rule second — order splines were used i.e., the piecewise linear functions. The spline nodes were picked up from the point of view of physical considerations. For example, for the regime $P_o = 20$ bar and $M_\infty = 6$, the steady flow period is 40 ms, the setting period of the steady wall regime is 5 ms. So, the nodes were located at the points $\tau = 0$, 2.5, 5.0, 20 and 40 ms. In the cases of in adequate approximation the node location and number were changed. In some cases higher order splines were used.

The distribution of the heat flux density over the blunted body surface without injection slot in impinging shock — bow shock wave interference is presented as the ratio q/q_{so}. Here q_{so} is the heat flux in the symmetry line without injection. The value q_{so} depends on the surface temperature T_w. So, for each sensor the value of its own q_{so} was used, which was determined by conversion of the experimental results by the formula:

$$q_{so} = kP_{so}^{0.5}(i_o - i_w),$$

where k is the coefficient obtained during the cylindrical blunted body tests without the shock generator at the same nominal values of P_o, M and some value of T_w, P_{so} is the total stagnation pressure downstream of the normal shock wave at the real value P_{so} in the given experiment, i_o is the total enthalpy, i_w is the gas enthalpy at the wall temperature T_w at the moment of measuring heat flux in the presence of the shock generator.

If to assume that heat exchange is governed by a convective law i.e.:

$$q = h(T_o - T_w) \quad \text{at} \quad h = \text{const,}$$

then

$$q/q_{so} \approx h/h_{so}.$$

To determine values of the coefficient k the investigation results of heat exchange on the isolated cylinder surface were used. Distribution of the heat flux $q(\varphi)$ was approximated by the $4-$order splines.

Numerical calculations and experiments have shown that in the experiments conducted the longitudinal heat overflow along the wall practically has no influence on the results of the heat flux measurements.

3. Results of experimental study of gas flow and heat transfer in absence of impinging shock

The experimental study was performed in air flow at the free stream Mach number of 6.03, stagnation pressure $P_o = 20$ bar, the stagnation temperature $T_o = 570$ K, Reynolds number $Re_\infty = \rho_\infty u_\infty R / \mu_\infty = 0.19 * 10^6$, where ρ_∞, u_∞ and μ_∞ are the gas density, velocity and viscosity in the free stream, R is the radius of the cylindrically blunted body. For a shock generator, a sharp wedge with the angle $\theta = 15°$ was used.

Gas was injected through a tangential slot located either in the symmetry line of the blunted body $\varphi_j = 0$ or at a distance of $\varphi_j = -33°$ from the symmetry line. In the second case gas was injected in the direction to the symmetry line. In both cases gas was injected into the region of the shock wave interference.

Air was mainly used as an injectant. In one set of experiments helium was applied. The shock generator location, the slot location, the slot, height, and the injectant pressure were varied.

The slot normalized heights were as follows: $h_j/R = 0.042$ at slot location of the exit section $\varphi_j = +4°$; $h_j/R = 0.015$ and 0.01 at $\varphi_j = +6°$; $h_j/R = 0.017$ at $\varphi_j = -33°$, Fig. 6.

The injectant pressure in the cylinder P_j was from 1 bar to 42 bar.

3.1. Step effect on flow and heat transfer

Presence of the step, which is formed by installing of the injection device, can result in change of the flow and heat flux to the bluntness surface. Figures $9-11$ present the shadowgraphs of models 1, 2 and 4 with and without injection $(P_j = 0)$, respectively.

The shadowgraphs does not allow us to reveal in details the flow pattern near the step. However, a shock wave of a small strength is seen on model 2, it impinges on the cylindrical surface from the step edge, Fig. 10. This shock wave is induced by the technological step bevel with angle $\gamma = 10°$ and 2.6 mm long on the given model, Fig. 6.

On model 4 upstream of the step located at the angular distance $\varphi_j = -33°$, a small separation region with a corresponding weak shock wave is formed, Fig. 11.

Some supplements to the flow pattern can be made on the basis of analysis of the heat flux distribution (Figs. $12-14$). If the step is located near the symmetry line, then the stagnation line is apparently displaced from the symmetry line to the surface of the injection device. Gas flowing from the stagnation line downstream (in direction of negative values of the angle φ) separates from the step edge and attaches the cylindrical surface at some distance from the step (Fig. 10). In the narrow separation region the heat flux is smaller and at the reattachment line (at from $\varphi = -3°$ to $\varphi = -6°$) it is greater than on the cylindrically blunted body surface (Fig. 13). The greater is the step height the longer in the separation region. The bevel γ on the model 2 (Fig. 6) results in additional increase of the heat flux.

decreases. Upstream of the step a separation region causing a substantial heat flux decrease is formed (region $\varphi = -25^{\circ}$, Fig. 13). The separated boundary layer attaches the surface of the injection device where the heat flux was not measured.

3.2. Injection effect on flow and heat transfer

3.2.1. Slot in the symmetry line, $\varphi_j = 0$

The shadowgraphs of the flow pattern are presented in Figs. 9 and 10. It is seen that even at low injectant pressure P_j (at low mass flow rate G_j), the injectant pushes aside the main stream flow and changes the "effective" shape of the body bluntness. At low values of the injectant flow rate $G_j^* \leq 0.11$ ($P_j \leq 1.94$ and 3.75 bar for models 1 and 2, respectively) the effective shape of bluntness is close to cylindrical. It happens because of the fact that the injectant layer thickness and the step height are approximately equal. However, such a coincidence is likely possible only in a rather narrow range of the injectant mass flow rate.

At high values of $G_j^* \geq 0.4$ (for example, at $P_j \geq 20$ bar on model 2) the injected jet after its expansion exceeds the step height and the effective shape of the bluntness noticeably differs from a cylindrical one.

At a very high mass flow rate $G_j^* \geq 1.6$ the bow shock wave is "washed away". This indicates that at such values of injection noticeable fluctuations of the compressed gas thickness can be observed between the bow shock wave and the bluntness surface.

The heat flux distribution at different injectant pressures is shown in Figs. 15 and 16 for models 1 and 2, respectively. It is seen that even at low values of the injectant pressure a noticeable reduction in the heat flux occurs over all bluntness surface. At the coolant pressure of 1.69 bar and more the bluntness surface near the slot was not heated but cooled that is the heat flux values were negative. This took place because the model temperature before the experiment was somewhat higher than the stagnation temperature of the injectant.

With increasing the coolant pressure the heat flux maximum is displaced to the model stern. This is due to decrease in effectiveness of injection with increasing the distance from the slot. Here, effectiveness is implied as the value $1 - q/q_o$, where q is the heat flux at the surface point with injection and q_o is the heat flux at the same point without injection.

Change of the ratio q/q_o characterising the injection effectiveness with the angular distance is illustrated in Figs. 17 and 18. At low injectant pressure, it decreases with increasing the distance from the slot. At the high injectant pressure the injection effectiveness on a greater part of the cylindrical bluntness is close to 1, that is the ratio q/q_o is close to zero.

3.2.2 Slot at a distance from the symmetry line, $\varphi_j = -33°$

For this case the flow pattern (Fig. 11) is essentially different from the above flow pattern. Even at a rather high pressure $P_j = 3.81$ bar which essentially exceeds the pressure downstream of the normal shock wave $P_{so} = 0.543$ bar ($P_j/P_{so} = 7.0$, run 7282), the injected jet cannot overcome the dynamic pressure of the main flow, it turns back and travels in the model tail direction. The injected jet somewhat distorts the bow wave shape near the step.

At a higher pressure $P_j = 6.54$ bar ($P_j/P_{so} = 11.6$) the injected jet not only reaches the line of symmetry but goes further and travels along the leeward bluntness surface to the model tail (Fig. 6b). With increasing the injectant pressure up to $P_j = 7.58$ bar the character of the flow pattern does not change. In this case the bow shock wave shape approximately corresponds to that in flow over cylindrical bluntness.

At a more high injectant pressure $P_j = 15.1$ bar the bow shock wave shape in the leeward region of the bluntness is distorted and its nonstationarity features appear.

The heat flux distribution corresponds to the flow pattern described. It essentially depends on the injectant pressure, Figs. 19 and 20. At $P_j = 3.81$ bar injection practically does not change the heat flux to the bluntness surface in the region of

$\varphi \geq -20°$ since the injectant does not get there. With the pressure increase up to $P_j \geq 7.58$ bar an essential decrease in the heat flux is observed over the whole model bluntness; the injection effectiveness $1 - q/q_o$ is close to 1 on the windward surface (up to the symmetry line). At $\varphi > 0$ it decreases, however the injection results in substantial decrease of heat flux on the leeward surface even at $\varphi > 40°$.

Comparison of the presented results shows that gas injection through the slot located in the symmetry line (i. e., injection in the main flow direction) leads to a substantially greater decrease in the heat flux than injection through the slot located at a distance from the symmetry line (i. e., injection facing the main flow) , Figs. 21, 22.

4. Results of experimental study of gas flow and heat transfer in presence of impinging shock

4.1. Step effect on flow and heat transfer without injection

4.1.1. Step in the symmetry line, $\varphi_j = 0$

The shadowgraphs of the flow patterns without injection are presented the first at each Figs. 23.÷28 with the inscription $P_j = 0$.

At a large distance between the impinging shock and the bluntness $X^* = 1.24$ the type IVa interaction is realized, Fig. 23. The high dynamic pressure jet H, which is formed as a result of the impinging shock/bow shock wave interference, gets on the injection device. The flow features such as: expansion waves and local shocks at deflection of the high dynamic pressure jet, a shock wave at the junction point of the compensator and the cylindrical blunted body and so on are clearly seen in the photo. Some additional flow distortions are caused by the model edge effects but they are simply distinguished from the main flow part.

Approach of the planar impinging shock to the model at a distance of only $\Delta X^* = 0.11$ resulted in change of the interaction type: the type IV interaction is formed, Fig. 24. A flow separation is noticeable upstream of the step. Flow of the low entropy jet portion is clearly seen directly behind the step.

A further detachment of the planar shock wave up to $X^* = 0.86$, Fig. 25, and further up to $X^* = 0.53$, Fig. 26, qualitatively does not change the flow pattern near the step. It is only seen a decrease in the flow distortions near the step. At $X^* = 0.53$ a separation region upstream of the step is clearly seen. At $X^* = 0.33$ the flow similar to the type III interaction is formed. The gas flow distortions near the step are almost unobserved, Fig. 27. In our experiments at a minimum value of $X^* = 0.23$ the type III interaction was realized, Fig. 28.

Thus, analysis of the shadowgraphs shows that the step presence in the symmetry line mainly results in formation a separation region ahead of the step. Change of the impinging shock location can have a noticeable effect on the important flow elements:

— The bow shock wave detachment from the bluntness X_w is practically independent on variation of the distance between the impinging planar shock and the bluntness X^*, Fig. 29.
— The minimum distance between the bow shock wave and the body surface X_1 essentially decreases (1.5 times) with increase of the distance between the impinging shock and the bluntness from $X^* = 0.33$ to $X^* = 0.86$, Fig. 30.
— The transmitted shock length L_1 at a great distance between the impinging shock and the bluntness is practically independent on X^*, Fig. 31, at $X^* < 0.5$ the length L_1 strongly increases (approximately 1.5 times) manifesting change of the interference.

The heat flux measurements results on model 1 are presented in Figs. 32÷34. The heat flux value is normalized by the heat flux value in the symmetry line of the same model without the injection device and compensator. The maximum heat flux value was observed at the shock location $X^* = 0.40$, Fig. 33. The maximum normalized heat flux is equal to $q/q_{so} = 9.24$, it was located on the generatrix at $\varphi_m = -37°$ (Fig. 34). The heat flux distribution in the vicinity of the peak point is symmetric, Fig. 32, $X^* = 0.33$; value $q/q_{so} = 2.5$ corresponds to move away from the peak to the both sides $\varphi_m = \pm 15°$. Indirectly, this indicates that a small step on the bluntness in the region $\varphi_j = 0$ has no substantial effect on the heat transfer at the peak point. It should be noted that the maximum heat flux for the type IV interaction($X^* = 1.13$) is smaller than for the type III (X^* is from 0.53 to 1.13).

At the impinging shock positions $X^* > 1.13$ the type IV interference turns to the type IVa interference, Figs. 23, 24. It result in abrupt change of the position of the heat transfer peak, Fig. 35.

The effect of the normalized step height h_w/R and its location φ_j on the flow in the presence of the impinging shock at different shock wave locations X^* can be revealed on the basis of comparison of the flow pattern shadowgraphs Figs. 23÷28, 35, 36 as well as the results of the heat flux measurements. In analysis it should be taken into account that models 2 and 3 differ only in the slot height and this has no effect on the flow without injection.

Comparison of the shadowgraphs of models 2 and 3 ($h_w/R = 0.140$, $\varphi_j = 0$) and model 1 ($h_w/R = 0.173$) shows that variation in the step height practically did not change the character of the flow over the bluntness.

A decrease in the step height from $h_w/R = 0.173$ (model 1) to $h_w/R = 0.140$ (model 3) does not cause change in all above−mentioned characteristics of the flow elements: the bow shock wave detachment X_w, the minimum distance between the transmetted shock and the bluntness surface X_1 and the transmitted shock length L_1.

The maximum heat flux values depending on the shock location X^* and the heat flux peak location φ_m are also well agreed with each other, Figs. 32, 33.

4.1.2. Step at a distance from the symmetry line, $\varphi_j = -33°$

Variation of the step location φ_j essentially effects the flow over the bluntness, Figs. 38, 25. Even at a rather small distance between the impinging shock and the bluntness $X^* = 0.65$, the high dynamic pressure jet H is deflected upward, i. e., the type IVa interaction is realized. At $X^* = 0.44$ the type IV and not type III interaction is realized as it happens with the step in the symmetry line and without step. With the further decrease in the distance between the impinging shock and the bluntness up to $X^* = 0.30$ the flow pattern does not change qualitatively.

Variation of the step location from $\varphi_j = 0$ to $\varphi_j = -33°$ practically did not change the bow shock wave location, Fig. 29. However, minimum distance between the transmitted shock and the bluntness surface X_1 at $\varphi_j = -33°$ noticeably increased, Fig. 38: approximately by a factor of 0.25, i. e., it is more than by the step height ($h_w/R = 0.14$). The transmitted shock length L_1 essentially decreased, Fig. 31: approximately by a factor of 1.8, this is indicative of a substantial change of the flow pattern with injection through the slot at $\varphi_j = -33°$ in comparison with injection through the slot at $\varphi_j = 0$.

The heat flux maximum is realized at the shock location $X^* = 0.44$, Figs. 39, 33. In this case the maximum value is by 16% less than with the step location in the symmetry line. That is why the further experiments with gas injection on model 4 ($\varphi_j = -33°$, $h_w/R = 0.14$) were performed at the impinging shock position $X^* = 0.44$.

The heat flux maximum location at the slot position $\varphi_j = -33°$ is approximately 20° closer to the symmetry line than it is at $\varphi_j = 0$ (Fig. 35).

Thus, variation of the step location resulted in essential change of the flow pattern near the bluntness and a small decrease in the heat flux to the body surface.

4.2 Injection effect on flow and heat transfer

Injection was studied at the injectant pressure $P_j = 3.5 \div 30.2$ bar, the normalized pressure $P_j^* = P_j/P_{so} = 6.6 \div 54.2$, the normalized mass flow rate $G_j^* = G_j/\rho_\infty u_\infty b = 0.35 \div 2.29$ and the normalized jet momentum $I_j^* = \rho_{je} u_{je} h^2 / \rho_\infty u_\infty^2 R = 0.017 \div 1.43$, Table 3. Air was mainly used as an injectant. In one series of experiments helium was used.

The distance X^* btween the lanar impinging shock and the bluntness was varied from 0.23 to 1.13. The normalized slot height was $h_j/R = 0.042$ at the slot location $\varphi_j = +4°$ (model 1), $h_j/R = 0.01$ at $\varphi_j = +6°$ (model 3), $h_j/R = 0.017$ at $\varphi_j = -33°$ (model 4).

4.2.1. Slot in the symmetry line, $\varphi_j = 0$

The shadowgraphs are presented in Figs. $23 \div 28$ and 36, 37. A detailed quantitative analysis of photographs was performed. The following values characterizing the flow pattern: the distance X_m (between the bow shock wave and the bluntness surface in the symmetry line), the minimum distance X_1 (between the transmitted shock and the bluntness surface) and the transmitted shock length L_1 were determined. These data are useful for interpretation of the heat flux measurements results. They can be also used for testing of the calculation methods. In the last chapter the flow pattern calculation results are compared with the experimental data.

The shape of the injected jet changes substantially depending on the pressure P_j. At a moderate pressure (up to $P_j = 15.3$ bar, Fig. 25b) the boundary and the symmetry plane of the injected jet near the slot are parallel to the front model surface or inclined to it at a small angle ζ, Fig 1. With increasing pressure up to 30.2 bar the boundary and the symmetry plane of the injected jet are substantially deflected from the front model surface. This is due to the fact that after ejection from the slot the jet width is essentially greater than the slot height because of the pressure drop in the jet and because of its mixing with an external flow. At a high pressure $P_j = 30.2$ bar barrel shock waves near the jet boundaries, Mach disk and other flow details of the injected jet are clearly seen in the photographs.

Analysis of the shadowgraphs as well as the calculation presented below show that there exit 3 types of injectant effect on the interference flow:

1. At an insufficient injected jet momentum the injectant does not penetrate onto the windward body surface. Meeting the high dynamic pressure jet H (Fig. 40) the injectant is deflected upward and overflows to the leeward body surface. The bow shock wave detachment X_w increases and the triple point 1 displaces downstream.

2. At a greater injected jet momentum (Fig. 1) one jet portion is again deflected upward and overflows onto the leeward body surface and the other jet portion penetrates to the windward body surface through the high pressure region of the interference region. In this case, not only geometrical flow characteristics change and the interaction type itself changes as well (see Fig. 26): the type IV interference when the high total pressure jet strikes the body surface, transits into the type III flow when a mixing layer strikes the body surface.

3. At a very high injected jet momentum the bow wave/impinging shock interference practically has no effect on the flow over the front model surface: the front model surface is wetted by the jet ejected through the slot and by the gas passed only through the bow shock wave.

Dependence of the bow wave detachment value X_w on the injectant mass flow G_j^* is presented in Fig. 41. The bow wave detachment increase with injection is approximately proportional to the quantity of the injected gas overflowing on the leeward bluntness surface.

At a rather large distance between the impinging shock and the bluntness $X_j^* \geq 0.53$ and at a minimum injection $G_j^* = 0.28$ the additional bow shock wave detachment δX_w is approximately proportional to the additional injected gas. This is due to the fact that the injected gas momentum is insufficient for penetrating the shock wave interaction region and practically all injected gas flows along the leeward bluntness surface.

At a small distance between the impinging shock and the bluntness $X^* \leq 0.33$ the bow wave detachment X_w is essentially less than at $X^* \geq 0.55$ at all injection rate. This is due to the fact that $X^* < 0.33$ the injected jet moves away the high dynamic pressure jet H and a larger part of the injected gas flows along the leeward surface.

These conclusions are confirmed by a character of dependence of the minimum distance between the transmitted shock and the bluntness surface X_1 on the flow rate G_j^*, Fig. 42. The value of X_1 depends on the quantity of the injected gas flowing along the windward bluntness surface and on the type of shock wave interaction as well.

At a large value of $X^* \geq 0.86$ and a weak injection $G_j^* = 0.27$ the injection leads to decrease in the value X_1^*. This occurs because the high dynamic pressure jet is displaced downstream of the flow increasing the gas density in the minimum passage section and does not allow the injected gas to flow on the windward model surface.

At a small value of $X^* \leq 0.33$ and a weak injection $G_j^* = 0.27$ the injection leads to an essential increase in the value X_1^*. This is evident of increasing the quantity of the injected gas flowing on the windward bluntness side.

With further increase in the injection mass flow and injection momentum for all values X^* the minimum distance between the bow wave and the bluntness X_1 increases approximately proportionally to increase in mass flow of the injected gas. This is evident of increasing the quantity of the injected gas flowing on the windward bluntness side.

The transmitted shock wave length L_1 is approximately proportional to the gas quantity entering the mixing layer. The value L_1 is greater in case of a small and large injection in comparison with a mean injection, Fig. 43. This is evident of an essential change of shock wave interaction structure with injection rate.

Now let us consider the heat flux measurement results with injection. As an example change of the absolute value of the heat flux q with the angle φ at the largest distance of the impinging shock from the bluntness surface $X^* = 1.13$ is presented in Fig. 44. From the results presented it follows that the spacing thermocouples is sufficient small, this allows all heat transfer peculiarities including the narrow heat flux peaks to be revealed.

For convenience, further the heat flux values are normalized by the heat flux on the symmetry line of the cylindrical bluntness without an injection device and injection itself.

The key results of the heat flux measurement are presented in Figs. 44÷49. The heat transfer with a tangential gas injection into the shock wave interference region is qualitatively different from the heat transfer with a tangential injection into a uniform gas flow. In the second case a maximum decrease in the heat flux occurs at the initial jet part near the slot exit where there is an inviscid core in the injected jet. Downstream of the initial part the injection effectiveness monotonously decreases because of the jet mixing with the external flow. At injection into a uniform flow cooling is attained due to shielding the surface with the cold injected gas.

At gas injection through the slot into the shock wave interference region two factors influence the heat transfer:

1. The jet injection changes the flow pattern as described above. A decrease in the heat flux with injection takes place because of the pressure decreasing in the interference region and also due to decreasing the angle of meeting of the high dynamic pressure jet H or mixing layer with the body surface. The jet effect on the heat transfer depends not only on its characteristics but on location of the impinging shock and its strength as well.

2. The jet shields the body surface from effect of the hot free stream gas flow in the same way as in injection into a uniform flow. However, the length of the affecting region of the injected jet depends on the interaction of the shock waves and pressure in the interference region.

The joint action of both factors can lead to nonmonotonous change in the heat flux while moving away from the slot.

Due to the injection effect the heat flux peak is displaced to the side of negative values of the angle $φ_m$. The peak detachment is especially satisfactory substantial at a great distance between the impinging shock and bluntness. For example, at $X^* = 0.86$ (Fig. 46) without injection the heat flux peak is on the generatrix $φ_m = -20°$ and at a comparatively low pressure of the injected gas $P_j = 3.79$ bar it is on the generatrix $φ_m = -42°$ (run 7247).

There are positions of impinging shock $X^* \geq 0.86$ when small injection can lead not to decrease but to increase in the maximum heat flux. It is seen in Figs. 46 and 50 where the normalized heat flux is presented as a function of the normalized mass flow rate. In this case an increase in the heat flux is due to change in the flow pattern with the interference region detachment: the strength and quantity of the shock and

expansion waves change in the interference region. However, a strong injection results both in the peak detachment and decrease in the maximum heat flux as well.

The ratio of the local heat flux with injection to the heat flux at the same point without injection is essentially greater than 1 in many cases. The apparent negative effect of injection on the heat transfer is associated with the heat flux peak detachment.

Fig. 50 illustrates a strong effect of the impinging shock location on the degree of the maximum heat flux decrease due to injection. At a far shock distance ($X^* = 1.13$ and 0.86) the decrease in the heat flux is relatively small (as pointed out above, a small injection can result even in increase of heat transfer). This is due to the fact that at these shock locations a high dynamic pressure jet H is formed in the interference region (the type IV interaction), for whose deflection a high dynamic pressure of the injected jet.

At the smaller shock distances ($X^* = 0.53$, 0.33 and 0.23) when type IV interaction transits into type III injection leads to a substantially greater decrease in the maximum heat flux despite that in this case the interference region is essentially further from the slot than it is in the previous case. The gas injection has a greater effect in the absence of the impinging shock because the injected jet must not overcome the high pressure region counteraction.

From Fig. 50 it is seen that at all shock positions the maximum heat flux can be reduced up to a normal level, corresponding to the case without interference and injection. However, in the presence of the shock wave interference the required injectant mass flow rate is many times greater than in the absence of interference.

At all shock positions a strong injection displaces the heat flux peak into the region of high negative values of the angle φ_m ($\varphi_m \approx -60°$, Fig. 51).

4.2.2. Helium injection, $\varphi_j = 0$

To reveal the effect of the injected gas characteristics a series of experiments is performed with injection of helium at a distance between the impinging shock wave and the bluntness $X^* = 0.53$. The transition flow from the type IV to the type III interaction when the heat flux reaches its maximum corresponds to this. The shadowgraphs of the flow patterns at the different injection pressure are presented in Fig. 52. Due to a large difference in the air and helium density some flow features with helium injection are seen more clearly than with air injection.

The normalized values characterizing the bow wave detachment X_w, the minimum distance between the transmitted shock and the model surface X_1 and the transmitted shock length L_1 are presented in Figs. 53÷61. They are presented depending both on the normalized mass flow rate G_j^* and normalized momentum of the injected jet I_j^* and normalized volume flow rate $V_j^* = G_j/\rho_{je}u_eRb$. It is seen that the geometric flow characteristics with helium injection are correlated with the similar characteristics with air injection if these characteristics are presented as functions Vs the normalized jet momentum. This means that the normalized jet momentum is a more universal parameter than the normalized mass flow rate.

The heat flux distribution $q/q_{so} = f(\varphi)$ with helium injection is qualitatively of a similar behavior as with air injection, Fig. 62. The normalized value of the maximum heat flux q_m/q_{so} is shown in Figs. 63÷65 as a function three nondimensional parameters: G_j^*, I_j^*, V_j^*. It is seen that effectiveness of the helium mass flow is higher than the air mass flow effectiveness (Fig. 63) and as to the volume flow rate it is lower (Fig. 65). The heat flux maximum values with injection of air and helium are well correlated with each other if we use the normalized jet momentum I_j^* as the determining parameter (Fig. 64).

The heat flux peak location φ_m for helium is also well correlated with the similar value for air if we use the normalized jet momentum I_j^* as the determining parameter (Figs. 66÷68).

It should be noted a satisfactory agreement between dependence of the maximum heat flux on the peak location $q_m/q_{so} = f(\varphi_m)$ for helium and air (Fig. 69).

4.2.3. Slot size effect, $\varphi_j = 0$

Investigations of gas injection through the slot of a smaller height $h_j^* = h_j/R = 0.01$ on the model 3 were performed at a distance between the impinging shock and the bluntness $X^* = 0.22$. The normalized slot height of the basic model 1 was essentially larger: $h_j^* = 0.042$.

The shadowgraphs of the flow patterns at the various injection pressure are presented in Fig. 37. In terms of quality the flow patterns with injection through the small slot $h_j^* = 0.01$ are the same as with injection through the slot of a larger size $h_j^* = h_j/R = 0.042$ (see Fig. 28), the experiments were performed practically at a similar distance between the impinging shock and the bluntness $X^* = 0.22$. It should be only noted that downstream of a small slot the jet thickness is noticeably less than it is downstream of a larger slot at approximately similar injection pressure P_j.

The typical flow element dimensions X_w, X_1 and L_1 are shown in Figs. 70÷75. From analysis of the data presented it follows that at various slot sizes the results are correlated essentially better when we use the normalized jet momentum as a determining parameter and not the normalized mass flow. It should be noted that according to evaluations the small slot had a substantially greater ratio of the boundary layer detachment thickness to its height than the slot of a larger size. In calculations of the injection momentum we have used the effective slot height which was calculated by the formula: $h_j^* = G_j/\rho_j * u_j * b$. Probably, in more accurate calculation of the momentum of the injected gas agreement of the geometric flow characteristics for slots of different height will be more satisfactory.

The heat flux distribution $q/q_{so} = f(\varphi)$ for the slot of a small height is approximately the same as for the greater slot, Fig. 76. However, the degree of decrease in the heat flux when using than small slot height is essential less than for the greater slot if the injection pressure is the same in both cases (Fig. 77). This is due to the fact that in case of the smaller slot height the mass gas flow and the jet momentum are less than in case of a greater slot height. The normalized maximum heat flux q_m/q_{so} is better correlated with the normalized momentum value I_j^* than with the mass flow value G_j^*, Figs. 78, 79. The heat flux peak location φ_m is equally well correlated with the both parameters (G_j^* and I_j^*, Figs. 80, 81).

4.2.4. Slot at a distance from the symmetry line, $\varphi_j = -33°$

The experiment was performed at a single location of the impinging shock $X^* = 0.44$, this approximately corresponds to a maximum heat flux without injection. The shadowgraphs of the flow pattern are presented in Fig. 38b and the geometric flow characteristics in Figs. 82÷84.

The flow pattern for gas injection through the slot located on the generatrix $\varphi_j = -33°$, i. e., on the windward model surface is essentially different from the flow with injection through the slot located in the symmetry line of the model $\varphi_j = 0$. In the case under consideration the injected gas is supplied from the region where a higher pressure dominates (it is located downstream of the impinging shock + normal shock flow system), into the region of a lower pressure (it is located downstream of the normal shock). That is why even at a low injection pressure the high dynamic pressure jet H is deflected on the leeward model surface and the type IV transits into the type IVa interaction which is characterized by a smaller heat flux (see below Figs. 85, 38).

The gas injection in a certain range of the pressure values P_j^* and mass flow G_j^* ($G_j^* \leq 0.2$) practically has no effect on the bow shock wave detachment (Figs. 38b, 82). This is due to the fact that the jet width does not exceeds the step height.

With further increase in mass flow the effective body thickness increases and the bow shock wave detachment increases too. Since the impinging shock location remains unchanged its intersection point with the bow wave moves away from the nose surface (Fig. 38, $P_j = 6.33$ bar); correspondingly, the transmitted shock is elongated and the high dynamic pressure jet H is displaced downstream and impinges on the injection device. Due to this, as shown below at $G_j^* > 0.2$, the heat flux downstream of the slot strongly decreases. However, in this case the heat flux maximum is apparently located on the injection device surface, i. e., in the region which is not protected by the gas injection (heat flux was not measured in this region). Thus, it follows that in gas injection from the windward surface the mass gas flow is limited by a certain value G_j^* and apparently this limitation depends on the impinging shock location.

The heat flux distribution $q/q_{so} = f(\varphi)$ is presented in Fig. 86. It is seen that the maximum heat flux to the model surface q_m/q_{so} with injection decreases. Even at weak injection $P_j = 3.5$ bar a decrease in the heat flux occurs at a substantial distance from the slot.

Change of the maximum heat flux q_m/q_{so} with mass flow of the gas injected through the slot located on the generatrix $\varphi_j = -33°$ is close to similar change for the case of injection trough the slot located in the symmetry line $\varphi_j = 0$, Figs. 87, 88. Consequently, the direction of injection at a chosen shock wave location has a weak effect on the injection effectiveness.

The heat flux peak location is practically unchanged with increase in mass flow up to the $G_j^* \leq 0.22$, Figs. 89, 90. This is in agreement with the flow pattern described above.

5. Numerical simulation of inviscid gas flow

5.1. Statement of problem

Numerical calculations were performed within the framework of two—dimensional time—dependent Euler equations for a perfect gas with a constant specific heats ratio. All calculations were carried out using the first order Godunovs scheme with respect to space and time. A design region representing the ABCDEFGH polygon inside space is depicted in Fig. 91. A calculation grid, its segment is depicted in Fig. 92, is composed of two quadrangles: ACGH (128x64 cells) and CDEF (128x54 cells). The calculation grid is movable everywhere except the FGHI quadrangle with dimensions 128x10 cells.

The boundary conditions are formulated in the following way: at the movable boundaries AB and BCD Rankine—Hugoniot conditions for nonstationary shock waves, on the external injection device surface EF and on the cylinder surface GH the conditions of zero flux through the surface, at the boundaries DE and HA extrapolation condition which practically means no influence of these boundaries in the presence of supersonic normal velocity component in the cells adjacent to these boundaries; at the boundary FG pressure, density and velocity of the gas injected normal to the FG line, are prescribed.

Gas is injected along the whole length of the FG line and not along its part. This is done to increase the number of calculation cells in the vicinity of the injection point and hence to improve the calculation accuracy as a whole. The parameter values of the injectant in the line FG were calculated using the theory of the quasi—stationary gas flow in the duct with the variable cross—section area. It was assumed that the duct throat section was equal to the slot exit section and the duct exit section was equal the step height over which injection was performed.

5.2. Calculation results

The free stream air parameters corresponded to its nominal values in experiments: the Mach number $M_\infty = 6$, the angle of the wedge used as a shock generator was equal to $\theta = 15°$, the total pressure $P_o = 20$ bar.

The key model dimensions in calculations corresponded to dimensions of model 1 in experiments: the normalized step height $h_w/R = 0.17$ and the ratio of the slot height to the step height $h_j/h_w = 0.24$ (model 1).

On the basis of preliminary calculations performed without injection at various positions of the impinging planar shock characterized by X^* (Fig. 91) the version with $X^* = 0.383$ was adopted.

A tomogram of the Mach number for this case is presented in Fig. 93. It is seen that in the conditions mentioned the type IV interference both without the step $(h_w/R = 0)$ and with the step $(h_w/R = 0.17)$ is realized. It is also seen that even without injection, presence of the step results in displacement of the low entropy jet downstream and, hence, a decrease of effect of the low entropy jet on the cylinder surface can be expected. This takes place due to the injection device displacement action. Without injection the flow is stationary both with and without the step.

Further a calculation series for various values of the total pressure of the injected gas $P_j = 16$, 32, 8 and 4 bar was performed. It was assumed that injection is performed along the whole length of the line FG (Fig. 91). At isentropic gas expansion from the slot throat section to the step height, the Mach number of the injected gas in this line is $M_{j\infty} = 2.74$, this approximately corresponds to the experiment conditions with the slot located in the vicinity of the symmetry line ($\varphi_j = +4°$, model 1).

The ratio of the stagnation injectant temperature to the stagnation main flow temperature in calculations was equal $T_{jo}/T_o = 0.5$, this approximately corresponded to the experimental values of this parameter too.

It is convenient to begin consideration of the injection effect with the case of the injection pressure equal to 16 bar (Figs. 94÷96) at which the flow is also stationary. This figure illustrates isolines of all main flow parameters: the Mach number, entropy, pressure, density, velocity in the free stream direction and normal to it, total velocity and Bernoulli number (full enthalpy), correspondingly. At the top of each tomogram a reference scale of the corresponding values is presented. All values are normalized by the free stream parameters.

It is seen that the injected gas pushed away the high pressure jet H from the bluntness surface. A portion of the injected gas overflows on the leeward side of the bluntness. The high pressure jet H is substantially displaced downstream. Only a small portion of the high pressure jet overflows on the leeward bluntness side. Qualitatively, this flow pattern corresponds to the obtained experimental results.

It is also seen that in the injected jet and in the main stream at a distance from the slot a strong shock is generated which induces a reversed flow of the injected gas part on the leeward bluntness side. The separation flow occurs on the external surface of the injection device near the slot, Figs. 95, 96.

A small separation zone of the injected jet is observed in the region Ψ where local pressure increase ψ is generated by the high pressure jet H. Both an increase and a decrease in the injection pressure.

According to calculations can result in oscillation of the flow parameters and flow element dimensions, in particular, the bow shock wave detachment X_w. The Mach number and entropy at the tomograms maximum and minimum values X_w for each calculated version of the injection pressure are presented in Figs 97÷99.

Fig. 100a presents the normalized amplitude of the bow shock wave detachment $\Delta X_w/X_w$, where X_w is the averaged value of the detachment with respect to time. According to the calculation, the oscillation amplitude attains maximum value at the pressure $P_j = 4$ bar. The fluctuation frequency is about 2000 Hz.

Oscillations were not investigated in this experimental study. At high frequency they could be determined either by a statistic method with a great number of experiments or by using the corresponding cinematographic equipment. The fluctuations of high order cannot be determined by measuring the heat flux to the surface due to a great lag of the heating process of the bluntness wall.

Injection results in substantial decrease of pressure on the greater surface part, Fig. 101. Because of this with a strong injection $I_j^* \geq 1.6$ ($G_j^* \geq 2.7$) an essential decrease in the aerodynamic bluntness drag takes place, Fig. 100b.

The calculation results are in rough quantitative agreement with the data. On Figs. $102 \div 107$ are compared the bow shock detachment X_w, minimum distance between the transmitted shock and the bluntness surface X_1, and the transmitted shock length L_{1_l}.

.... Maybe, the proposed calculation methodology can be used to obtain an additional information about the complicated processes occurring in injection into the shock wave interference region.

Conclusions

1. In absence of the impinging shock the tangential gas injection from the symmetry line results in an essential decrease of the heat flux to the cylindrically blunted surface: at the normalized mass flow $G_j^* = 0.05$ the maximum heat flux decreases by a factor of 5 and at $G_j^* = 0.2$ the heat flux is close to zero over the whole front surface under the slot because the injected gas moves away the free stream gas from the body surface.
In case of injection in the opposite direction (to the symmetry line), in order to achieve the similar cooling an essentially greater mass flow is needed.

2. In presence of the impinging shock the tangential gas injection from the symmetry line into the interference region essentially changes the flow pattern near the front body surface: the bow shock wave detachment increases, the shock intersection points move away from the symmetry plane; at a significant mass flow the type IV transits into the type III interference.

3. In presence of the impinging shock as well as in its absence, gas injection from the symmetry line can result in abrupt decrease of the heat flux over the whole front body surface, under the slot, including the interference region. However, to achieve the similar effect as without the impinging shock the cooling gas mass flow should be greater by an order.
The mass flow needed for cooling depends on the impinging shock location: at a large distance between the impinging shock and the bluntness a greater mass flow is needed than at a small distance.

4. A decrease in the slot height results in decrease of the heat flux to the body surface at the same mass flow of the cooling gas.

5. A decrease in the cooling gas molecular weight (when air is changed for helium) leads to decrease in the heat flux to the body surface at the same mass flow of the cooling gas.

6. The normalized momentum of the injected gas I_j^* can be used as a correlation parameter for describing the experimental results obtained at various values of the slot height and molecular weight of the injected gas. With increase in the jet momentum a decrease in the heat flux to the blunted surface is observed.

7. In presence of the impinging shock, the tangential gas injection through the slot removed from the symmetry line ($\varphi_j = -33°$) towards the symmetry line is approximately as effective as the injection through the slot near the symmetry line.

This conclusion is related to the investigated impinging shock locations ($X^* = 0.44$) and limited the mass flow rate $G_j^* \le 0.2$; at $G_j^* > 0.2$ the heat flux peak is displaced from the region protected by injection onto the injection device surface.

8. Calculation of the inviscid gas flow has allowed to reveal the mechanism of influence of the tangential gas injection through the slot located near the symmetry line on the interference flow:

— At relatively low injection rates (up to $G_j^* = 0.7$) the injected gas practically does not penetrate into the high pressure interference region but it moves away the

interference region from the symmetry line and can change the type of interference; in this case all injected gas is deflected to the leeward body surface.

— At high injection rates ($G_j^* \geq 1.4$) the injected gas completely moves away the free stream gas from the front body surface.

— According to numerical calculations, almost periodical flow fluctuations with frequencies of an order of 2 kHz occur in a wide range of the normalized mass flow values; experimental study of flow fluctuations was not performed.

— The averaged values of the bow shock wave detachment and other geometric flow characteristics obtained as a result of numerical calculation are in rough agreement with experimental data.

References

1. V.Ya.Borovoy, V.N.Brazhko, G.I.Maikapar, A.S.Skuratov, I.V.Struminskaya "Heat Transfer Peculiarities in Supersonic Flows" Journal of Aircraft, vol. 29. No. 6, Nov.— Dec. 1992

2. B.E.Edney " Effects of Shock Impingement on the Heat Transfer around Blunt Bodies" AIAA Journal, vol. 6, Jan. 1968, pp. 16—24.

3. A.Wieting "Shock Interference Heating in Scramjet Engines"
AIAA Paper No.90—5238, October 1990.

4. M.S.Holden, K.M.Rodriguez and B.J. Nowak "Studies of Shock/Shock Interaction on Smooth and Transpiration—Cooled Hemispherical Nosetips in Hypersonic Flow" AIAA Paper No.91—1765, June 1991.

5. Majeskj,J.A., and Weatherford, R.H. "Development of an Empirical Correlation for Film—Cooling Effectiveness" AIAA Paper No.88—2624, June 1988.

6. E. Alzner and V. Zakkay "Turbulent Boundary Layer Shock Interaction with and without Injection" AIAA Paper No.70—91, January 1970.

7. M.S. Holden, R.J. Nowak, G. C. Olsen and K.M. Rodriguez "Experimental Studies of Shock Wave/Wall Jet Interaction in Hypersonic Flow" AIAA Paper No.90—0607, January 1990.

8. C.A. de Boor. "Practical Guide to Spline" New York—Heidelberg—Berlin. Springer Verlag. 1978

Table 1

Model parameters

Model	$\varphi_j{}^0$	h_w, mm	h_w/R	h_v, mm	h_j, mm	h_j/R
1	4	2.6	0.173	1	0.63	0.042
2	6	2.1	0.140	1	0.23	0.015
3	6	2.1	0.140	1	0.15	0.010
4	−33	2.1	0.140	1	0.25	0.017

Table 2

Angular coordinates of thermocouples
on a "thin wall"

Section I

N	φ^0	N	φ^0	N	φ^0	N	φ^0
2	+30	20	−12	38	−30	56	−48
4	+22	22	−14	40	−32	58	−50
6	+16	24	−16	42	−34	60	−52
8	+12	26	−18	44	−36	62	−54
10	+8	28	−20	46	−38	64	−56
12	+4	30	−22	48	−40	66	−58
14	0	32	−24	50	−42	68	−60
16	−4	34	−26	52	−44	70	−62
18	−8	36	−28	54	−46		

Section II

N	φ^0	N	φ^0	N	φ^0	N	φ^0
1	+26	23	−15	47	−37	69	−59
3	+18	25	−17	49	−39	71	−61
5	+14	27	−19	51	−41	73	−63
7	+10	29	−21	53	−43	75	−65
9	+6	31	−23	55	−45	77	−69
11	+2	33	−25	57	−47	79	−73
13	0	35	−27	59	−49	81	−77
15	−2	37	−29	61	−51	83	−81
17	−6	39	−31	63	−53		
19	−10	41	−33	65	−55		
21	−13	43	−35	67	−57		

Model 1

Table 3

X^*	P_j, bar	P_j^*	G_j^*	I_j^*	q_m/q_{so}	$\varphi_m, ^\circ$	X_w	X_1	L_1	Run	Fig.
1)	0	0	0	0	1.20	-3.0	0.55	-	-	7279	
	1.00	1.80	0.053	0.0157	0.16	-44.0	0.59	-	-	7278	9
	1.94	3.44	0.114	0.0473	0.05	-53.0	0.64	-	-	7277	
	3.78	6.79	0.258	0.1270	0.02	-72.0	0.66	-	-	7276	
1.24	0	0	0	0	4.15	1.0	1.23	0.45	0.57	7315	
0.96	0	0	0	0	6.87	-20.0	1.30	0.55	0.87	7314	
0.74	0	0	0	0	7.15	-25.0	1.20	0.51	0.94	7244	23
0.50	0	0	0	0	8.77	-34.0	1.26	0.43	1.13	7267	
0.40	0	0	0	0	9.24	-37.0	1.20	0.40	1.31	7308	
1.13	0	0	0	0	6.79	-19.0	1.24	0.49	0.92	7316	
	14.40	25.65	1.060	0.6240	4.51	-39.0	1.52	0.57	1.24	7317	24
	27.70	49.09	2.090	1.2900	1.35	-54.0	2.10	0.77	1.92	7318	
0.86	0	0	0	0	6.33	-21.0	1.23	0.52	0.91	7246	
	0	0	0	0	6.70	-22.0	1.27	0.53	0.90	7274	
	3.79	6.80	0.278	0.1370	6.61	-42.0	1.50	0.26	1.80	7247	
	3.81	6.81	0.268	0.1320	7.60	-43.0	1.51	0.38	1.81	7275	25
	7.57	13.55	0.544	0.2990	4.86	-42.5	1.57	0.36	1.85	7248	
	15.30	27.38	1.110	0.6600	3.00	-43.5	1.64	0.53	1.40	7249	
	30.20	54.20	2.280	1.4300	0.53	-70.0	2.38	1.00	2.26	7250	
0.53	0	0	0	0	8.59	-29.0	1.17	0.40	0.98	7255	
	0	0	0	0	7.83	-30.0	1.22	0.42	0.98	7256	
	3.69	6.58	0.262	0.1290	4.89	-45.0	1.60	0.53	2.45	7257	26
	7.35	13.15	0.538	0.2960	3.72	-48.0	1.53	0.41	1.70	7258	
	15.50	27.81	1.110	0.6590	2.09	-51.5	1.64	0.68	1.32	7254	
	30.20	53.53	2.210	1.3800	0.46	-70.0	2.32	1.21	1.57	7252	
0.33	0	0	0	0	8.79	-37.0	1.16	0.36	1.28	7268	
	3.79	6.79	0.264	0.1290	3.50	-50.0	1.50	0.55	2.47	7269	
	7.35	13.10	0.538	0.2930	2.73	-51.0	1.49	0.62	1.51	7270	27
	15.40	27.58	1.110	0.6580	2.06	-47.0	1.46	0.66	1.20	7273	
	22.60	40.20	1.650	1.0200	1.31	-58.0	1.90	0.92	1.51	7272	
0.23	0	0	0	0	8.11	-46.0	1.12	0.38	1.43	7309	
	7.32	12.99	0.530	0.2880	2.35	-51.0	1.37	0.60	1.28	7312	28
	14.90	26.66	1.080	0.6370	1.71	-48.5	1.46	0.64	1.21	7311	
	28.90	51.57	2.160	1.3400	0.61	-63.0	1.80	1.11	1.32	7310	

Model 1   Helium injection

X^*	P_j, bar	P_j^*	G_j^*	I_j^*	q_m/q_{so}	$\varphi_m^{\ 0}$	X_w	X_1	L_1	Run	Fig.
0.53	3.73	6.64	0.096	0.1210	4.77	-44.5	1.23	0.51	2.34	7266	
	7.19	12.81	0.196	0.2670	3.56	-46.0	1.68	0.81	1.40	7265	
	14.30	25.33	0.383	0.5620	1.99	-51.0	1.64	0.68	1.40	7262	
	14.00	24.93	0.376	0.5500	1.85	-52.0	1.64	0.77	1.34	7263	52
	21.70	38.90	0.594	0.8910	1.44	-58.0	1.98	0.98	1.66	7264	
	25.70	45.78	0.718	1.0700	0.97	-63.0	2.01	1.07	1.43	7260	
	24.70	43.94	0.692	1.0200	1.01	-61.0	1.87	0.92	1.43	7261	

1) - without wedge

Model 2   Table 3 (continue)

X*	P_j,bar	$P_j{}^*$	$G_j{}^*$	$I_j{}^*$	q_m/q_{s0}	$\varphi_m{}^0$	X_w	X_1	L_1	Run	Fig.
1)	0	0	0	0	1.41	-0.2	0.55	-	-	7227	
	0	0	0	0	1.33	-0.6	0.56	-	-	7228	
	0	0	0	0	1.46	-0.1	0.57	-	-	7229	
	0	0	0	0	1.08	-1.5	0.57	-	-	7233	10
	3.75	6.69	0.084	0.0420	0.64	-19.0	0.58	-	-	7230	
	20.00	34.44	0.406	0.2460	0	-	0.66	-	-	7232	
	47.70	83.11	1.580	1.0300	0	-	0.70	-	-	7231	
0.75	1.95	34.53	0.389	0.2370	-	-	1.62	1.00	1.50	7239	36
0.30	3.84	6.68	0.060	0.0296	-	-	1.21	0.30	1.36	7241	
	9.86	17.14	0.180	0.1010	-	-	1.65	0.47	1.24	7240	

Model 3

X*	P_j,bar	$P_j{}^*$	$G_j{}^*$	$I_j{}^*$	q/q_{s0}	$\varphi_m{}^0$	X_w	X_1	L_1	Run	Fig.
0.22	0	0	0	0	8.25	-47.0	1.15	0.32	1.38	7302	
	3.86	6.87	.035	0.0174	8.16	-48.0	1.19	0.32	1.36	7303	
	3.86	6.89	0.040	0.0194	7.75	-47.0	1.26	0.43	1.38	7304	37
	7.74	13.81	0.106	0.0587	4.50	-47.5	1.35	0.28	1.68	7305	
	22.90	40.79	0.548	0.3380	1.86	-50.0	1.70	1.00	1.57	7306	

Model 4

X*	P_j,bar	$P_j{}^*$	$G_j{}^*$	$I_j{}^*$	q_m/q_{s0}	$\varphi_m{}^0$	X_w	X_1	L_1	Run	Fig.
1)	0	0	0	0	0.97	-9.0	0.53	-	-	7280	
	0	0	0	0	0.93	-7.0	0.53	-	-	7281	
	3.81	7.01	0.131	0.0651	0.90	4.0	0.57	-	-	7282	11
	7.58	13.43	0.261	0.1430	0.29	32.0	0.62	-	-	7283	
	22.50	39.96	1.150	0.7060	0.19	35.0	1.23	-	-	7285	
0.86	0	0	0	0	1.70	-2.0	1.15	0.68	0.49	7290	38 a
	0	0	0	0	1.80	1.0	1.15	0.70	0.50	7291	
0.65	0	0	0	0	4.11	-6.0	1.15	0.68	0.57	7292	38 a
0.30	0	0	0	0	7.33	-14.0	1.24	0.63	0.68	7294	
0.44	0	0	0	0	7.80	-14.5	1.17	0.66	0.64	7300	
	3.50	6.24	0.137	0.0664	5.31	-12.5	1.17	0.70	0.64	7296	
	5.40	9.57	0.220	0.1160	4.71	-14.0	1.26	0.75	0.68	7298	38 b
	6.33	11.28	0.250	0.1350	0.14	-26.0	1.37	0.51	1.03	7299	
2)	0	0	0	0	1.00	0	0.41	-	-	7225	
							0.41	-	-	7226	

1) - without wedge
2) - cylinder alone

Table 4

P_j, bar	P_j^*	G_j^*	I_j^*	$X_{w\ min}$	$X_{w\ max}$	$X_{1\ min}$	$X_{1\ max}$	$L_{1\ min}$	$L_{1\ max}$	C_x^*
4	7.3	0.68	0.40	1.136	1.559	0.395	0.730	1.105	2.410	0.91
8	14.6	1.36	0.80	1.249	1.494	0.576	0.750	1.110	1.110	1.10
16	29.1	2.72	1.60	1.471	1.487	0.846	0.903	0.984	0.984	0.70
32	58.2	5.45	3.19	2.109	2.495	1.428	1.520	1.370	1.790	0.36
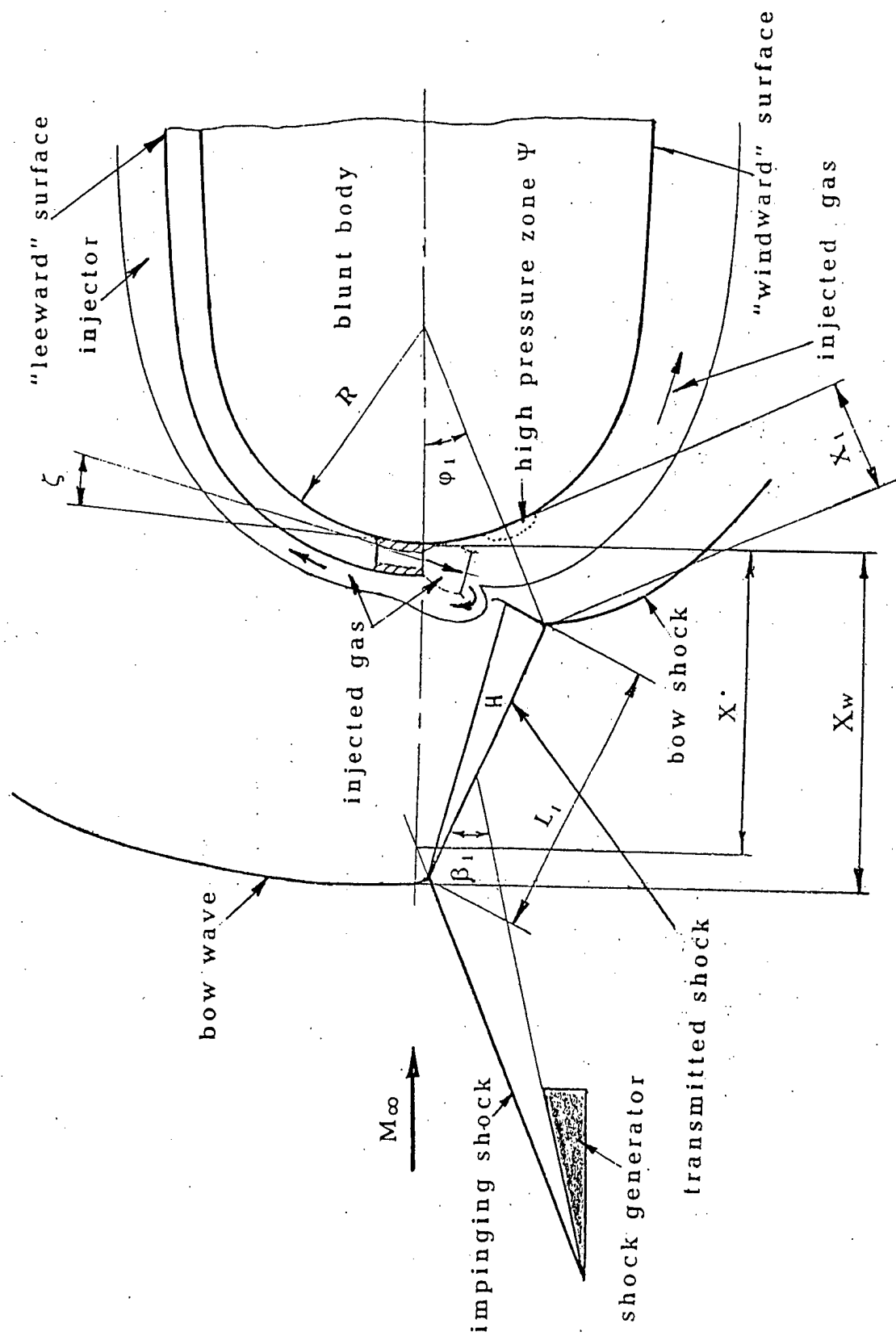
Fig. 1
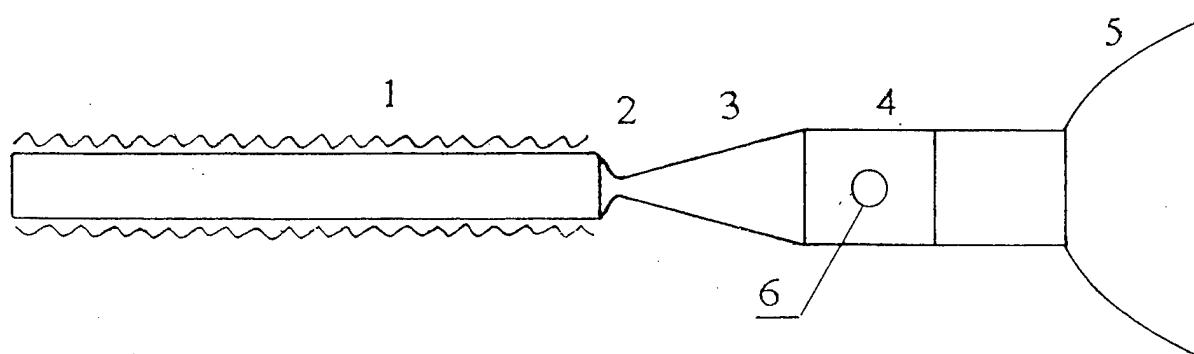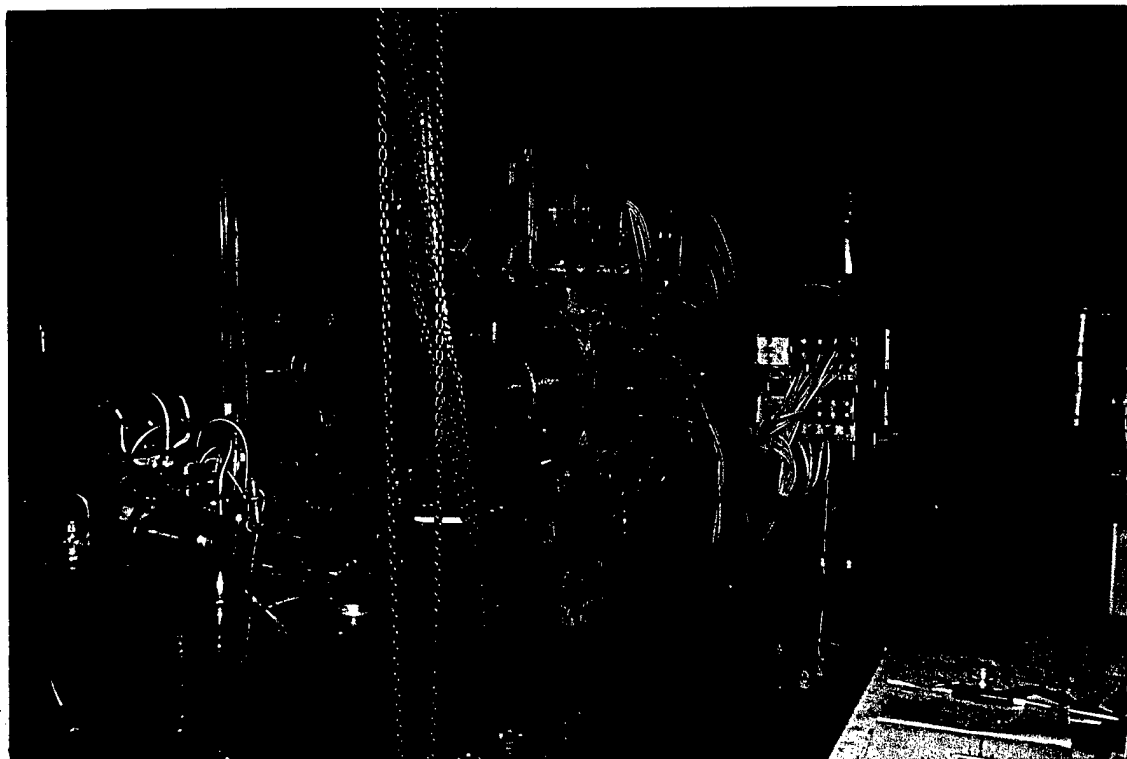
1 - Heating Chamber
2 - Diaphragm
3 - Nozzle
4 - Test Section
5 - Exhaust Chamber
6 - Window

Fig. 2

1 - Flash Lamp
2 - Optical Filters
3 - Model
4 - Shock Generator
5 - Lens
6 - Knife
7 - Photographic Film

M_∞

Fig. 3

M_∞

y

x

$U = f(P_\delta)$

$U = f(t^\circ)$
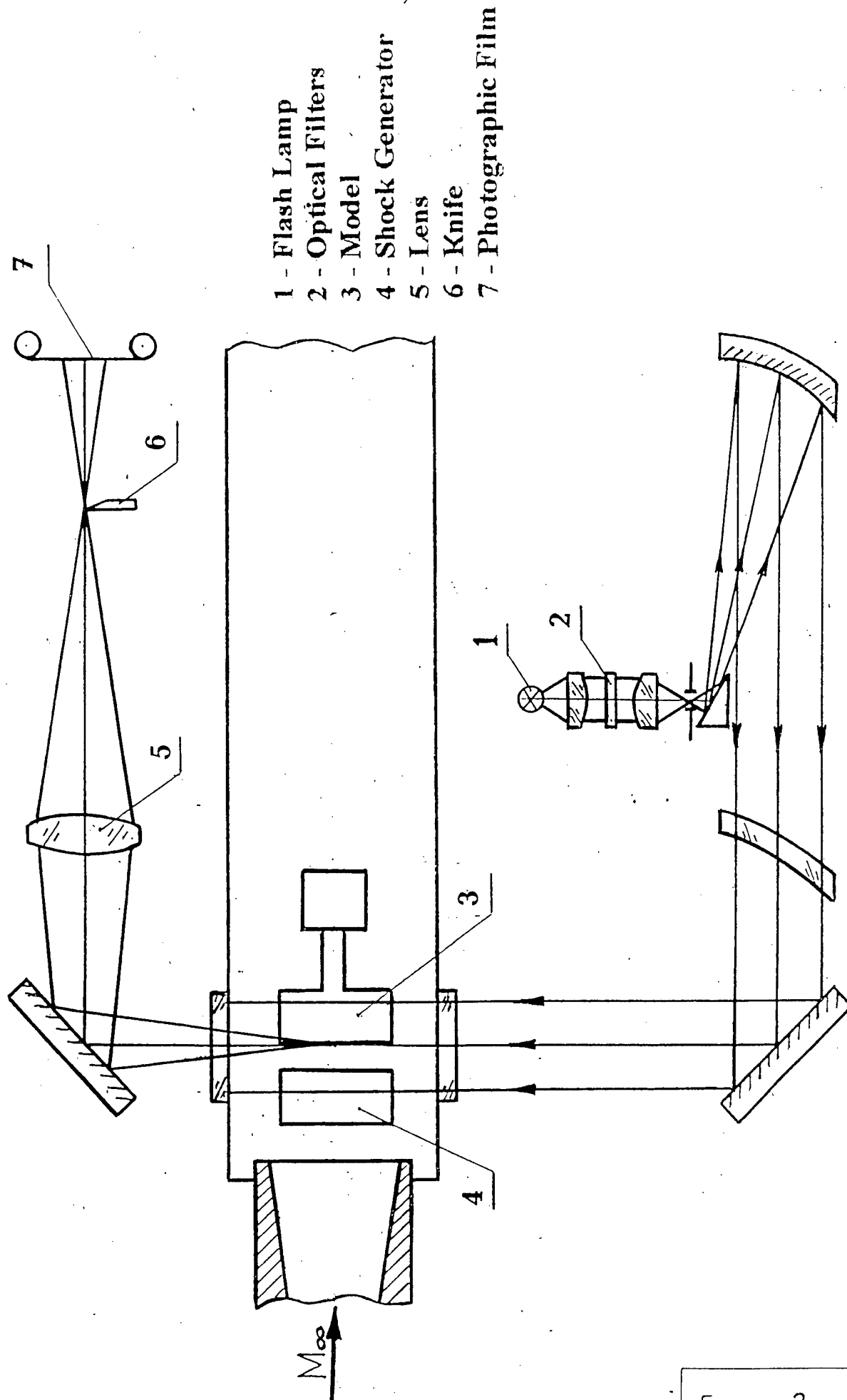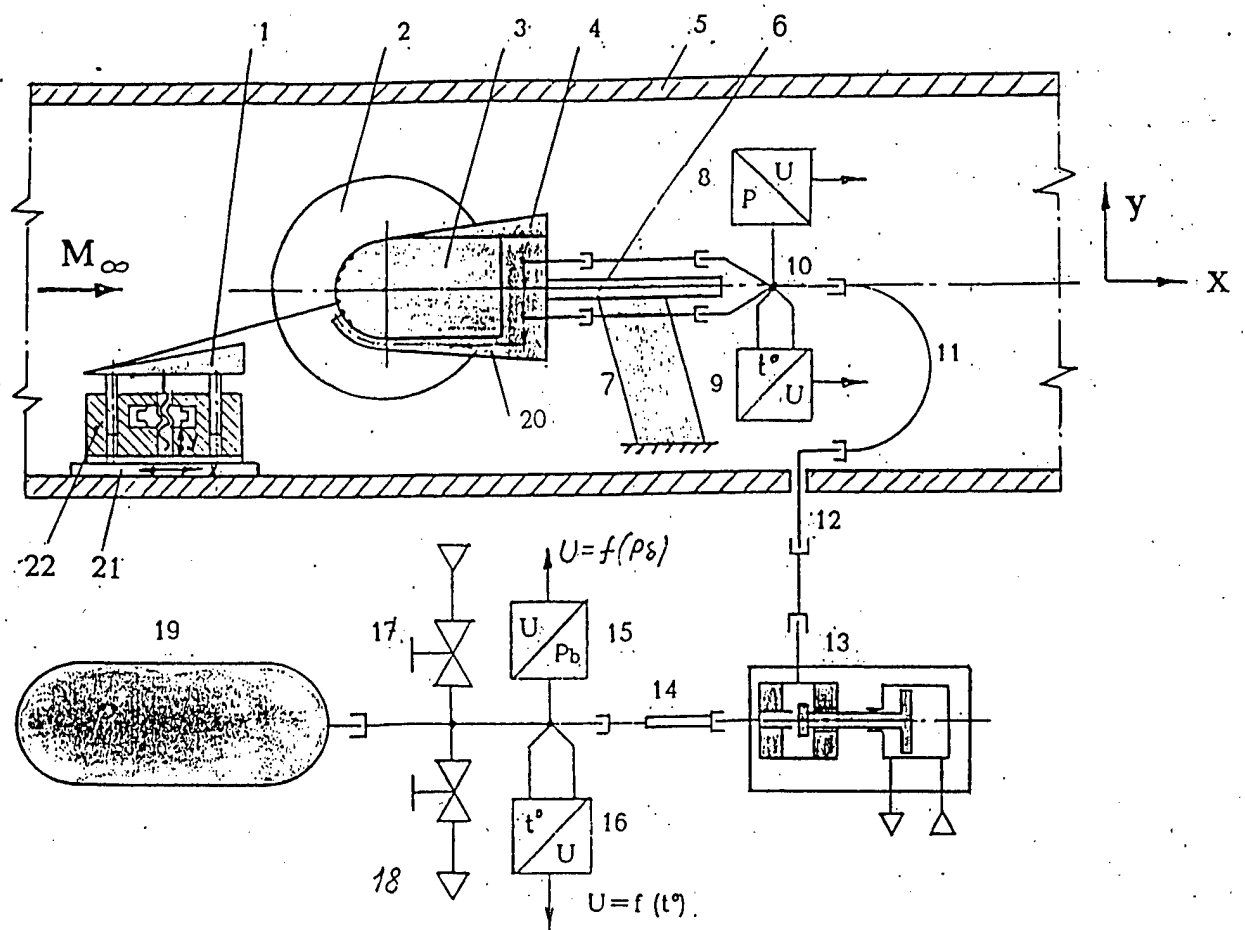
1 - sharp wedge (impinging shock generator)
2 - optical window in UT-1 test section
3 - blunt body
4 - compensator
5 - walls of test section
6 - cylindrical holder
7 - pylon of model
8 - pressure gage at model inlet
9 - temperature gage at model inlet
10,11,12,14 - gas supply pipe
13 - electrical quick-response pressure transducer
15 - vessel pressure gage
16 - vessel exit temperature gage
17 - vessel filling valve
18 - vessel pressure release valve
19 - vessel
20 - gas injection device
21 - slide
22 - pylon of sharp wedge

Fig. 4

a)   M 1:2

M∞ →

R 15

injector 1

4°

30mm

Y

compensator 3

" blunt plate " 2

15°

X

generator

" thin wall "

II

8mm

b 150 mm

I

60mm

b)   M 2:1

+φ

−φ

" thin wall "

Fig. 5

Model 1, 2, 3

a)

Model 4

b)

Fig. 6

Fig. 7

Legend:
◇ Model 1
□ Model 1, helium
△ Model 2
+ Model 3
✻ Model 4

Axis labels: G_j, kg/s (vertical), P_j, bar (horizontal)
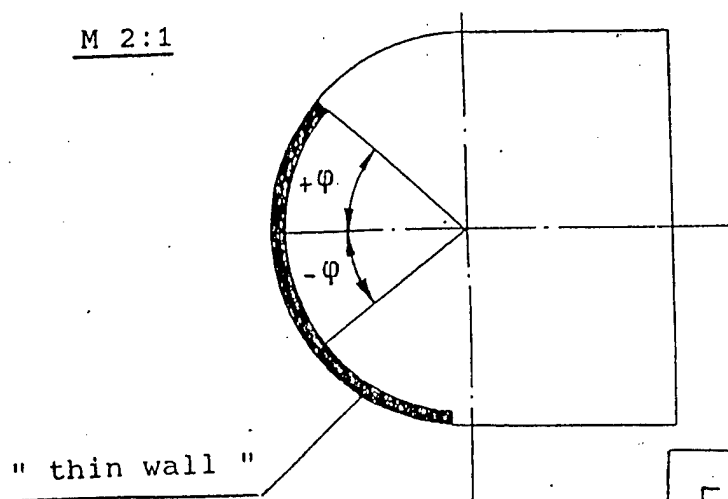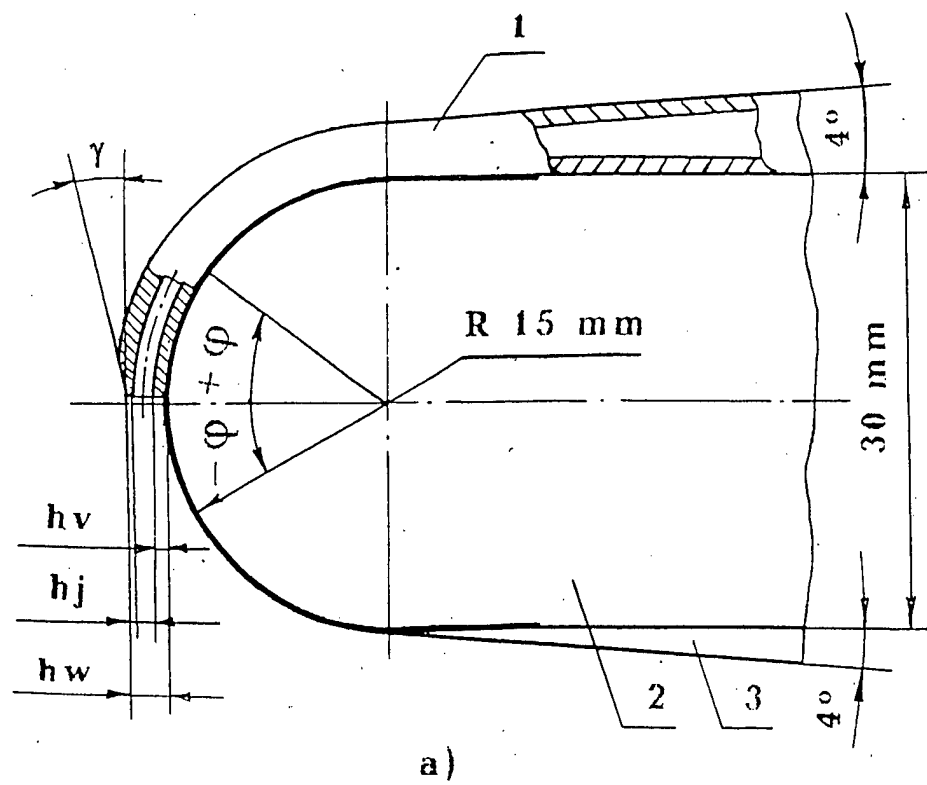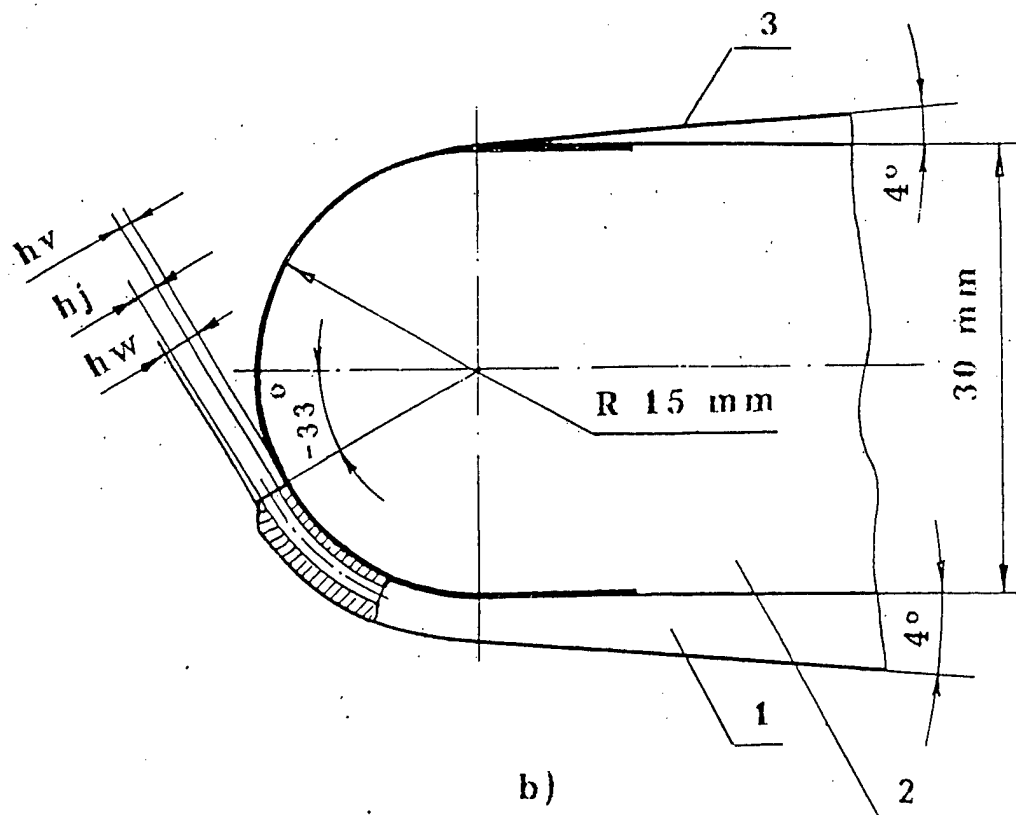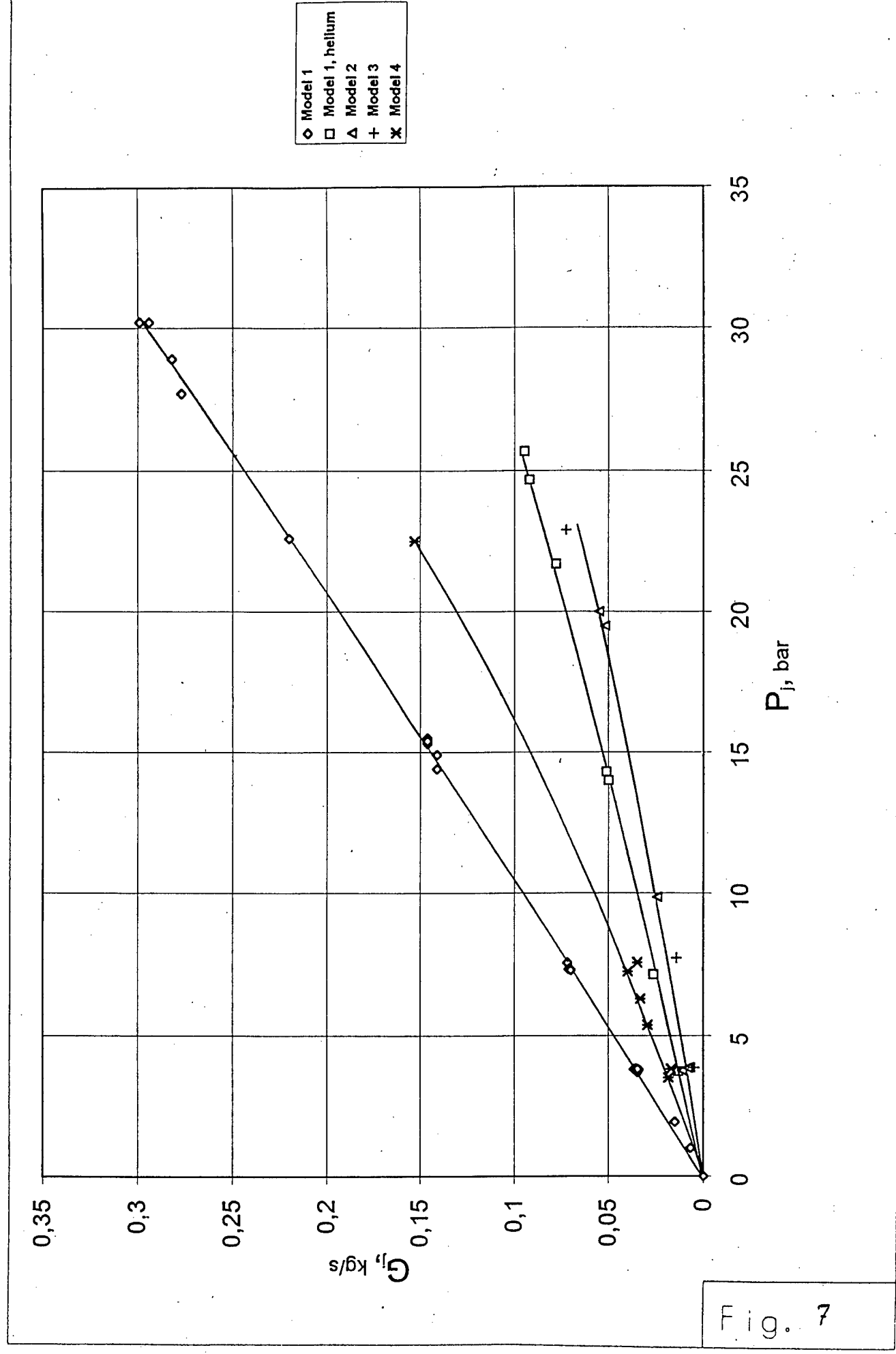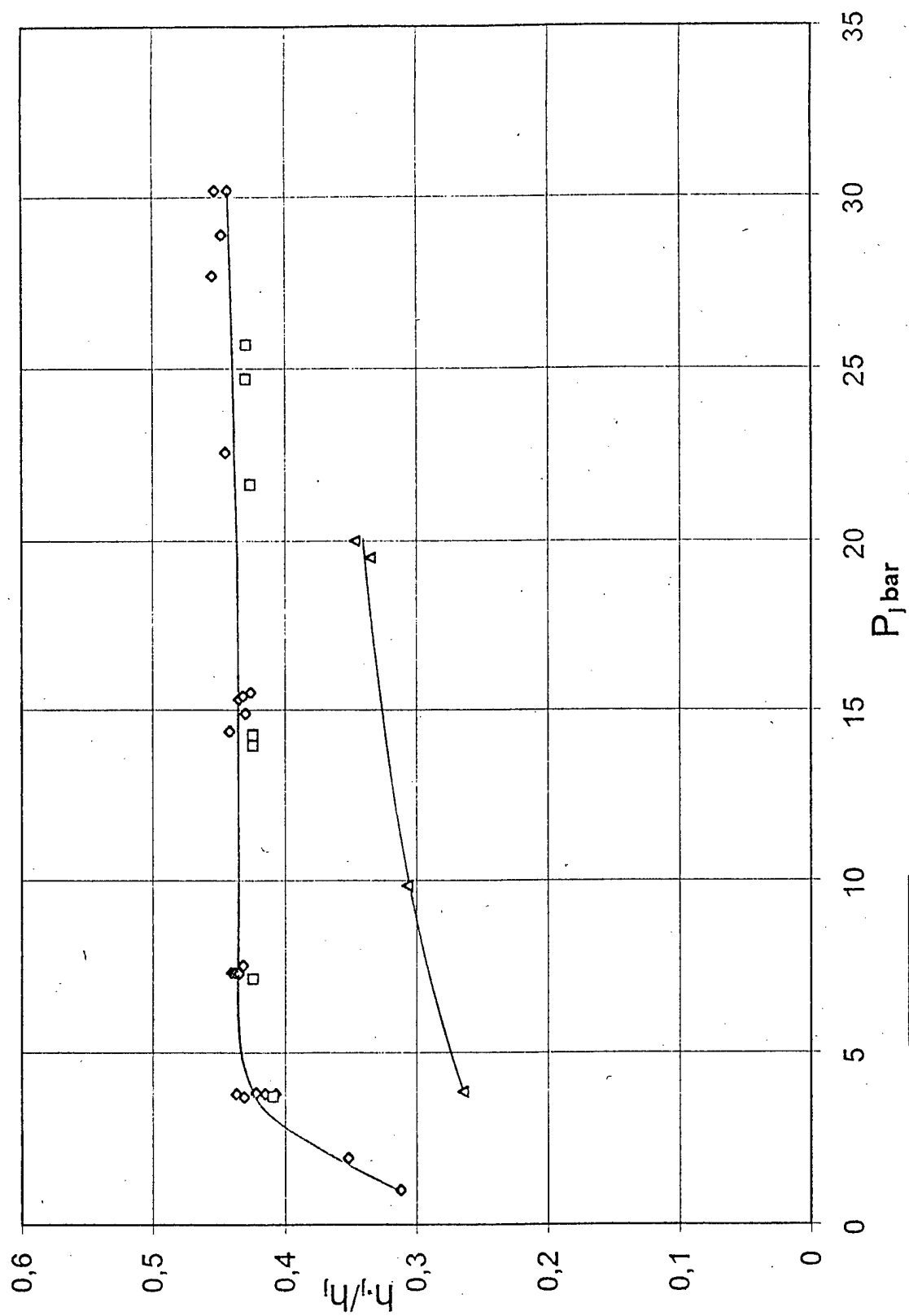
Fig. 8

Model 1

$P_j = 0$

Run 7279

$P_j = 1.00$bar

Run 7278
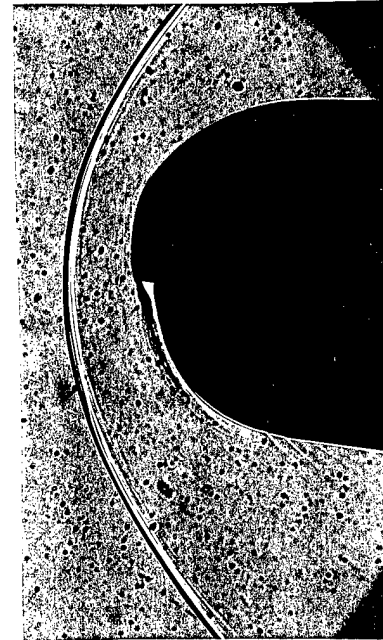
$P_j = 1.94$ bar

Run 7277

$P_j = 3.78$ bar

Run 7276

Fig. 9
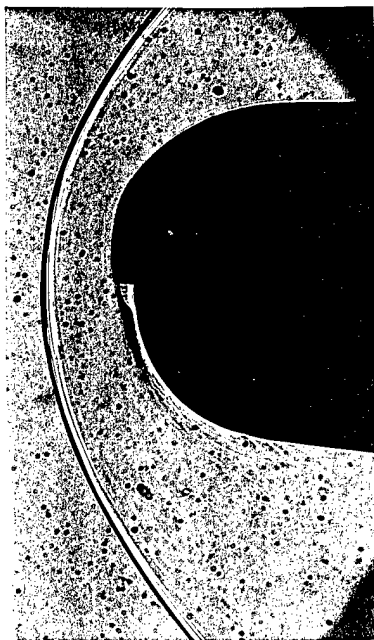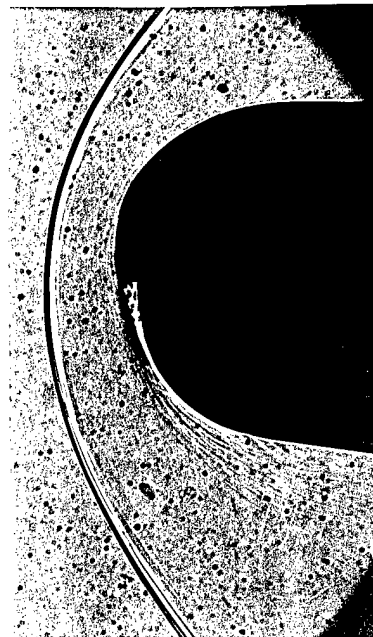
Model 2

$P_j = 0$

Run 7233

$P_j = 3.75$ bar

Run 7230

$P_j = 20.0$ bar

Run 7232

$P_j = 47.7$ bar

Run 7231

Fig. 10
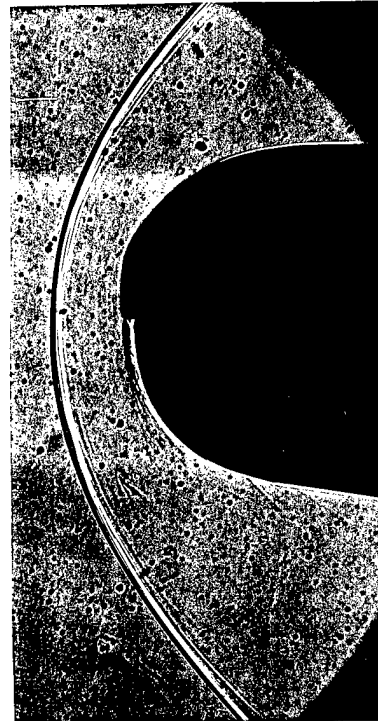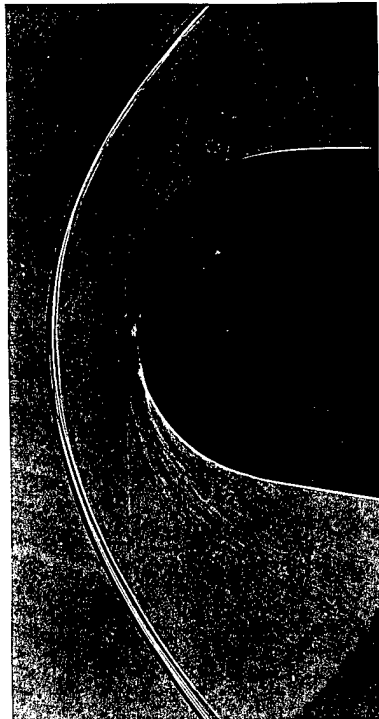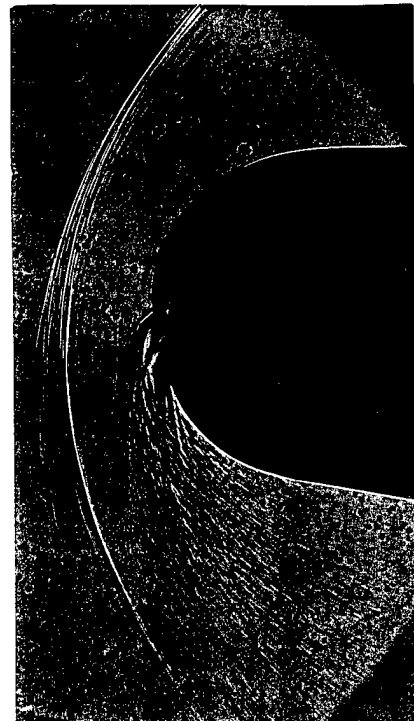
Model 4

$P_j = 0$

Run 7280
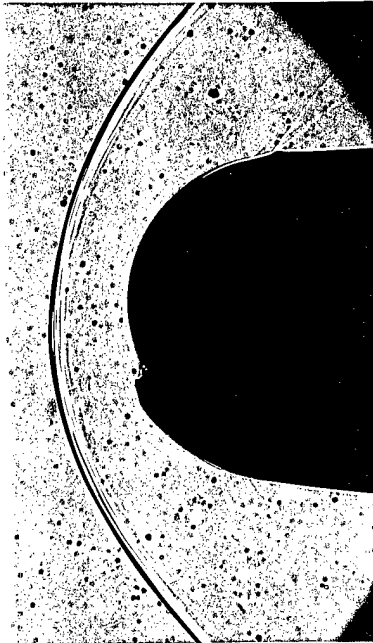
$P_j = 3.81$ bar

Run 7282
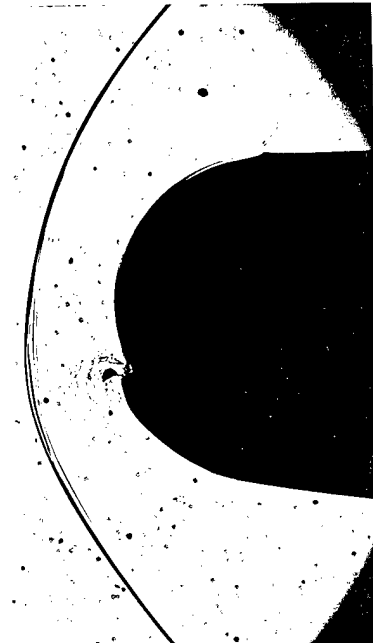
$P_j = 6.54$ bar

Run 7289

$P_j = 7.58$ bar

Run 7283

Fig. 11 a
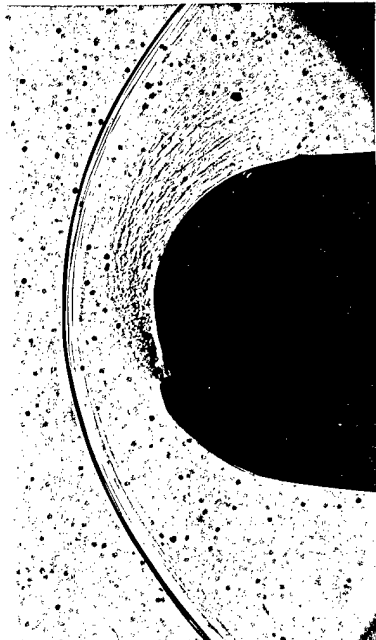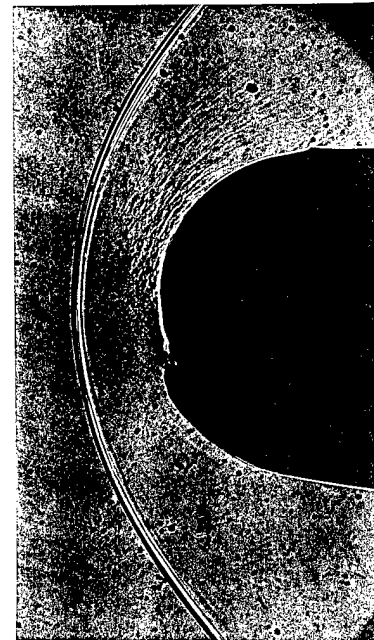
Model 4

$P_j = 15.1$ bar

Run 7284
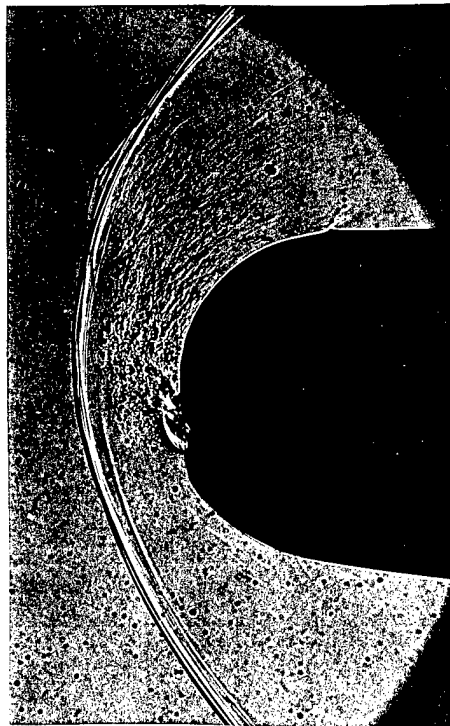
$P_j = 30.3$ bar

Run 7286
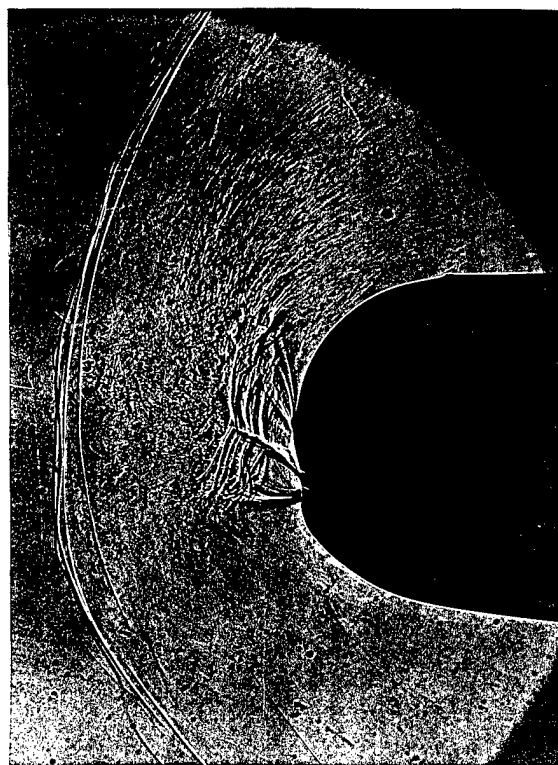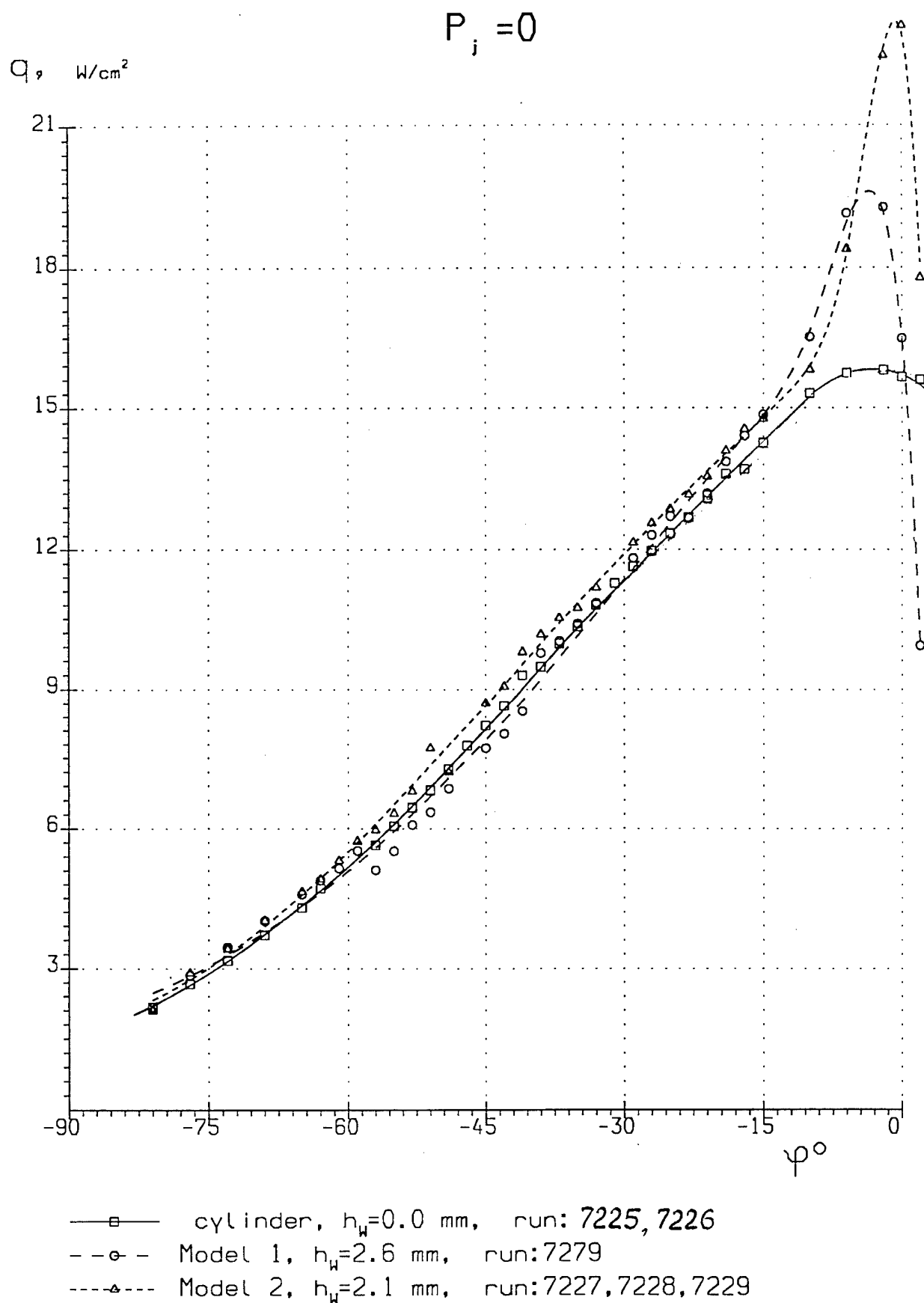
Fig. 11 b

$P_j = 0$

q, W/cm²

$\varphi°$

cylinder, h_w=0.0 mm, run: **7225, 7226**

Model 1, h_w=2.6 mm, run:7279

Model 2, h_w=2.1 mm, run:7227,7228,7229

Fig. 12

$P_j = 0$

q/q_{so}

φ°
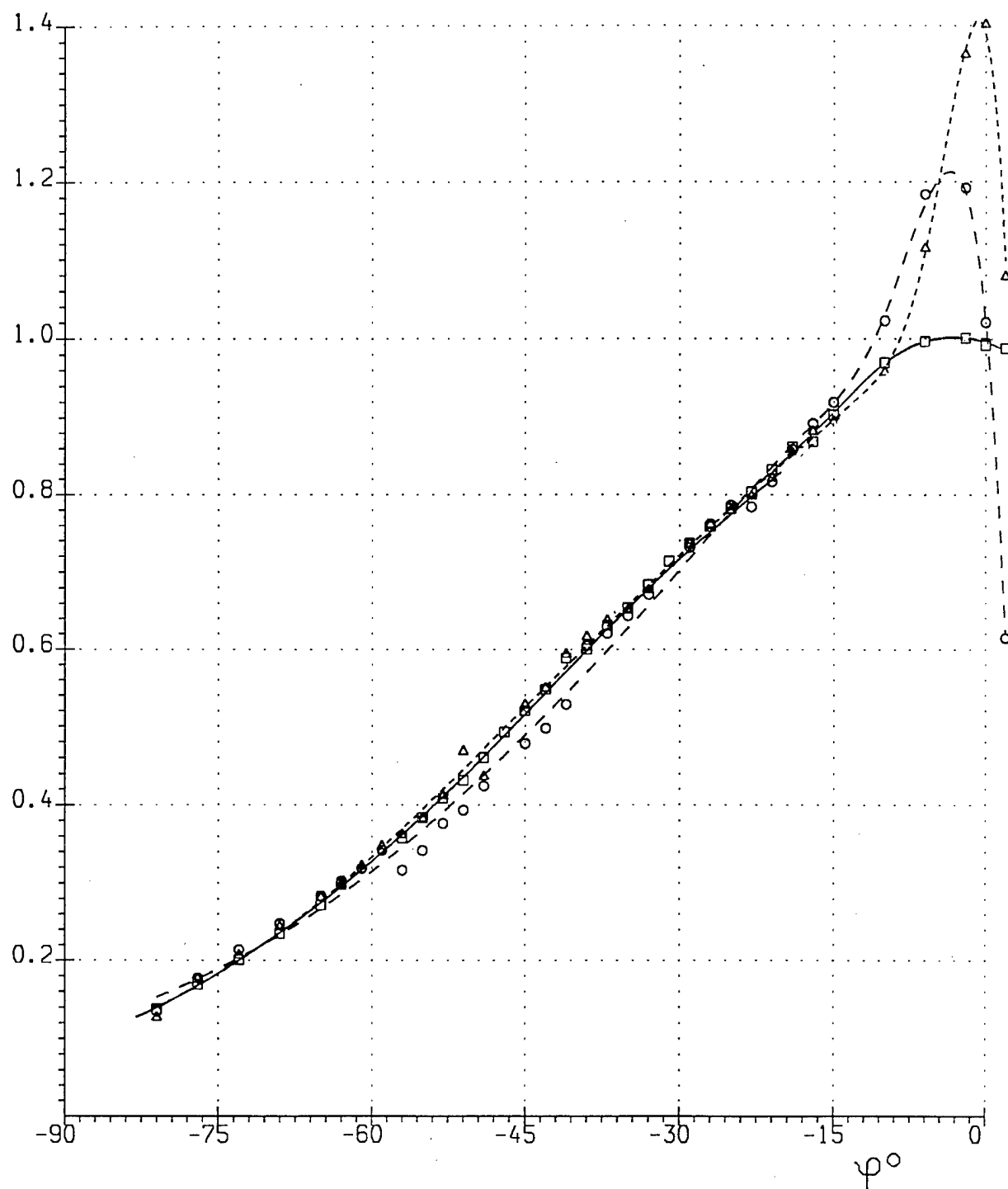
cylinder, $h_w=0.0$ mm, run:**7225, 7226**
Model 1, $h_w=2.6$ mm, run:7279
Model 2, $h_w=2.1$ mm, run:7227,7228,7229

Fig. 13

Model 4

$P_j = 0$
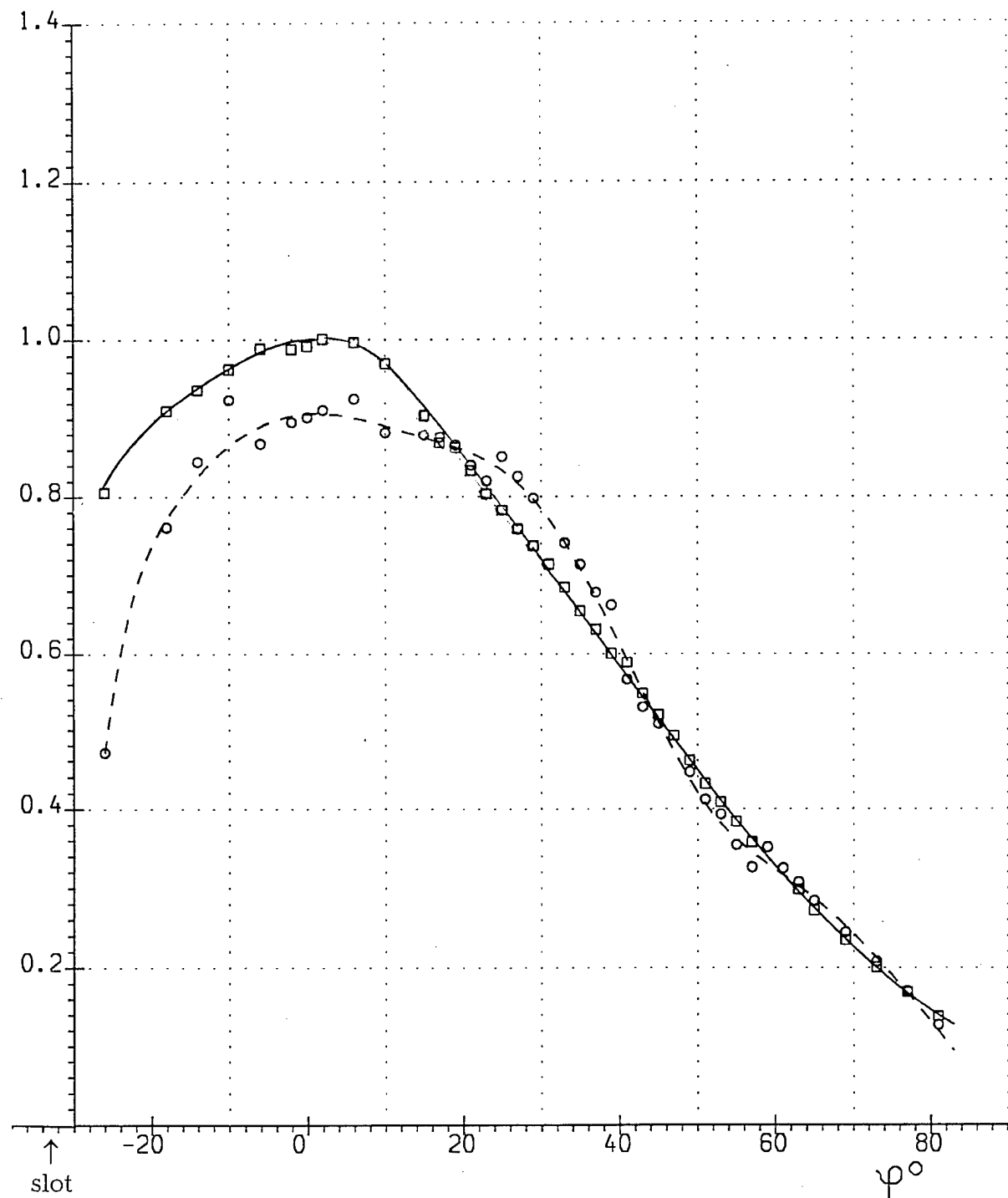
Fig. 14

Model 1   without wedge
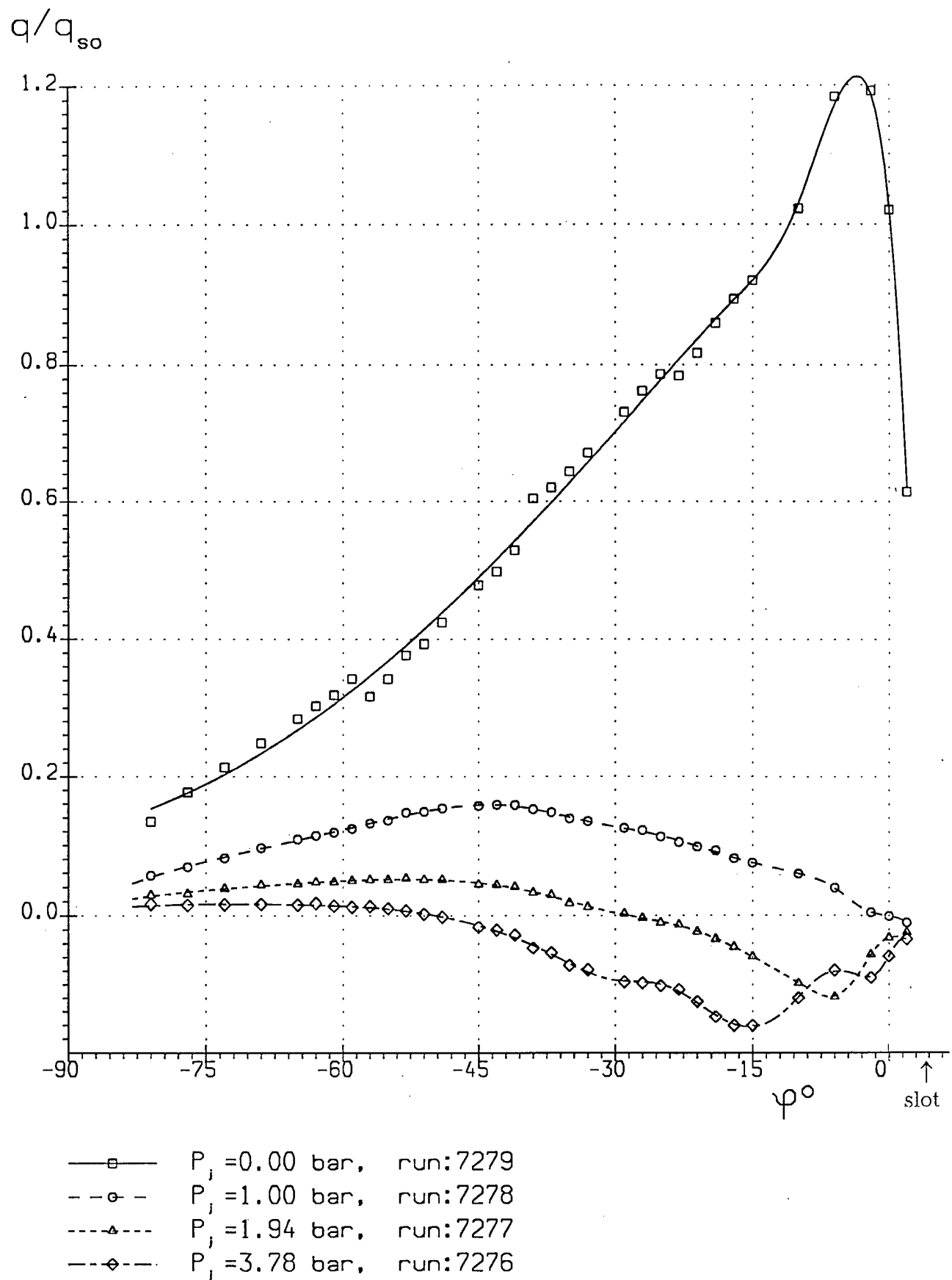
Fig. 15

Model 2   without wedge
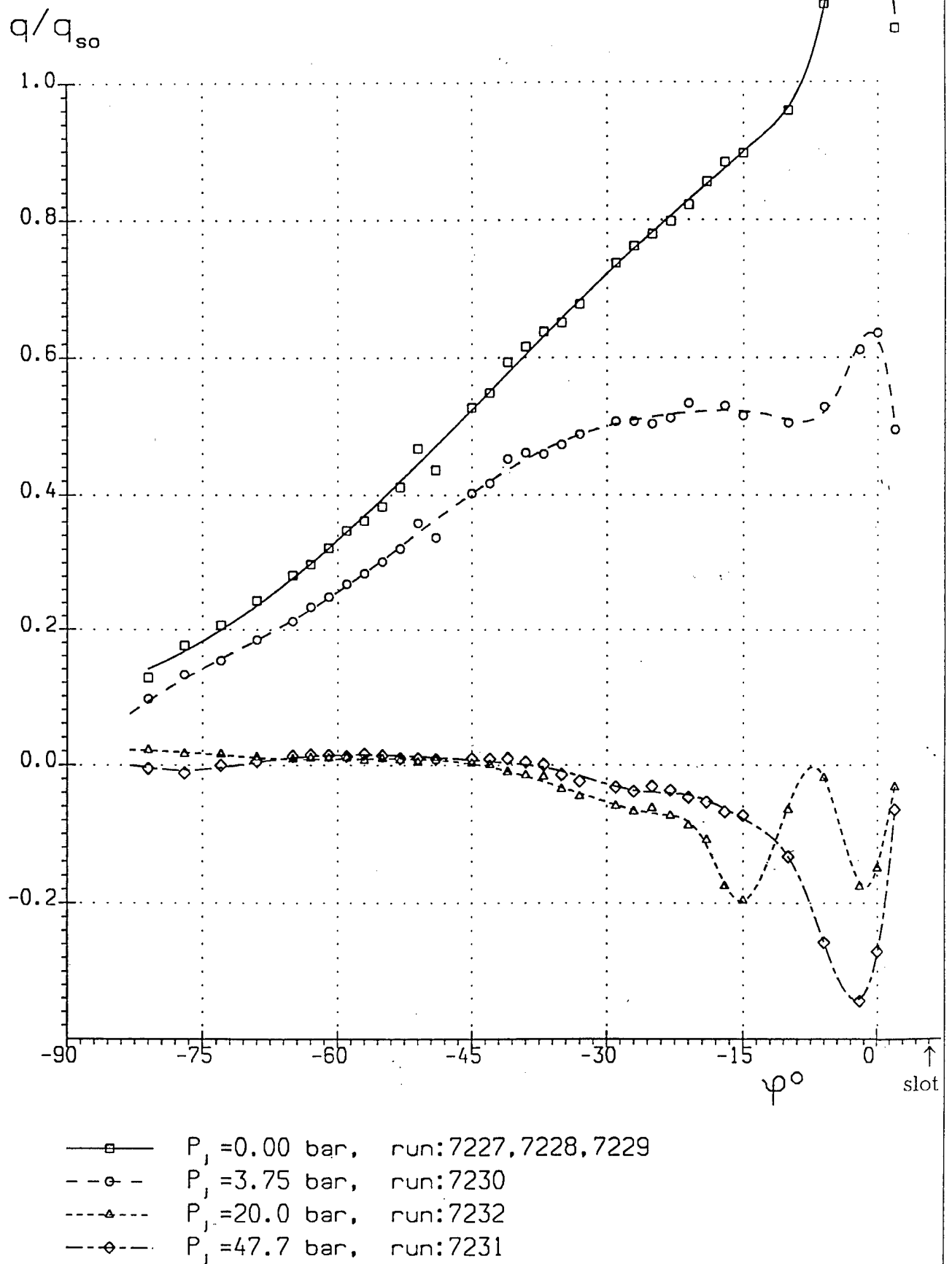
Fig. 16

Model 1   without wedge

q/q_o

Fig. 17

Model 2   without wedge

q/q$_o$

$\varphi°$

slot

--o--   P$_J$ =3.75 bar,   run:7230
---△--- P$_J$ =20.0 bar,   run:7232
--◇--   P$_J$ =47.7 bar,   run:7231
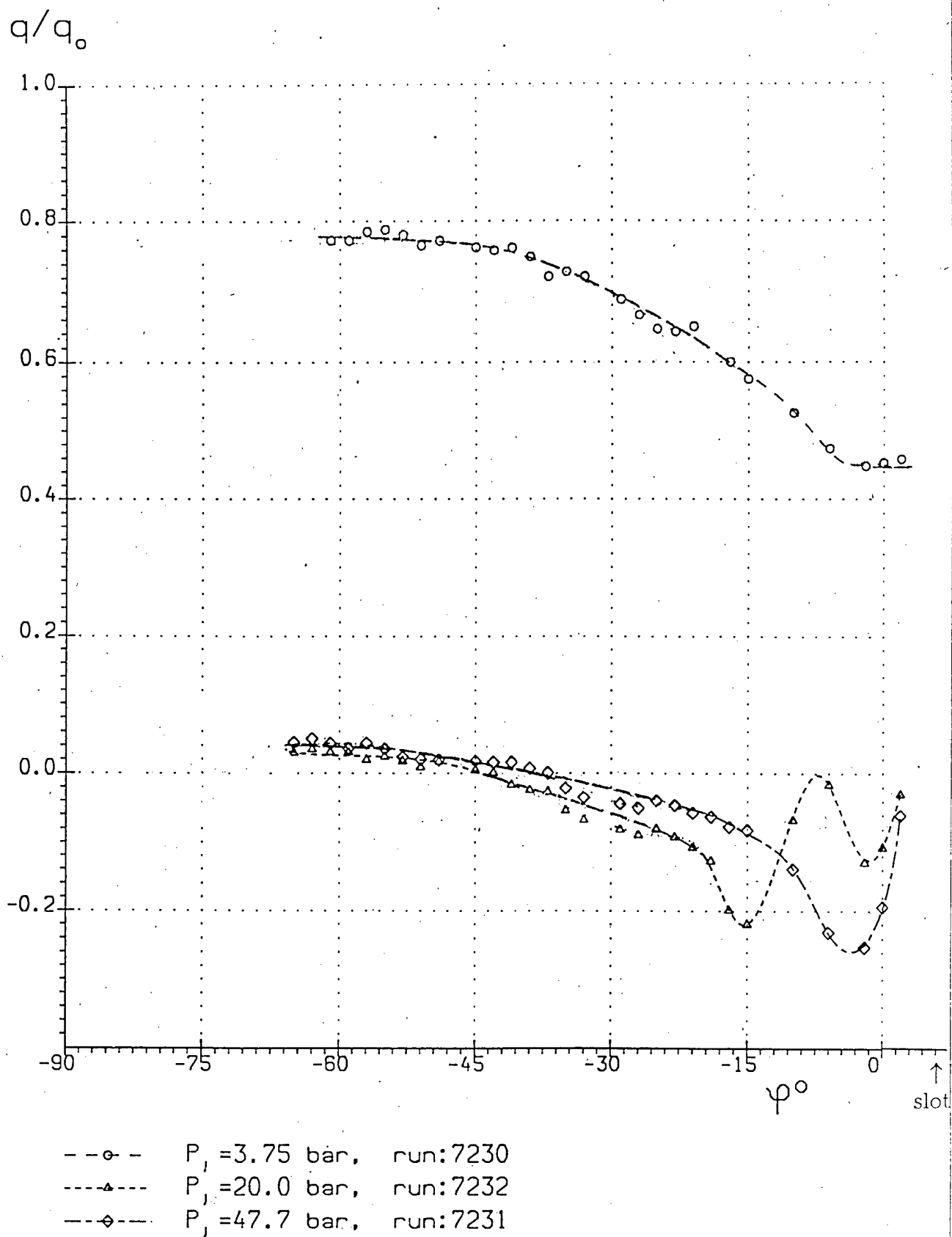
Fig. 18

Model 4   without wedge
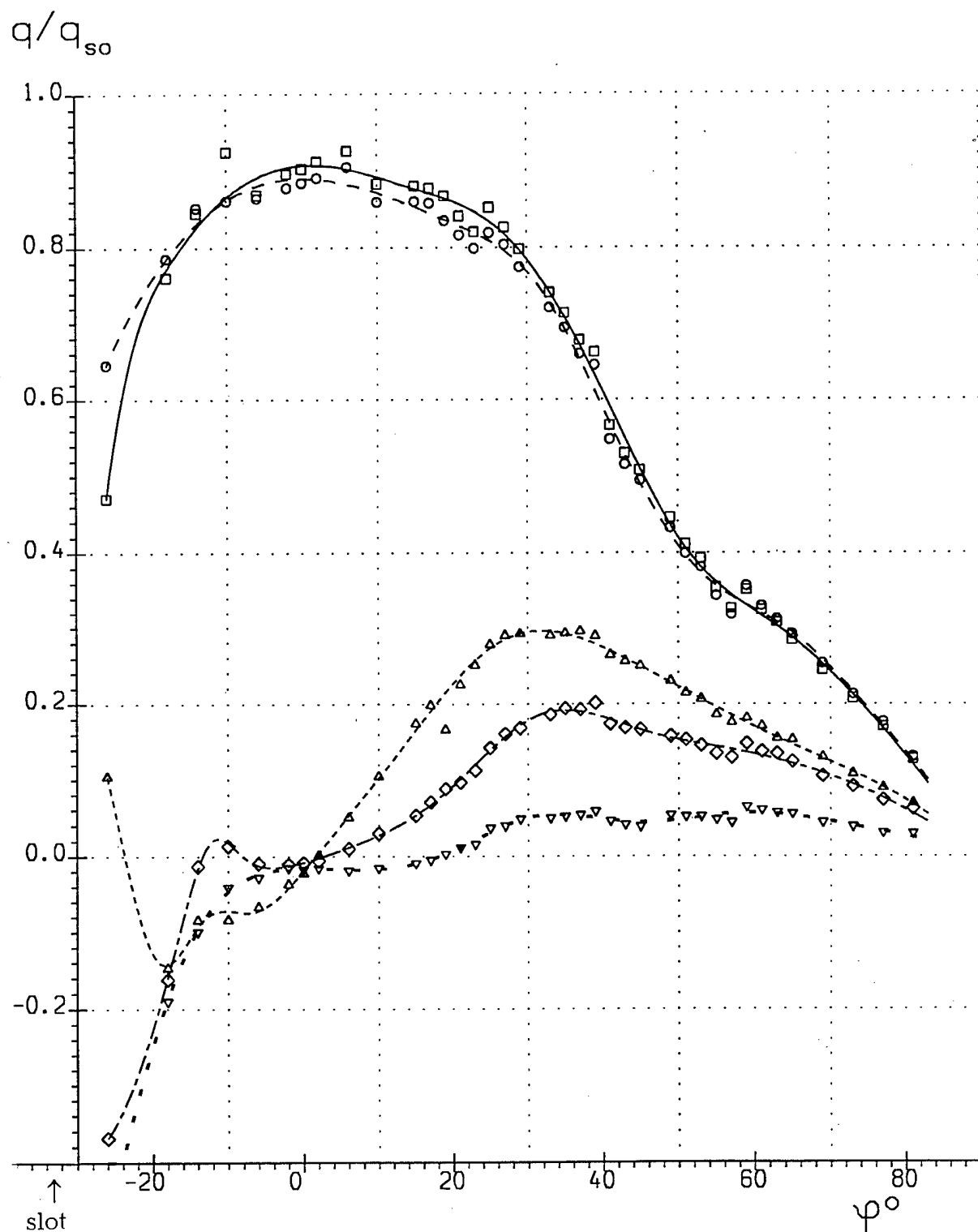
Fig. 19

without wedge

q_m/q_{so}

G_j^*

Model 1
Model 2
Model 4
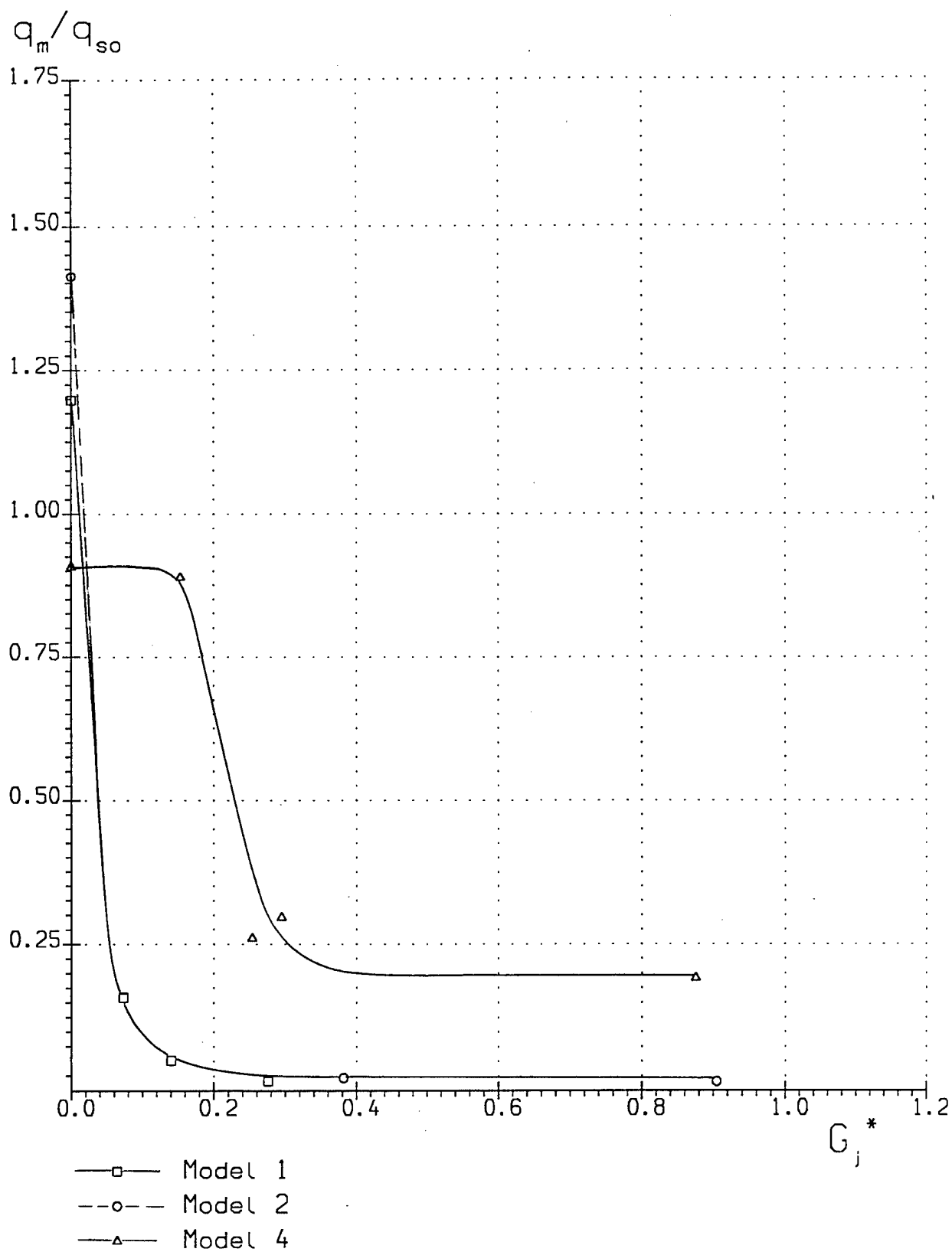
Fig. 21

without wedge
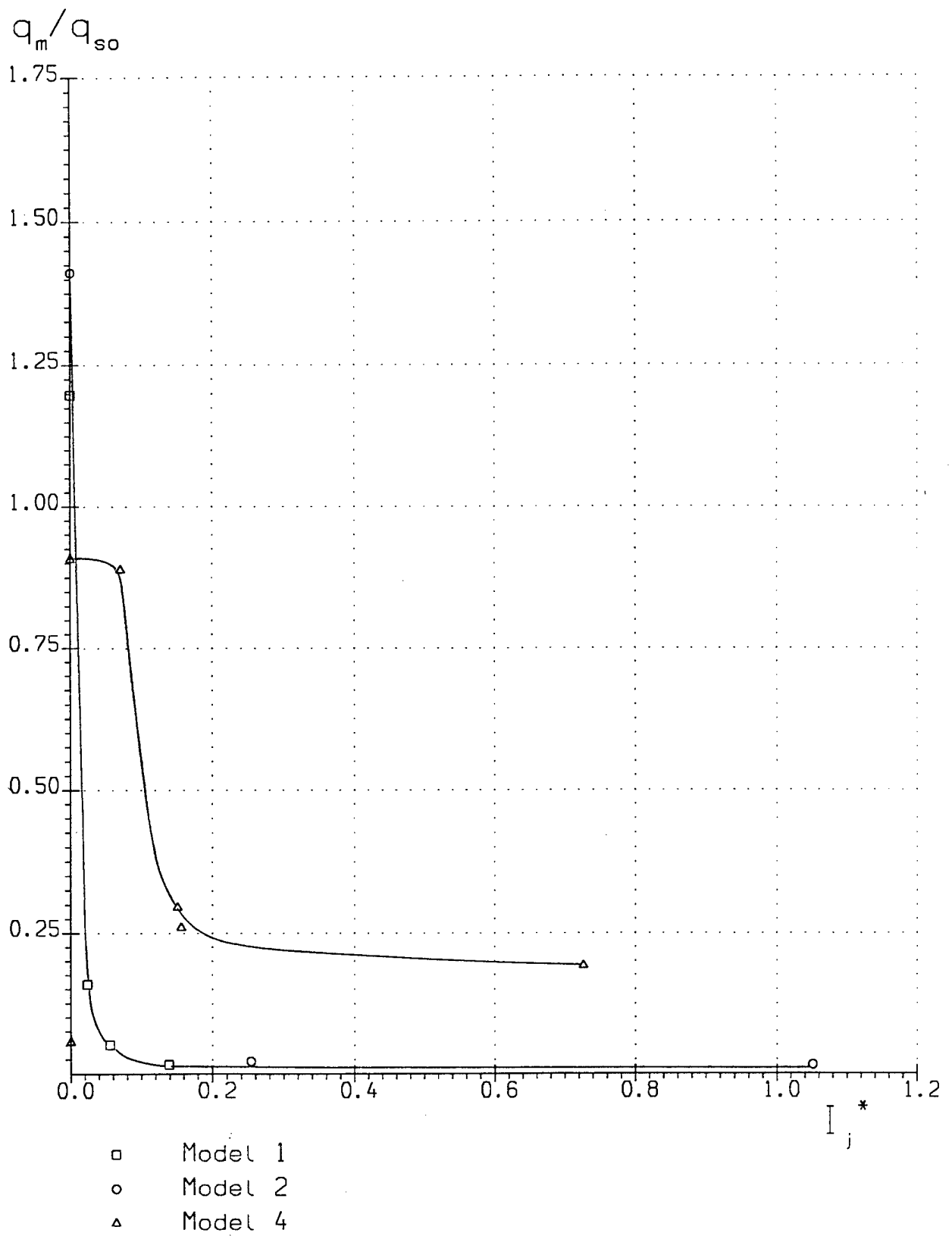
Fig. 22

Model 1

$$X^* = 1.24$$

$P_j = 0$
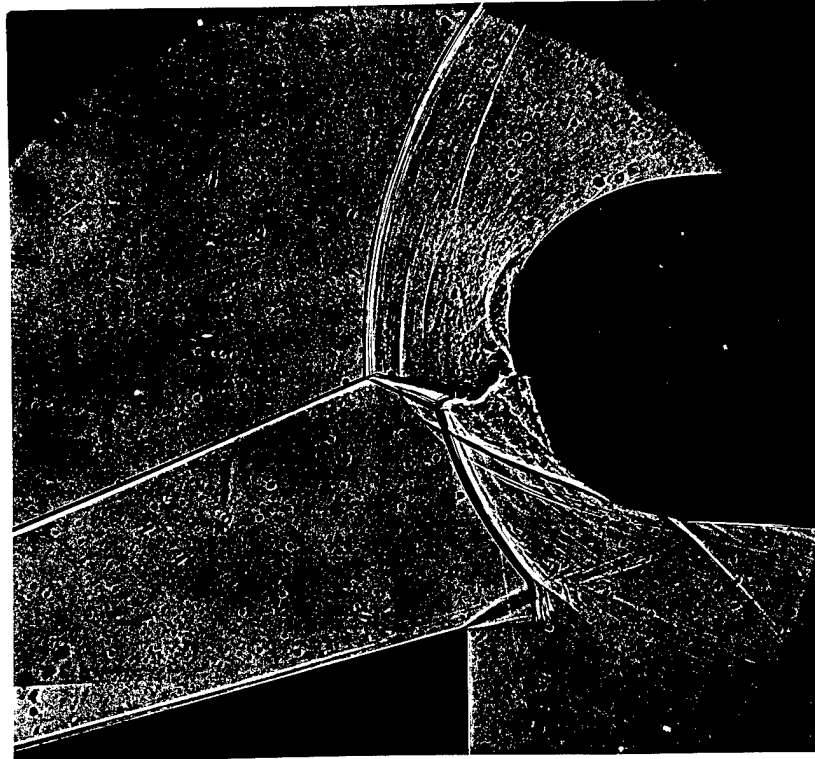
Fig. 23

Model 1

$$X^* = 1.13$$

$P_j = 0$

Run 7316

$P_j = 14.4$ bar

Run 7317

$P_j = 27.7$ bar

Run 7318

Fig. 24
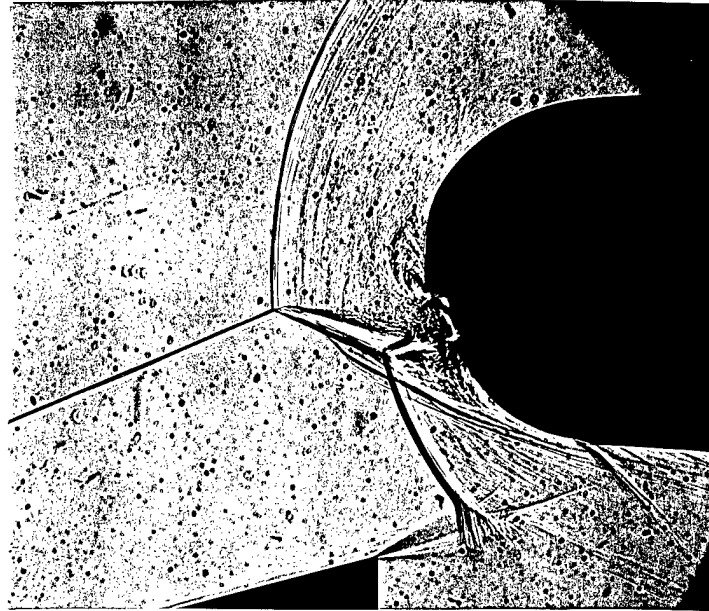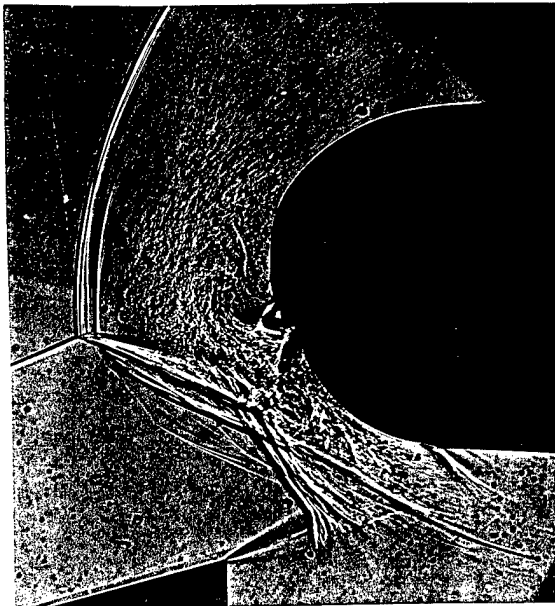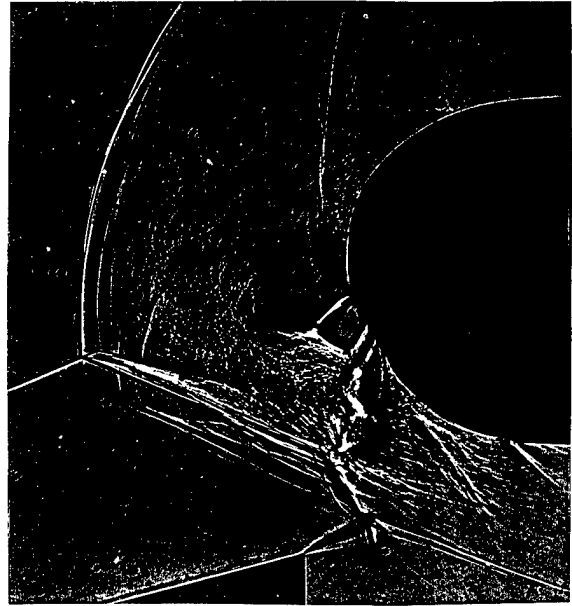
Model 1

$$X^* = 0.86$$

$P_j = 0$

Run 7274
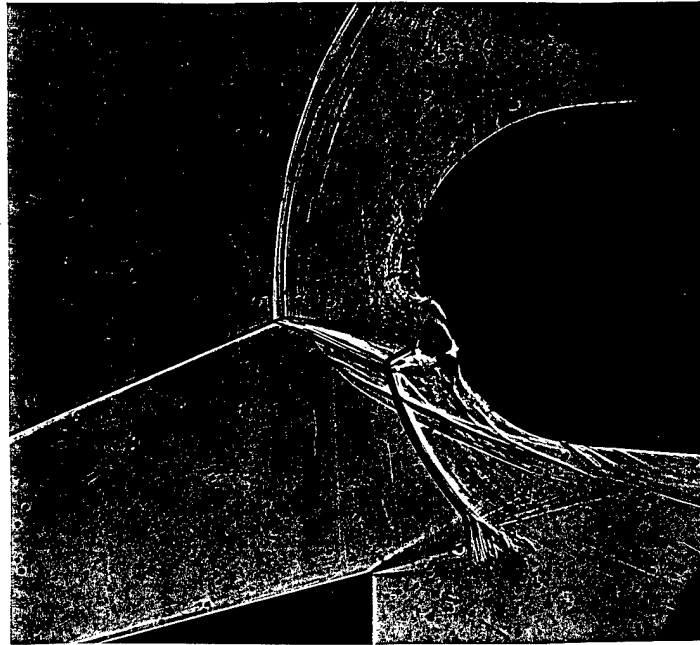
$P_j = 3.81$ bar

Run 7275

$P_j = 7.57$ bar

Run 7248
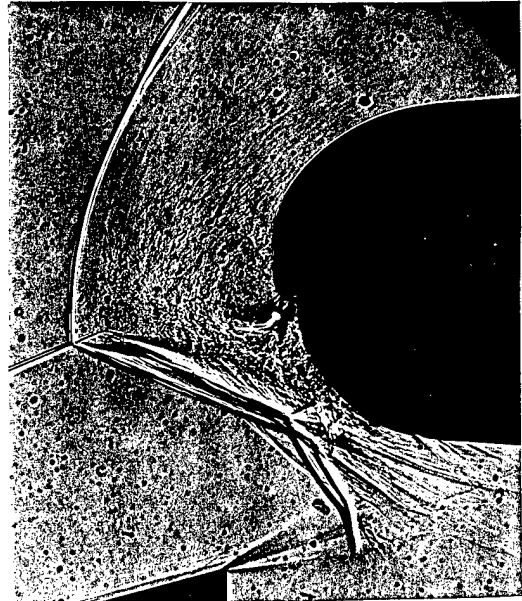
Fig. 25 a

Model 1

$X^* = 0.86$

$P_j = 15.3$ bar

Run 7249

$P_j = 30.2$ bar

Run 7250

Fig. 25 b

Model 1

$$X^\star = 0.53$$

$P_j = 0$

$P_j = 3.69$ bar

$P_j = 15.5$ bar

$P_j = 30.2$ bar

Fig. 26
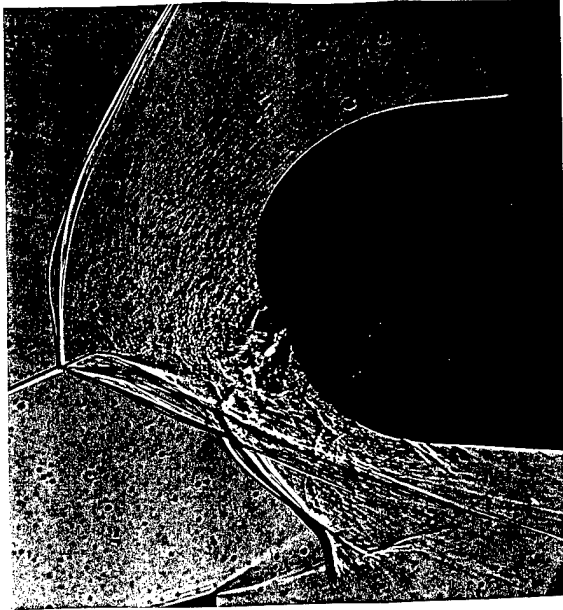
Model 1

$$X^* = 0.33$$

$P_j = 0$

Run 7268
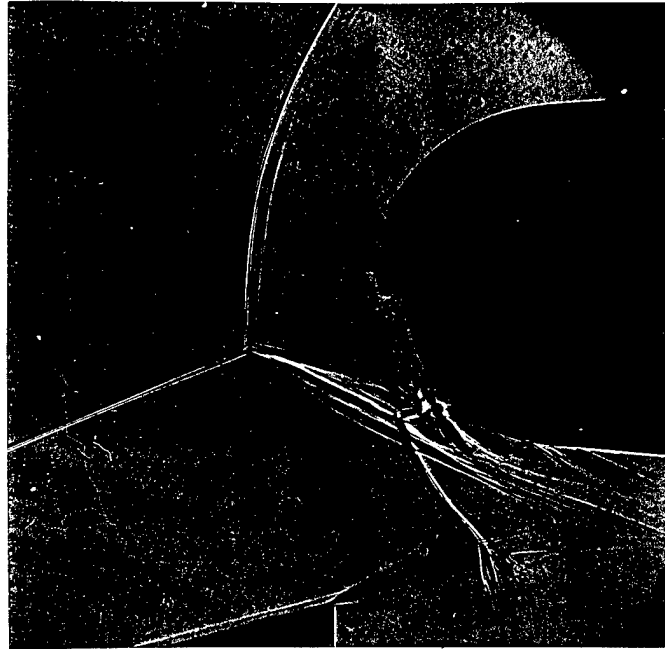
$P_j = 3.79$ bar

Run 7269
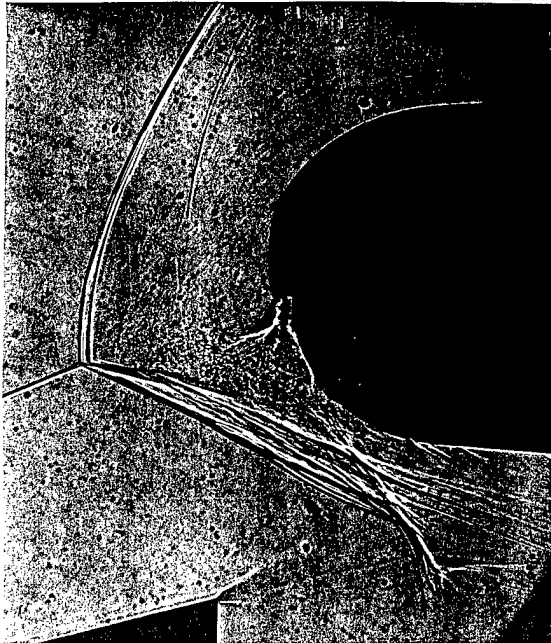
$P_j = 7.35$ bar

Run 7270
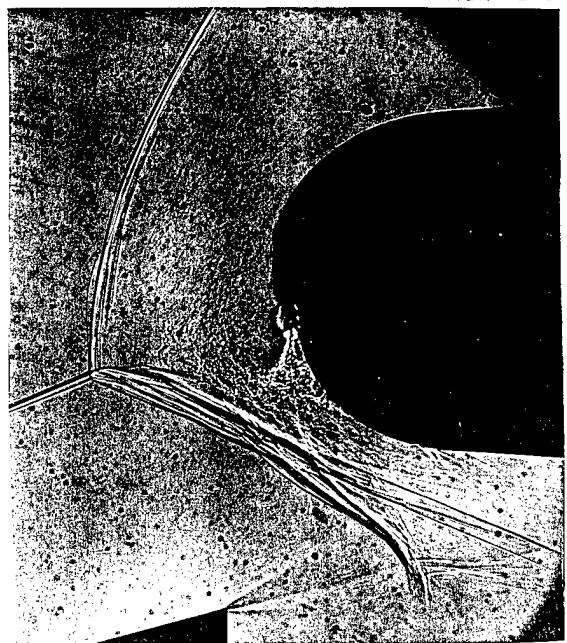
Fig. 27a

Model 1

$$X^\star = 0.33$$

$P_j = 15.4$ bar

Run 7273

$P_j = 30.3$ bar

Run 7271

Fig. 27 b
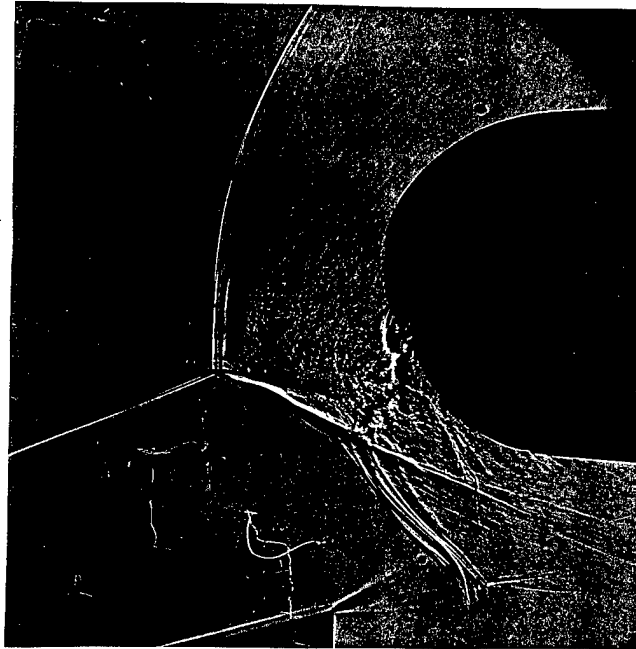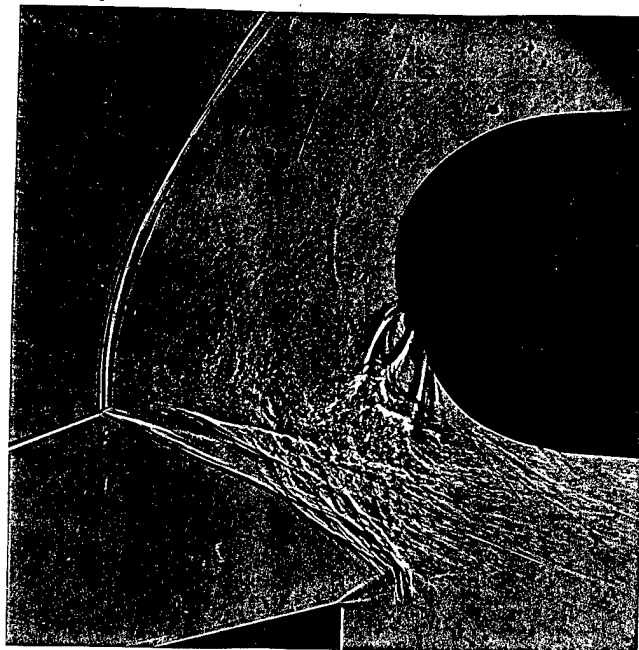
Model 1

$X^* = 0.23$

$P_j = 0$

Run 7309
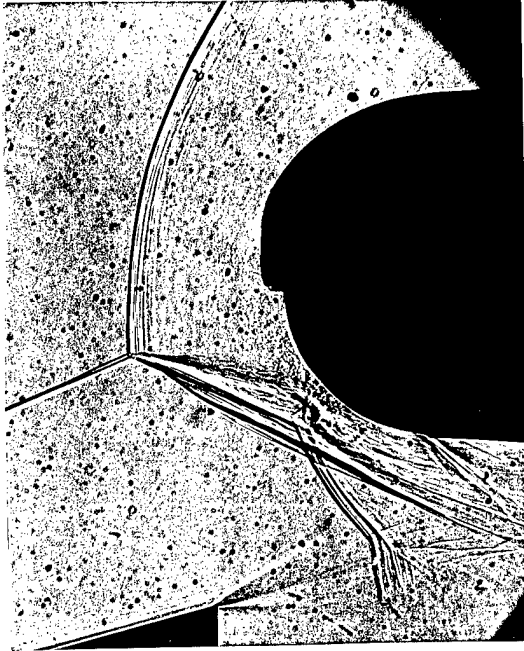
$P_j = 7.32$ bar
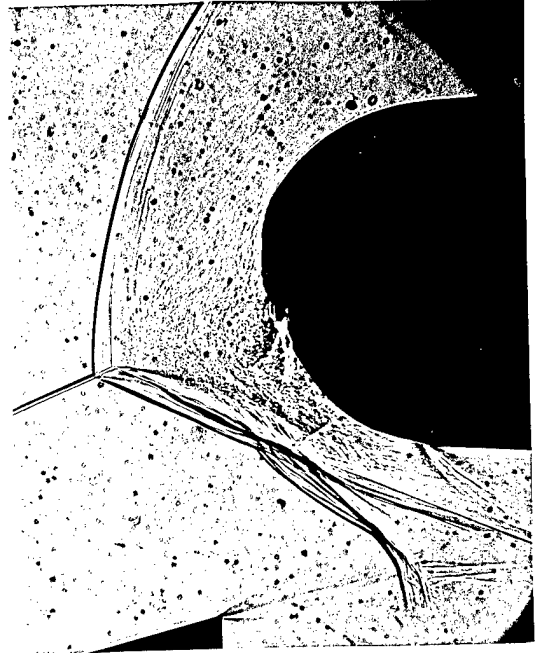
Run 7312

$P_j = 14.9$ bar
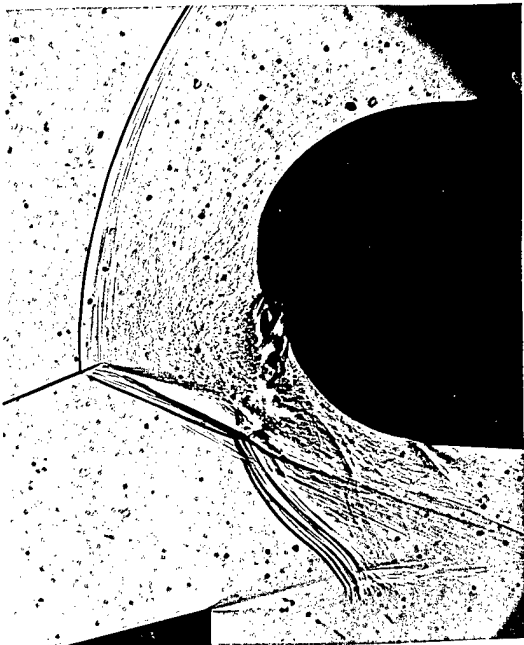
Run 7311

$P_j = 28.9$ bar

Run 7310

Fig. 28
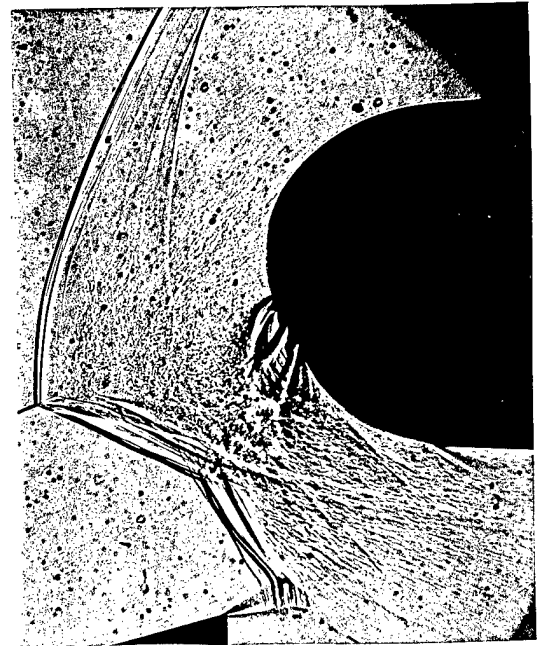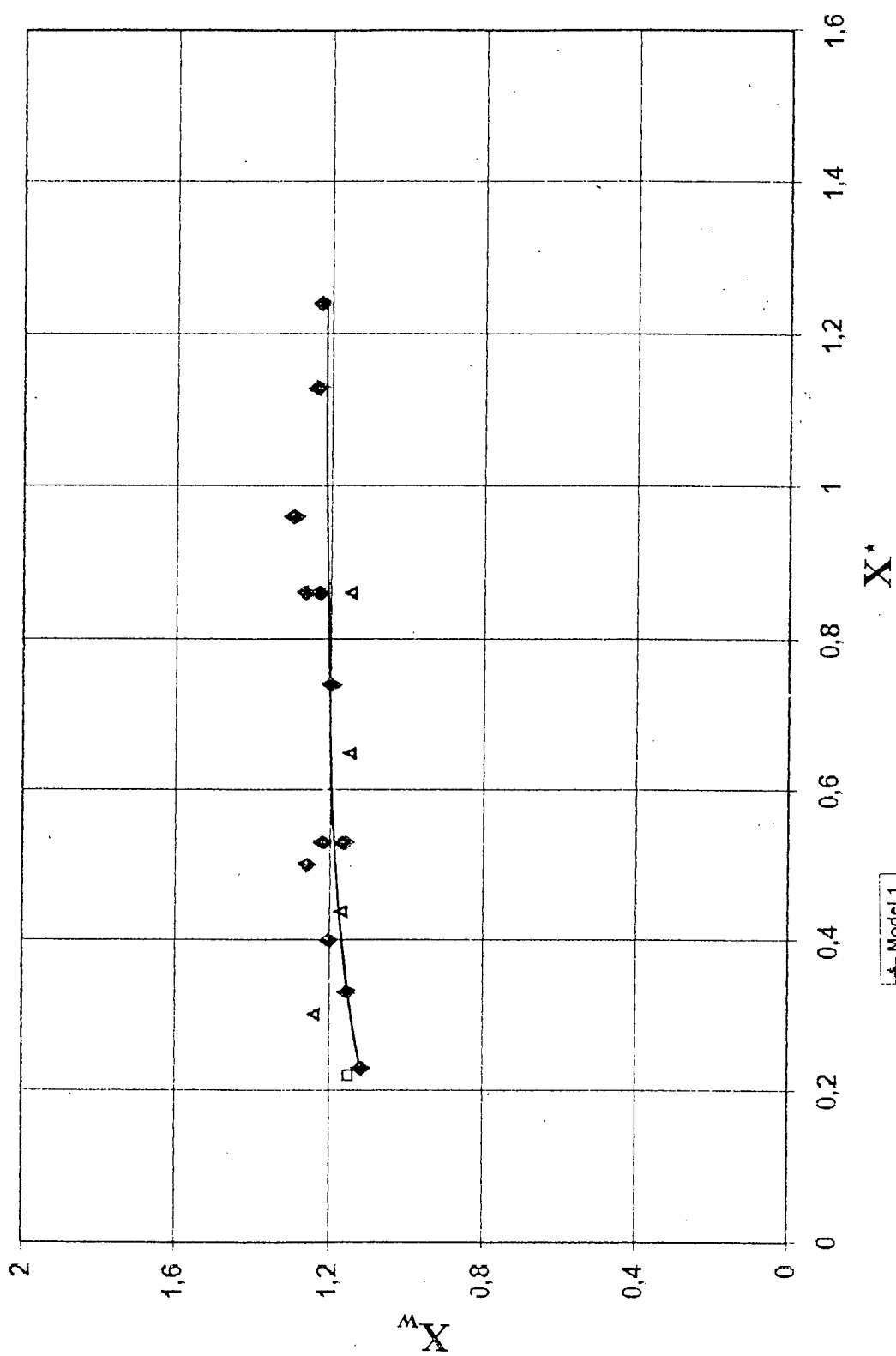
Fig. 29
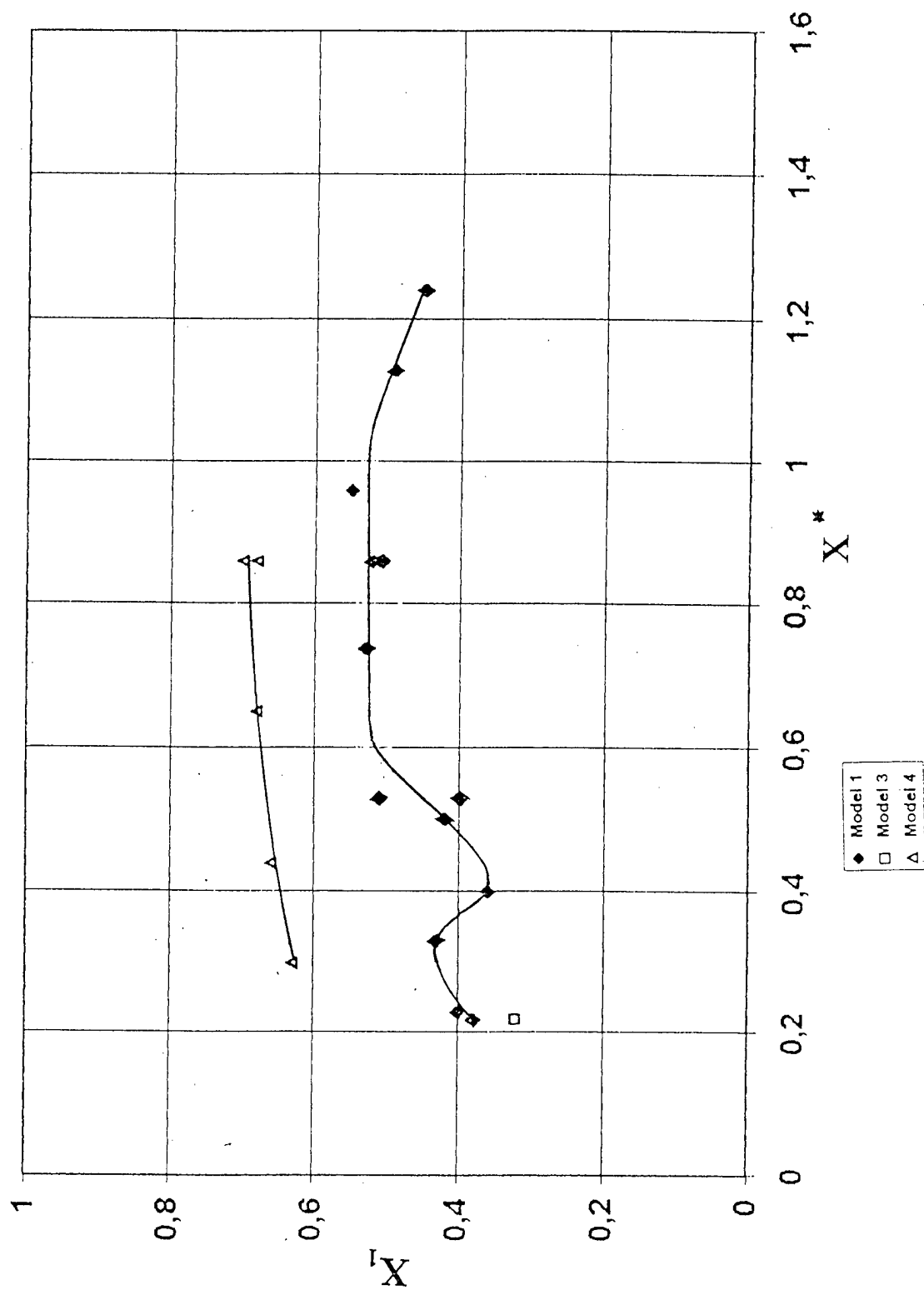
Fig. 30

Fig. 31

Model 1

$P_j = 0$
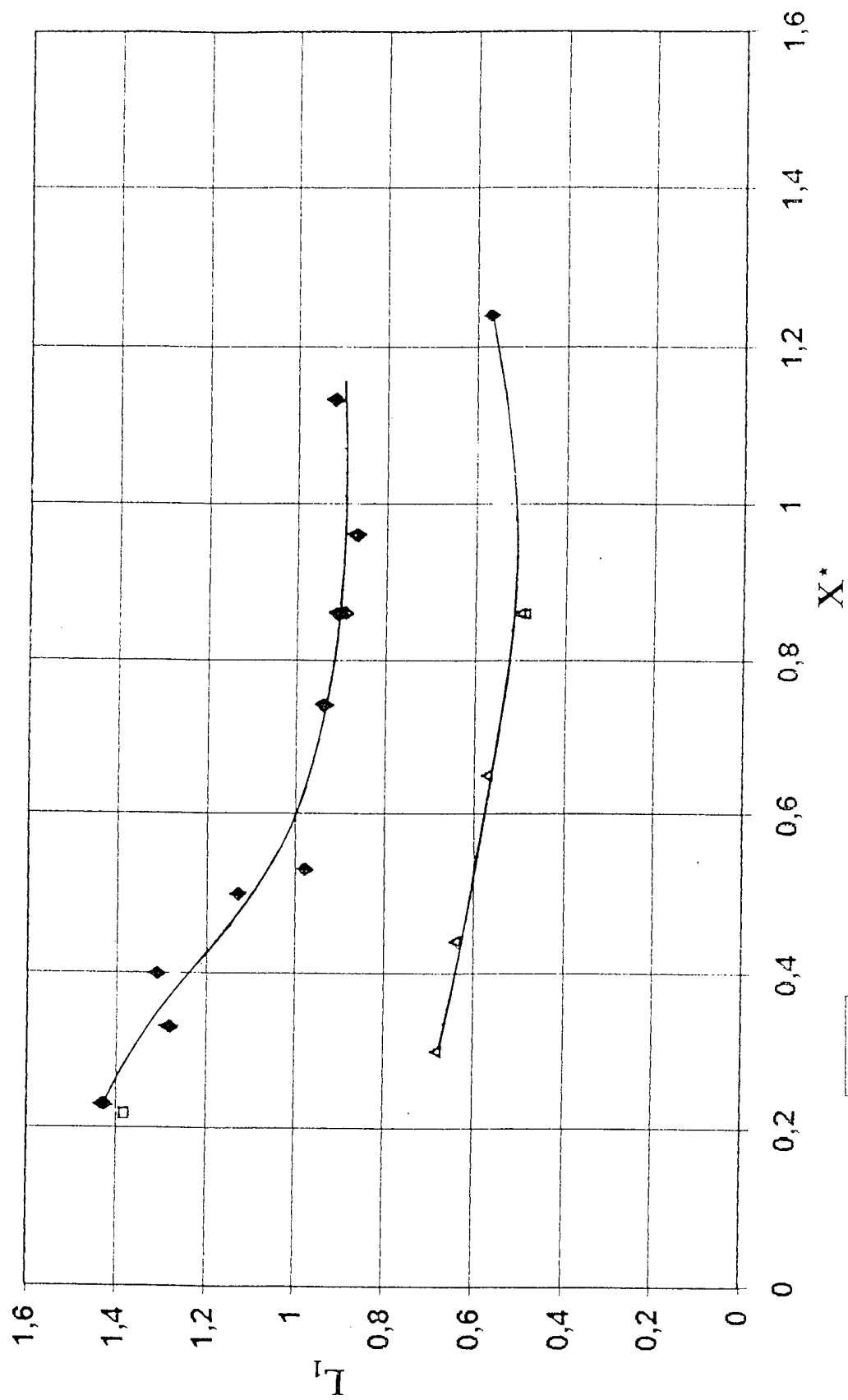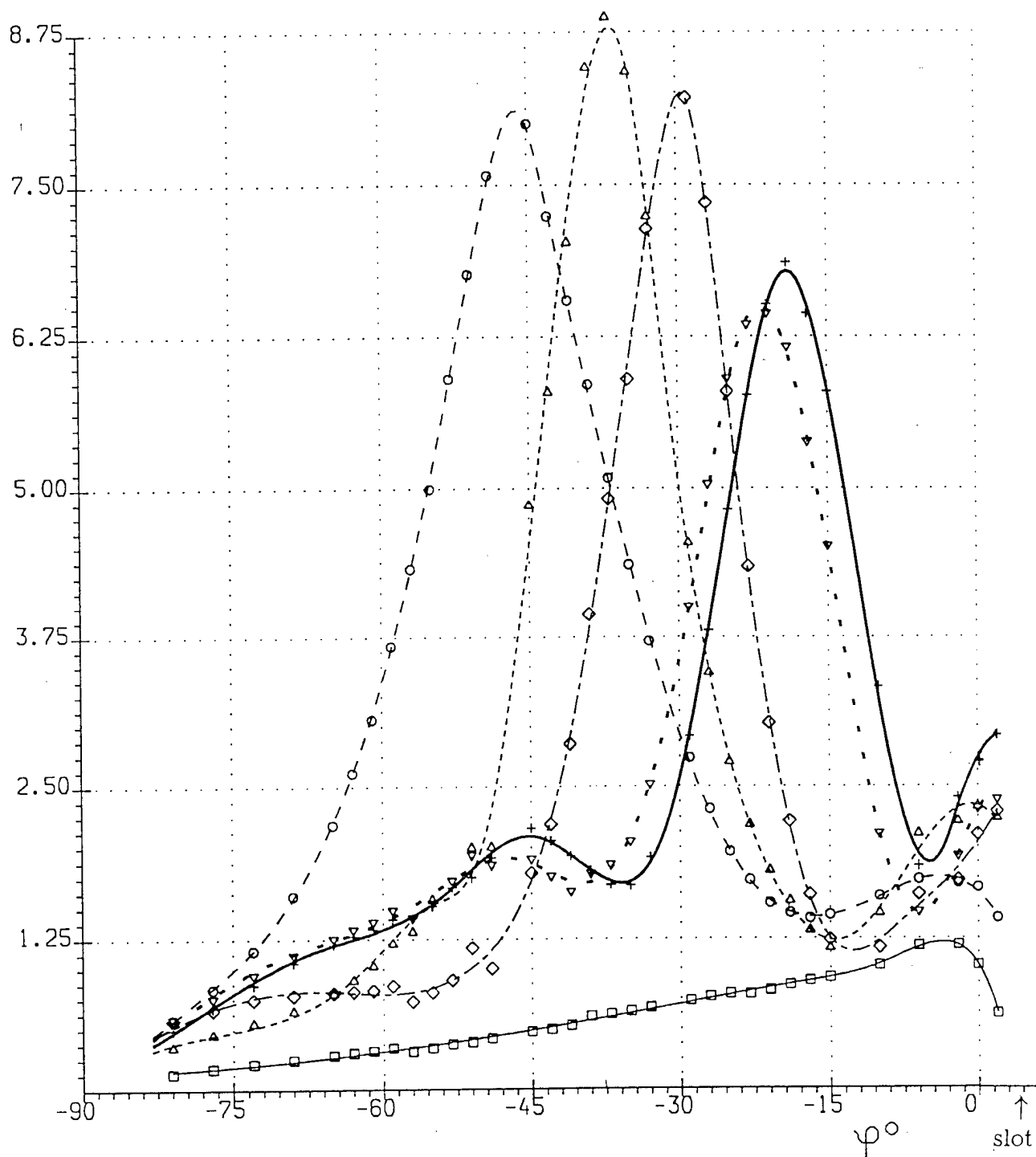
Fig. 32

Legend:
- without wedge, run: 7279
- $X^* = 0.23$, run: 7309
- $X^* = 0.33$, run: 7268
- $X^* = 0.53$, run: 7255, 7256
- $X^* = 0.86$, run: 7245, 7246, 7274
- $X^* = 1.13$, run: 7316

y-axis: q/q_{so}
x-axis: φ° ... slot

Fig. 33

$P_j=0$
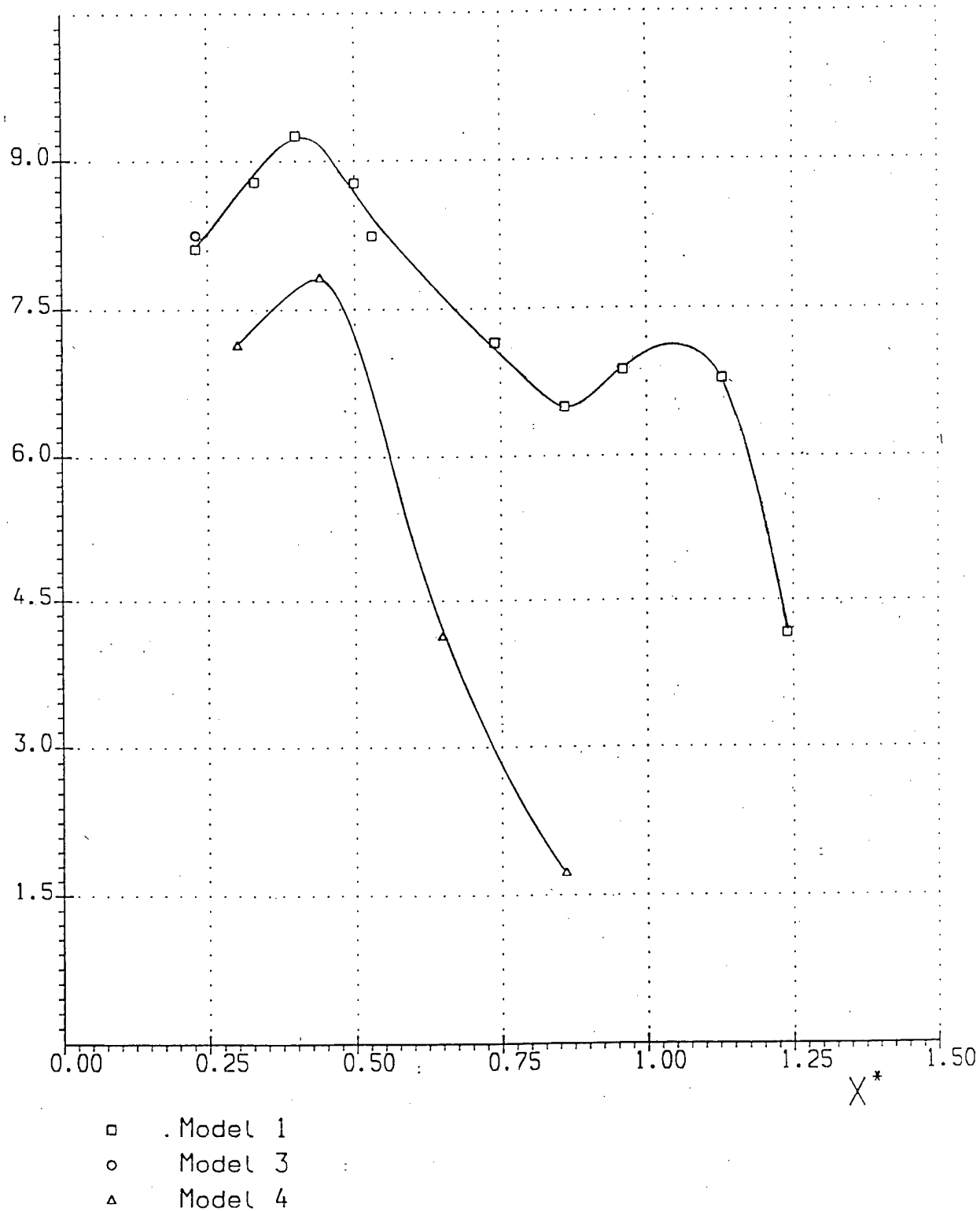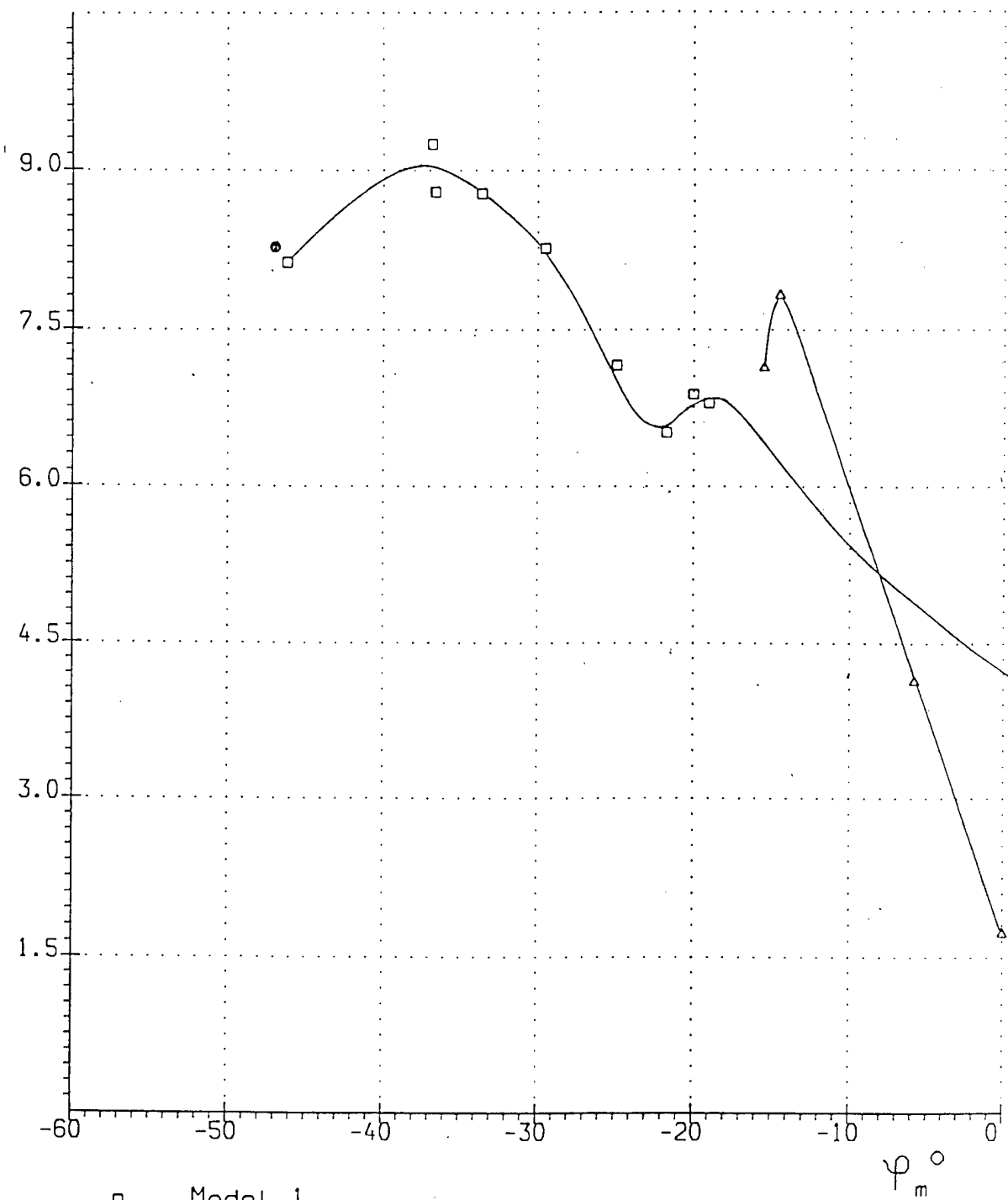
Fig. 34
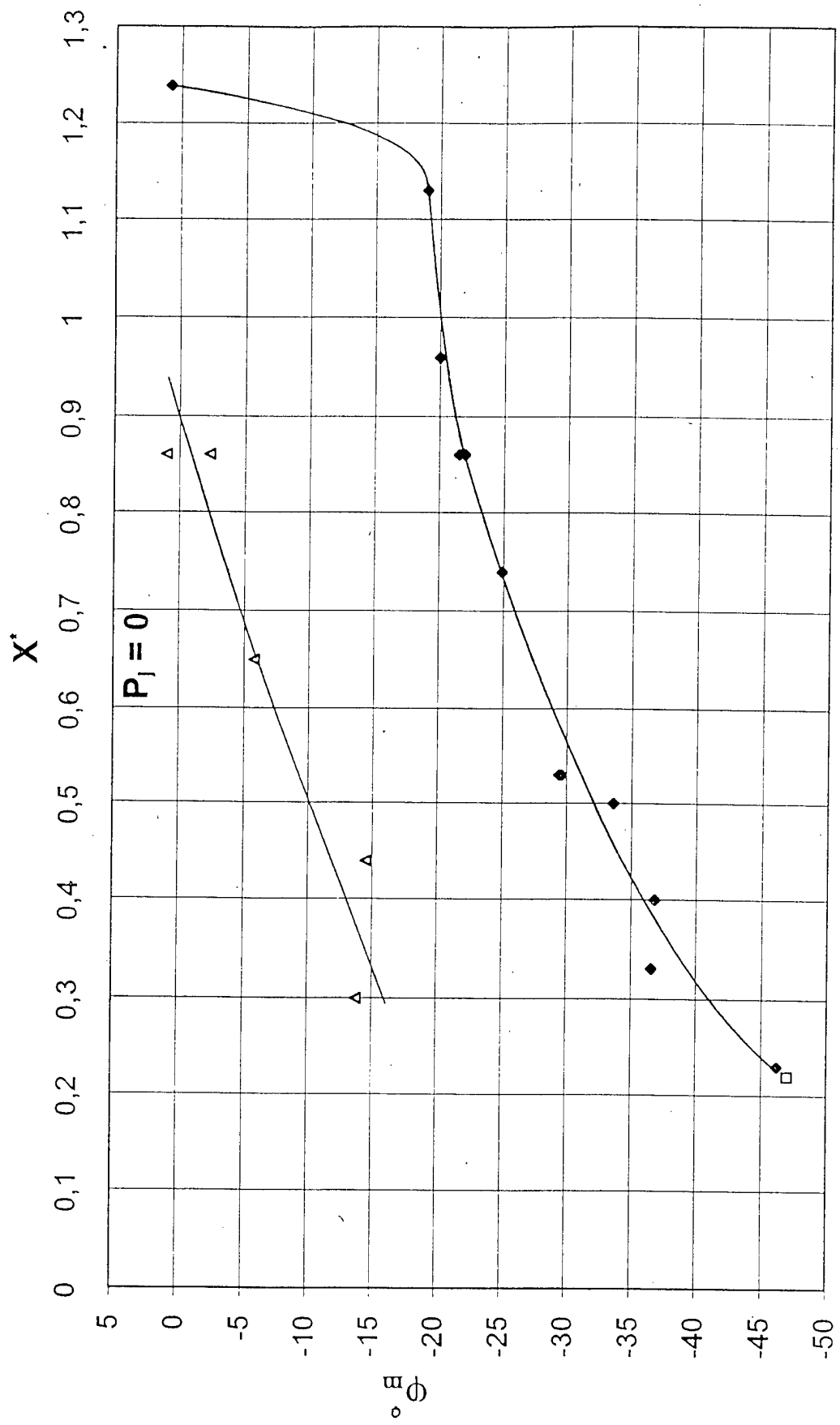
Fig. 35

Model 2

$X^{\star} = 0.75$

$P_j = 0$

Run 7238

$P_j = 19.5$ bar

Run 7239

Fig. 36
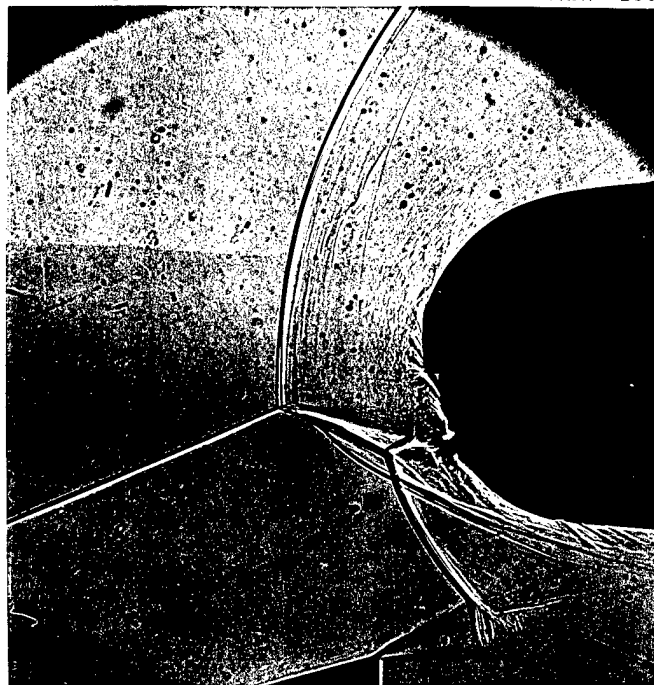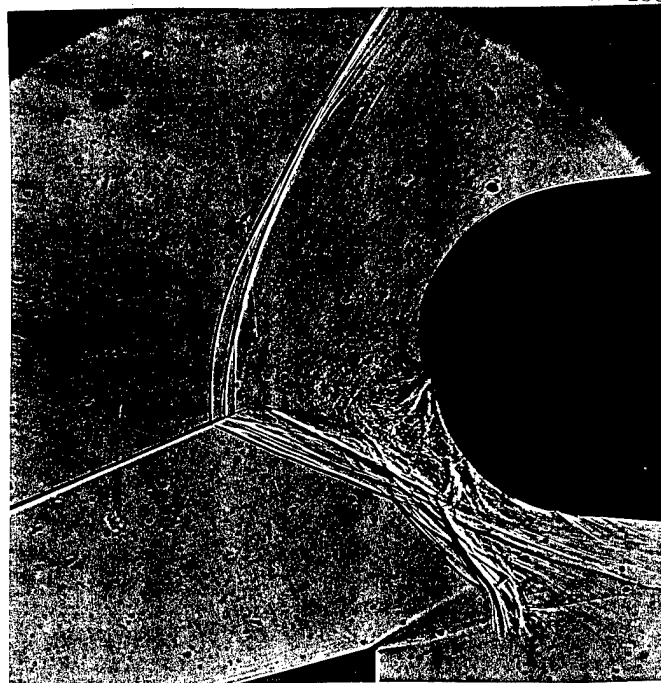
Model 3

X* = 0.22

$P_j = 0$

Run 7302
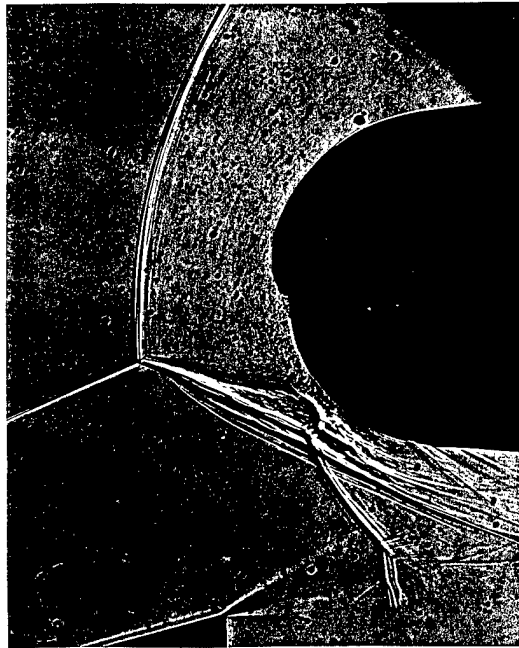
$P_j = 3.86$ bar

Run 7303
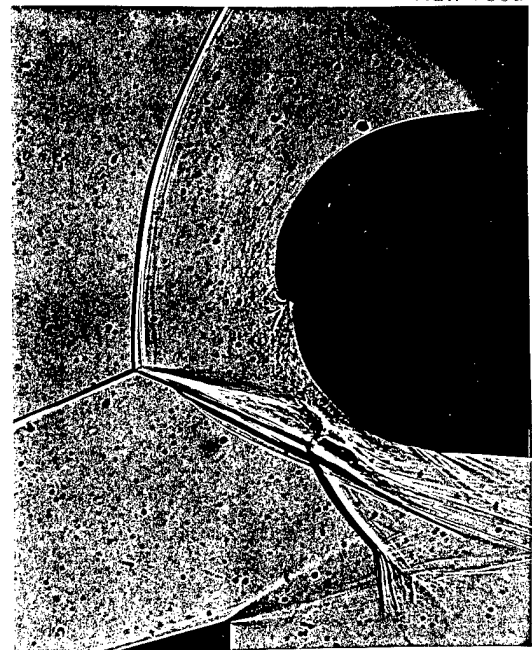
$P_j = 7.74$ bar

Run 7305

$P_j = 22.9$ bar

Run 7306

Fig. 37
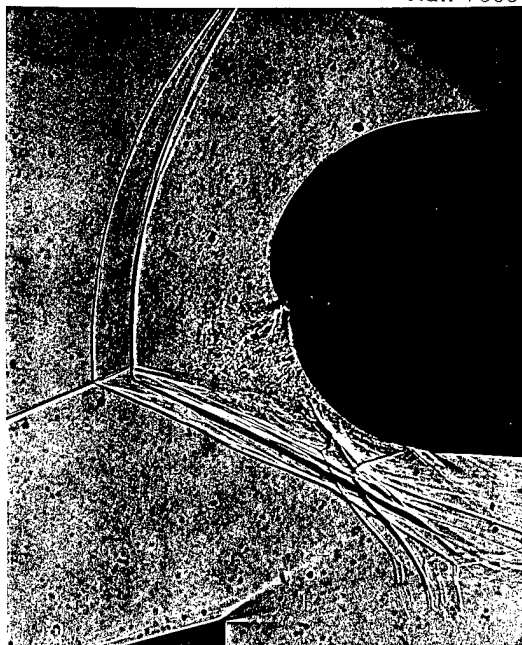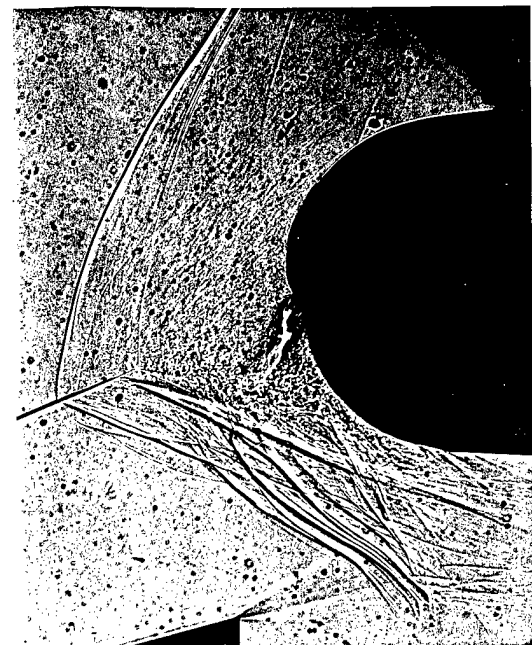
Model 4

$$P_j = 0$$

$$X^\star = 0.86$$

Run 7290
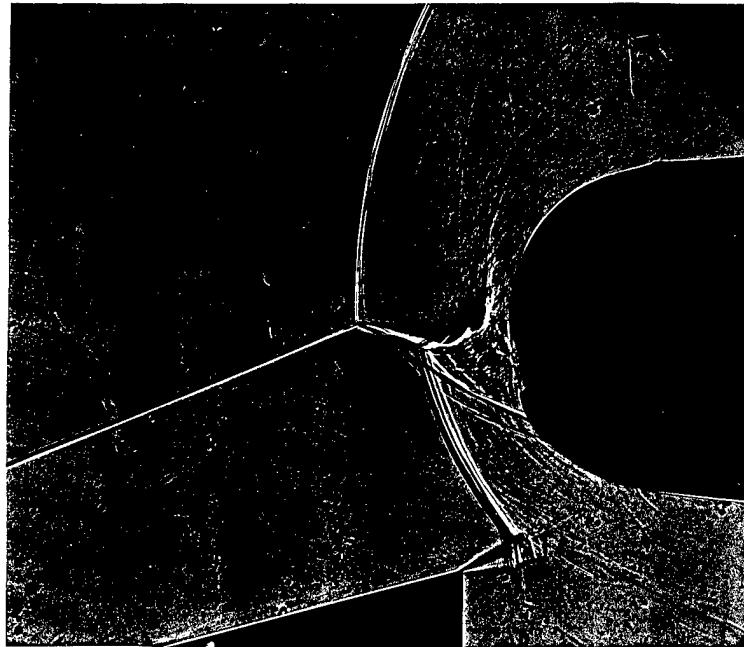
$$X^\star = 0.65$$

Run 7292
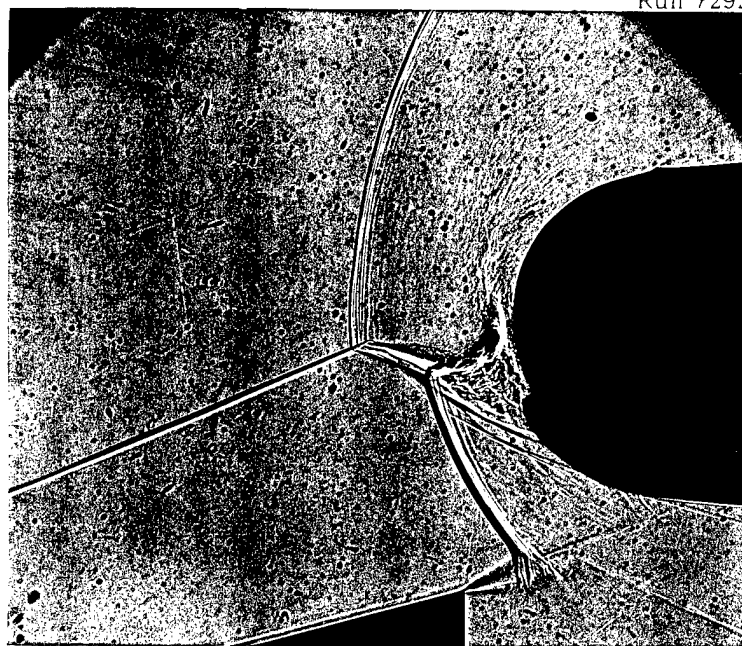
Fig. 38a

Model 4

$X^* = 0.44$

$P_j = 0$

Run 7300
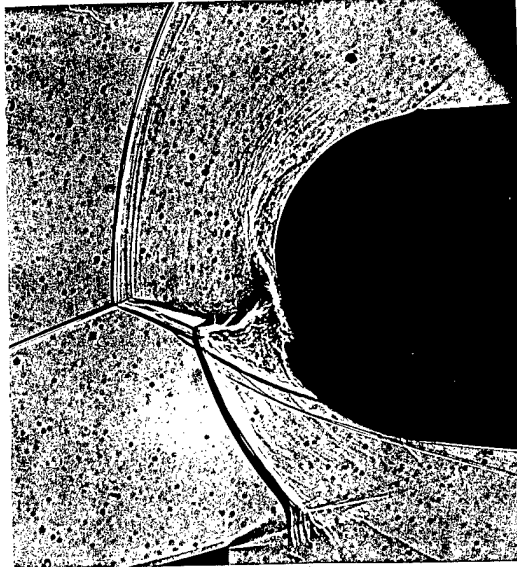
$P_j = 3.50$ bar

Run 7296
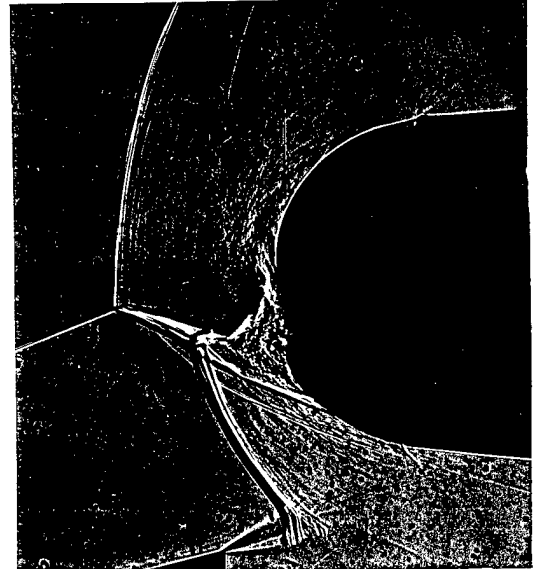
$P_j = 5.40$ bar

Run 7298
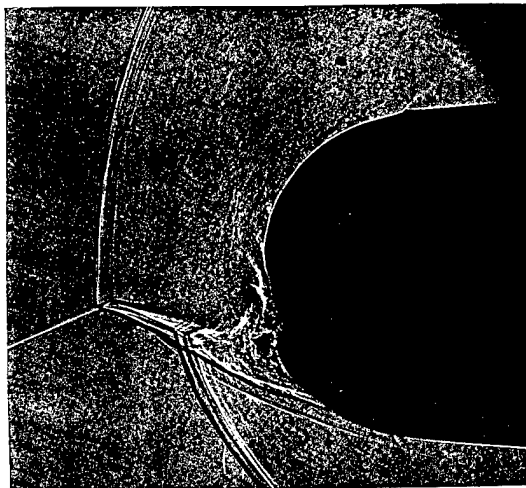
$P_j = 6.33$ bar

Run 7299
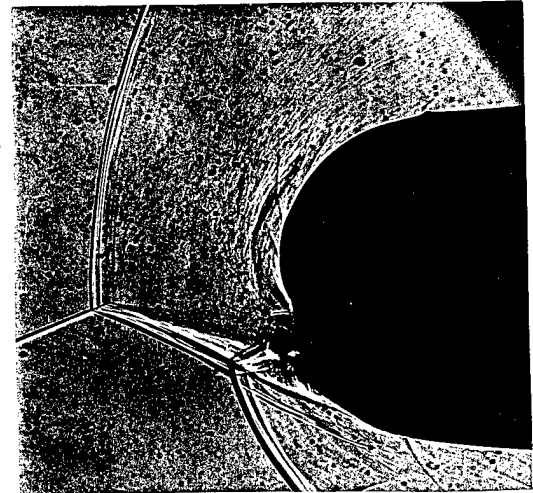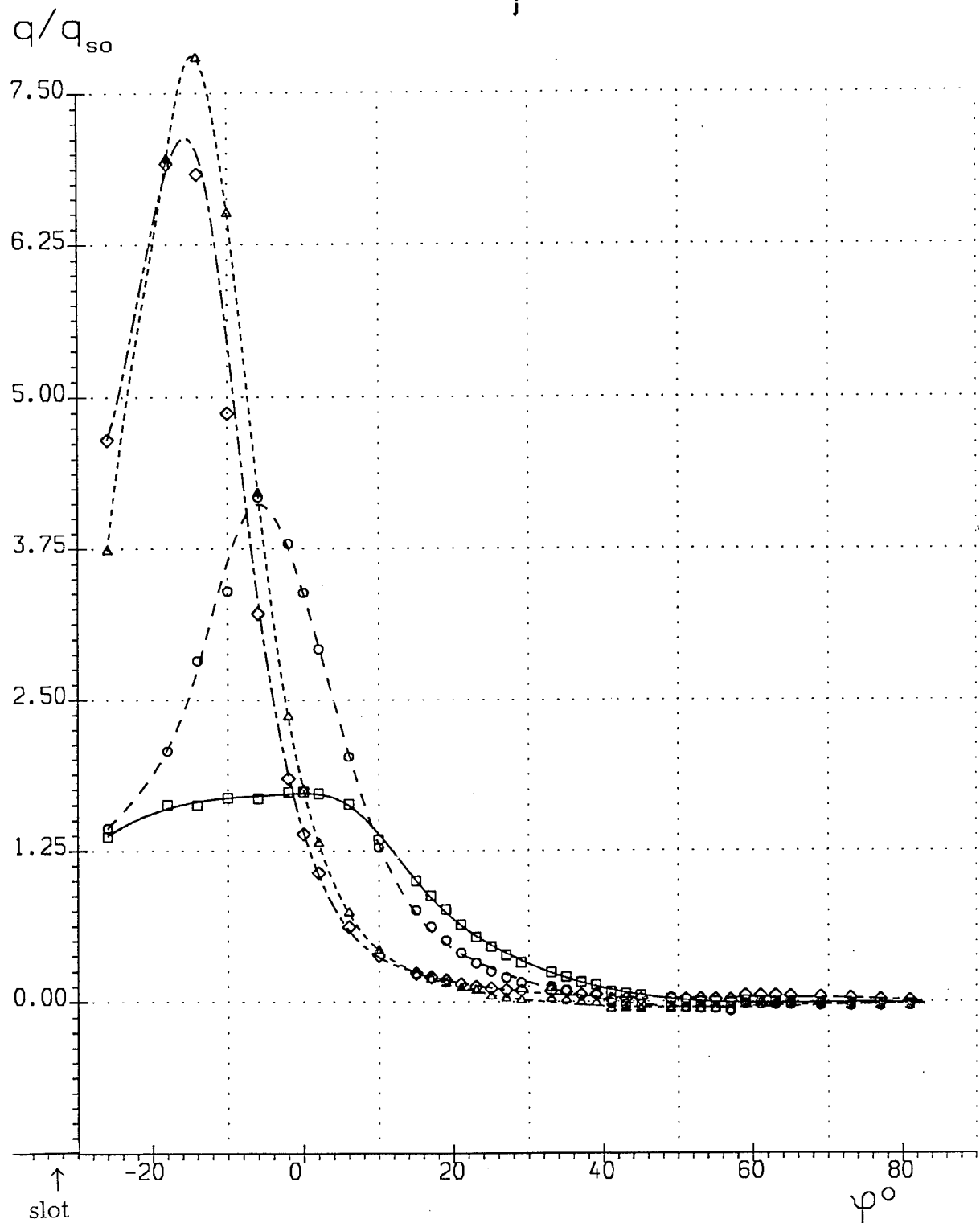
Fig. 38 b

Model 4

$P_j = 0$

q/q_{so}

Fig. 39

"leeward" surface

blunt body

high pressure zone Ψ

"windward" surface

bow shock

shock J

H

transmitted shock

bow wave

impinging shock

M_∞

shock generator

Fig. 40

Model 1

Legend:
- □ $X^*=1.13$
- ○ $X^*=0.86$
- △ -- $X^*=0.53$
- ◇ -- $X^*=0.33$
- ▼ $X^*=0.23$
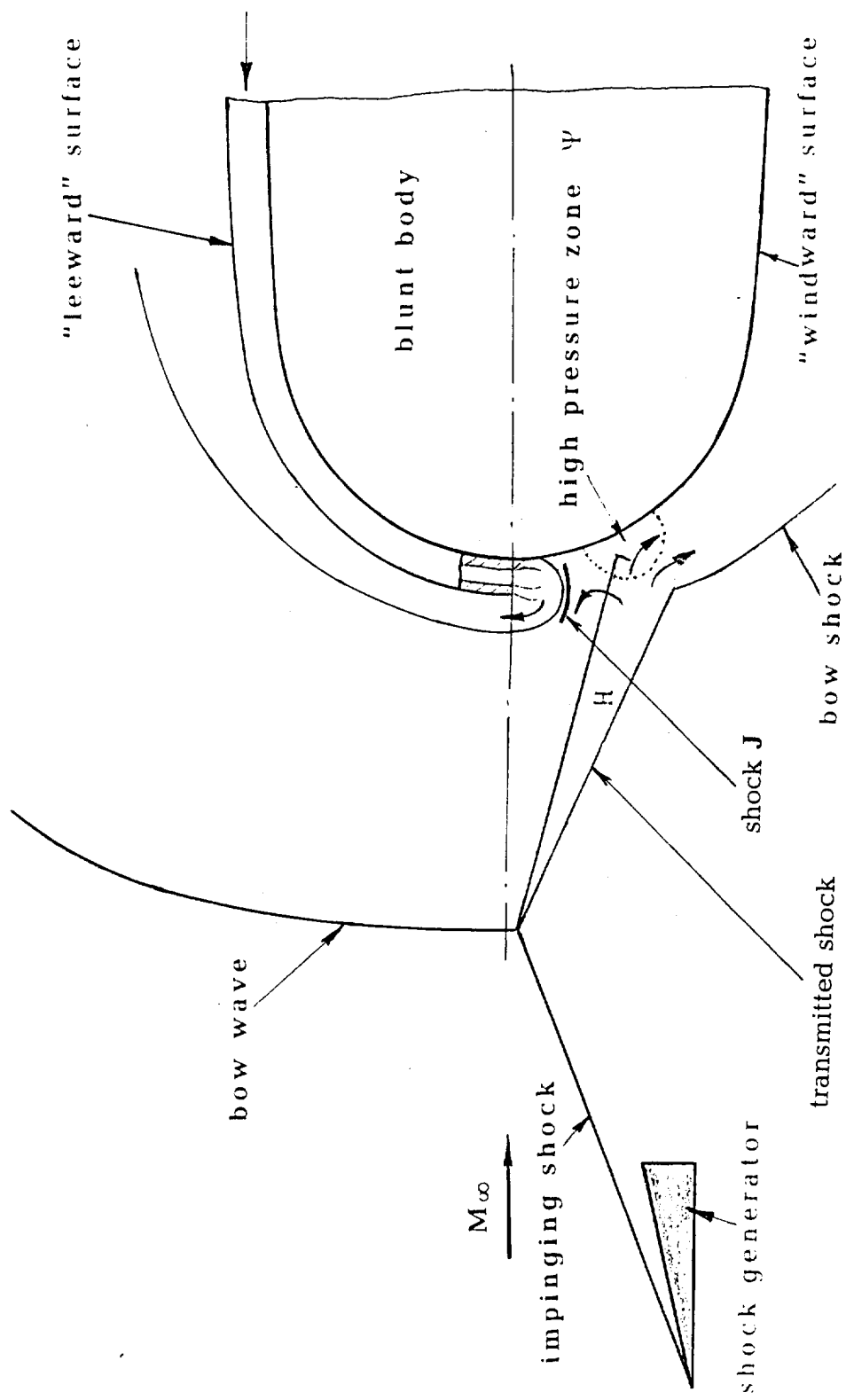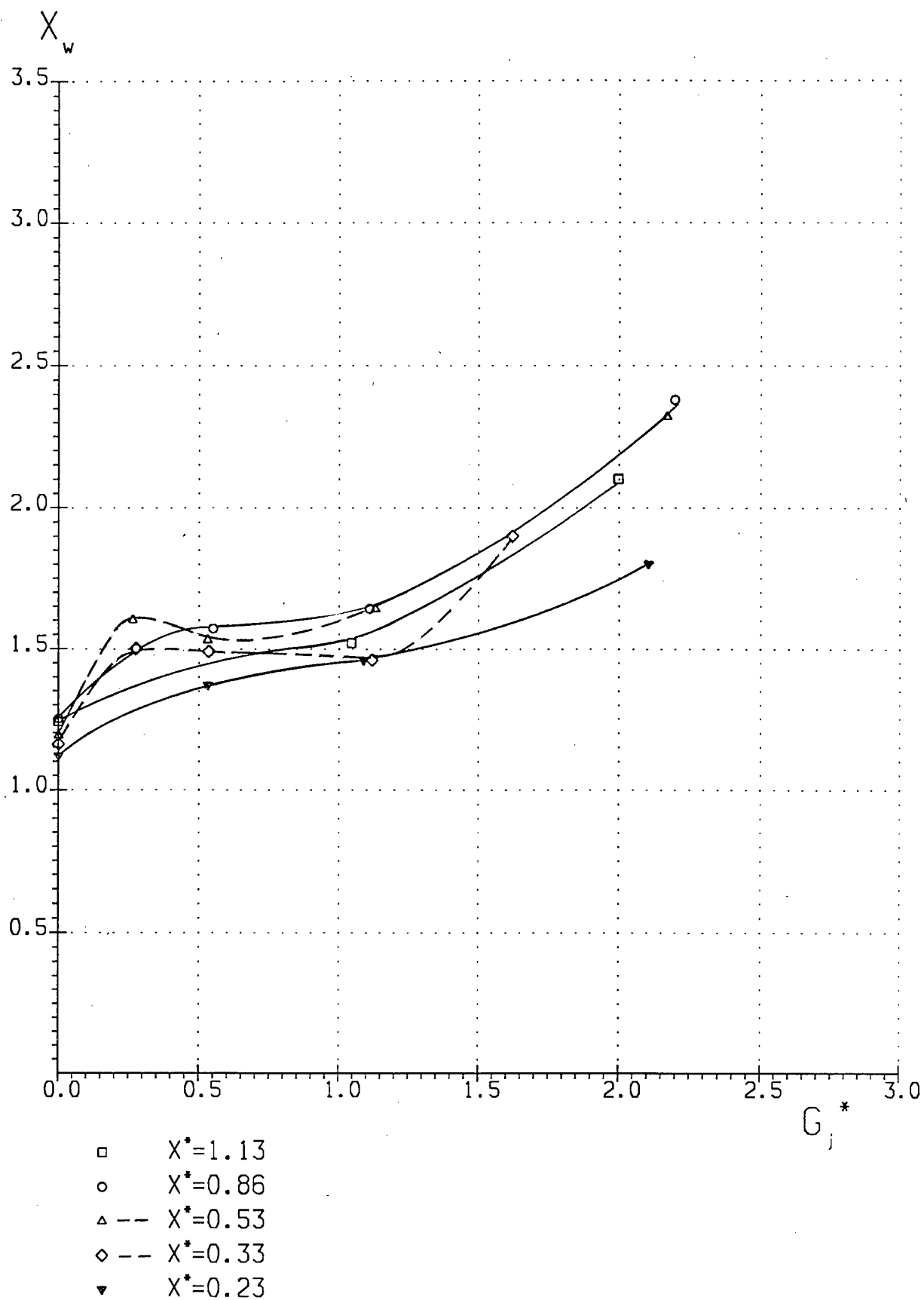
Fig. 41
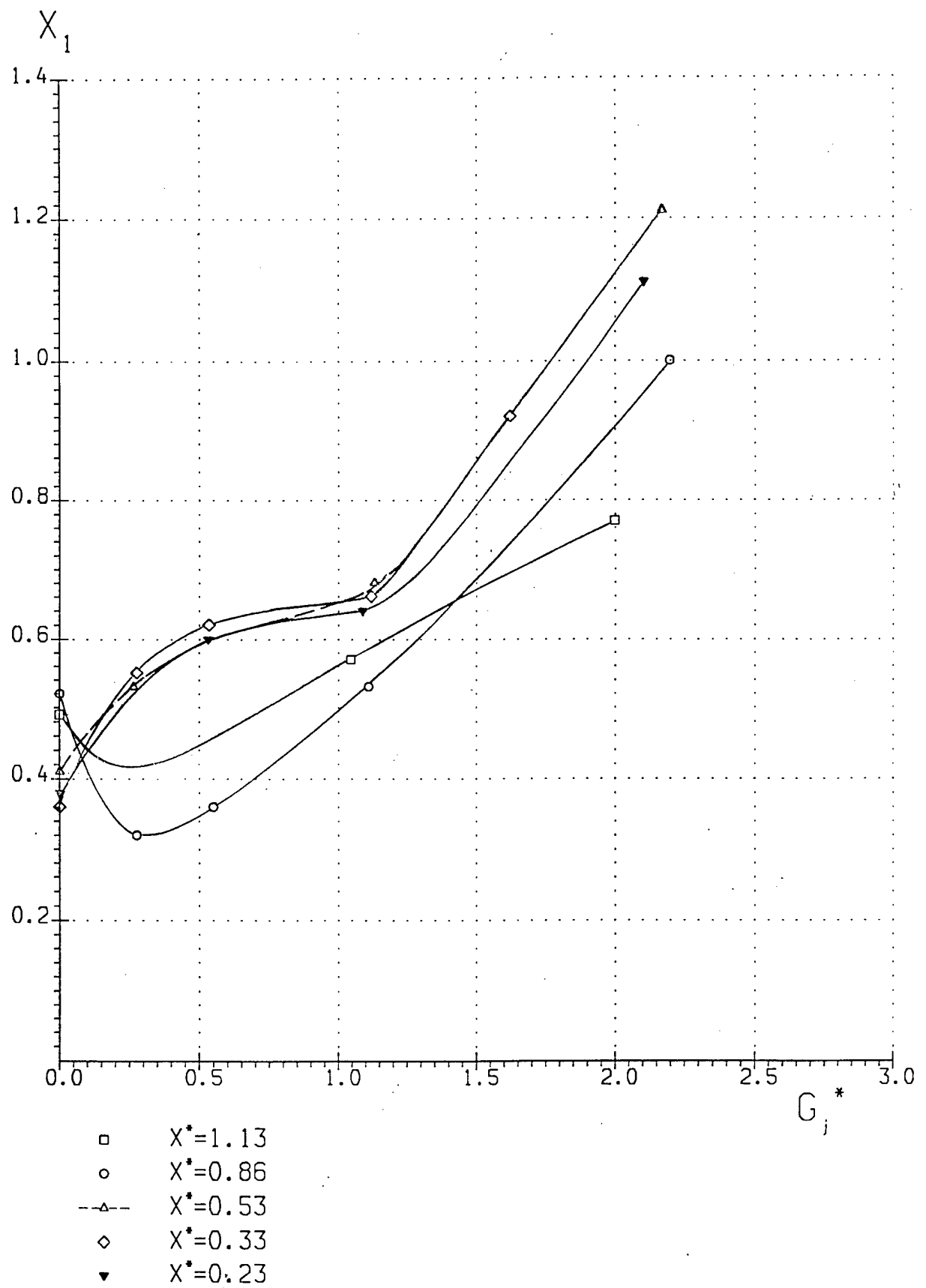
Model 1

Fig. 42

Model 1
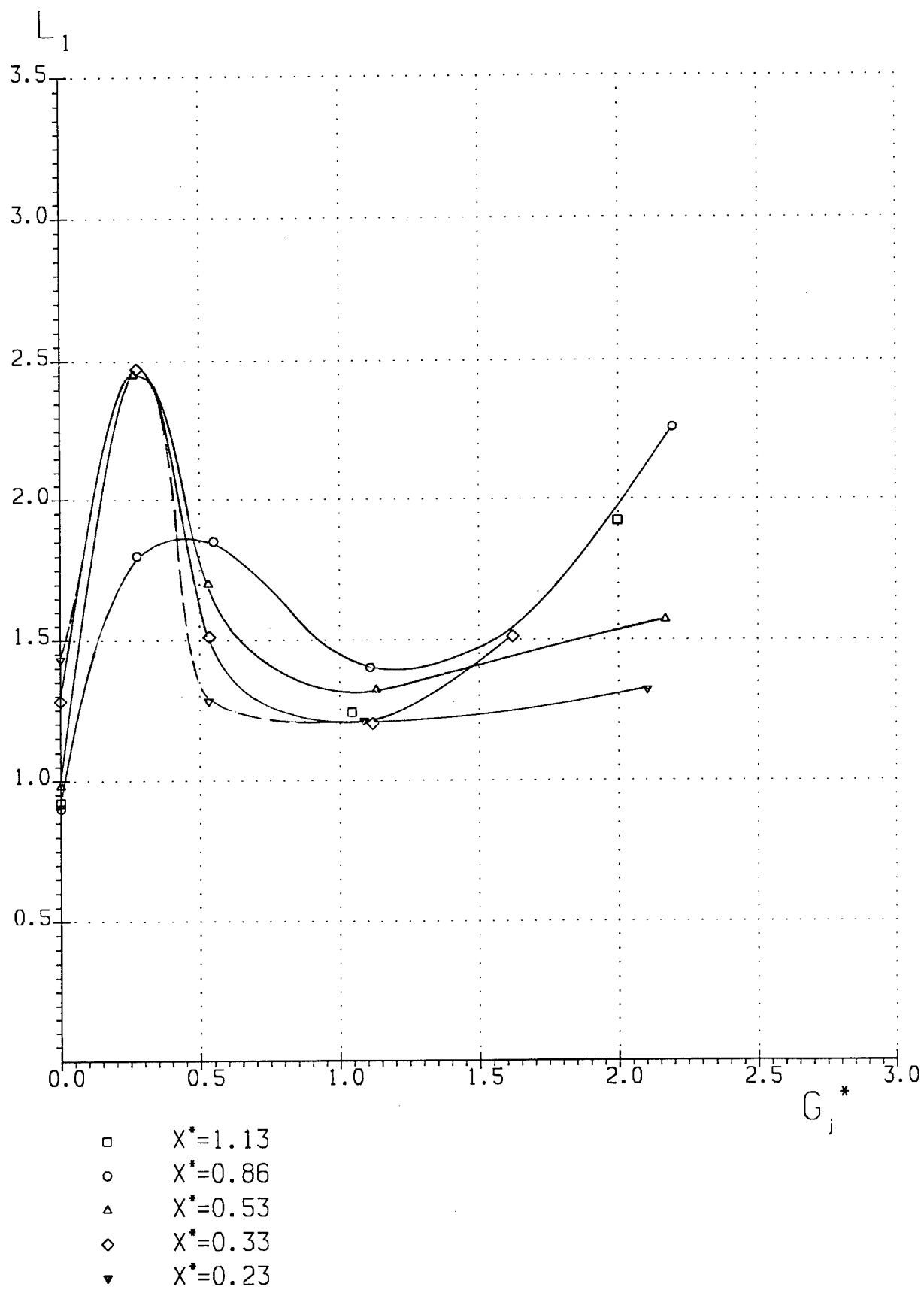
Fig. 43

Model 1   X*=1.13

q, W/cm²
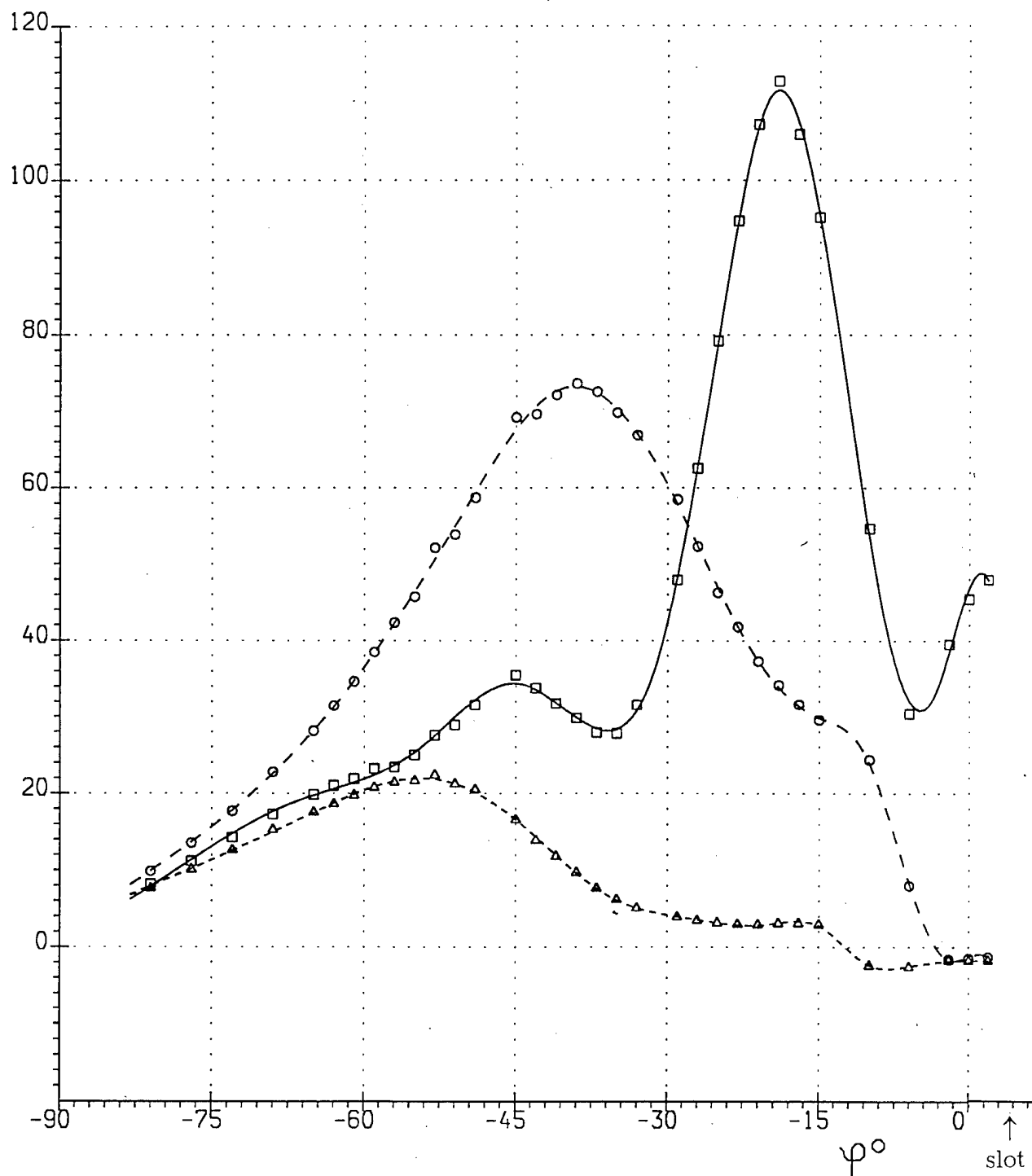
P_j =0.00 bar,   run:7316
P_j =14.4 bar,   run:7317
P_j =27.7 bar,   run:7318

Fig. 44

Model 1   X*=1.13
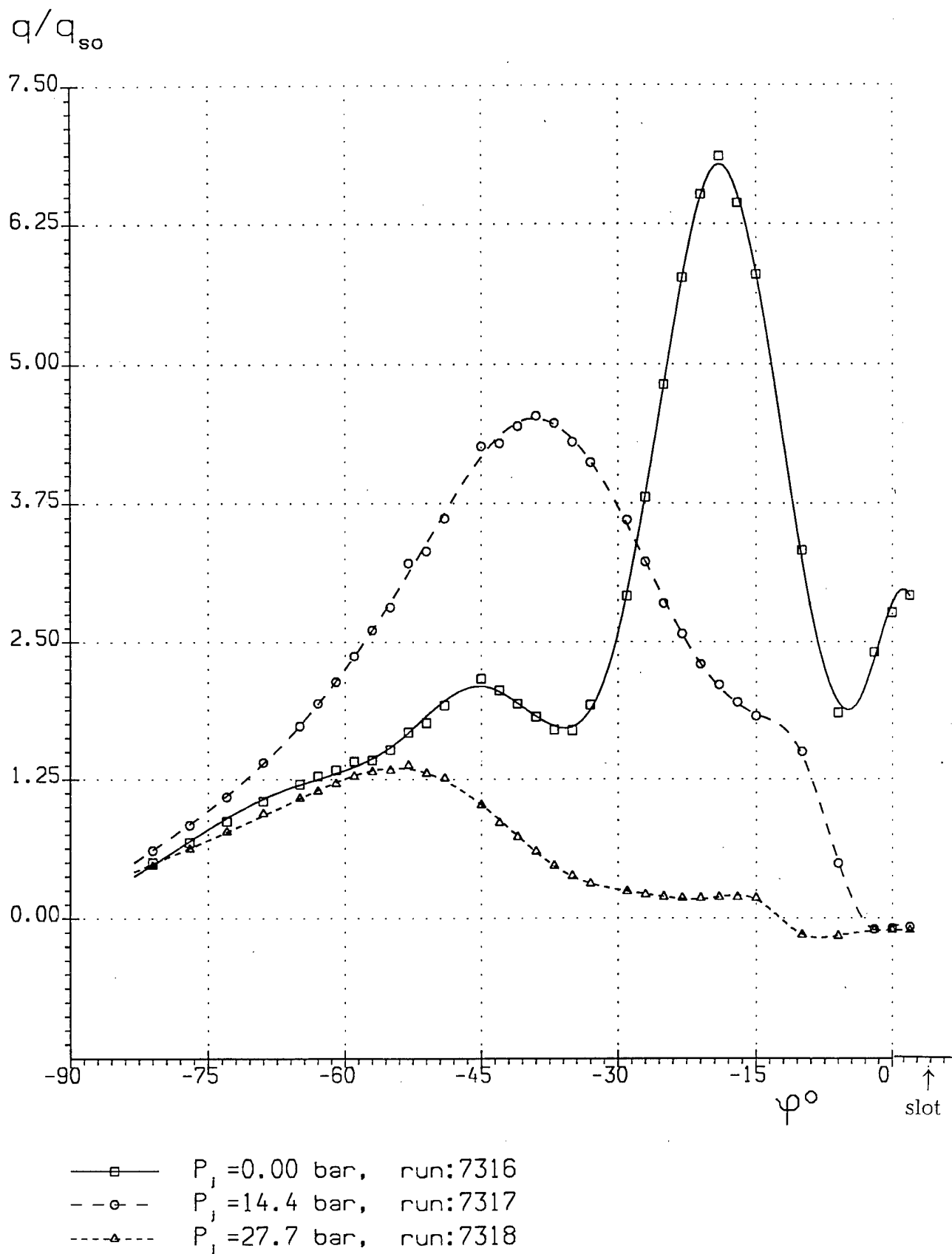
Fig. 45

Model 1   X*=0.86
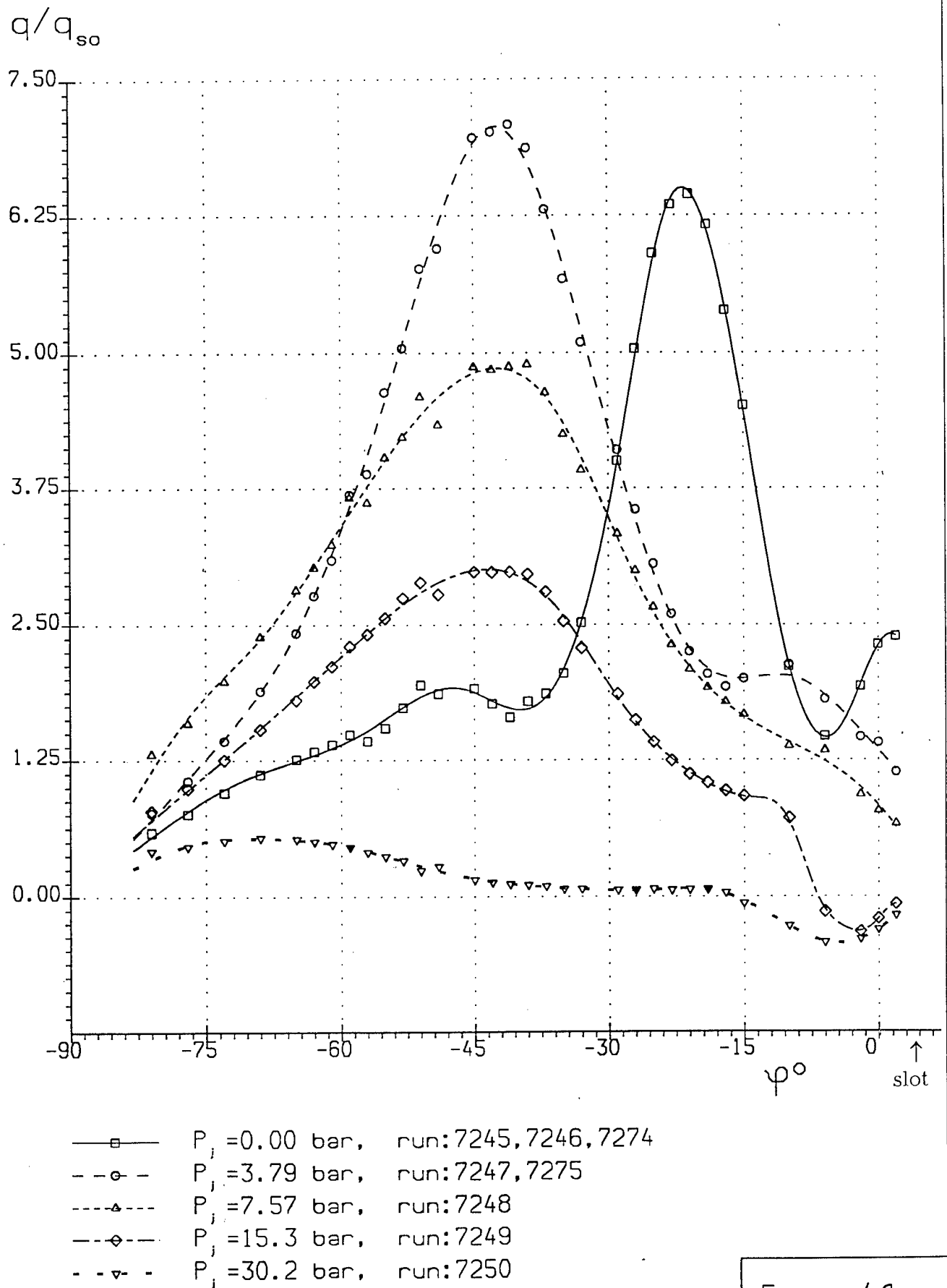
Fig. 46

Model 1   X*=0.53
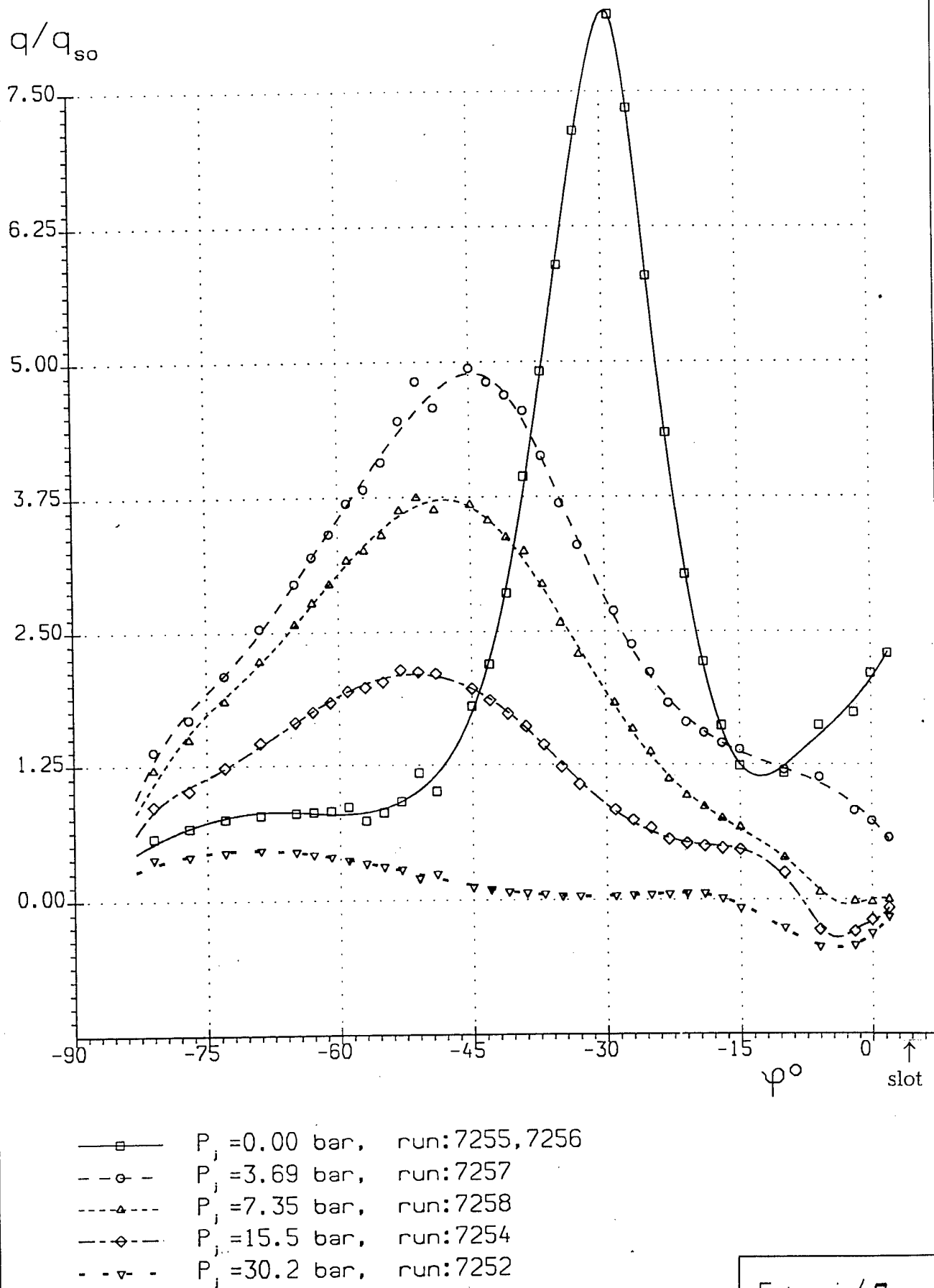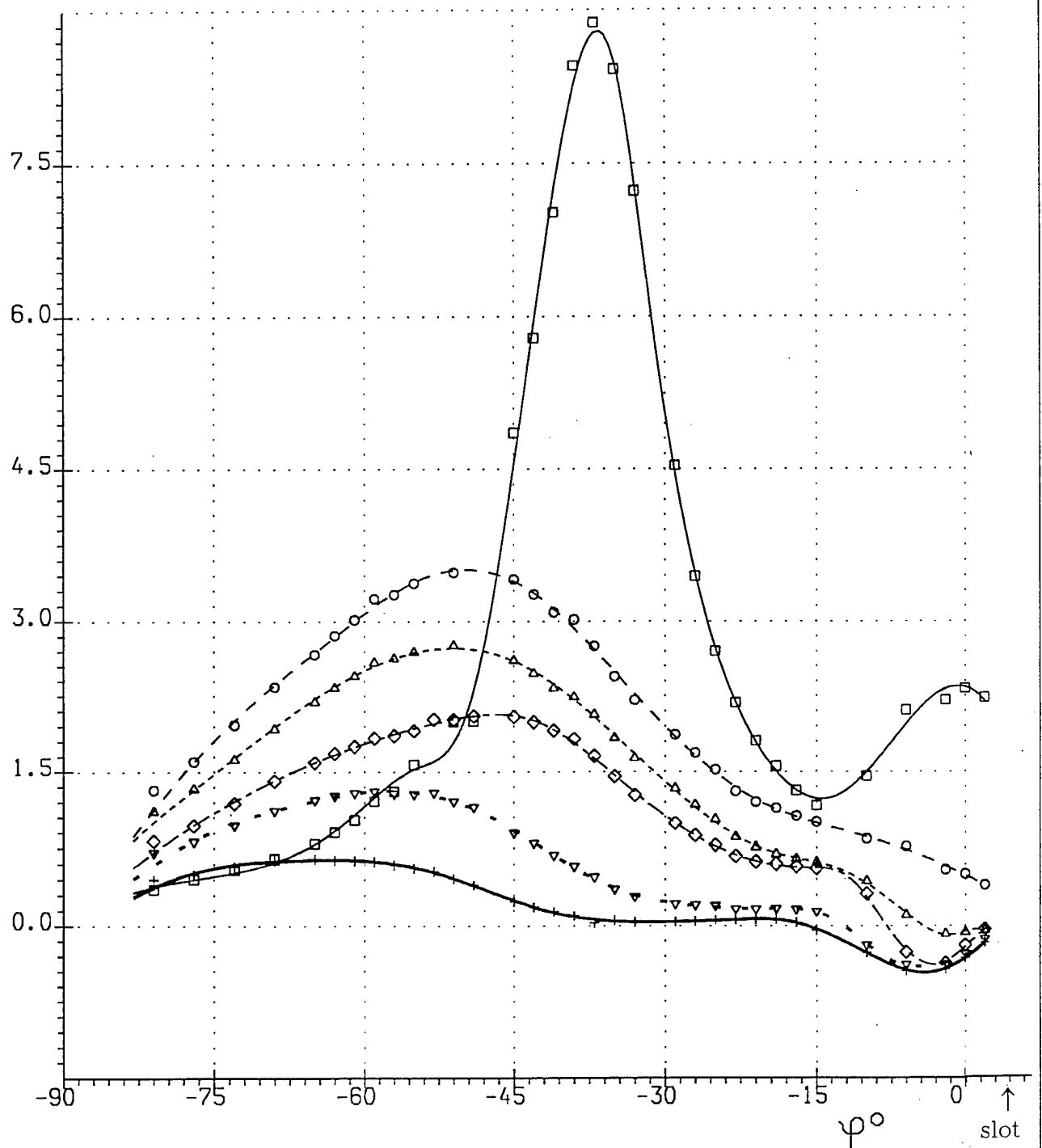
q/q_{so}

$\varphi°$

slot

P_j =0.00 bar,   run:7255,7256
P_j =3.69 bar,   run:7257
P_j =7.35 bar,   run:7258
P_j =15.5 bar,   run:7254
P_j =30.2 bar,   run:7252

Fig. 47

Model 1   X*=0.33

Fig. 48

Model 1 $X^*=0.23$

q/q_{so}

7.5

6.0

4.5

3.0

1.5

0.0

-90   -75   -60   -45   -30   -15   0 $\varphi°$ slot
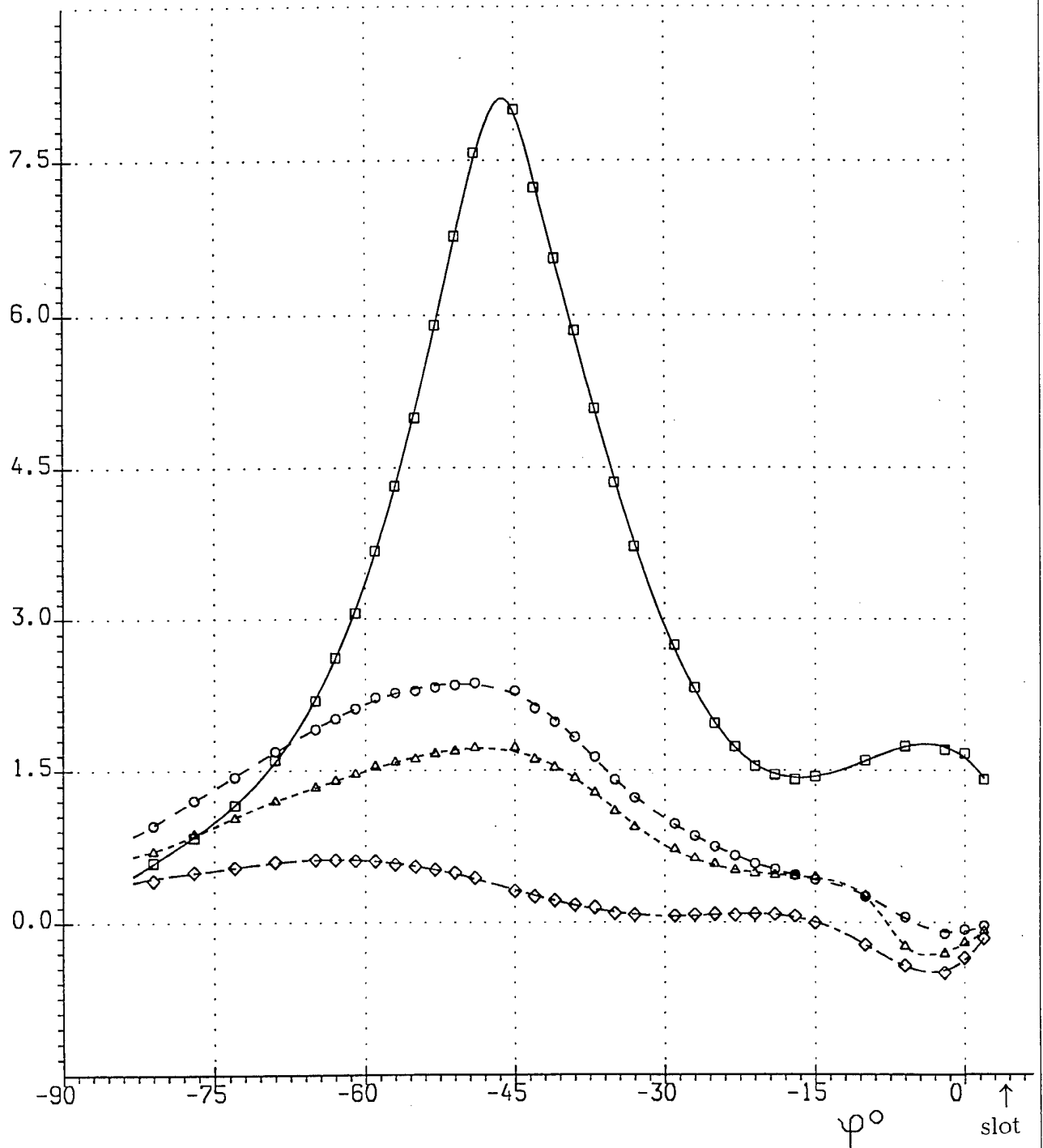
P_j =0.00 bar,   run:7309
P_j =7.32 bar,   run:7312
P_j =14.9 bar,   run:7311
P_j =28.9 bar,   run:7310

Fig. 49

Model 1

q_m/q_{so} versus G_j^*

Legend:
- $X^* = 1.13$
- $X^* = 0.86$
- $X^* = 0.53$
- $X^* = 0.33$
- $X^* = 0.23$

Fig. 50

Model 1

Legend:
- □ $X^* = 1.13$
- ○ $X^* = 0.86$
- △ $X^* = 0.53$
- ◇ $X^* = 0.33$
- ▽ $X^* = 0.23$

Vertical axis: $\varphi_m^{\,\circ}$

Horizontal axis: $G_j^{\,*}$
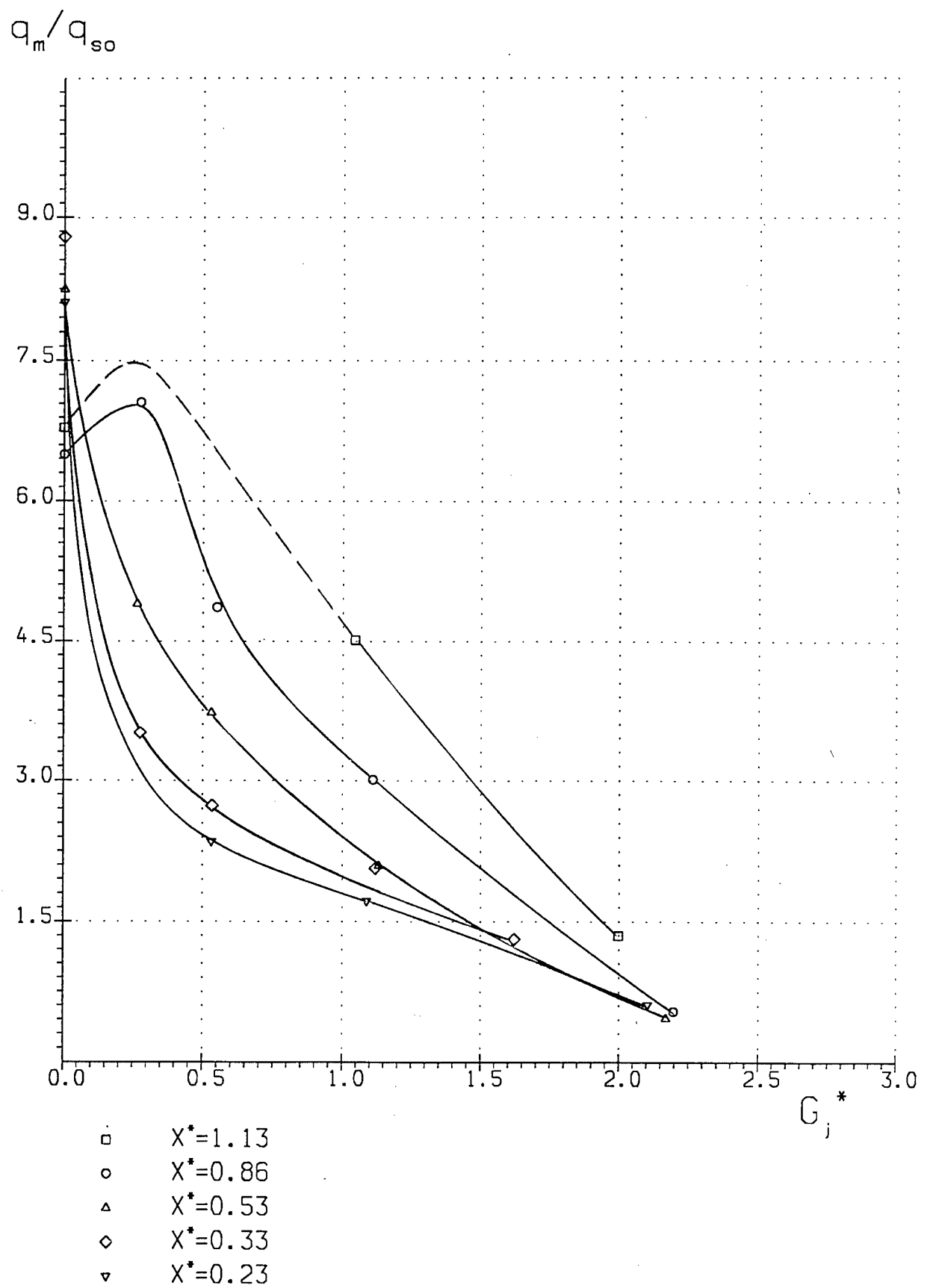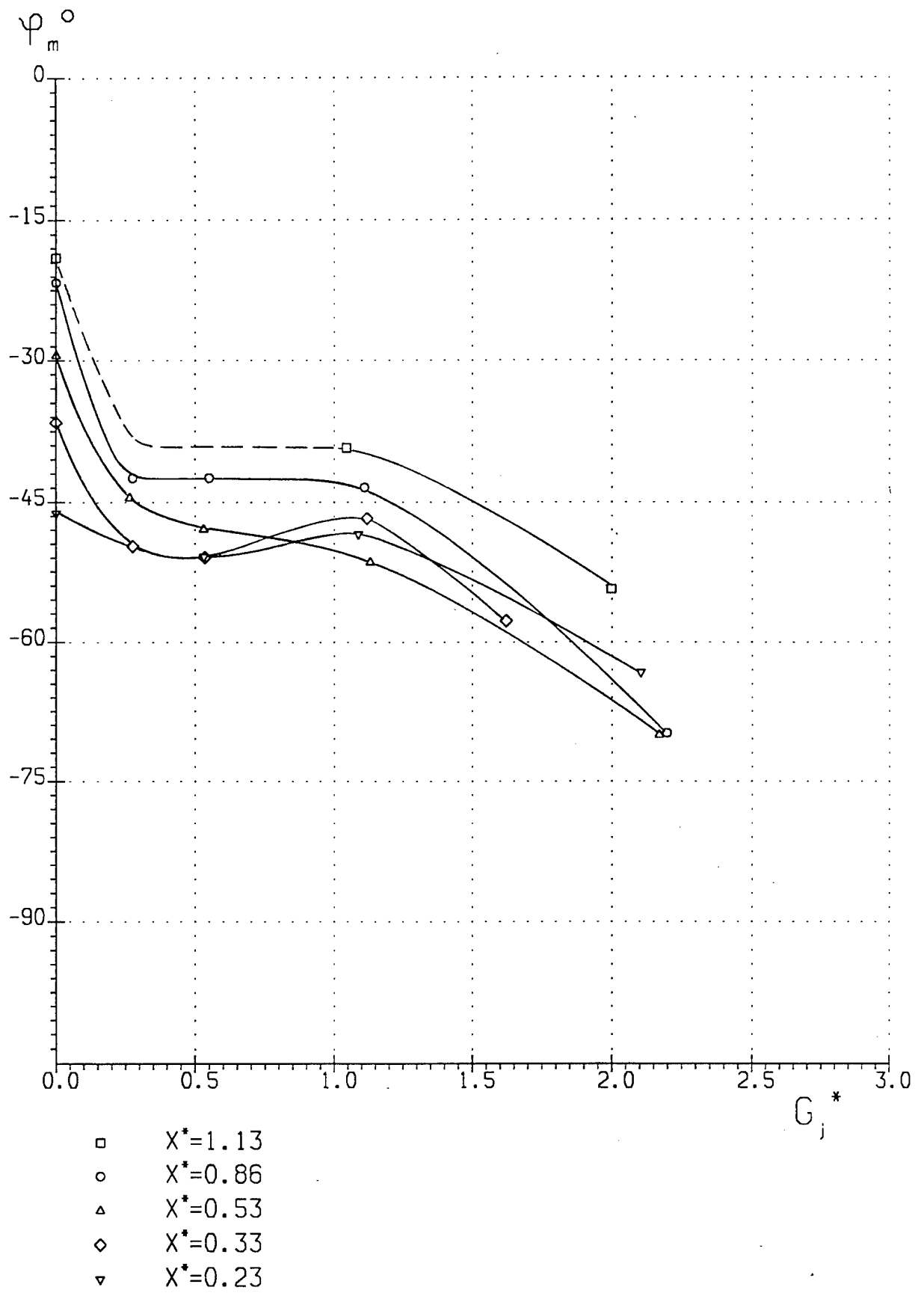
Fig. 51

Model 1

$$X^{\star} = 0.53$$

helium injection

$P_j = 0$

Run 7266a
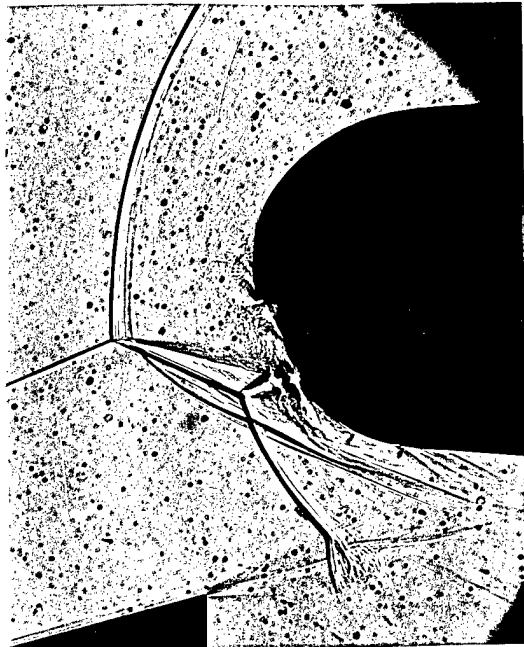
$P_j = 3.73$ bar

Run 7266
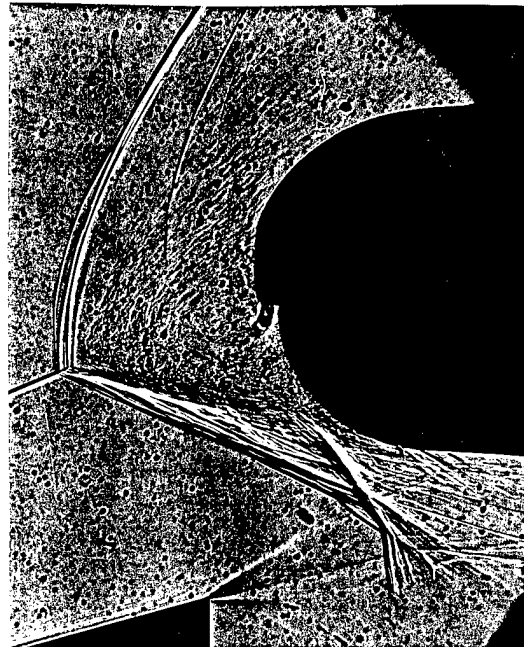
$P_j = 7.19$ bar

Run 7265

$P_j = 14.0$ bar

Run 7263

Fig. 52
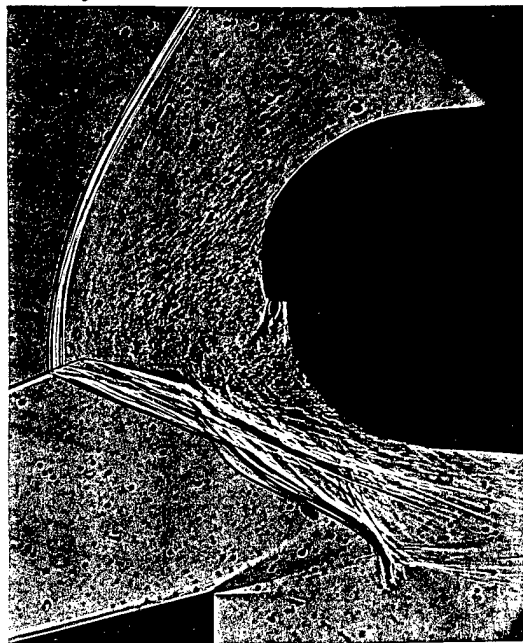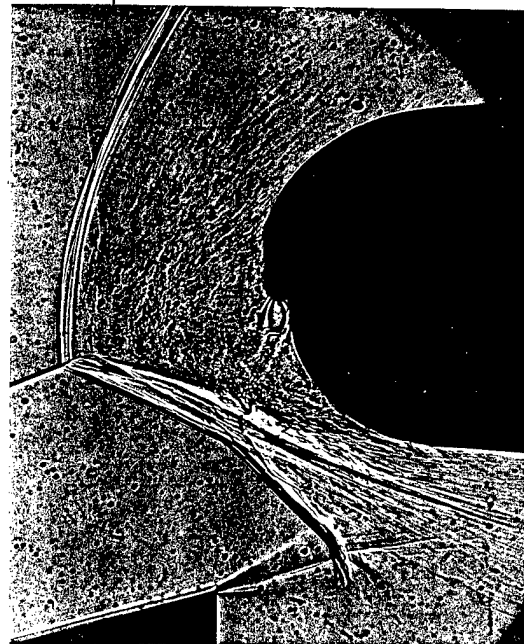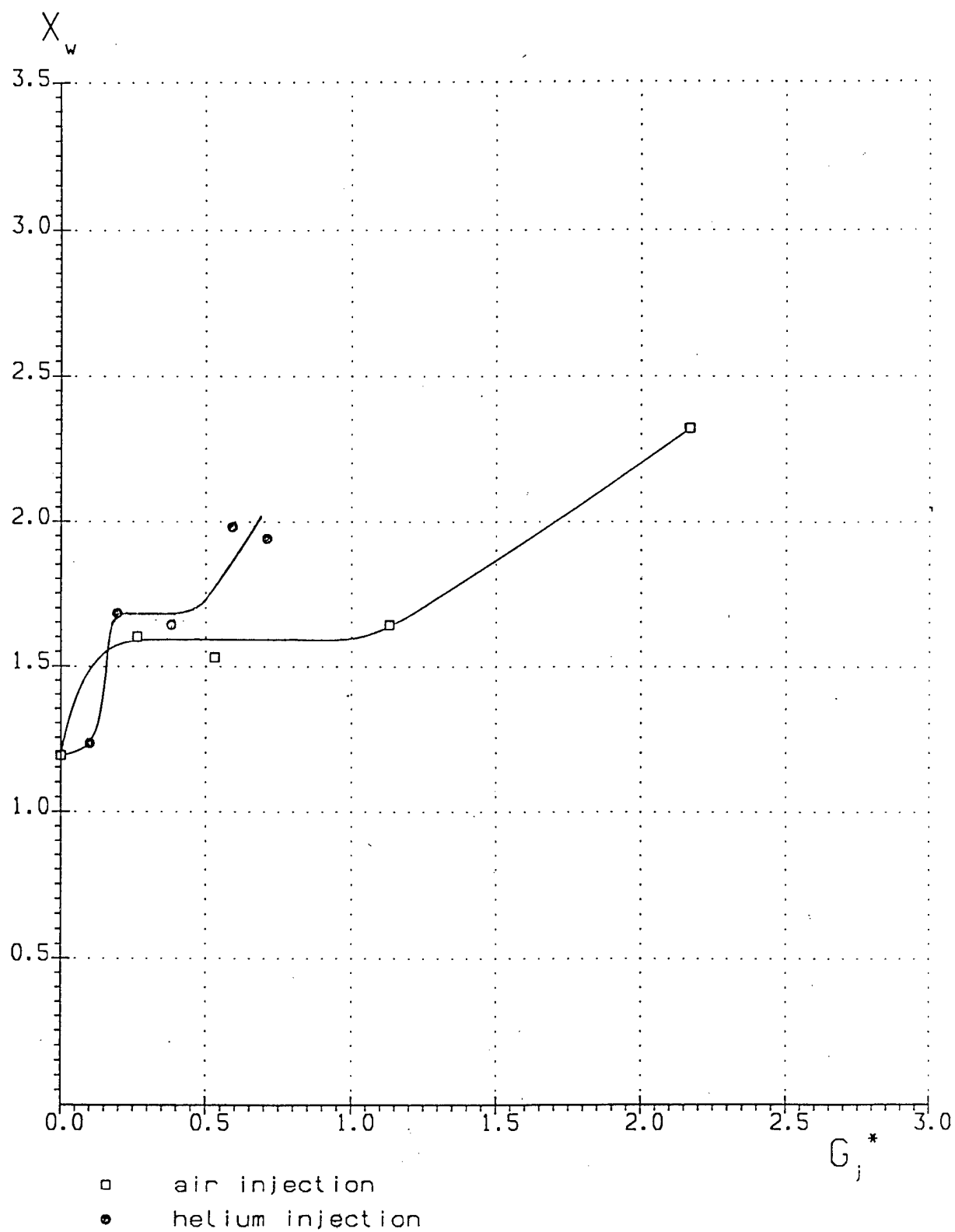
Model 1 X*=0.53

Fig. 53

Model 1   X*=0.53
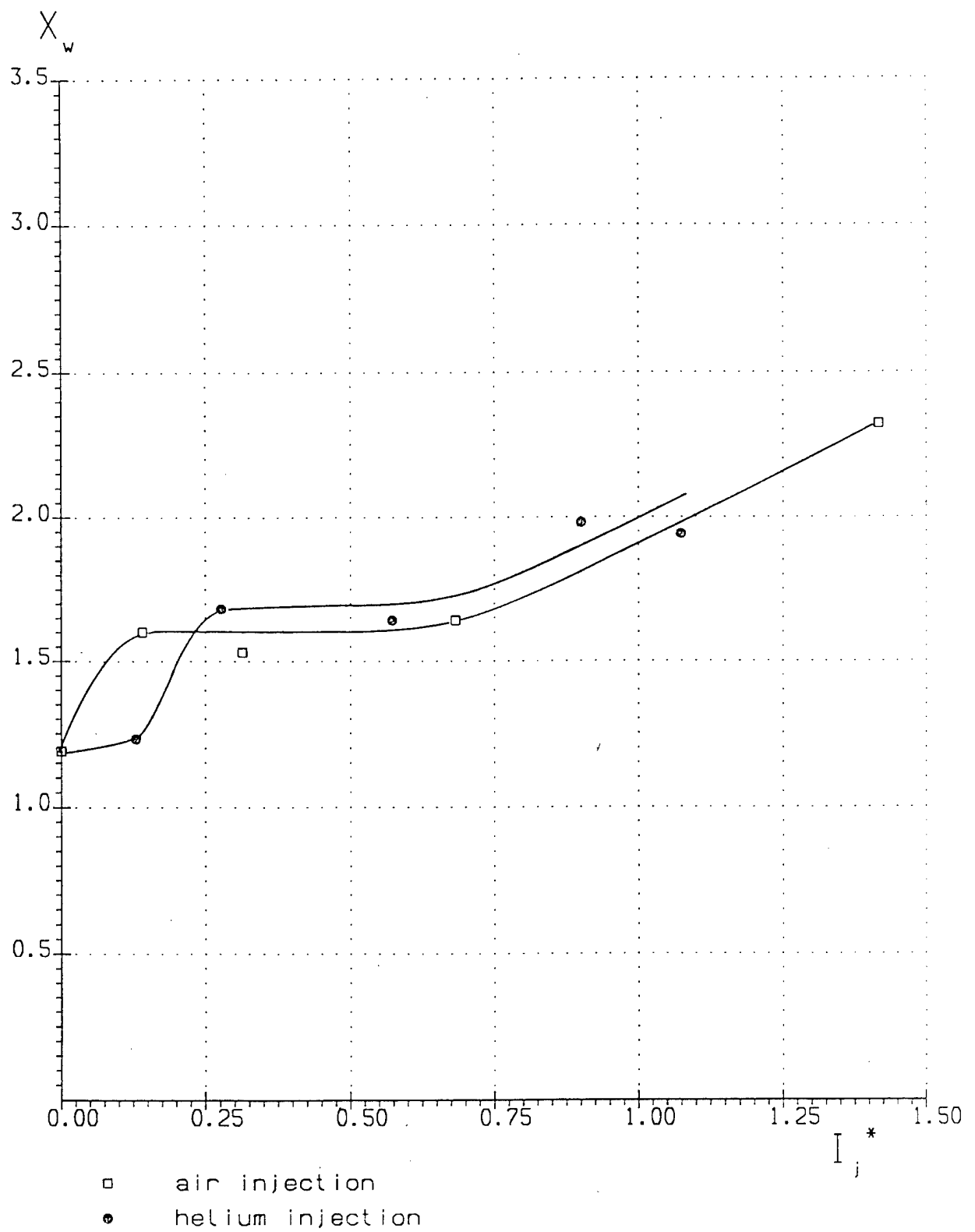
Fig. 54

Model   1 $X^*=0.53$
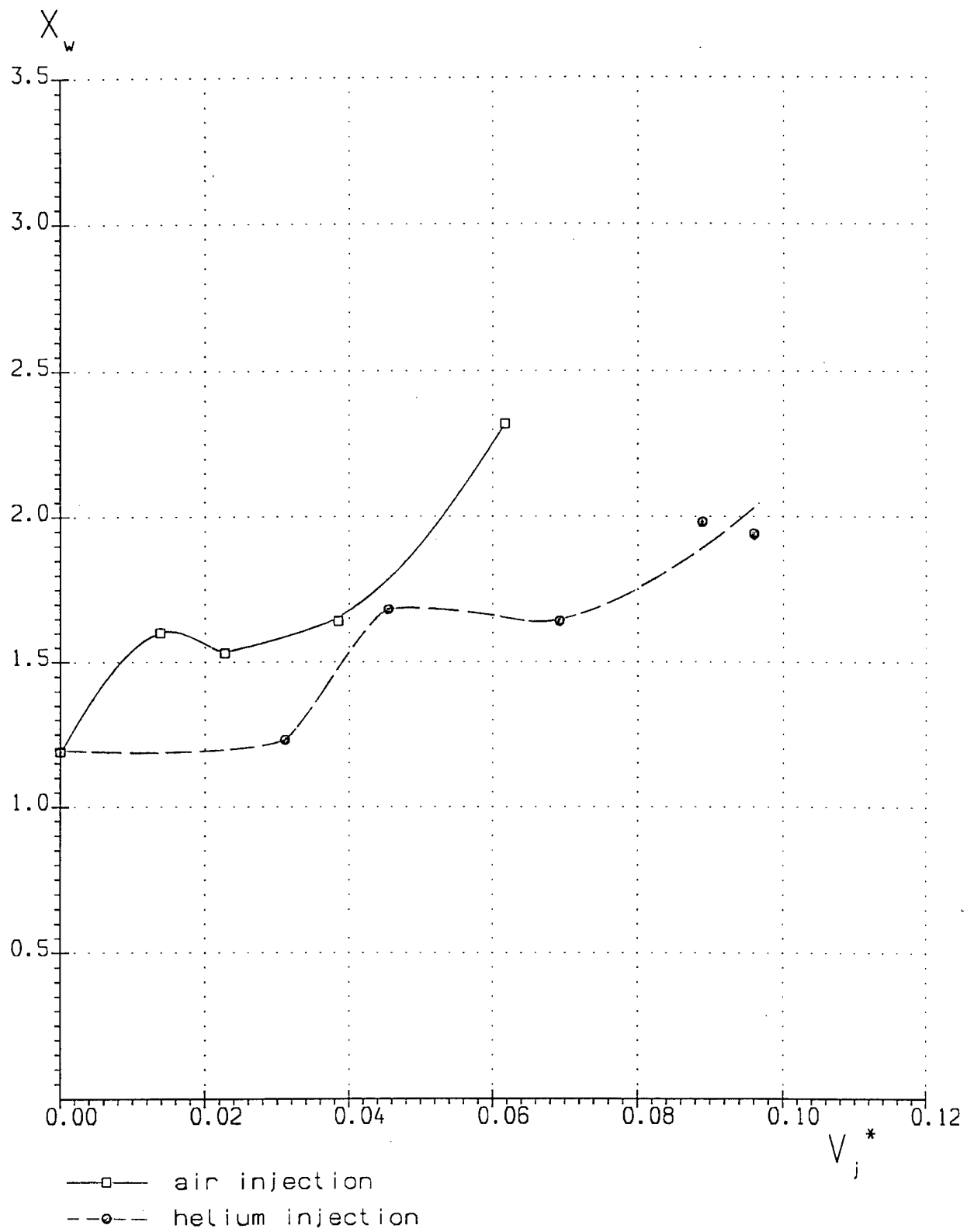
Fig. 55

Model 1   X*=0.53

Fig. 56

Model 1 X*=0.53
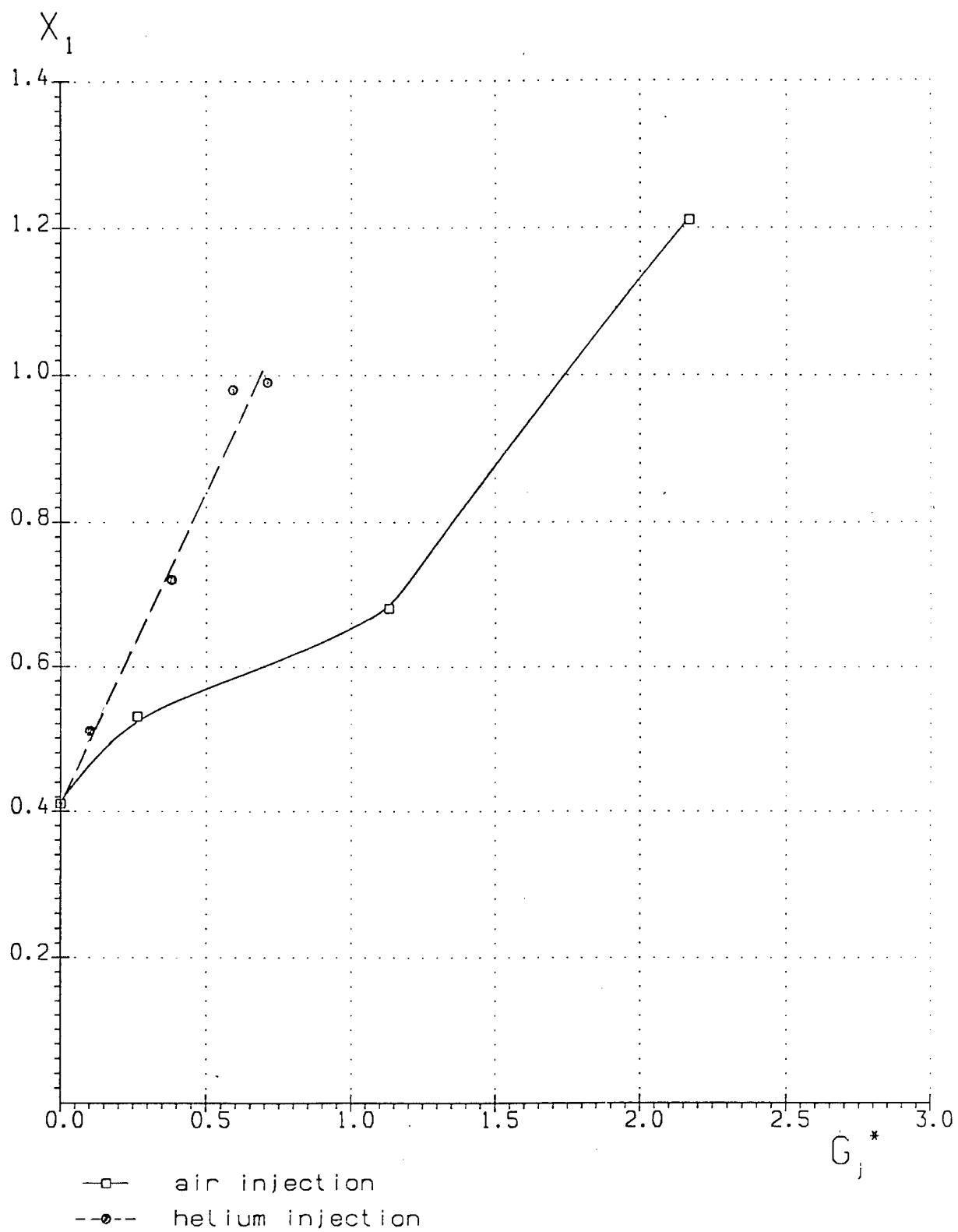
air injection
helium injection
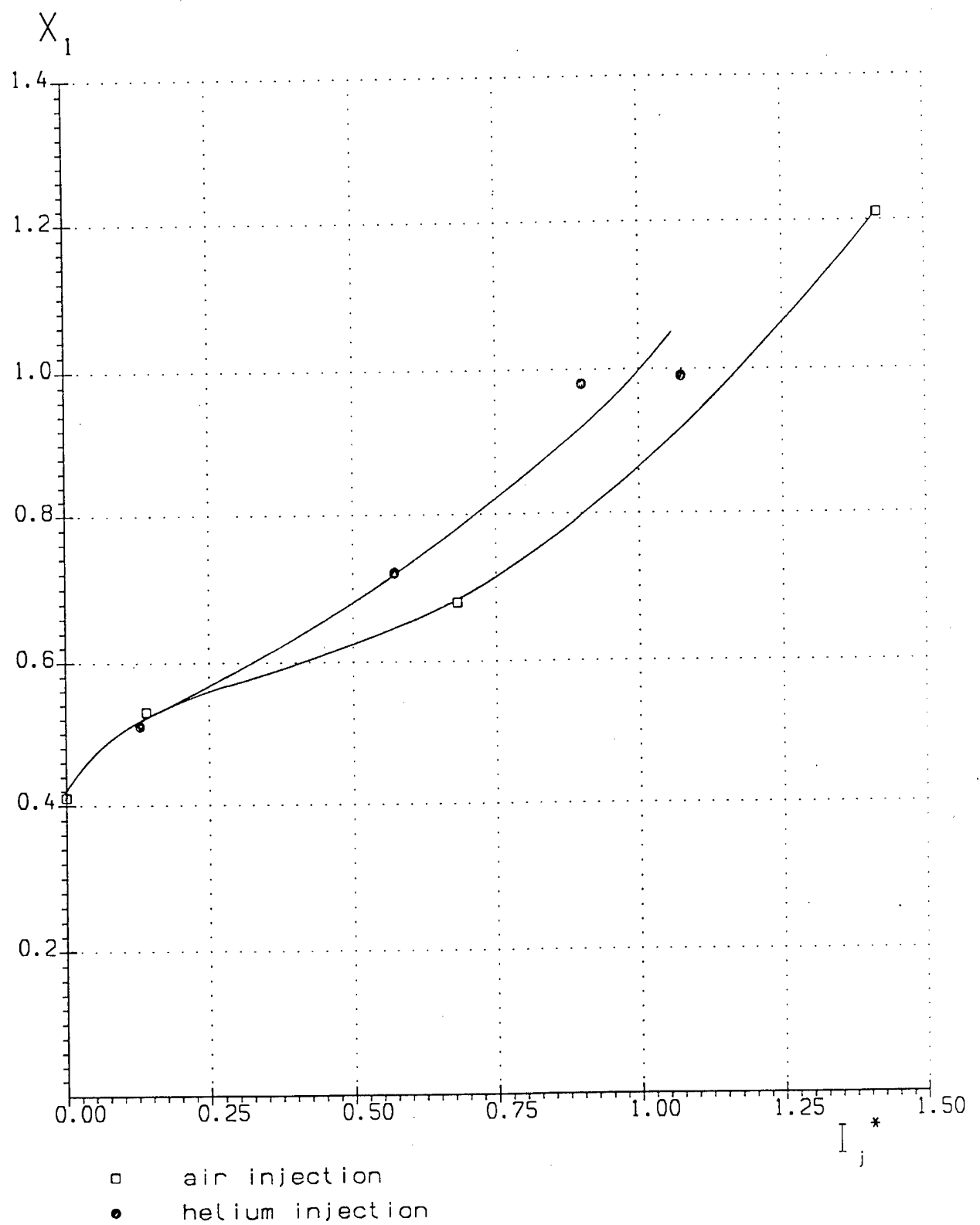
Fig. 57

Model 1   X*=0.53

Fig. 58

Model 1 X*=0.53
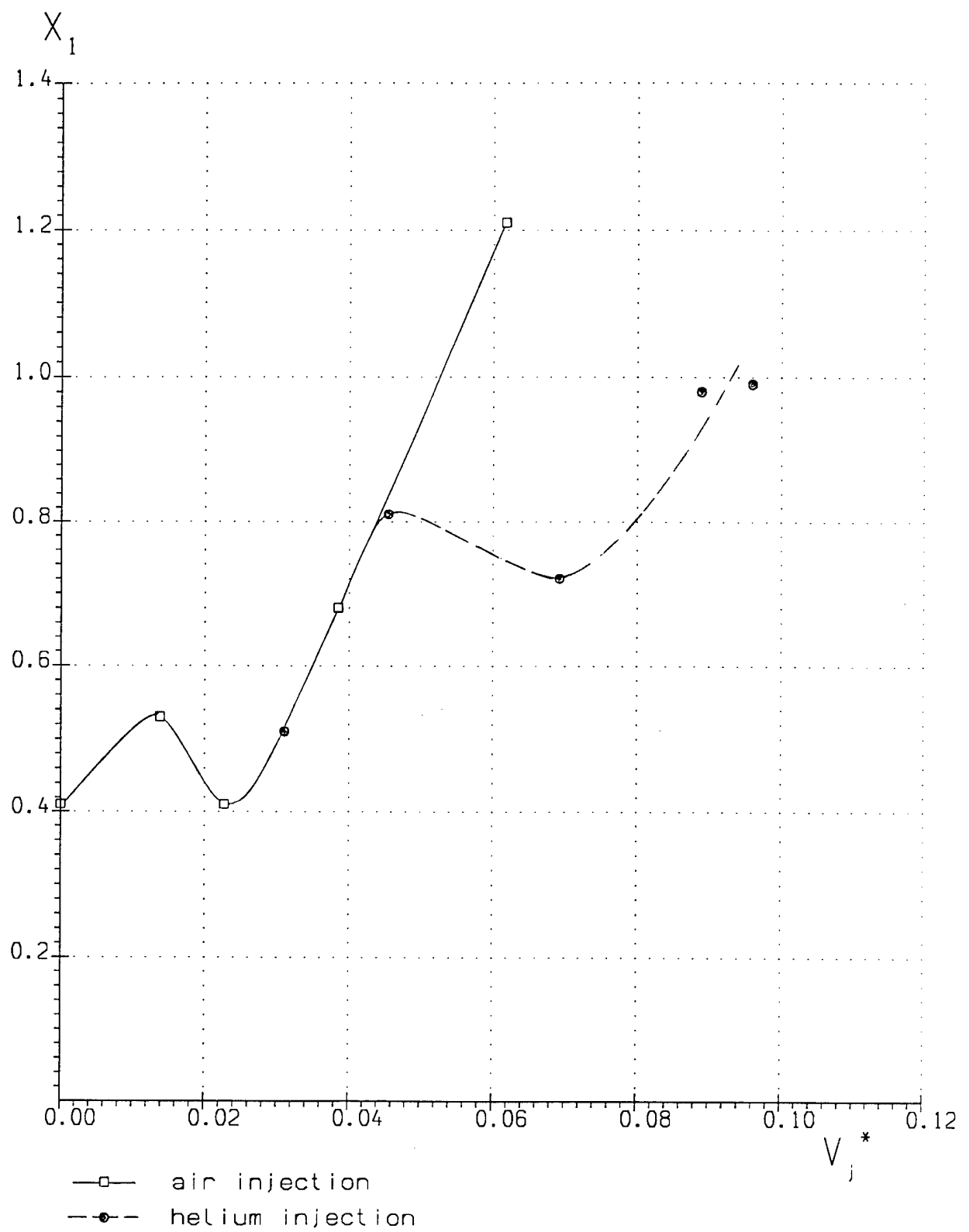
air injection
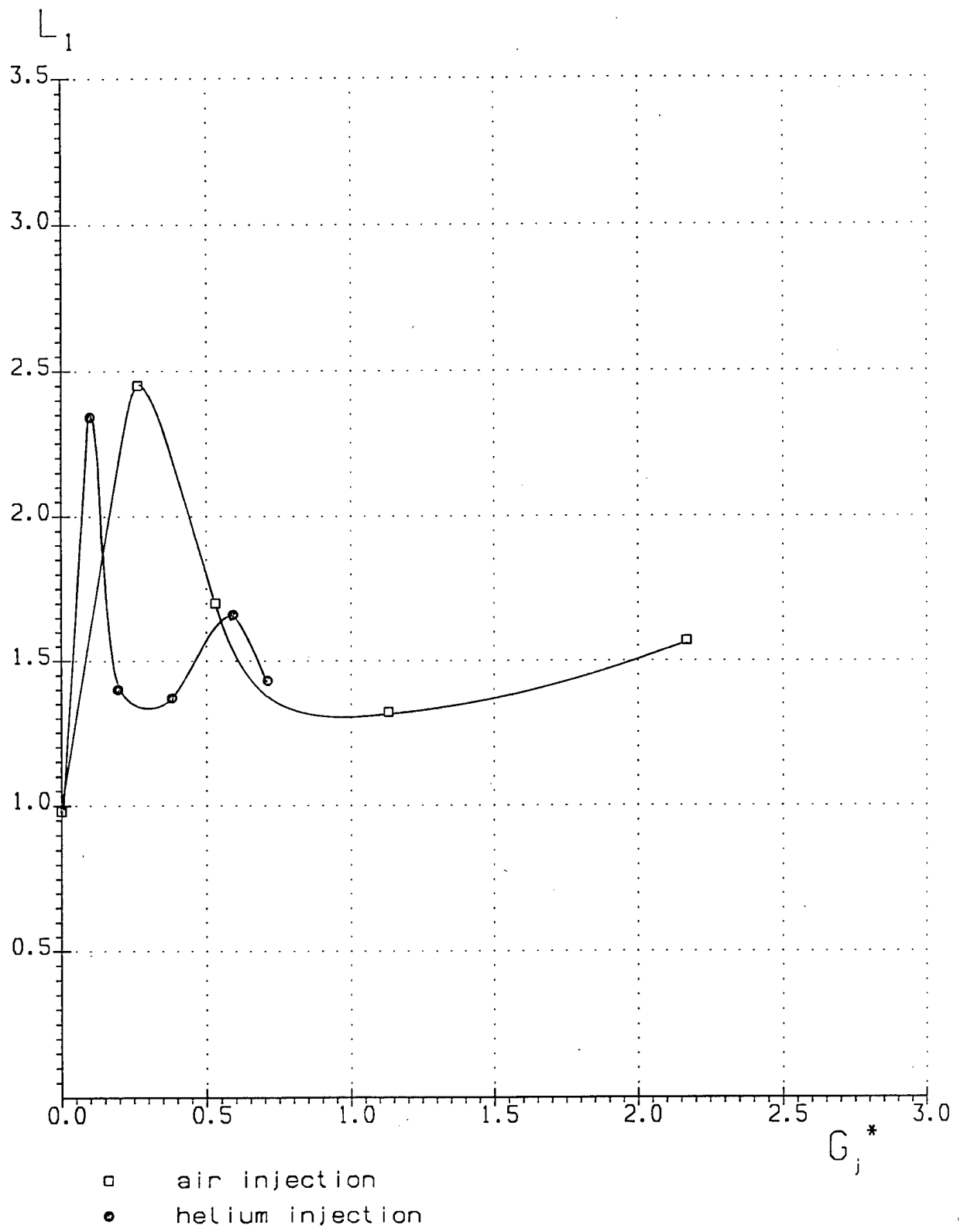
helium injection

Fig. 59
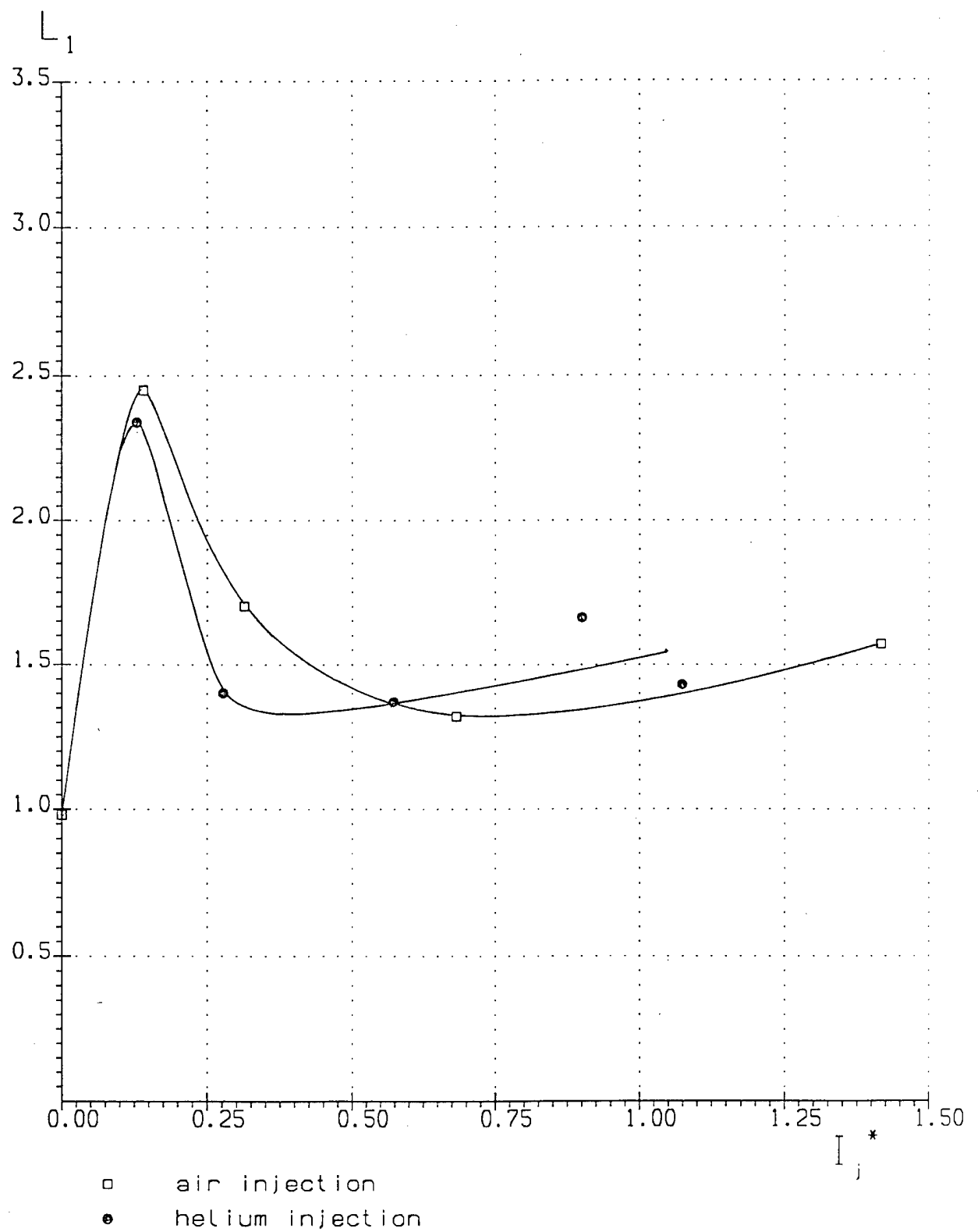
Model 1 X*=0.53

Fig. 60

Model 1 X*=0.53
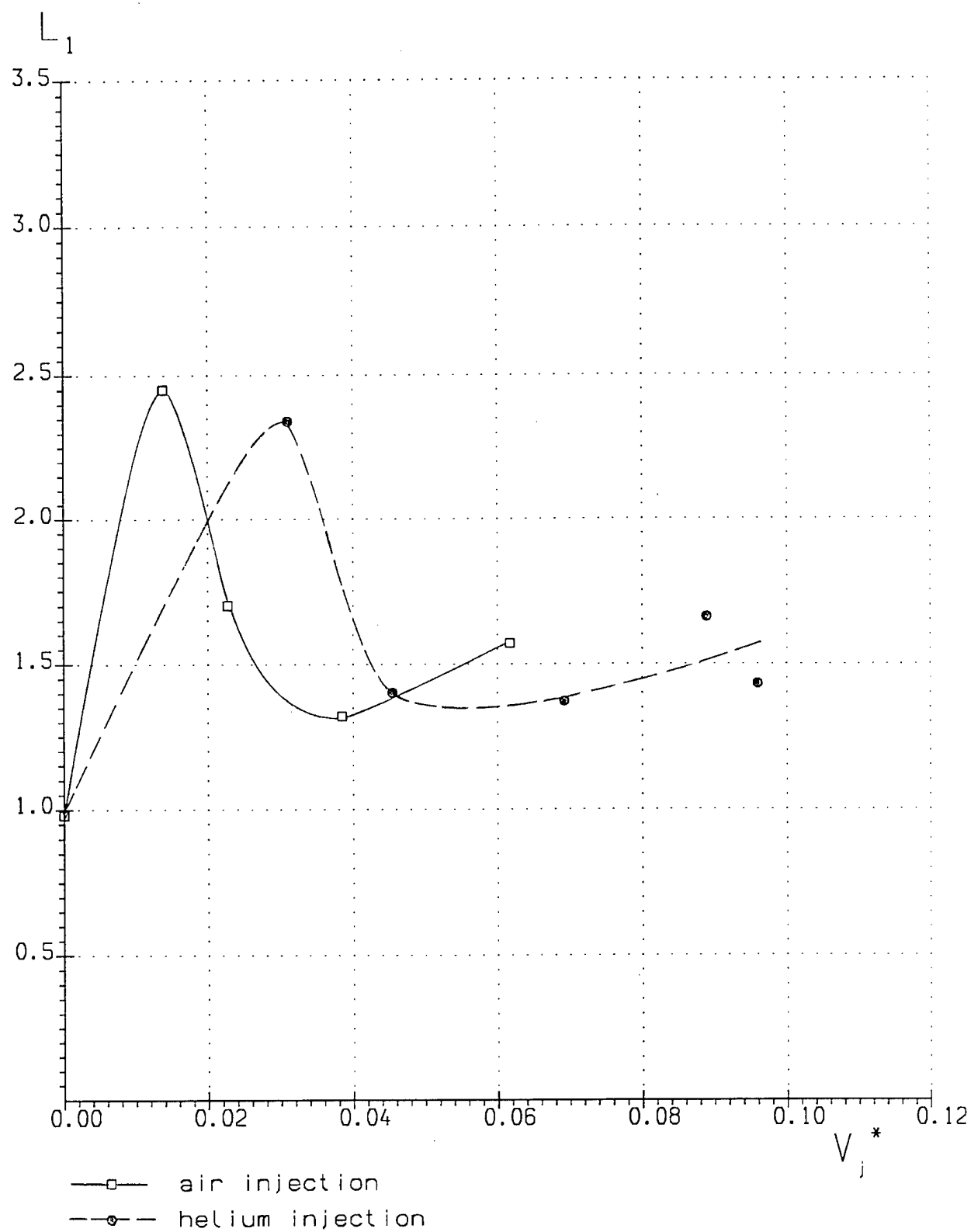
Fig. 61

Model 1   X*=0.53

helium injection
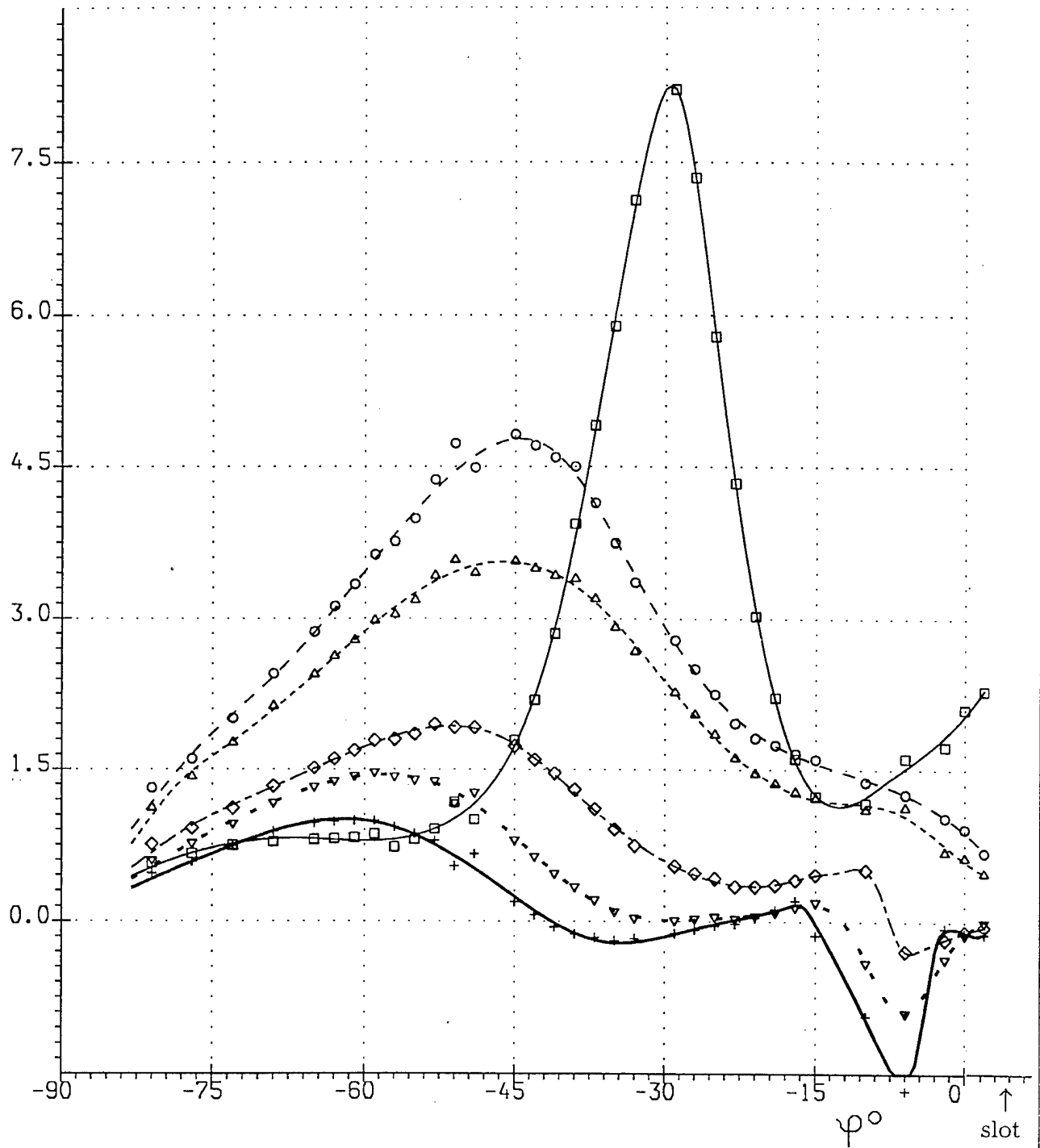
Fig. 62

Model 1 $X^*=0.53$

q_m/q_{so}

G_j^*

□ air injection
⊙ helium injection

Fig. 63

Model 1   X*=0.53

q_m/q_{sa}

I_j^*

□   air injection
●   helium injection

Fig. 64

Model 1   X*=0.53

air injection
helium injection
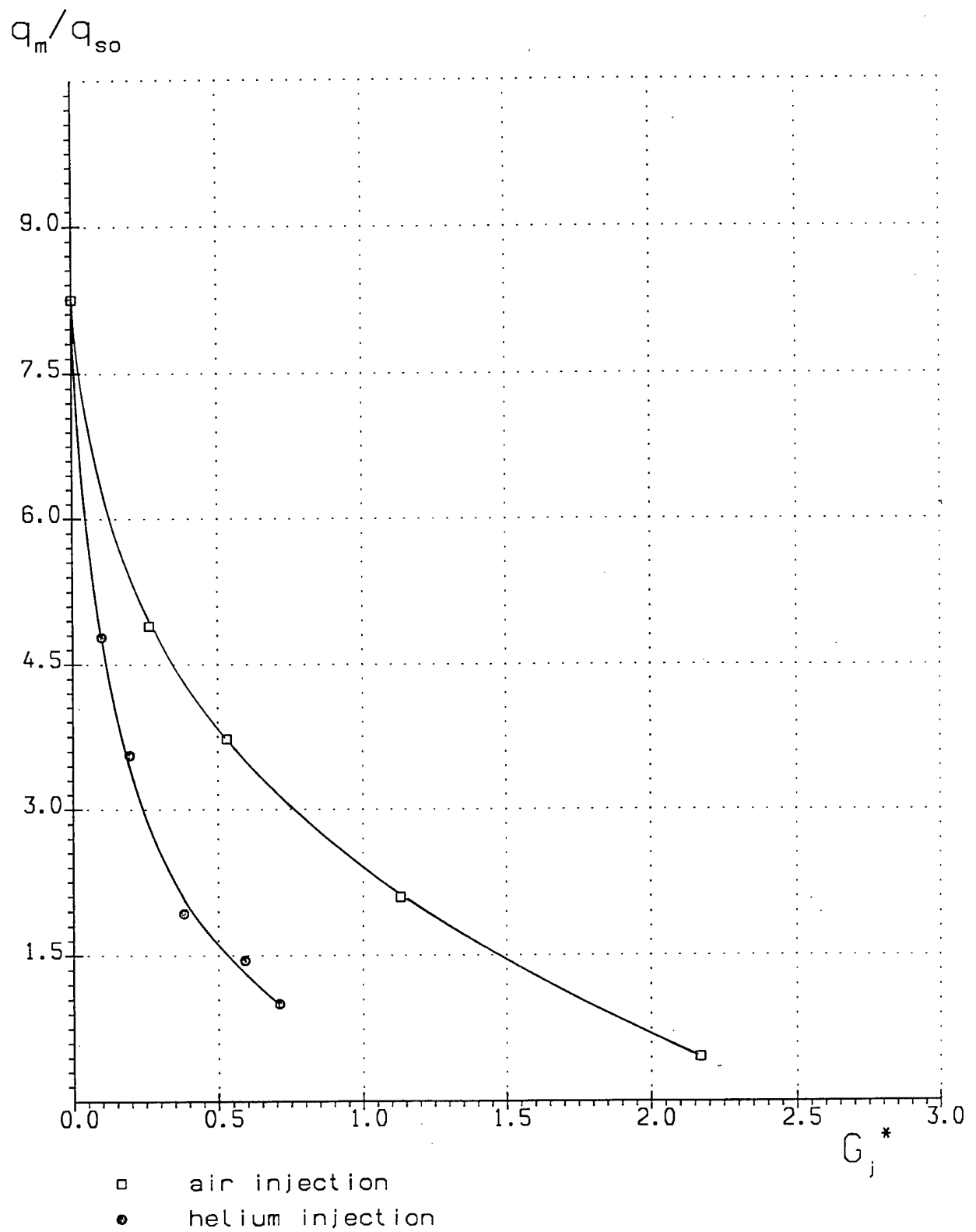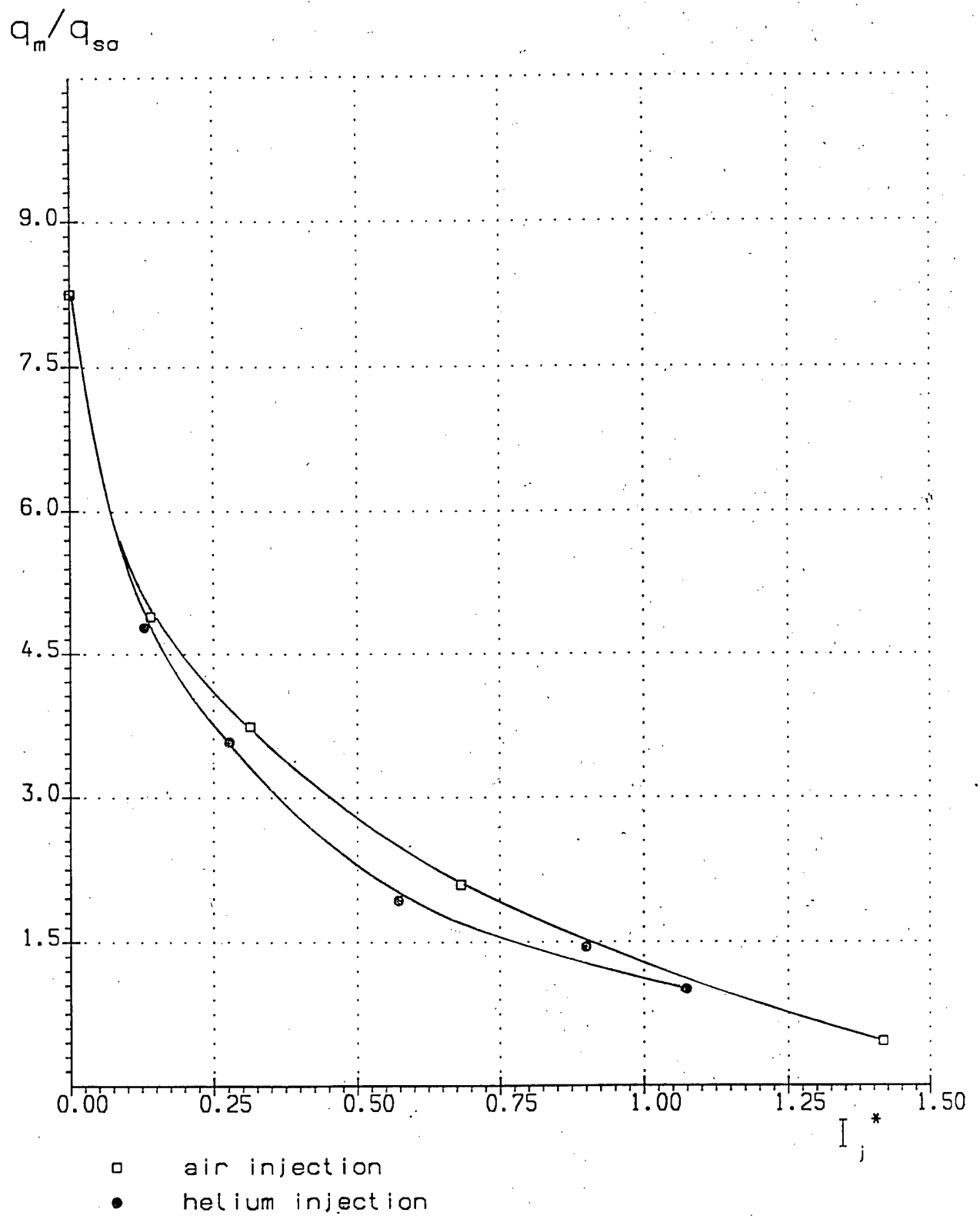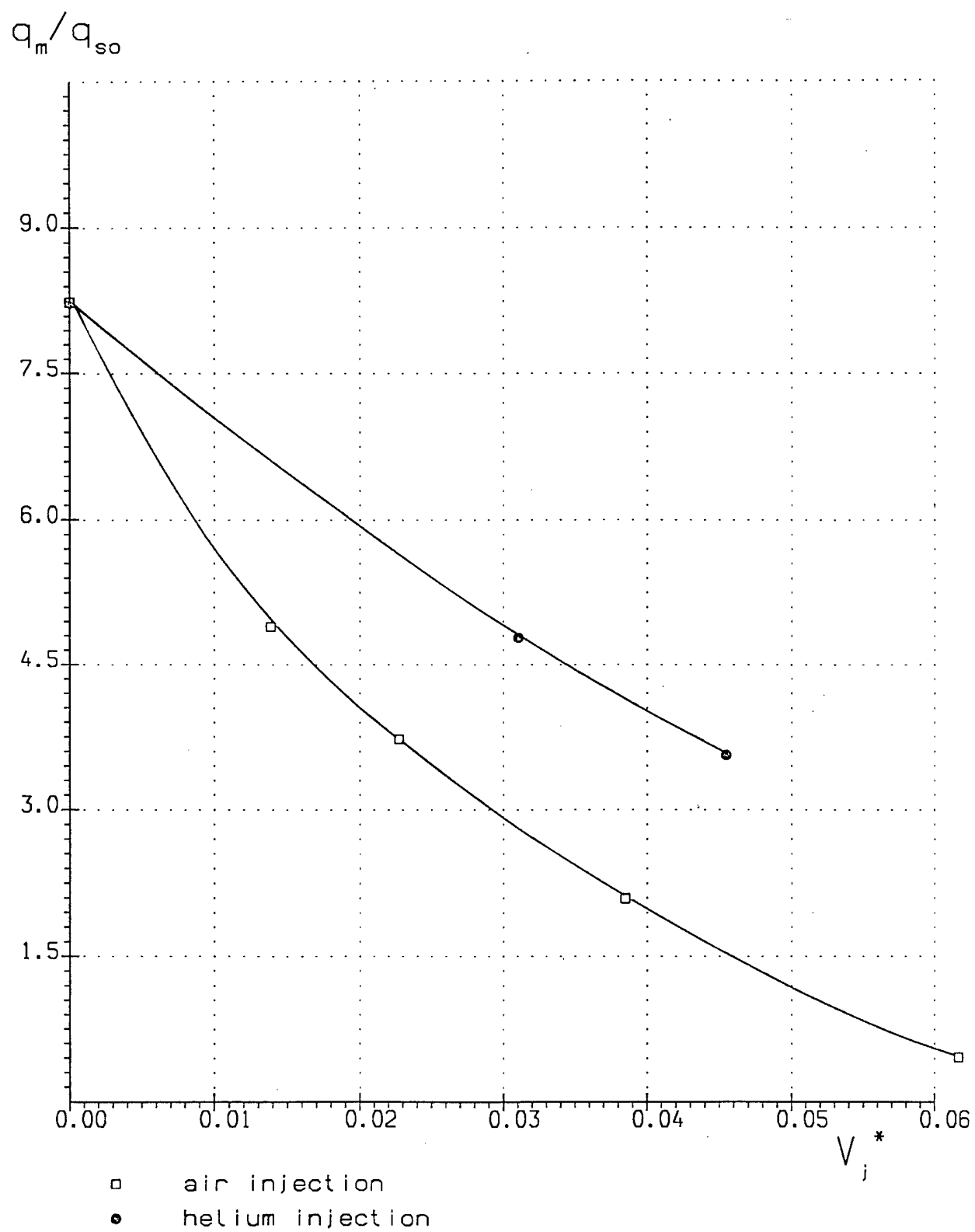
Fig. 65

Model 1 X*=0.53

Fig. 66

Model 1 X*=0.53

air injection
helium injection

Fig. 67

Model 1 X*=0.53

air injection

helium injection
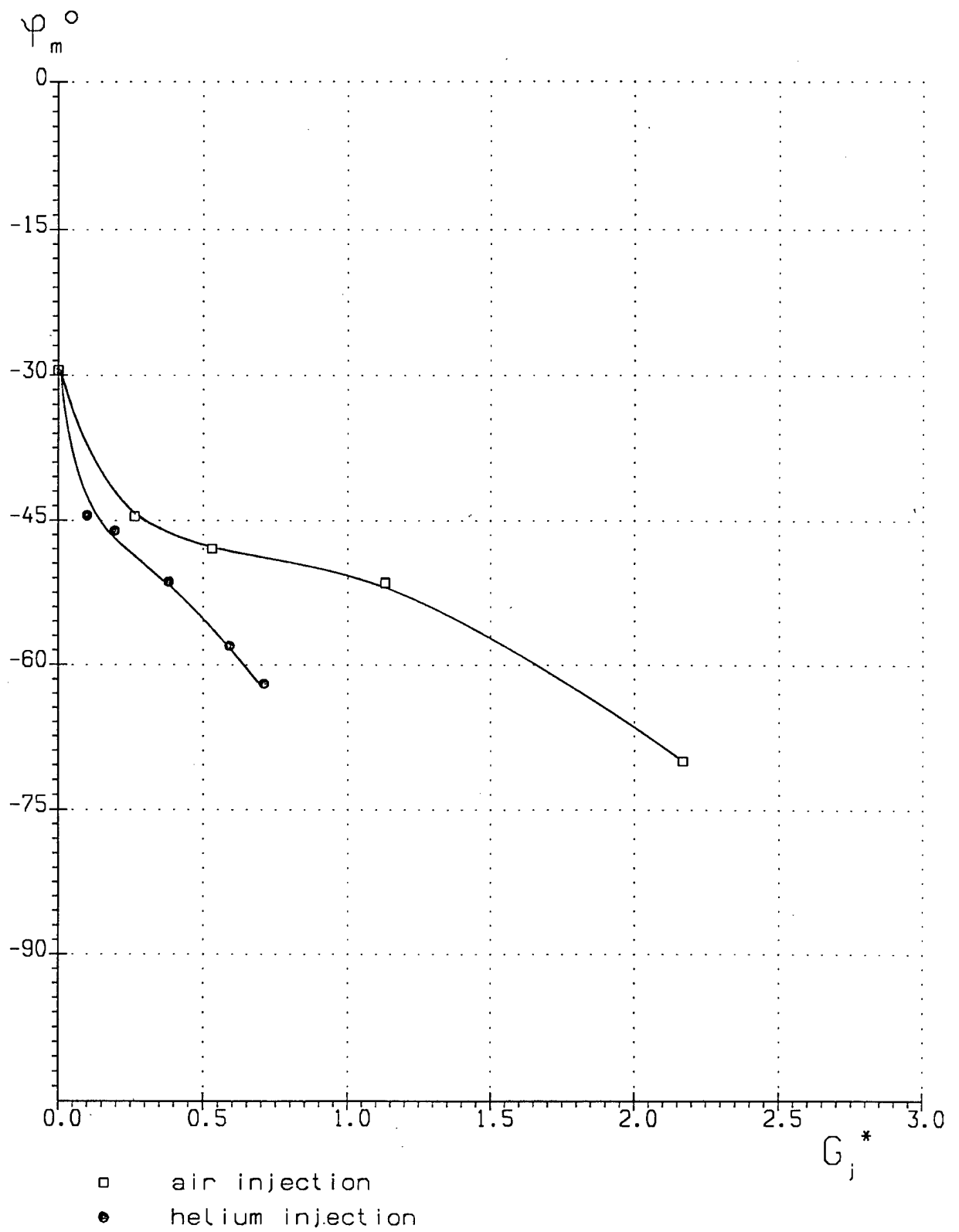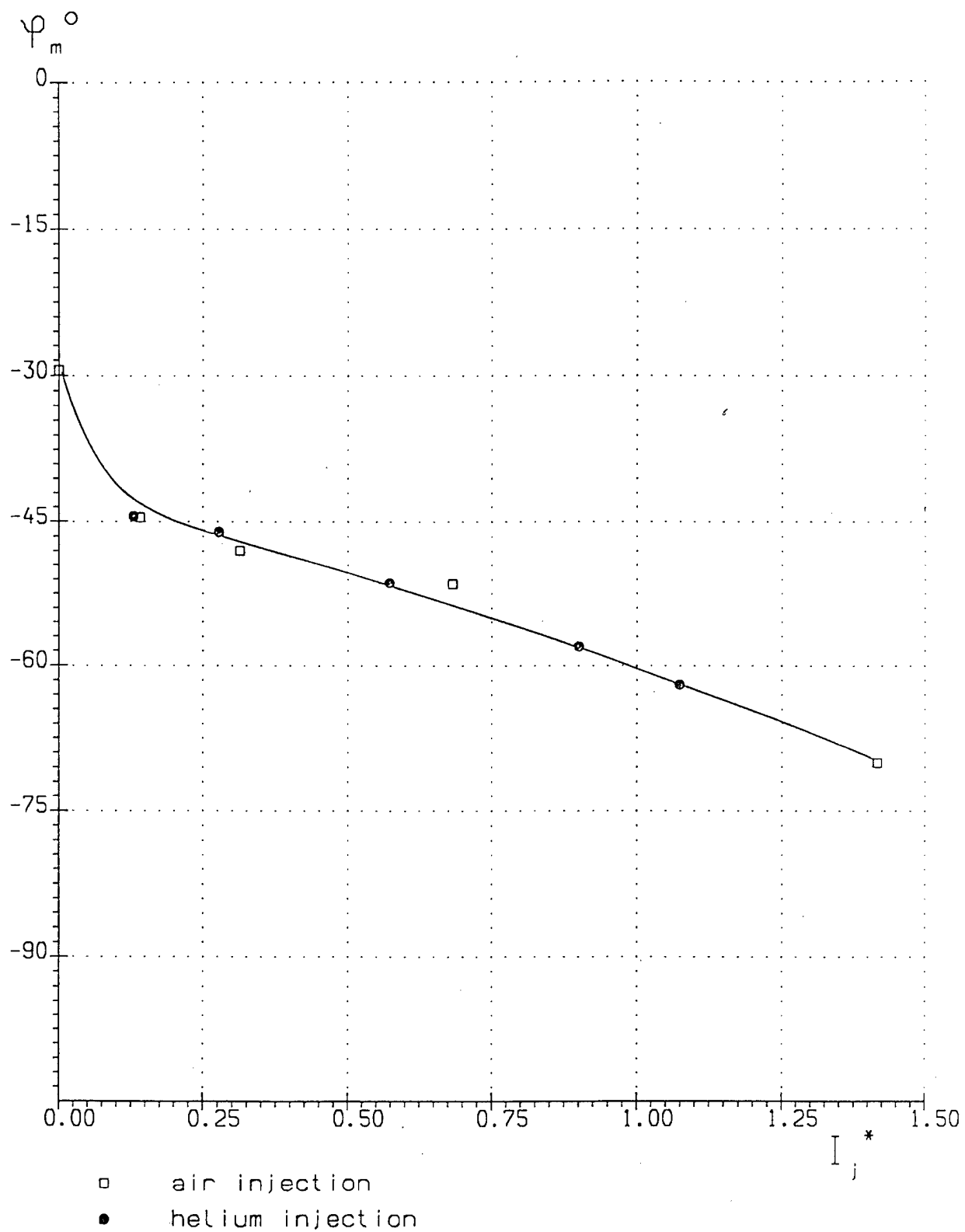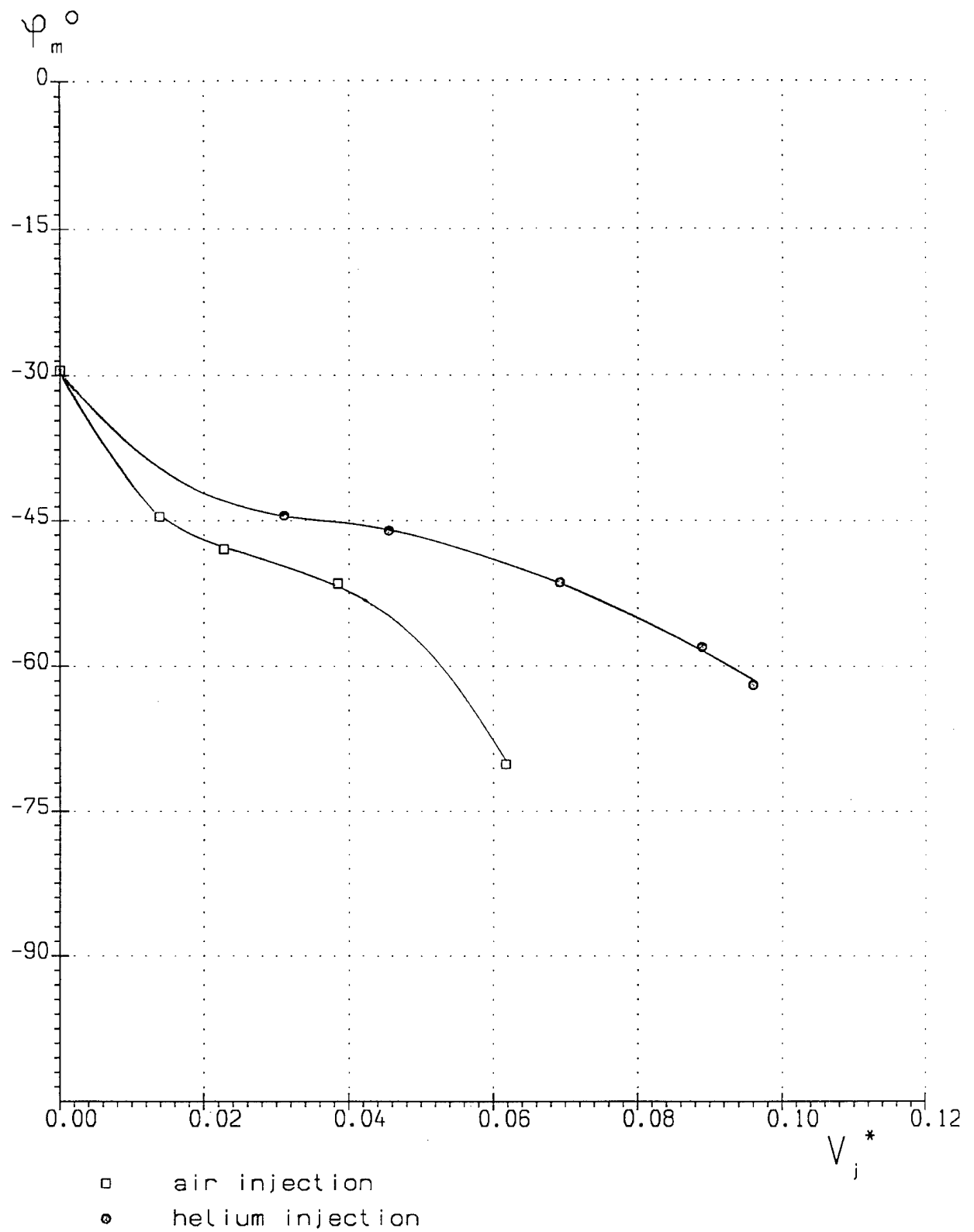
Fig. 68

Model 1   X*=0.53
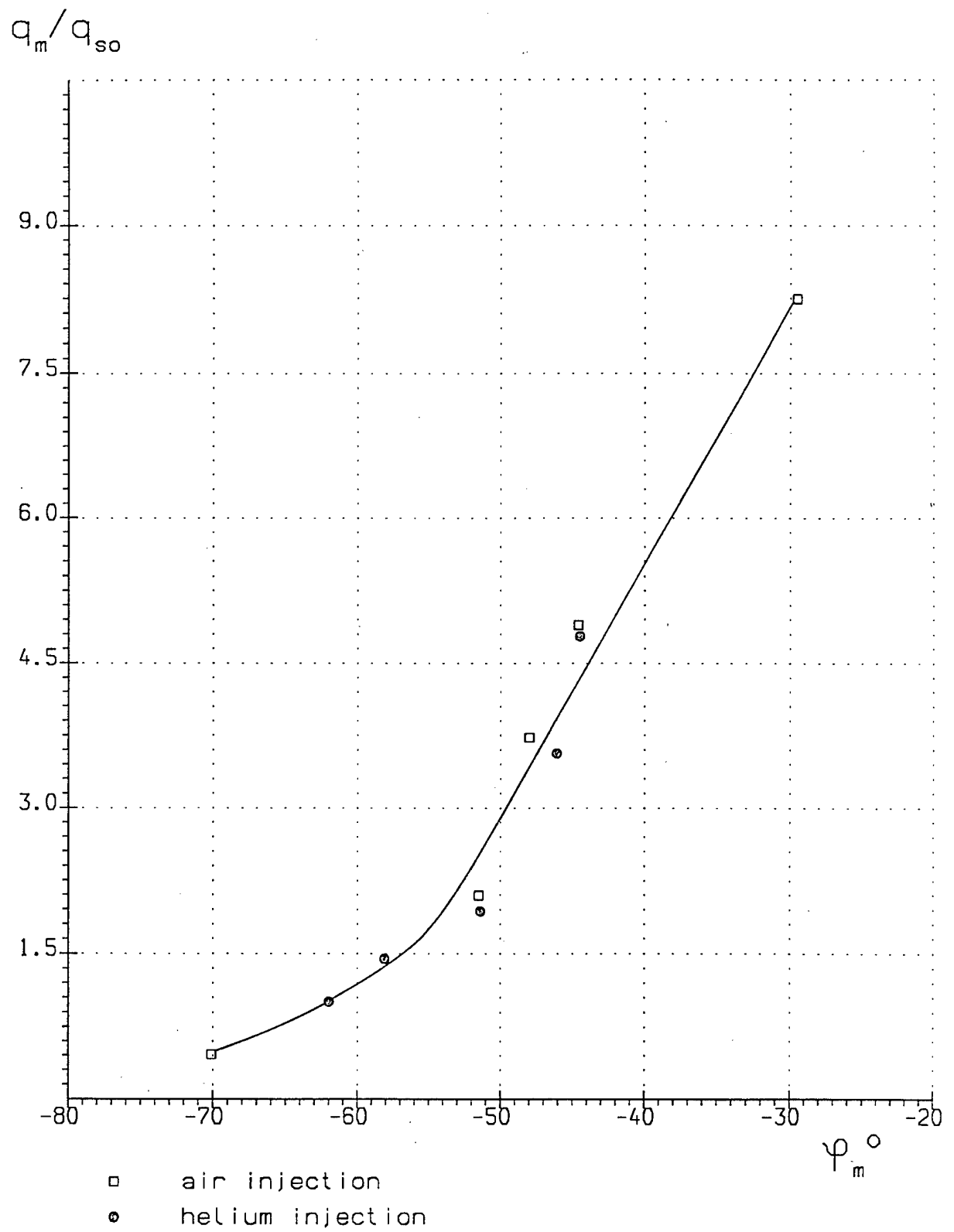
Fig. 69

$X^*=0.23$
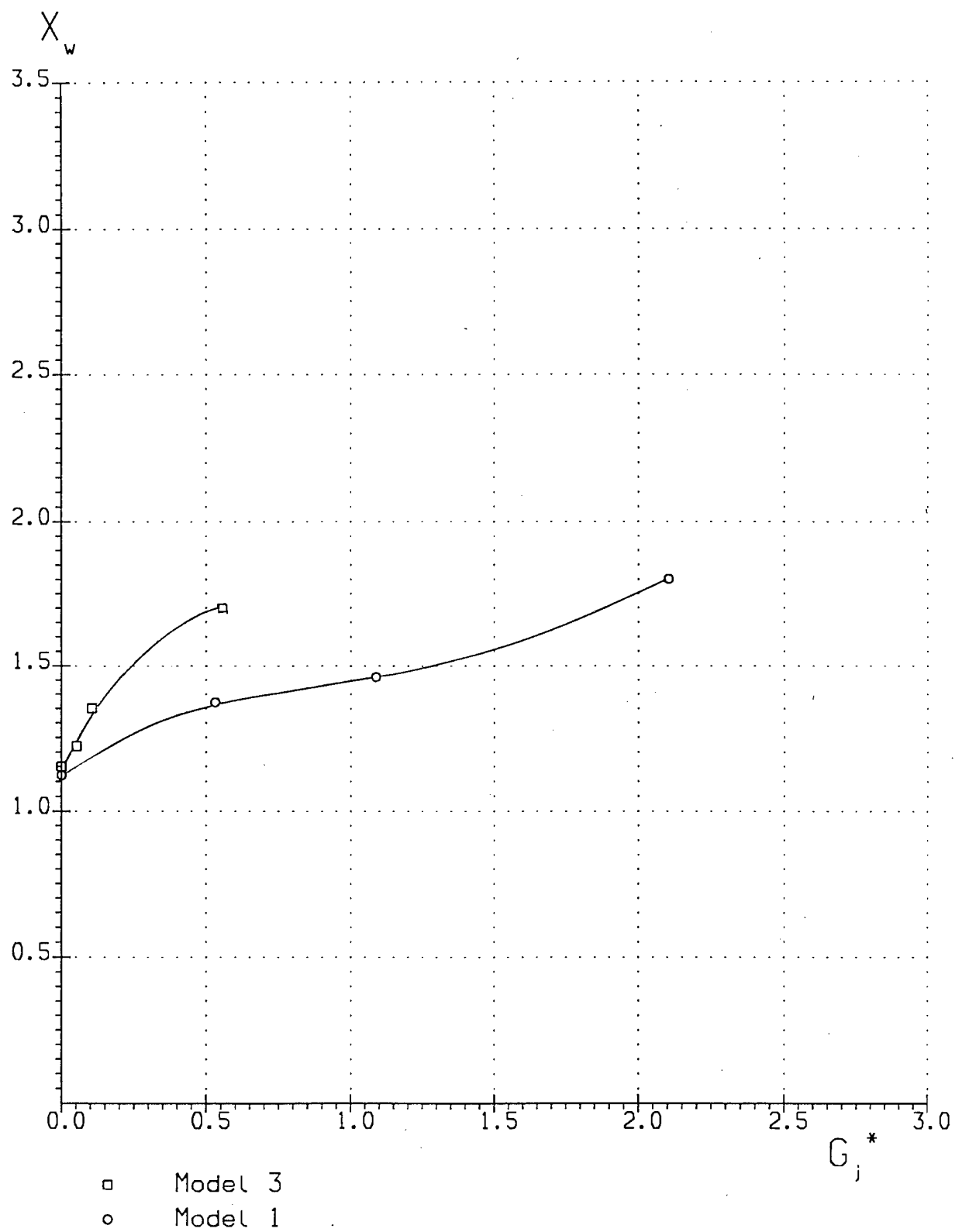
Fig. 70

X*=0.23
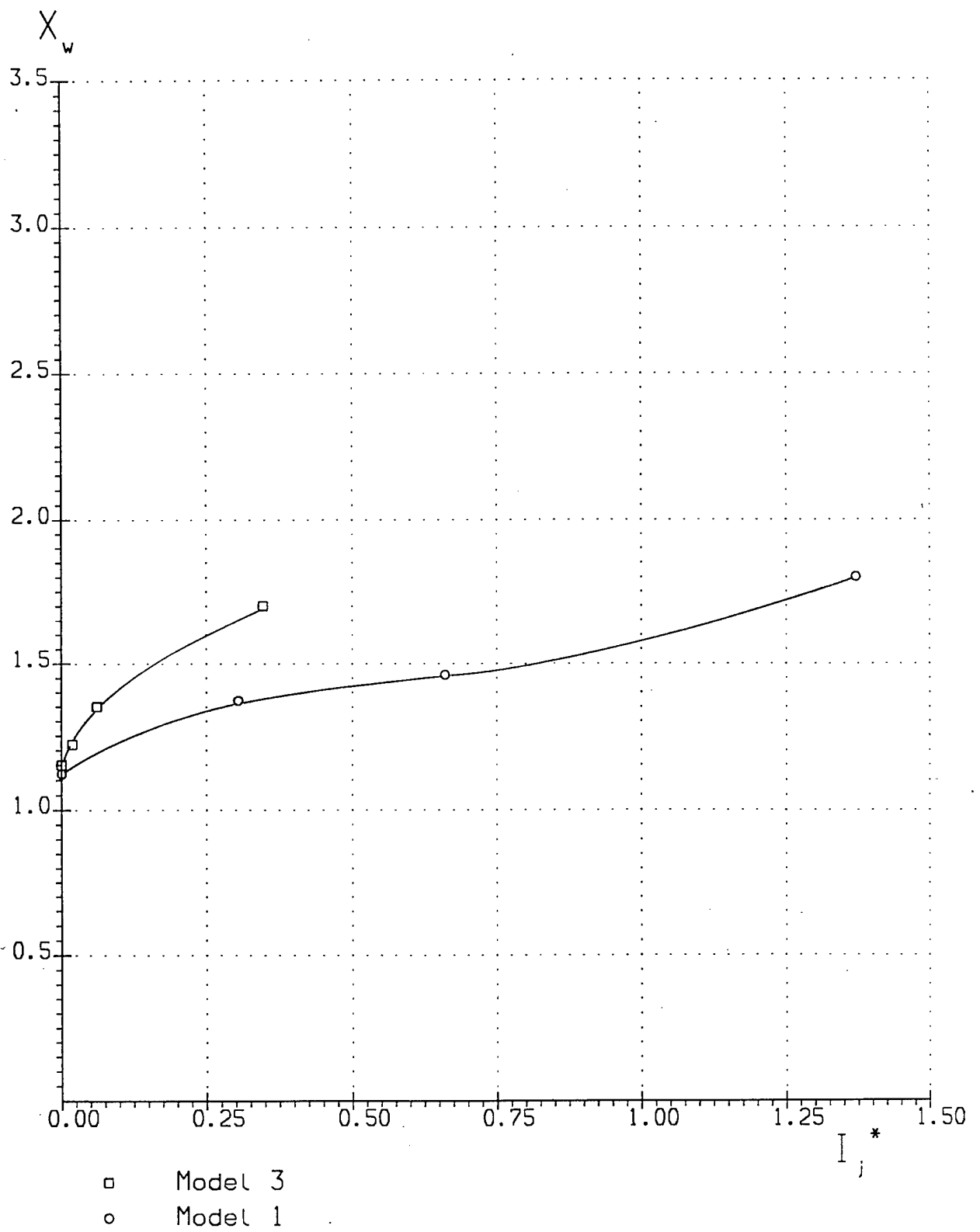
Fig. 71

$X^*=0.23$
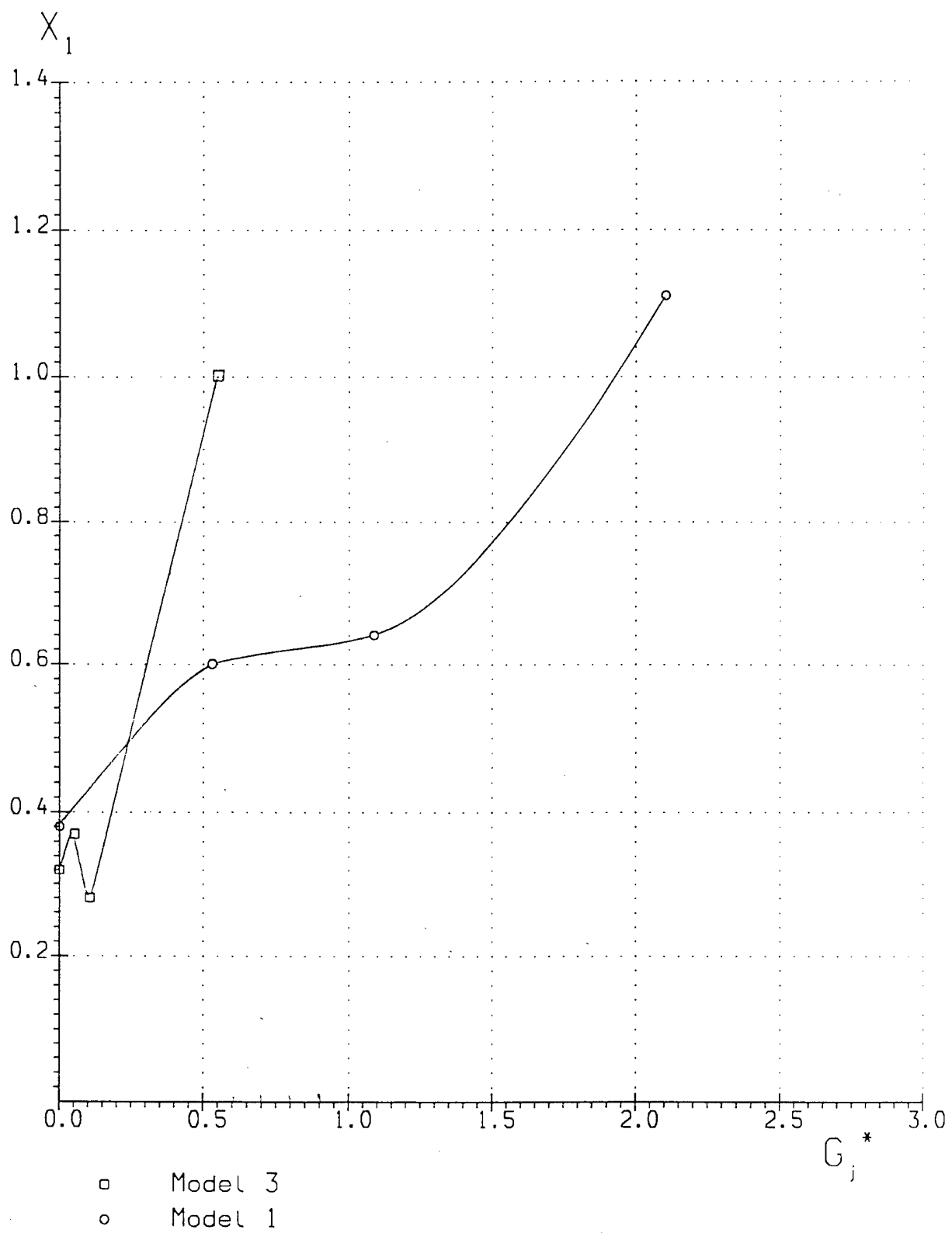
Model 3
Model 1

Fig. 72
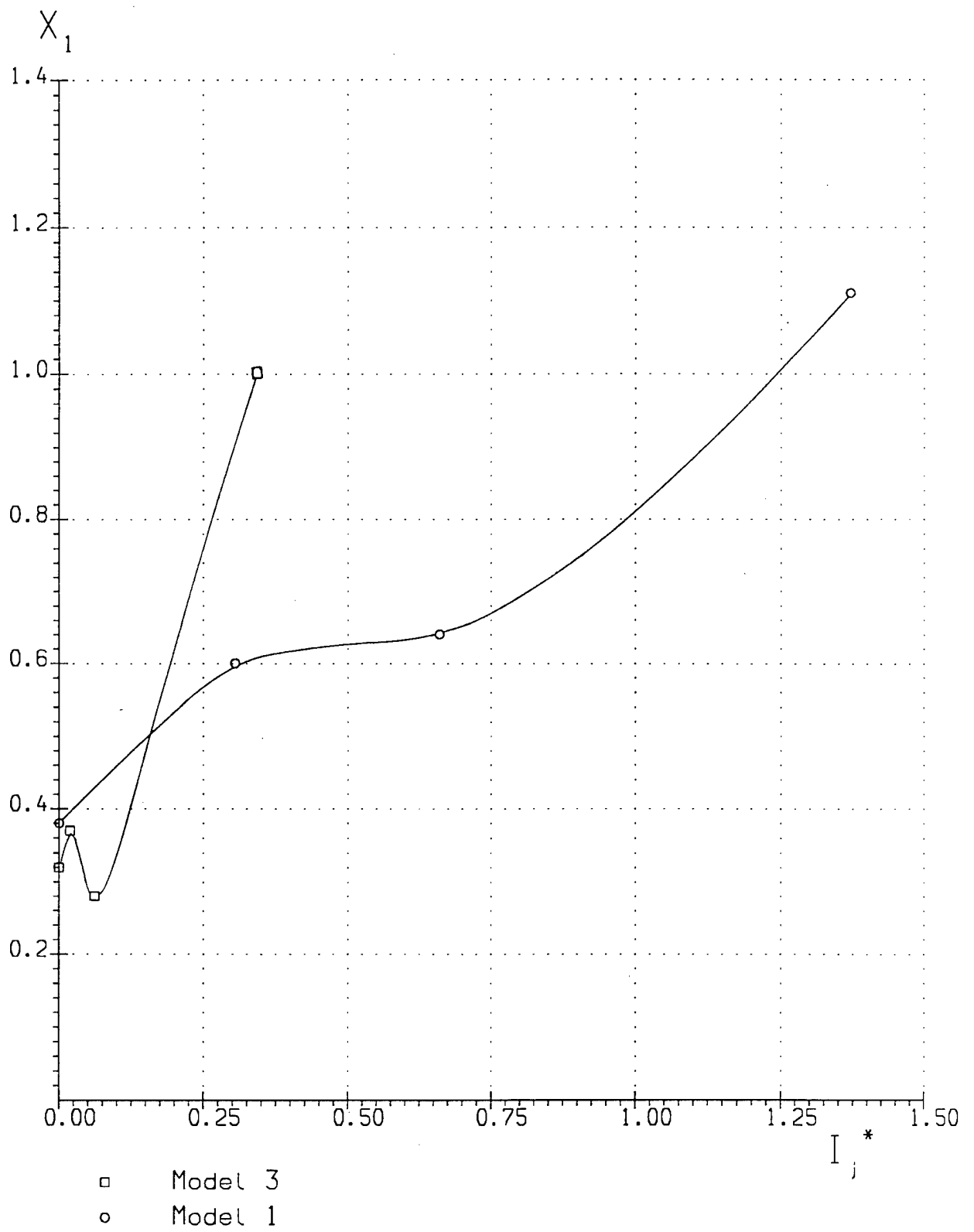
$X^* = 0.23$

Fig. 73

X*=0.23
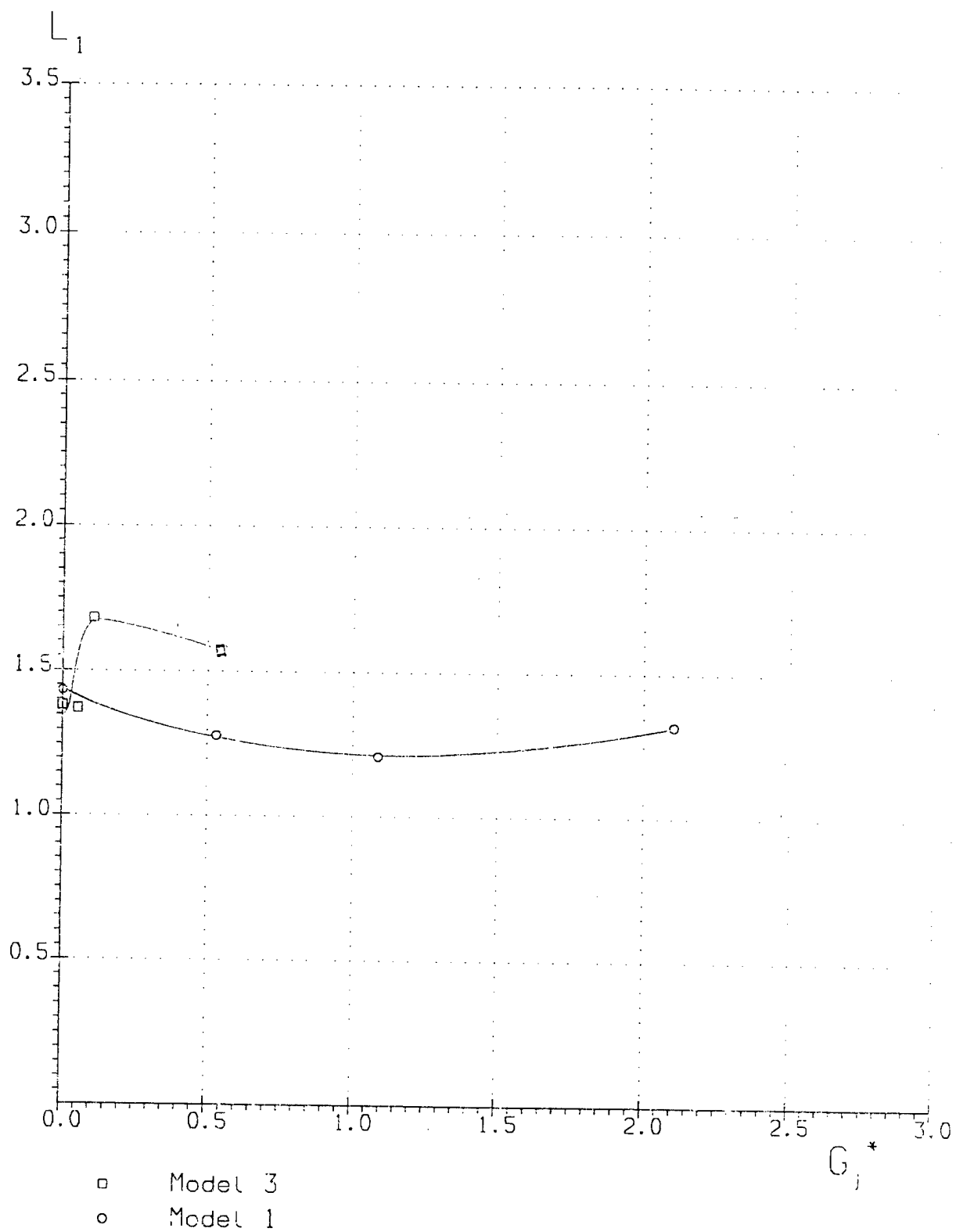
Fig. 74

X*=0.23
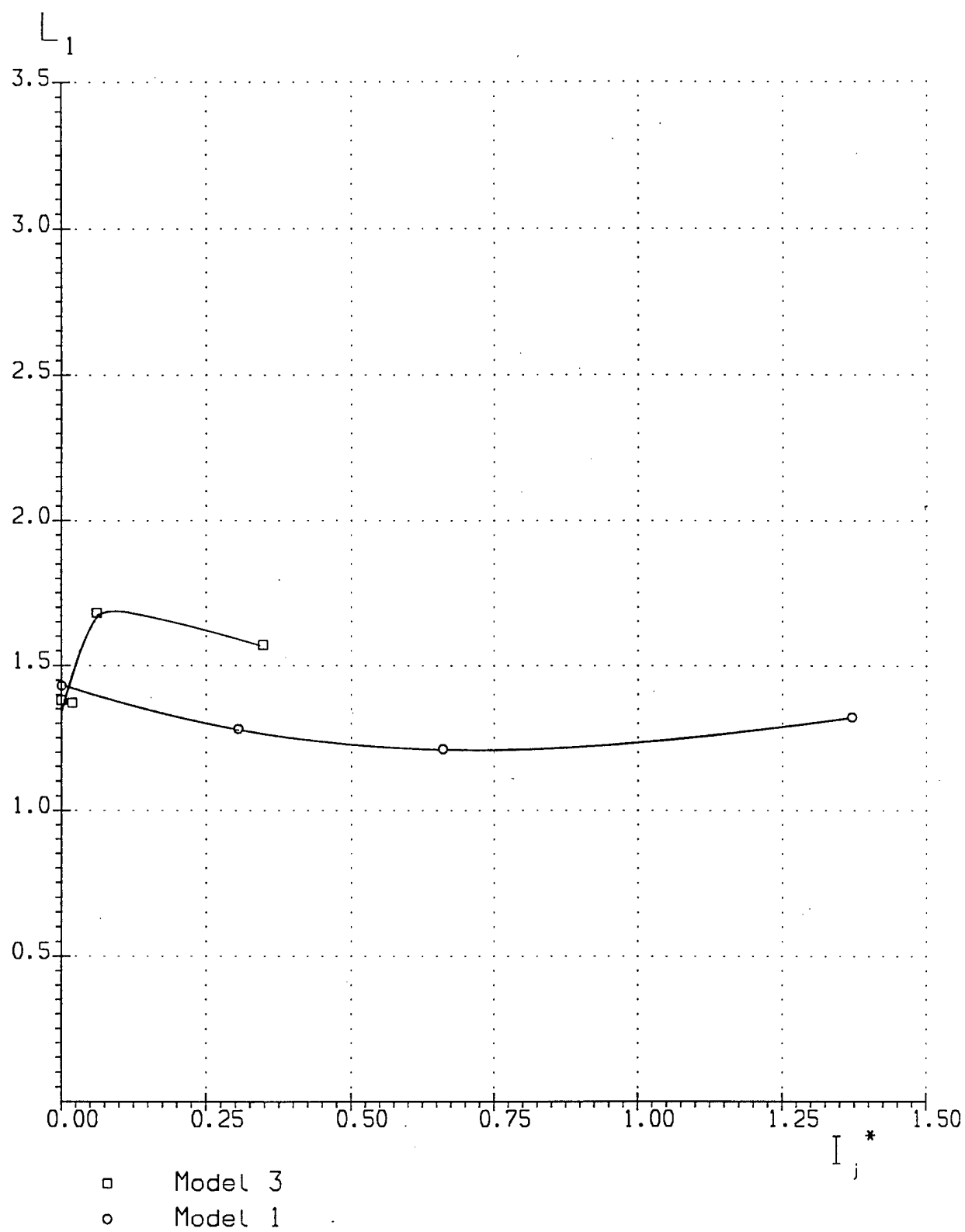
Fig. 75

Model 3   X*=0.23
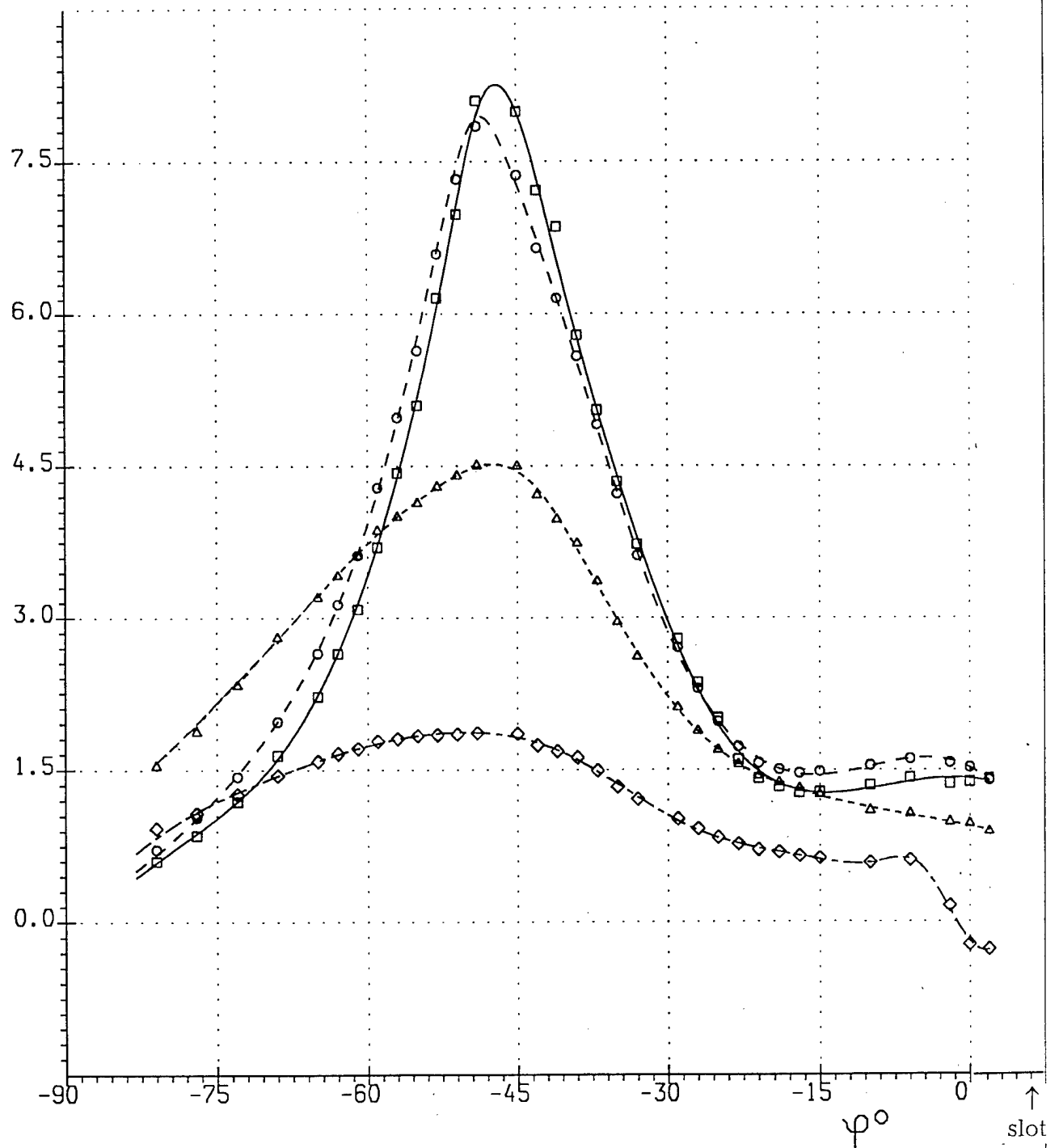
Fig. 76
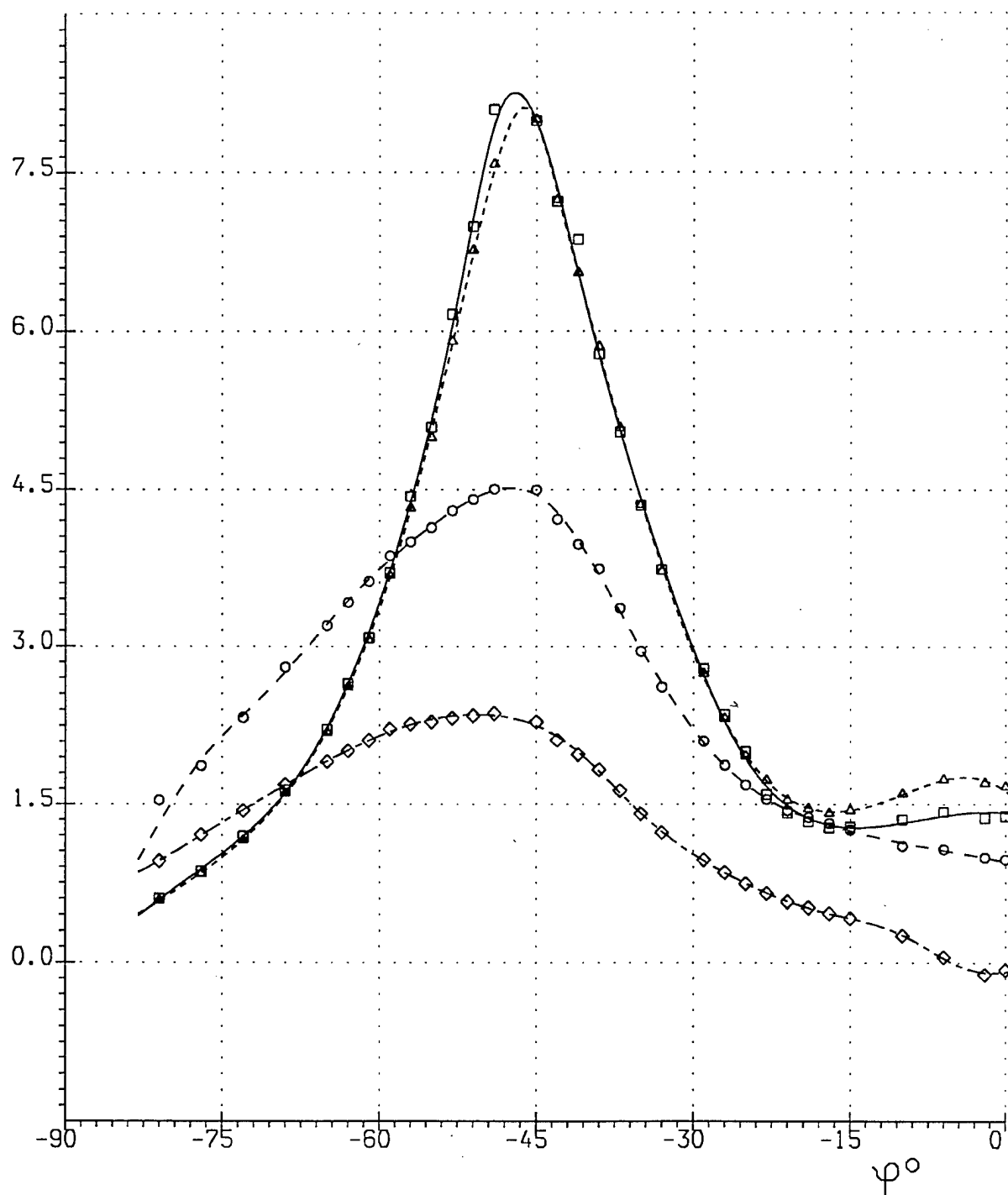
$X^* = 0.23$

Fig. 77
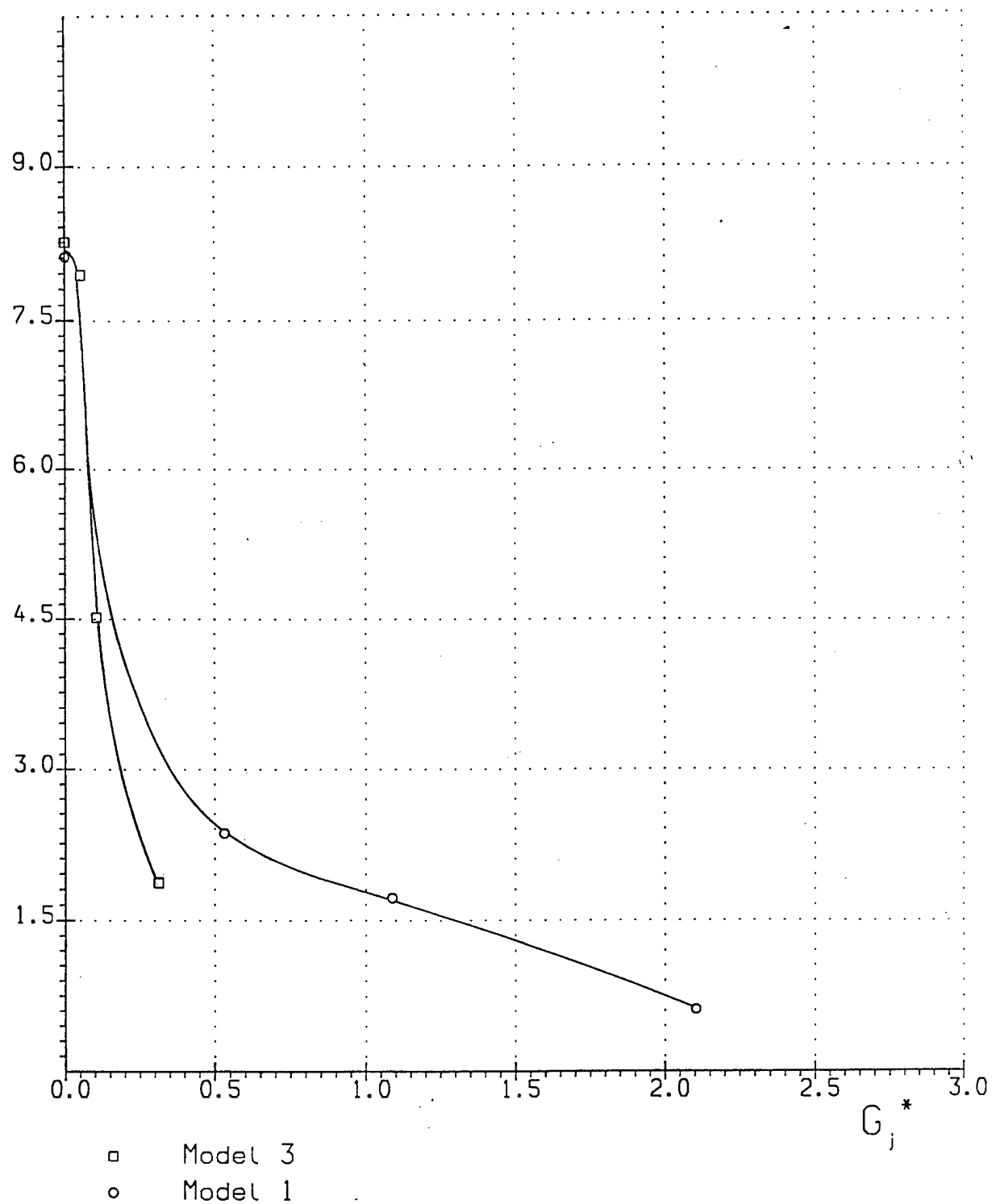
X*=0.23

Fig. 78
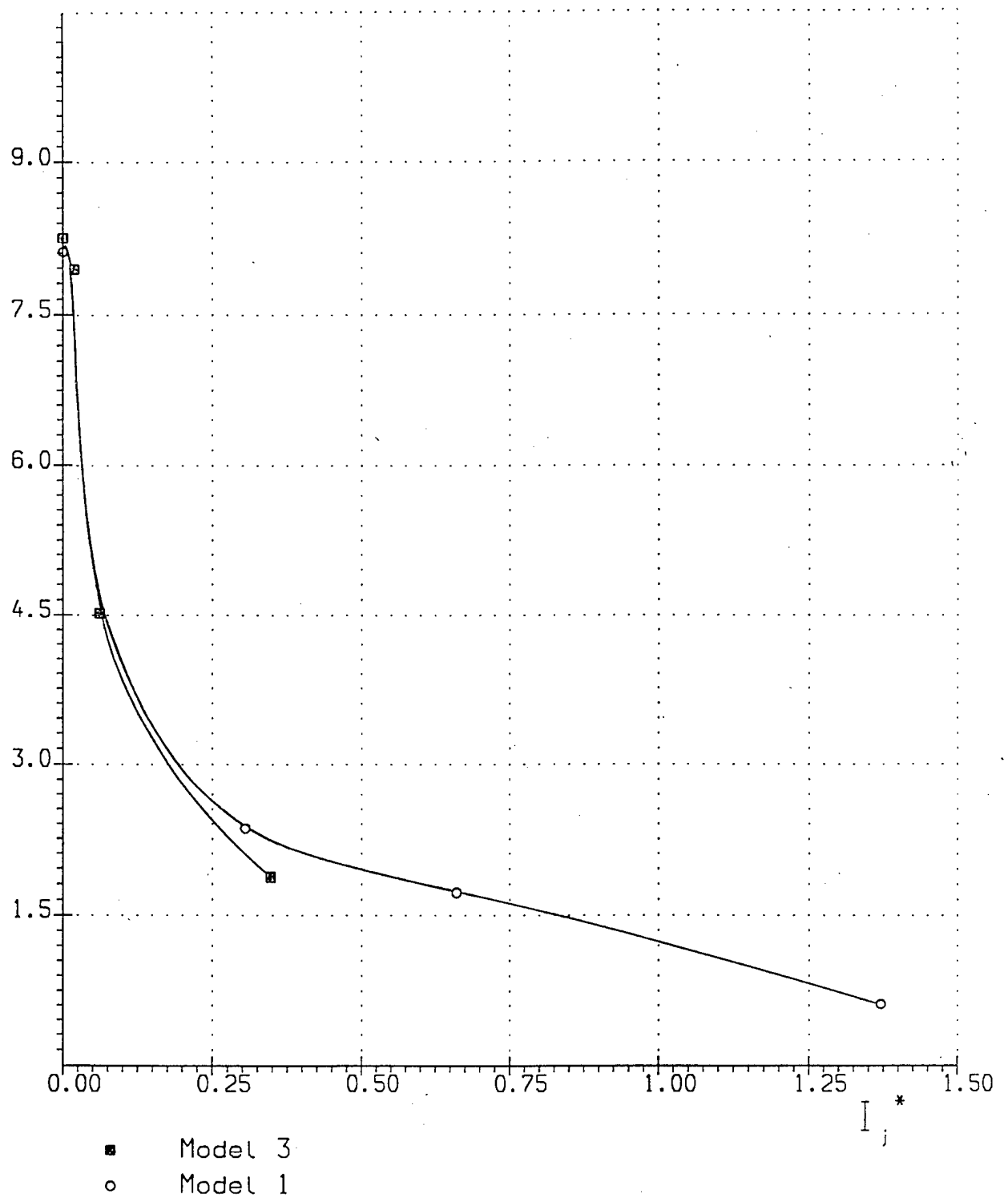
X*=0.23

Fig. 79
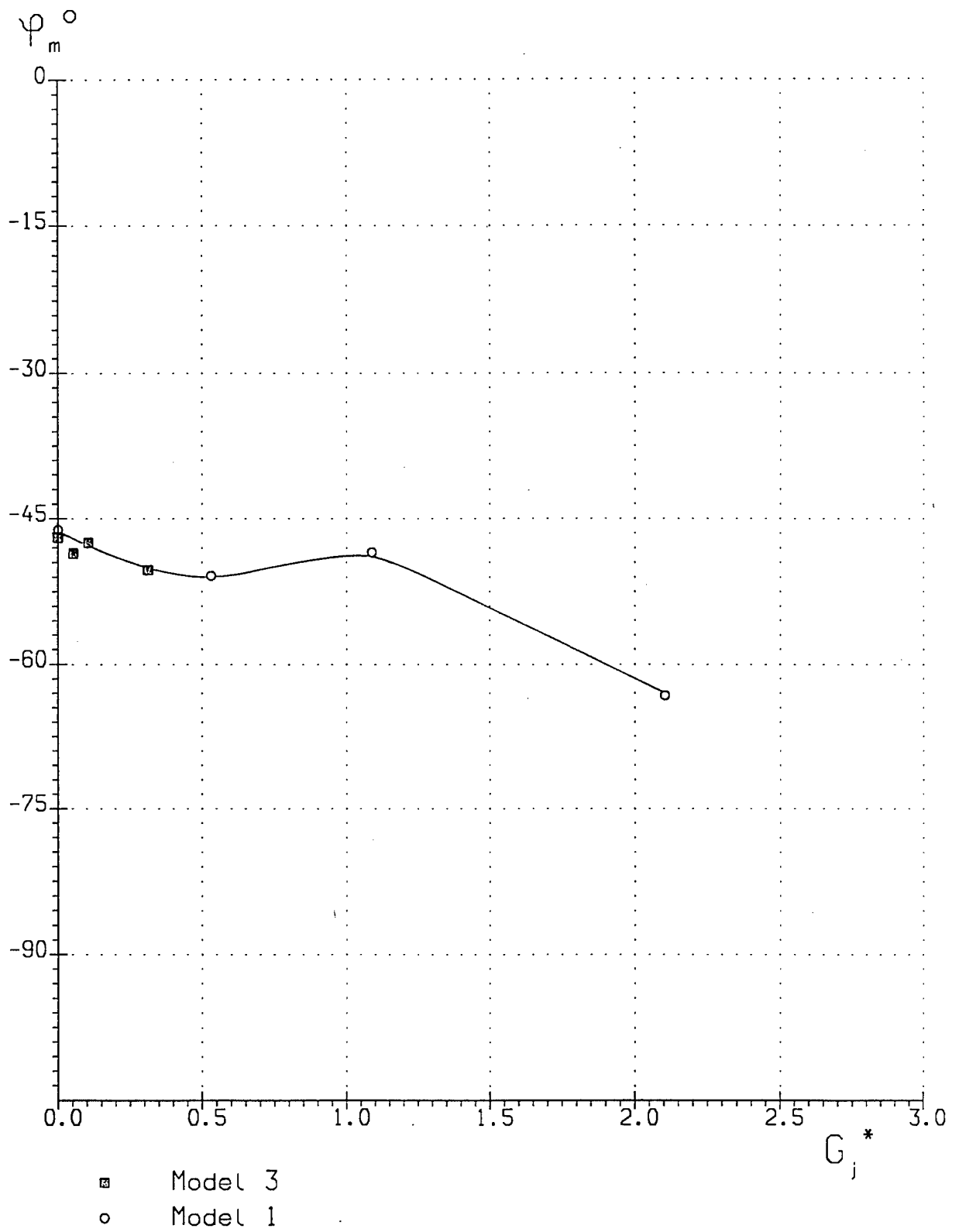
X*=0.23

Fig. 80

$X^* = 0.23$

Fig. 81

Fig. 82

Fig. 83

Legend:
- Model 4, $X^* = 0.44$
- Model 1, $X^* = 0.53$
- Model 1, $X^* = 0.33$

Axes: X_1 (vertical), G_j^* (horizontal)

Fig. 84

blunt body

injected gas

injected gas

bow shock

transmitted shock

shock generator

impinging shock

bow wave

M_∞

H

$\varphi_i = -33°$

Fig. 85

Model 4   X*=0.44

q/q_so

Fig. 86

Fig. 87

q_m/q_{so}

9.0

7.5

0.44; 4

0.53; 1

0.53; 1 — helium

0.86; 1

$X^* = 1.13$; model 1

6.0

4.5

3.0

0.23; 3

1.5

model 1, 2, 3

without wedge

0.23; 1

0.33; 1

model 4

0.00   0.25   0.50   0.75   1.00   1.25   1.50

I_j^*
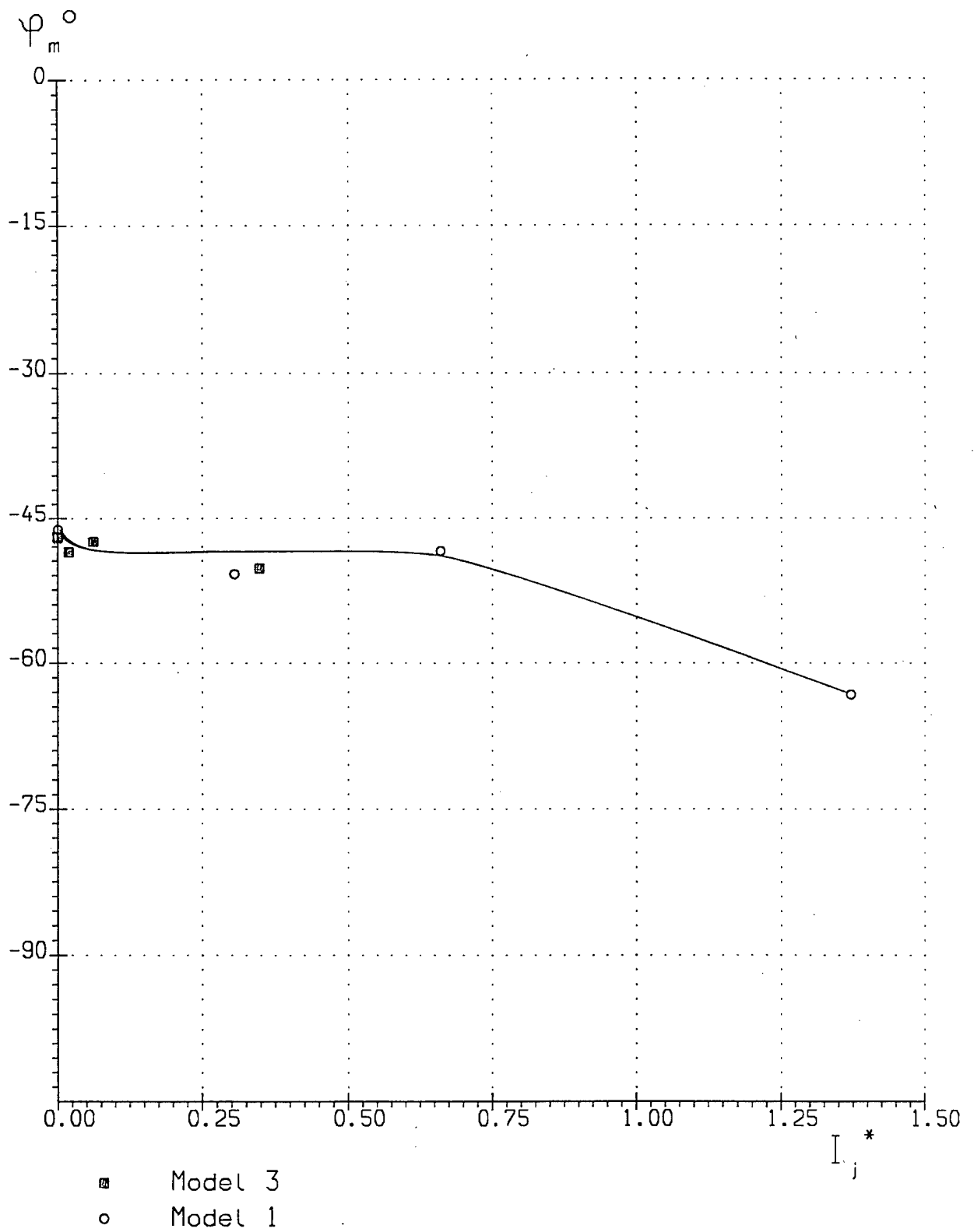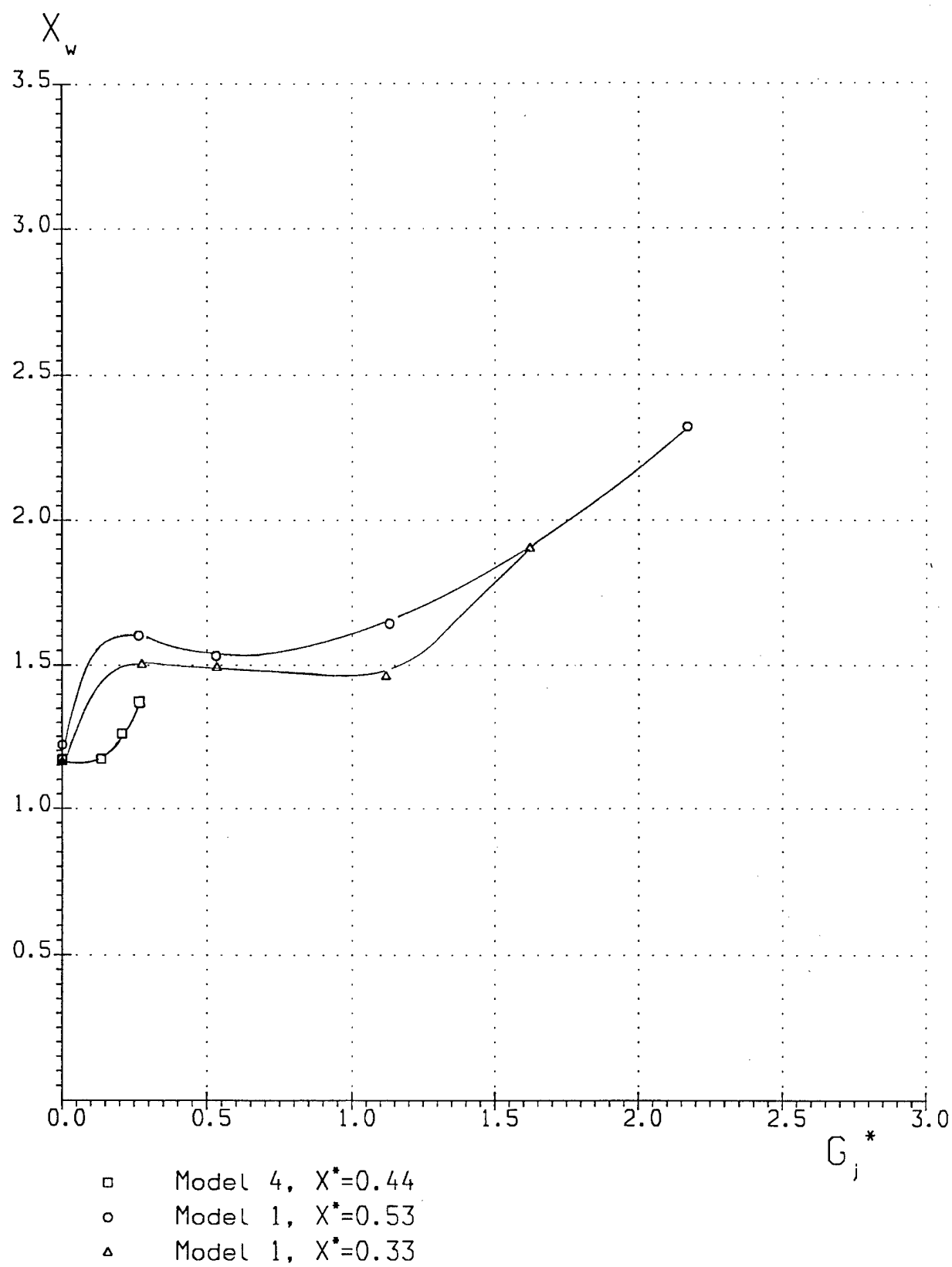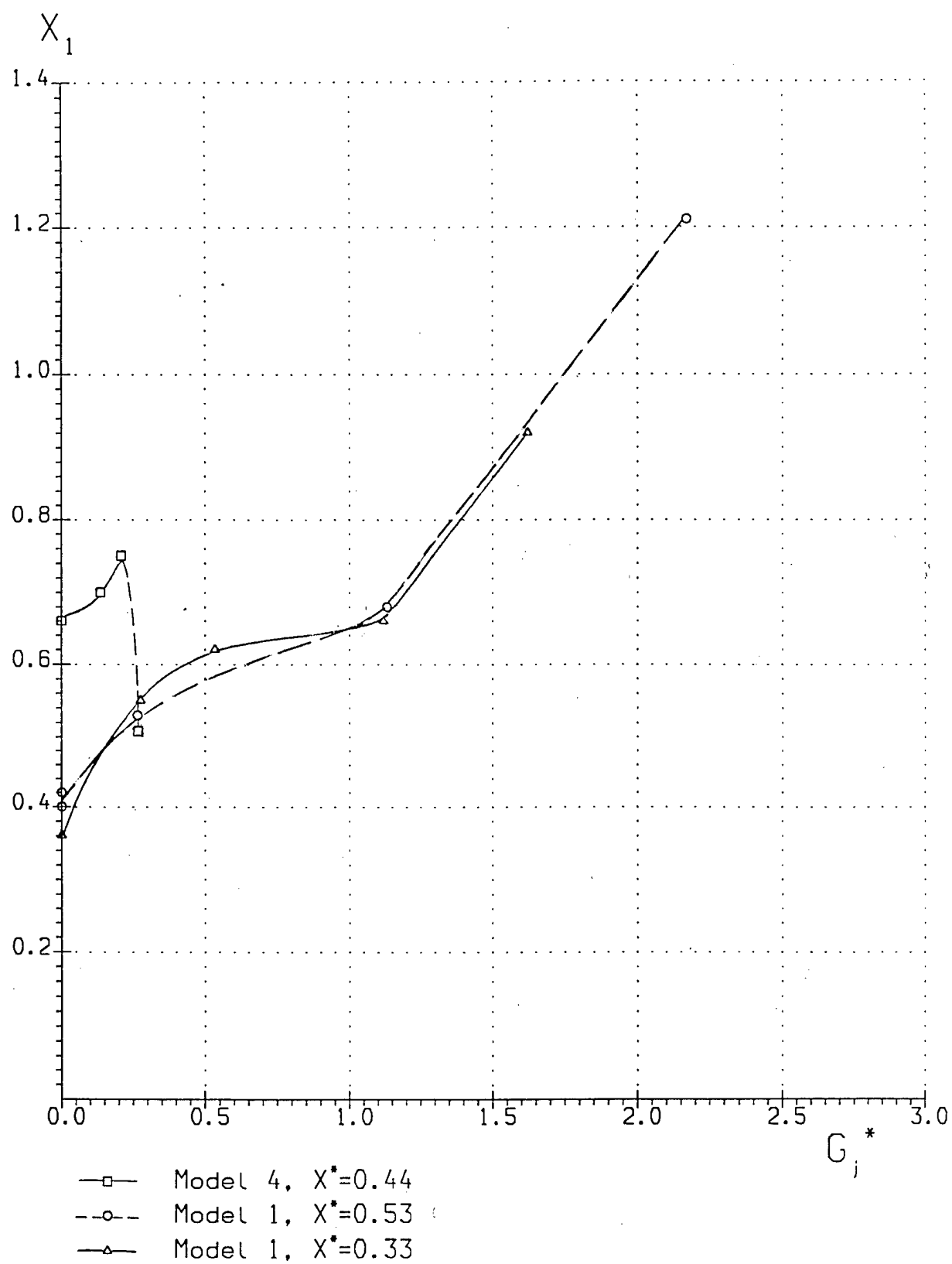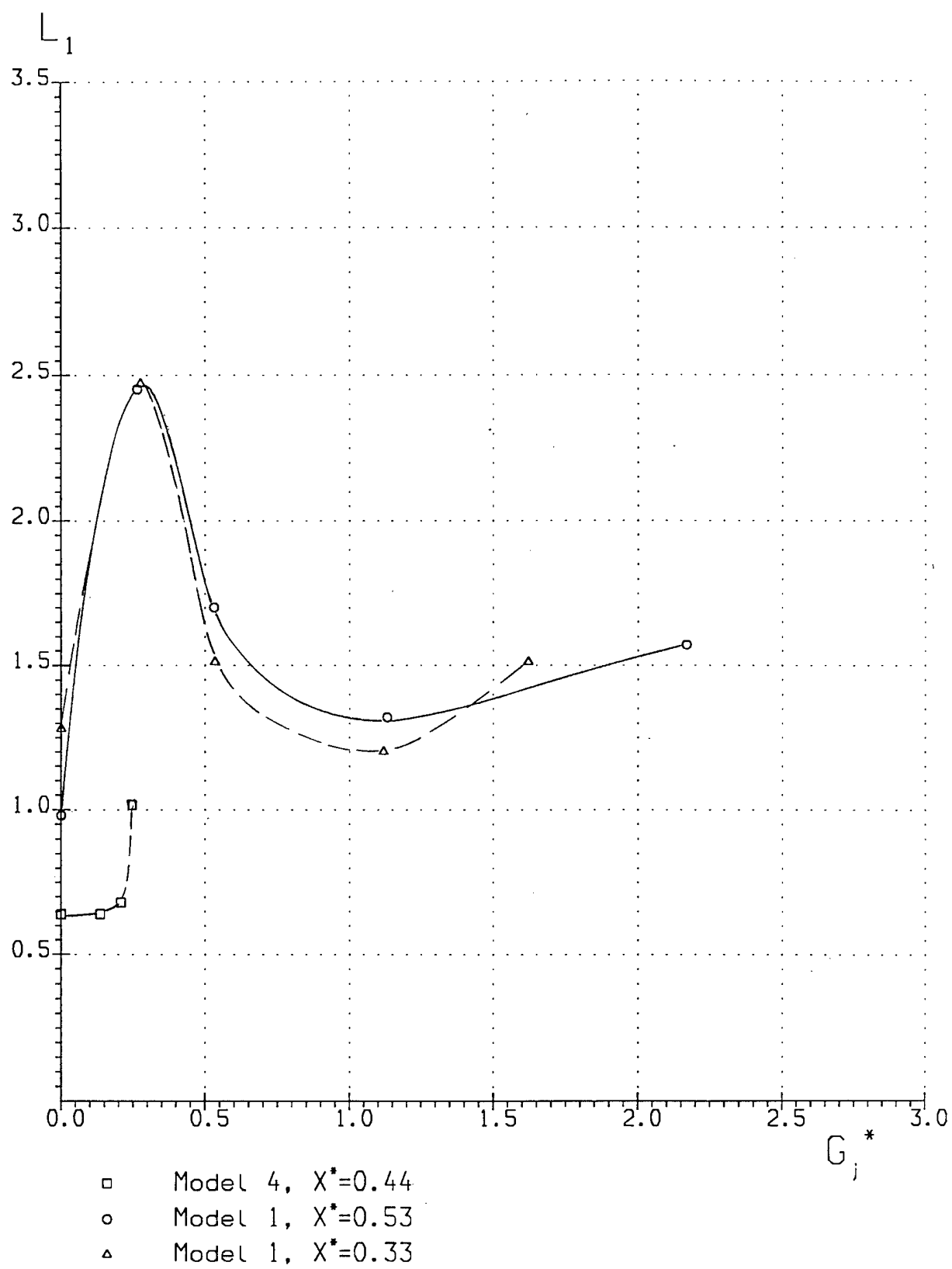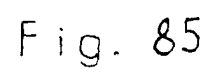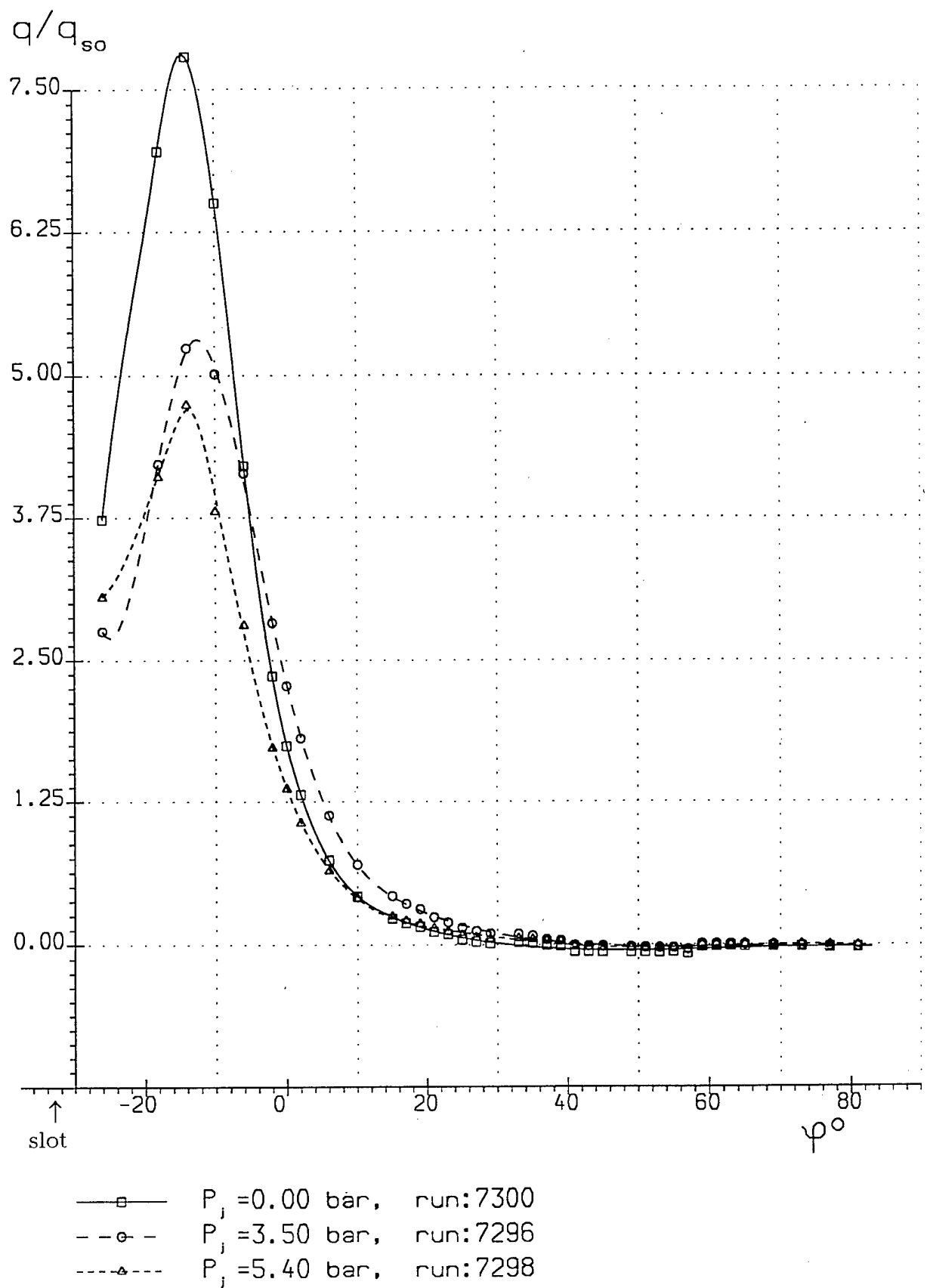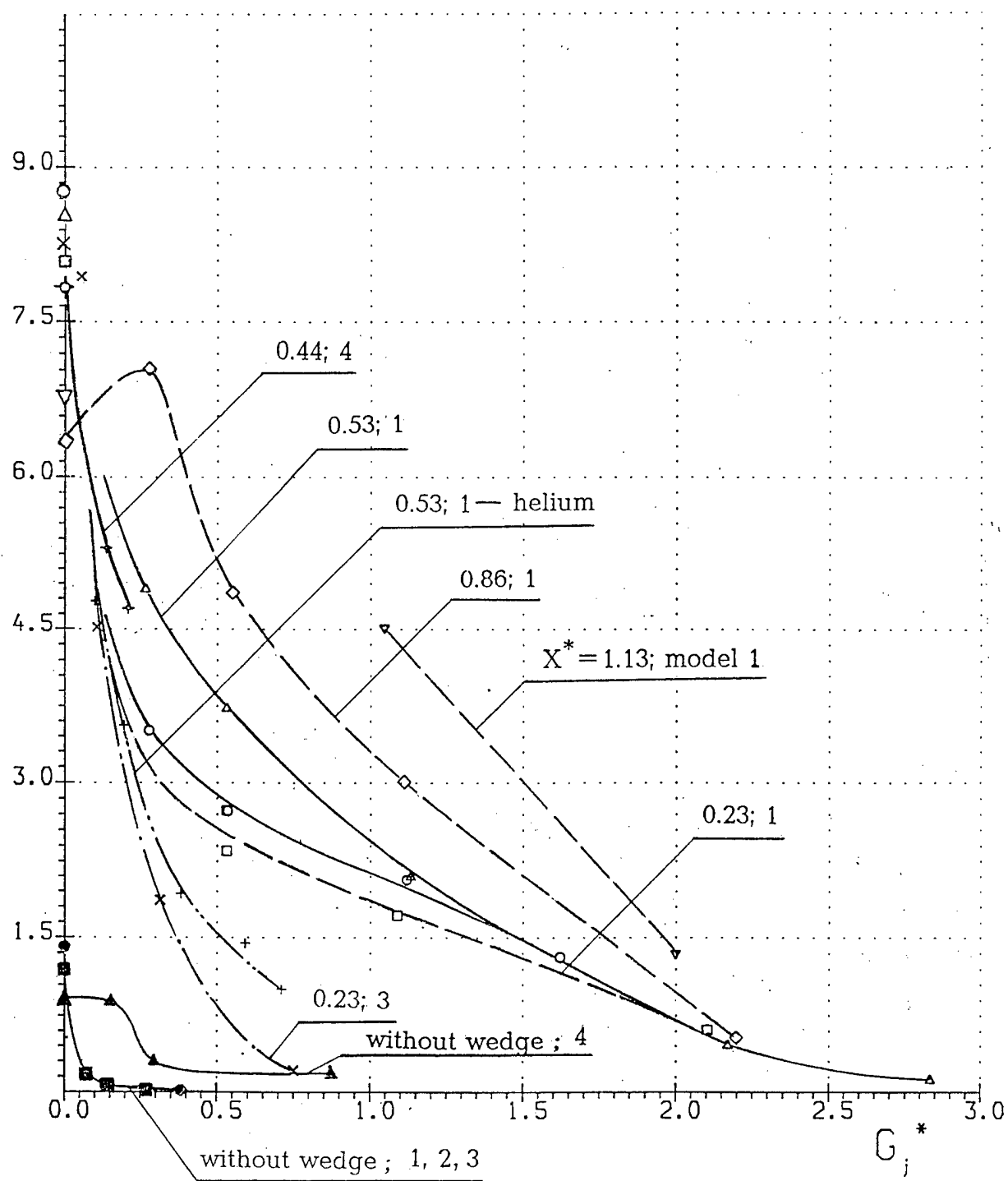
Model	φ_j,°	h_j./R
1	4	0.018
2	6	0.007
3	6	0.004
4	-33	0.0075

Fig. 88
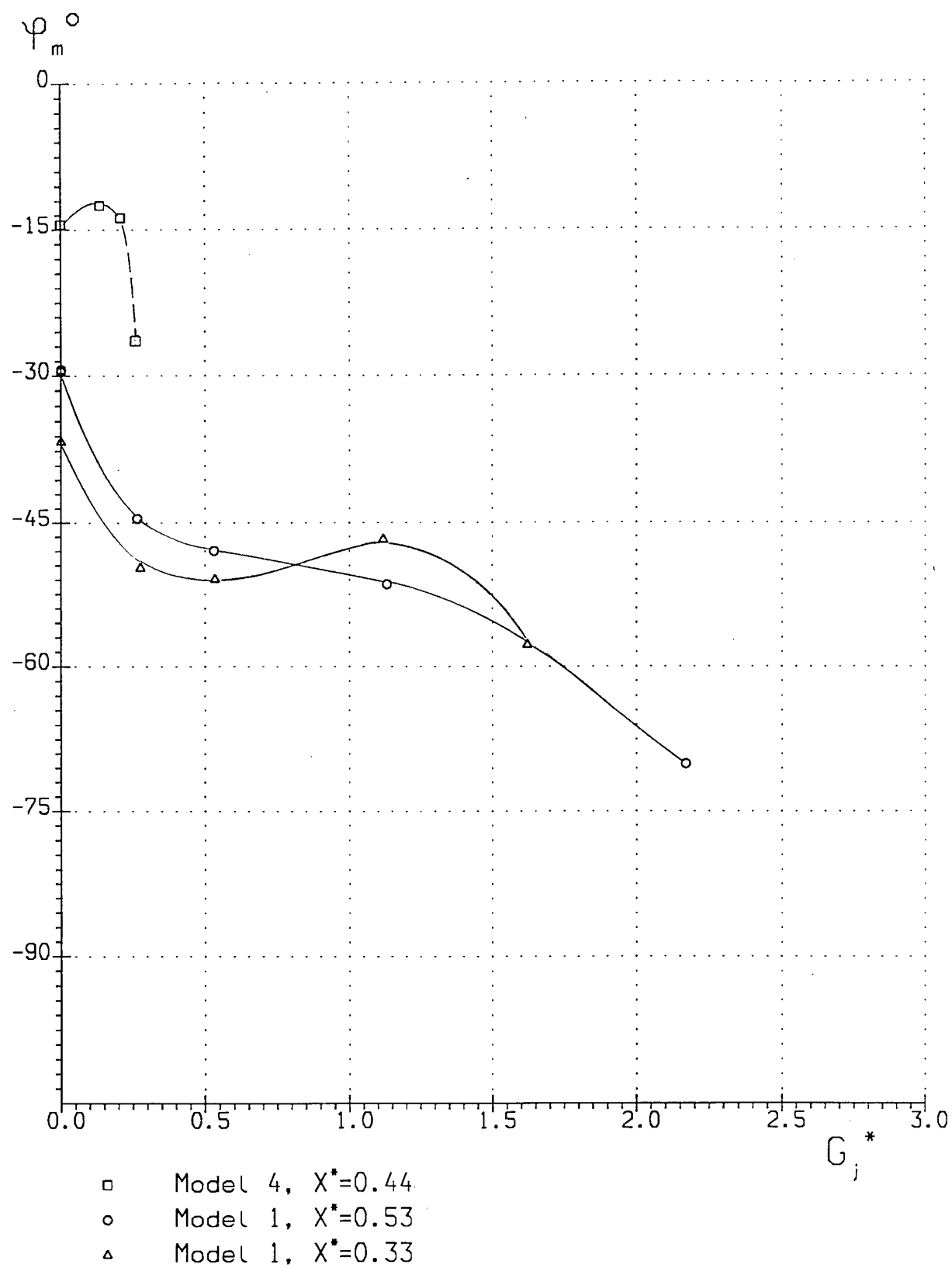
Fig. 89
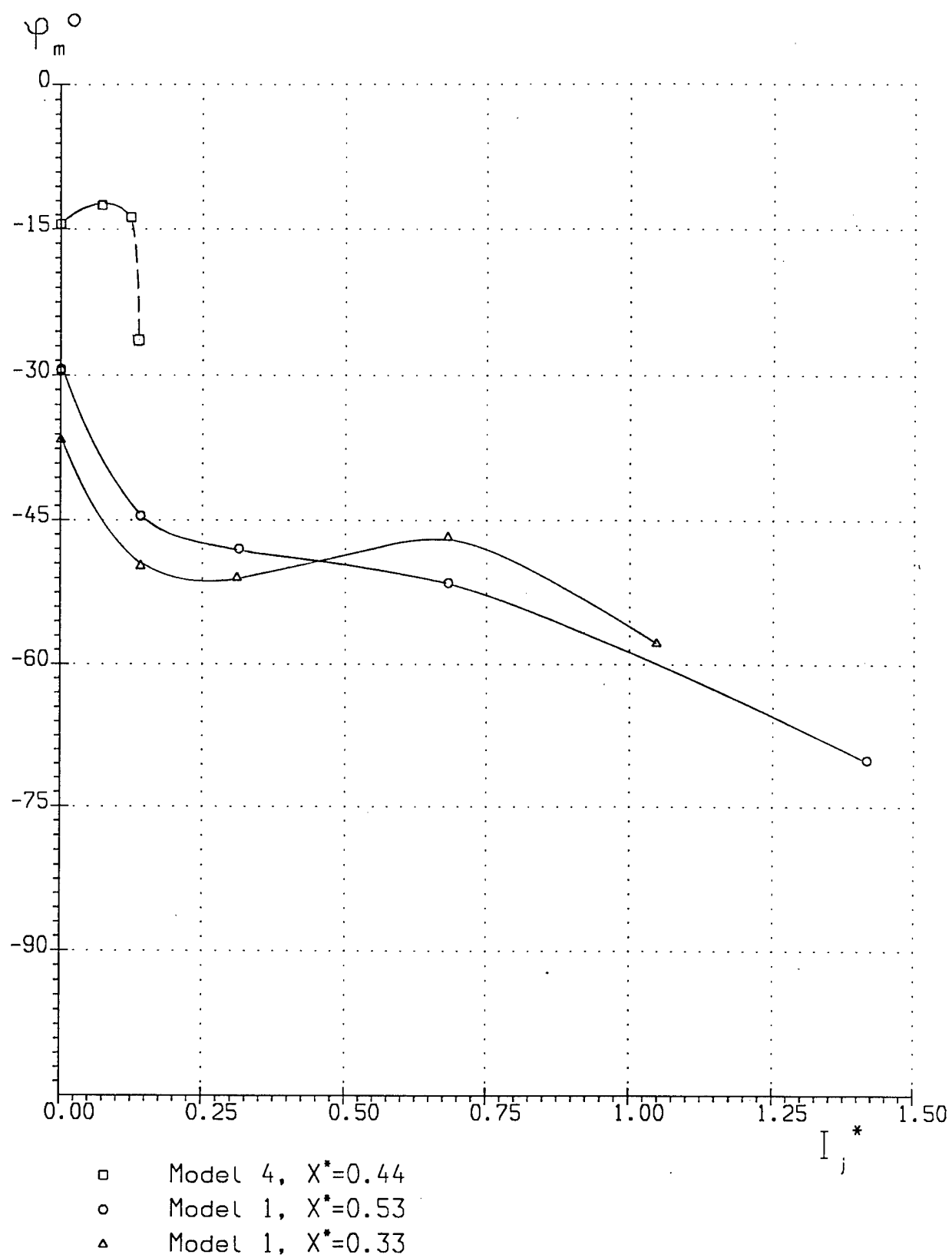
Fig. 90
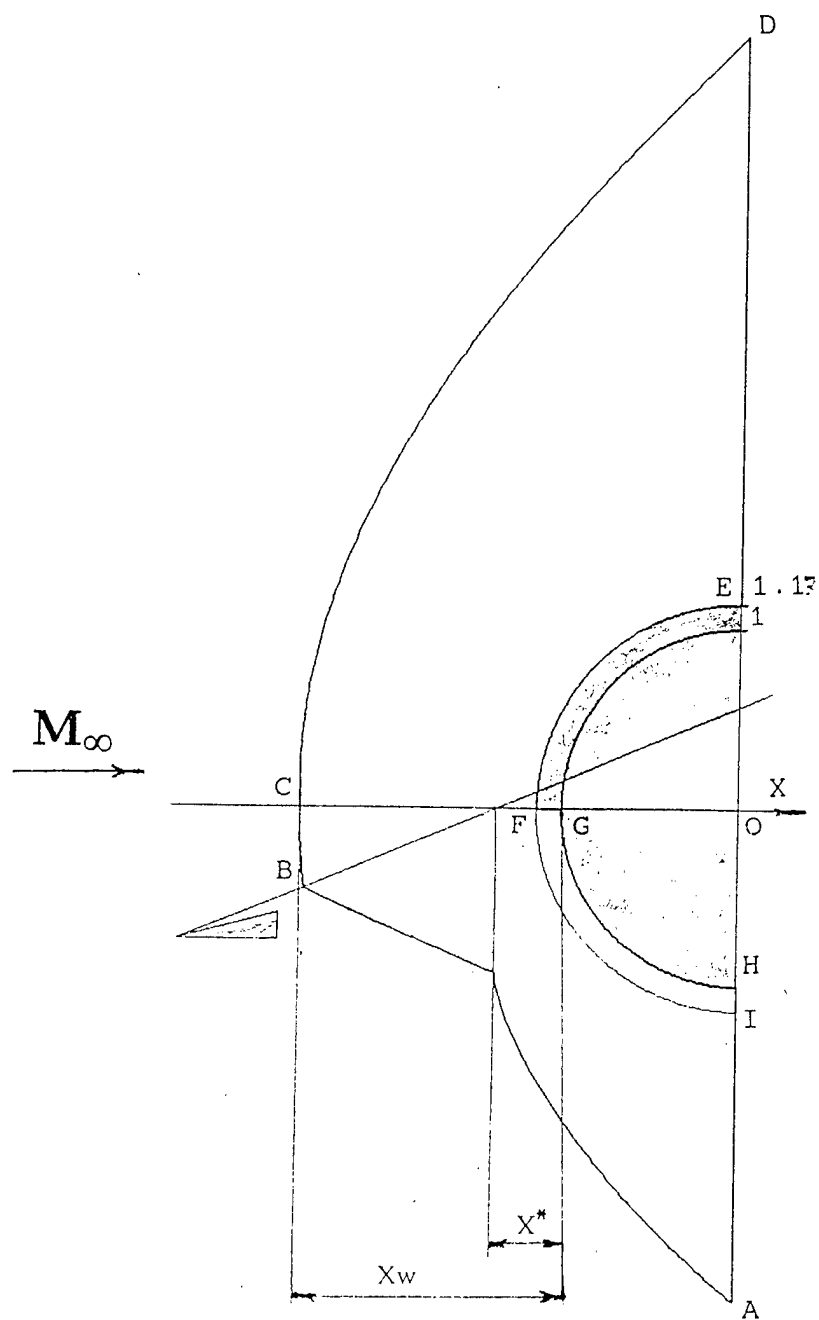
Fig. 91

Computational grid
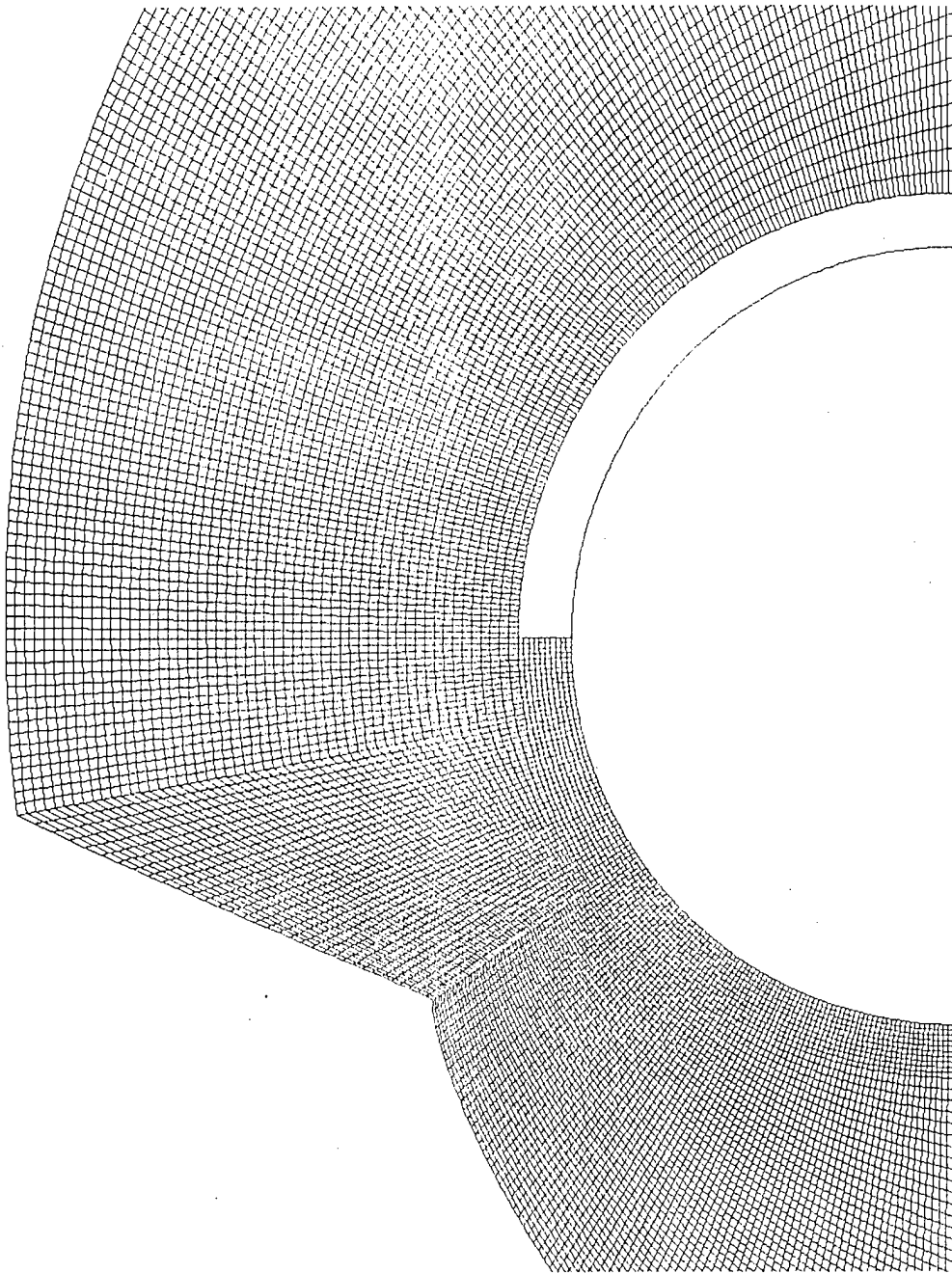
Fig. 92

Mach number
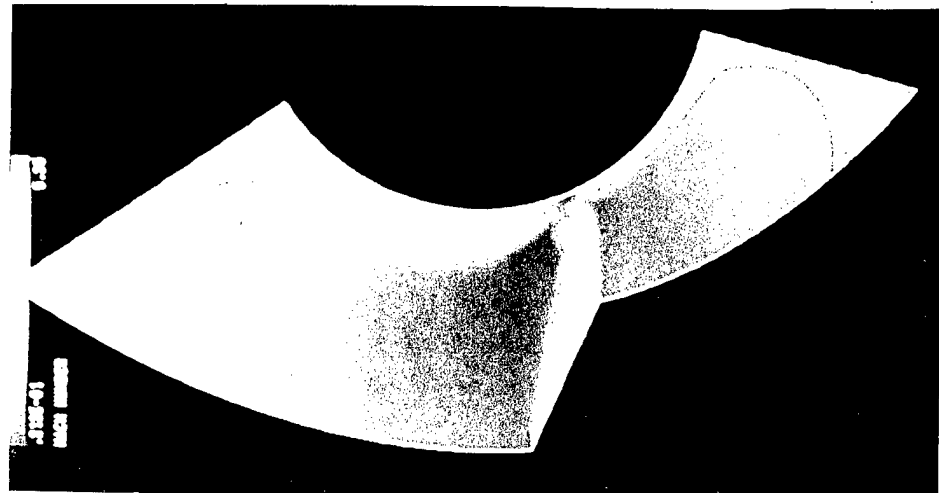
Without injection
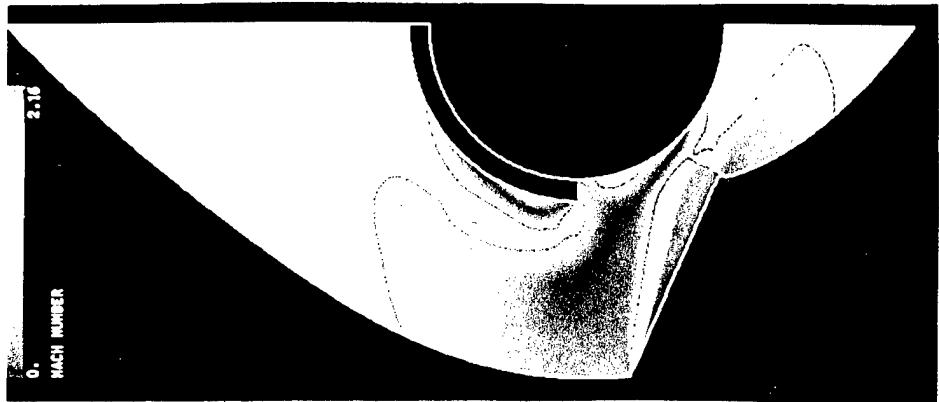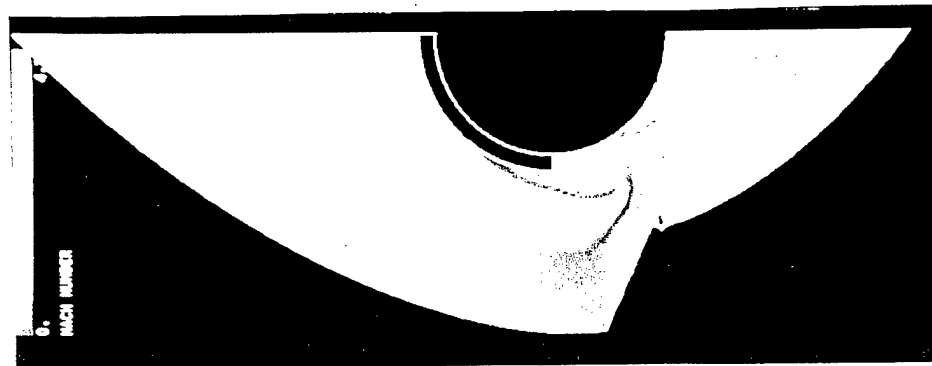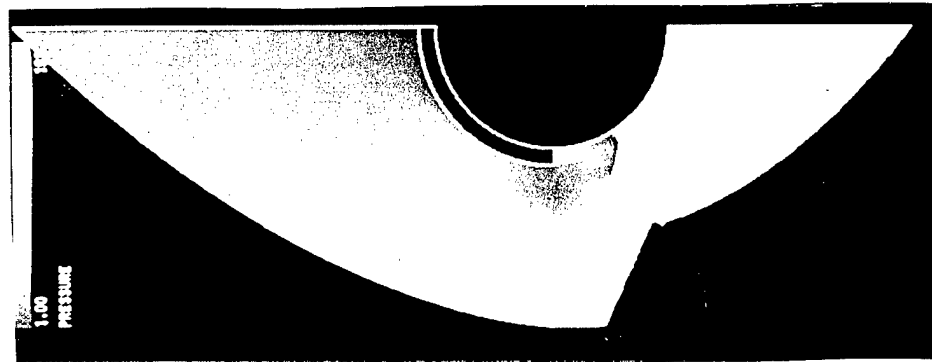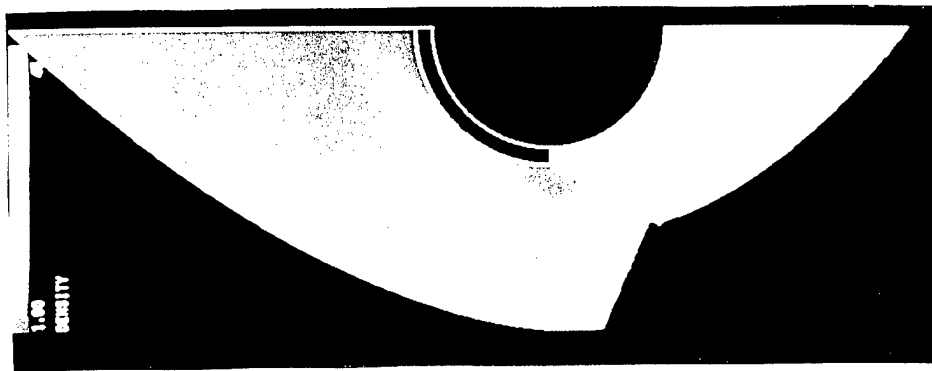
Without injector

Fig. 93

$$P_j = 16 \text{ bar}$$

Density

Pressure

Entropy

Mach number

Fig. 94a

$P_j = 16 \text{ bar}$

Bernully
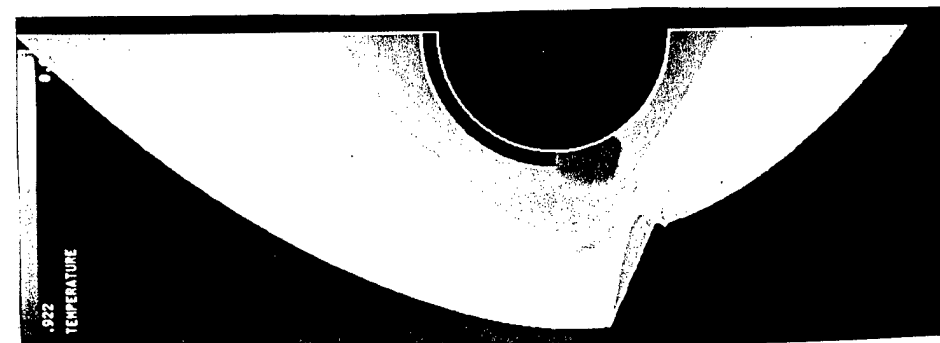
Full velocity

Velocity Uy

Velocity Ux

Temperature
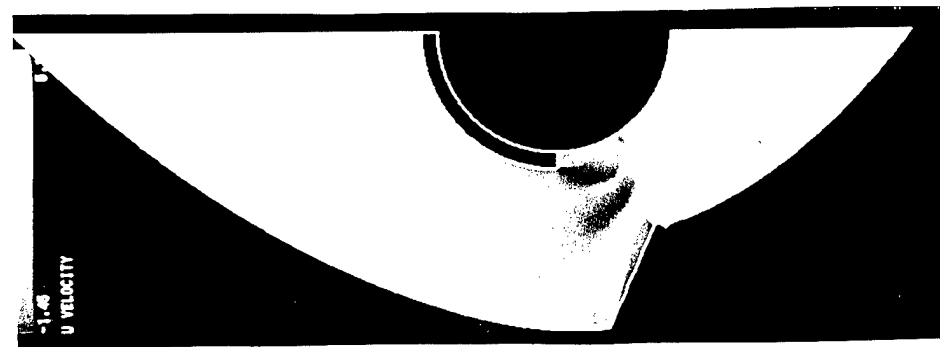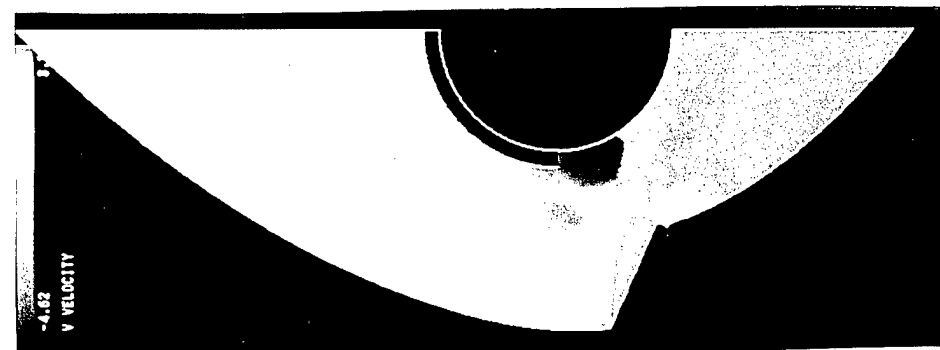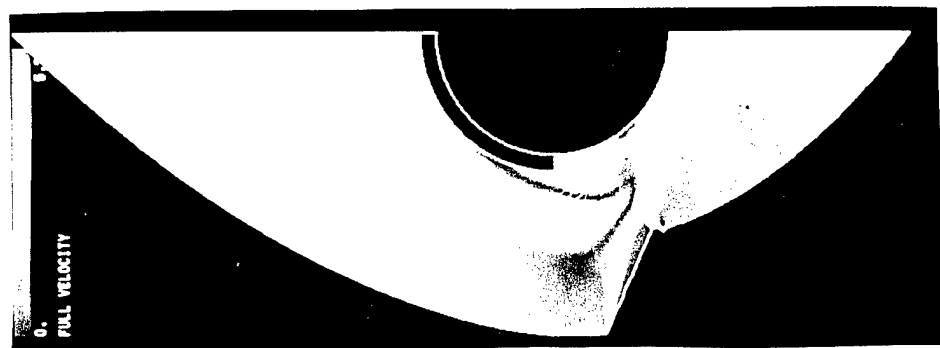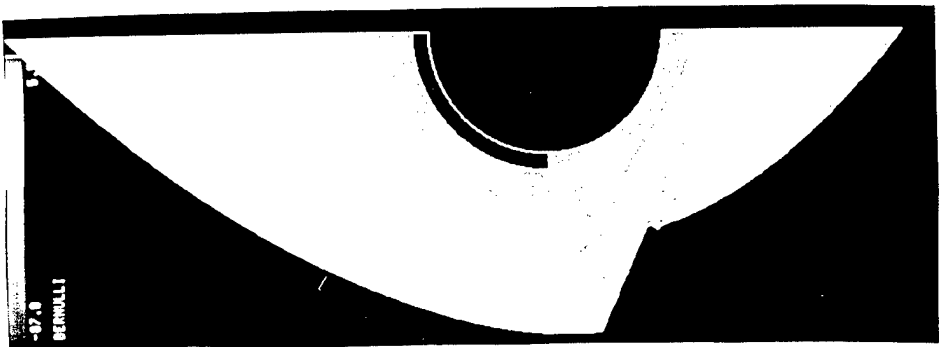
Fig. 94b

Much number
P_j=16 bar

M=1

stream lines

bow wave

"leeward" surface

M_∞

stream lines

separation zone

shock ξ

impinging shock

high pressure zone Ψ

H

M=1

"winward" surface

shock generator

stream lines

compression fan

M=1

transmitted shock
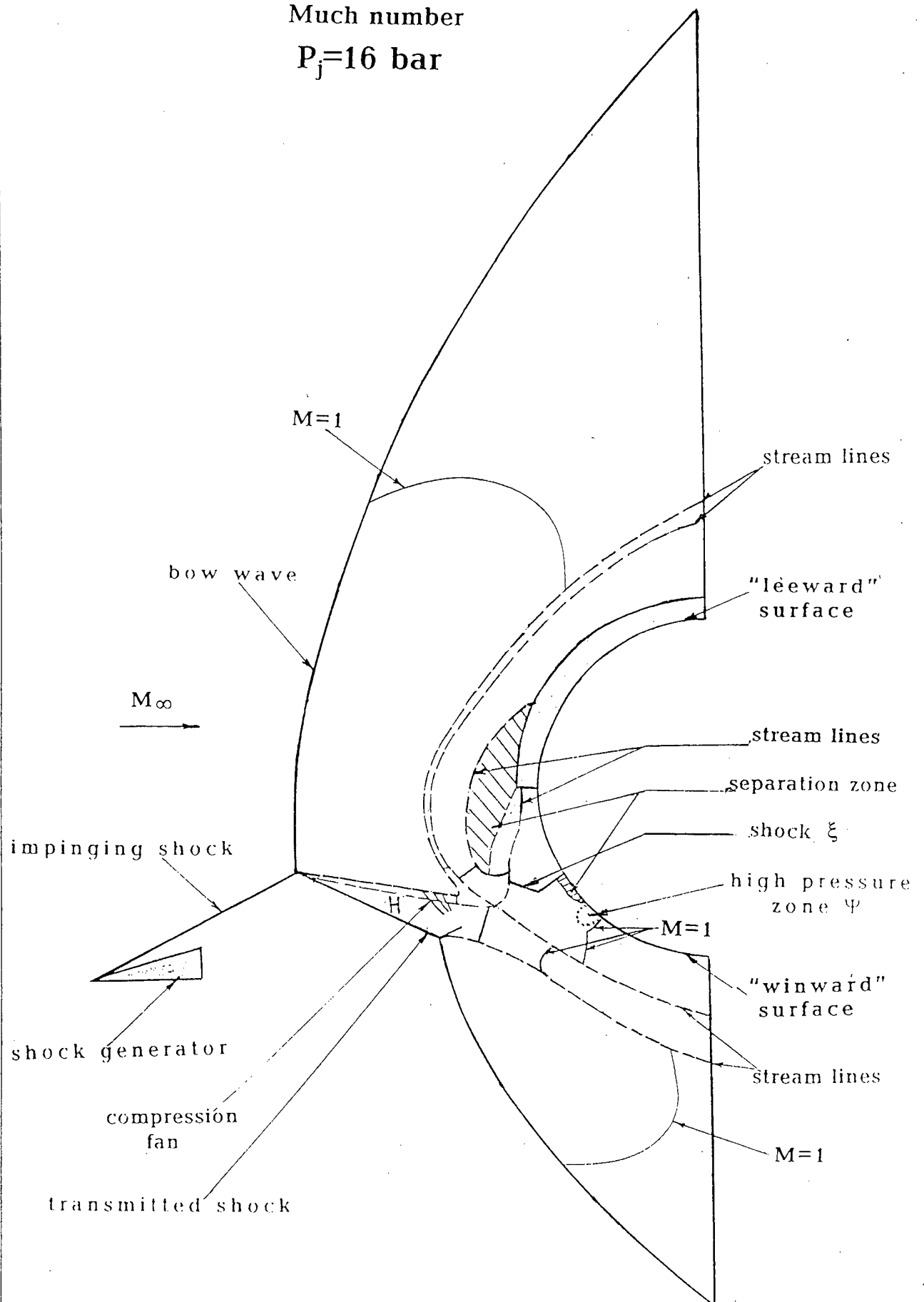
Fig. 95

Isolines of stream function

$P_i = 16$ bar

$M_\infty = 6$

23^0

15^0

separation zone

ξ

Fig. 96
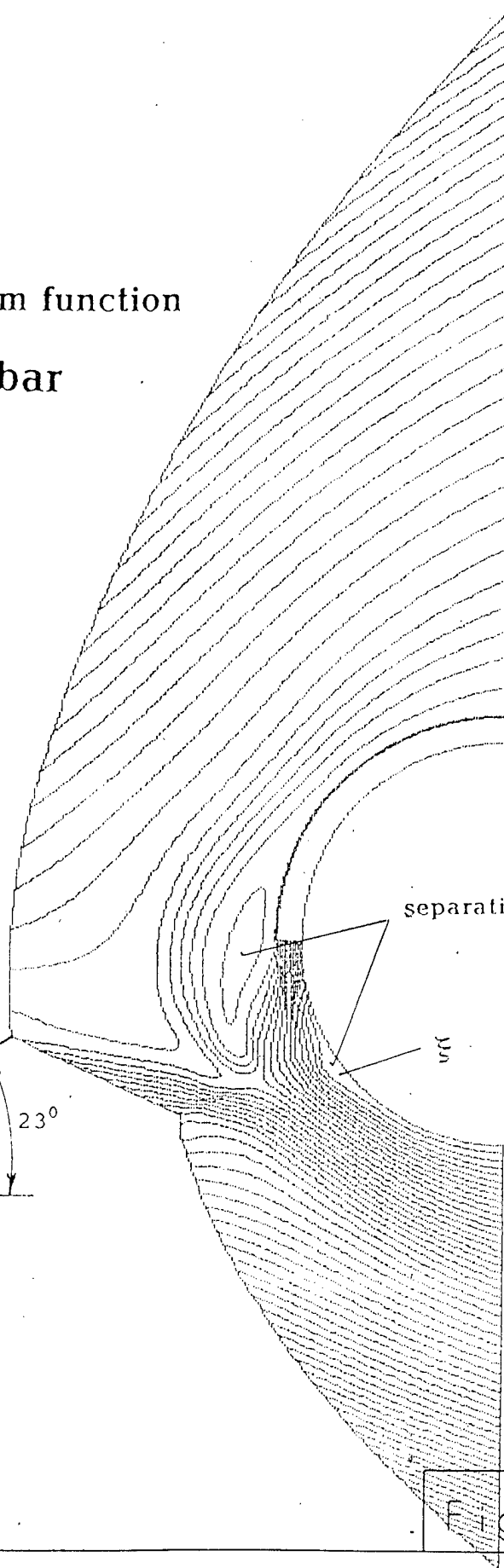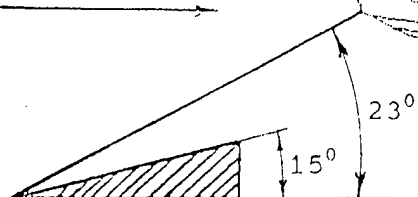
Entropy

$P_j = 32_{\text{bar}}$

Mach number

$X_{w\,\text{max}}$
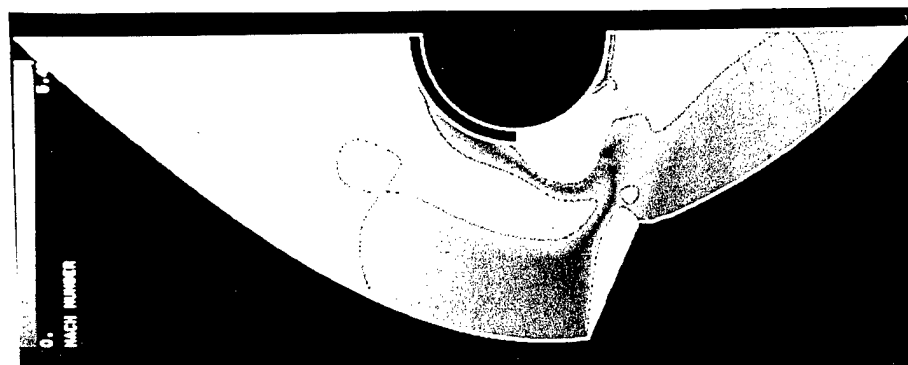
$X_{w\,\text{min}}$
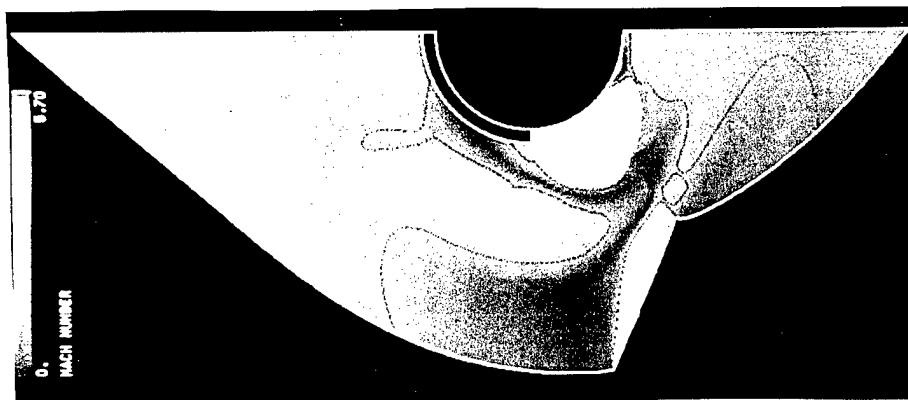
$X_{w\,\text{max}}$
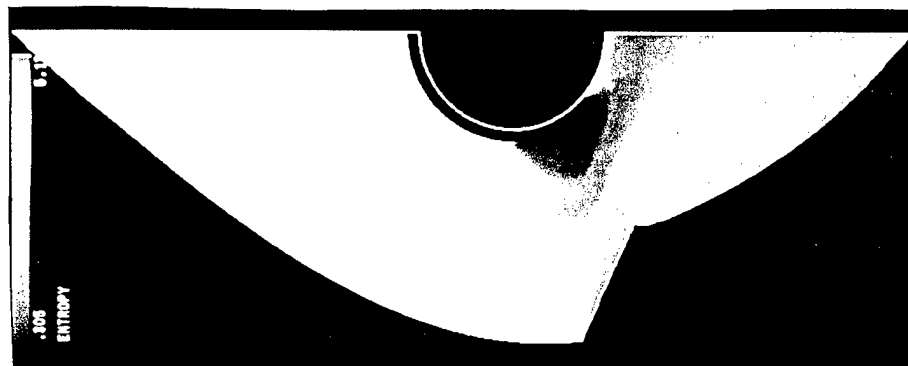
$X_{w\,\text{min}}$
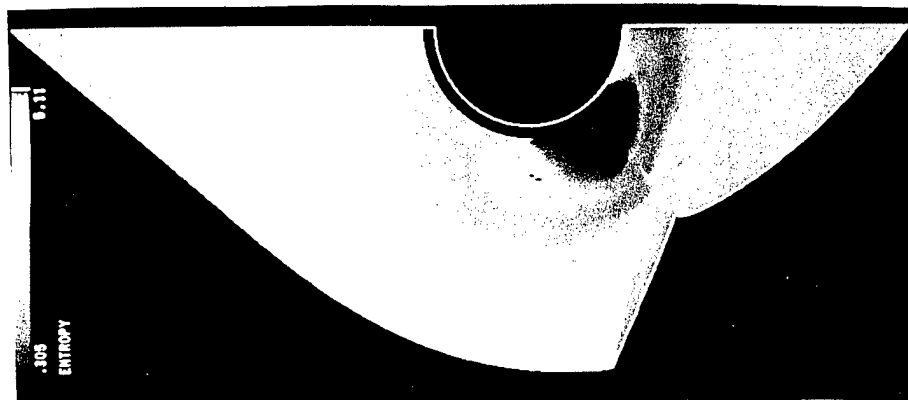
Fig. 97

Entropy

$X_{w\ max}$

$X_{w\ min}$

$P_j = 8$ bar

Mach number

$X_{w\ max}$

$X_{w\ min}$

Fig. 98

Entropy

$X_{w\,max}$

$X_{w\,min}$

$P_j = 4_{\,bar}$

Mach number

$X_{w\,max}$

$X_{w\,min}$

Fig. 99

b)

a)

Fig. 100

$X^* = 0.383$ $P_j = 16$ bar

p/p∞

1 – windward cylinder
2 – injector surface
3 – cylinder surface without injector

1

2

3

φ
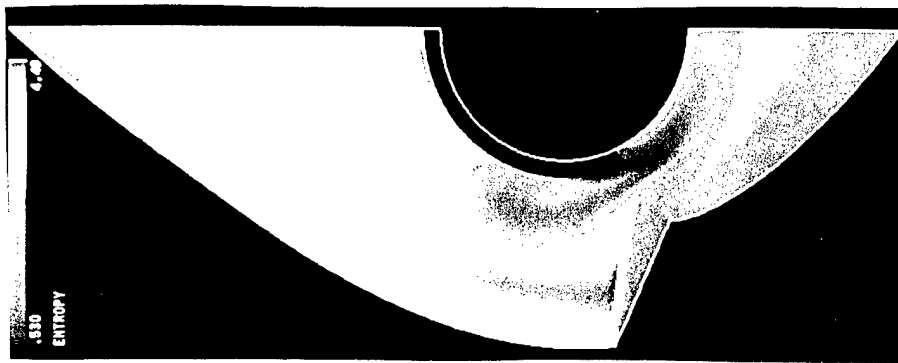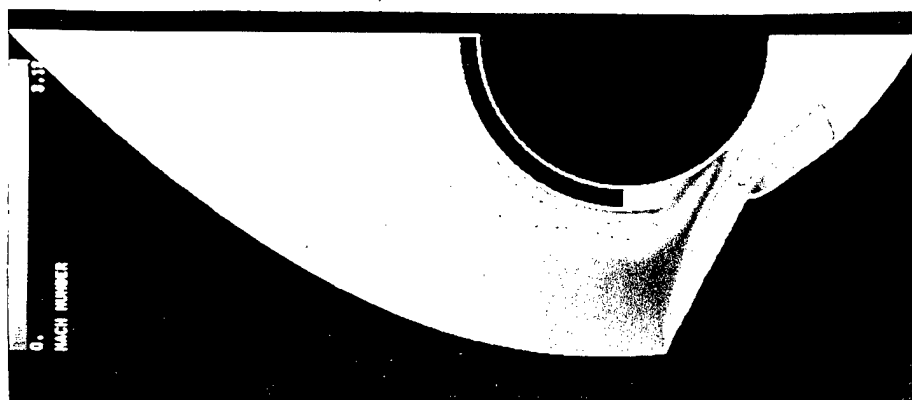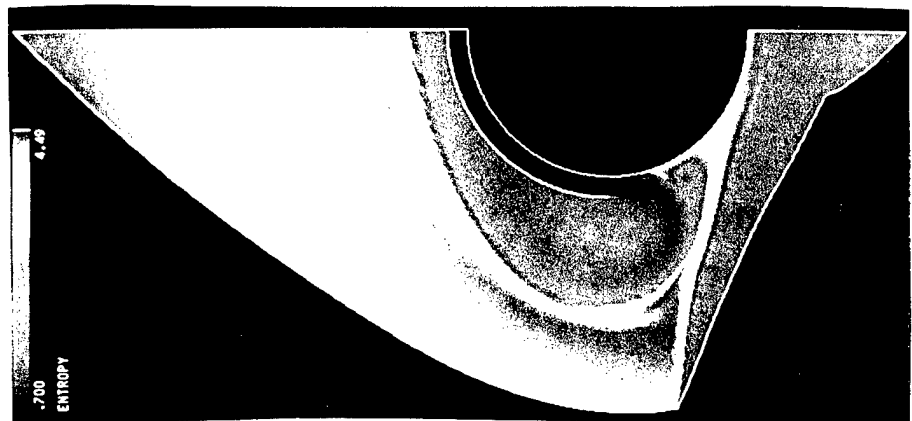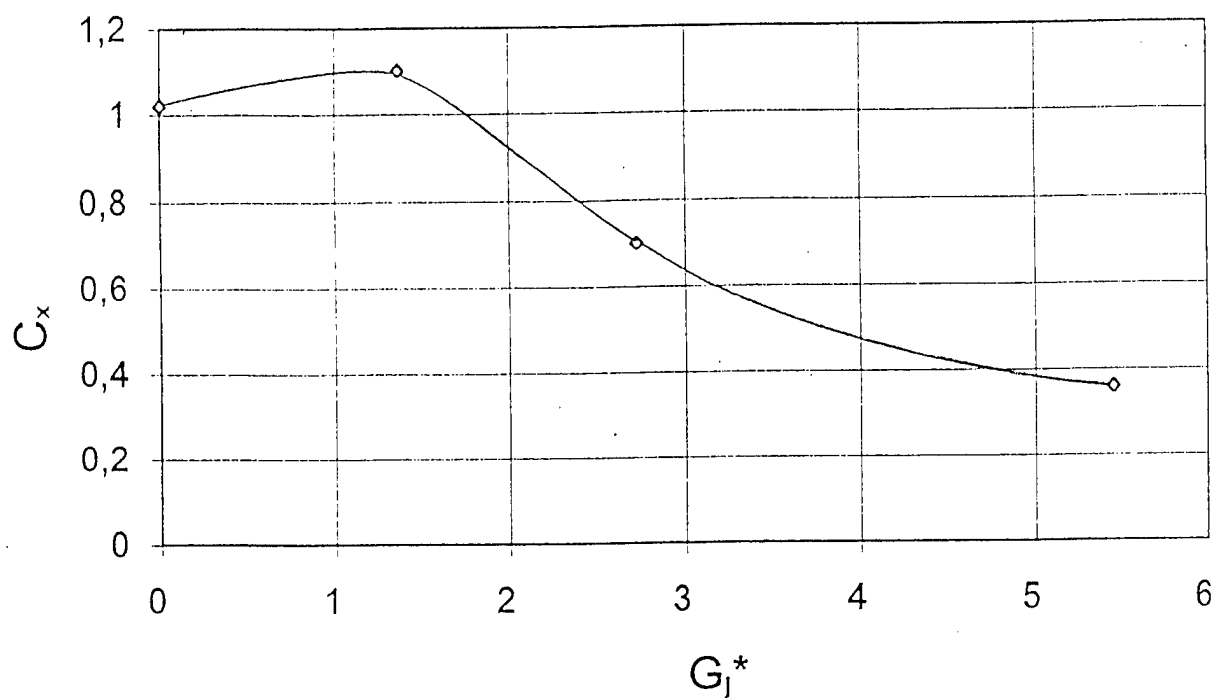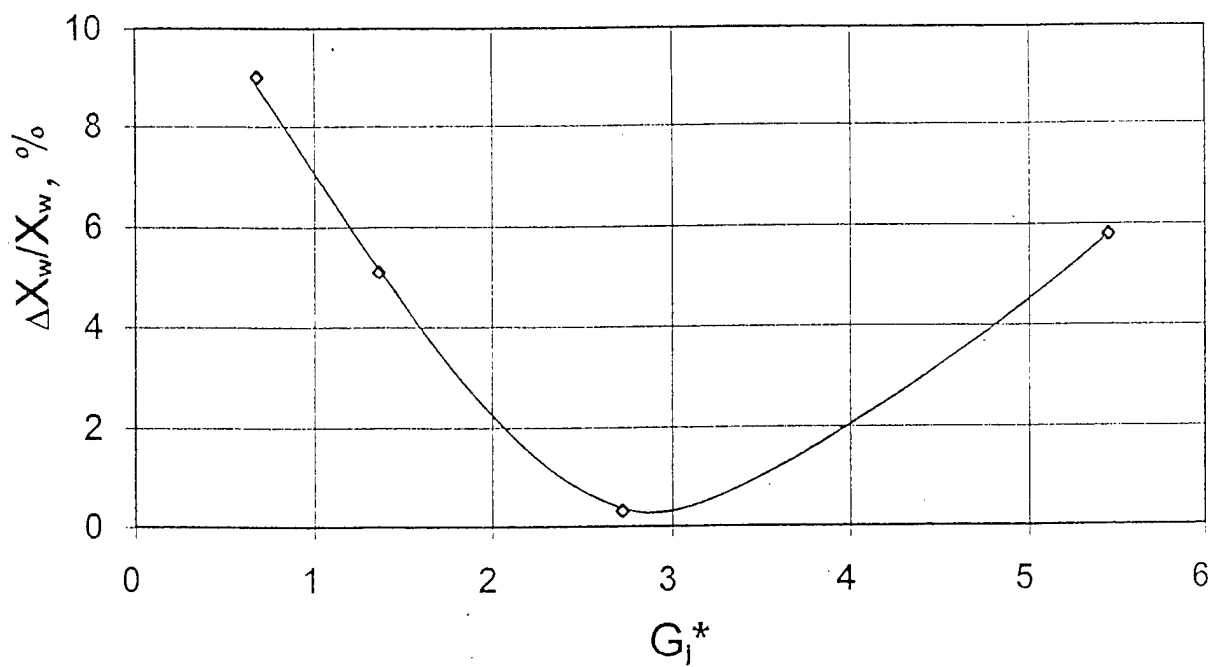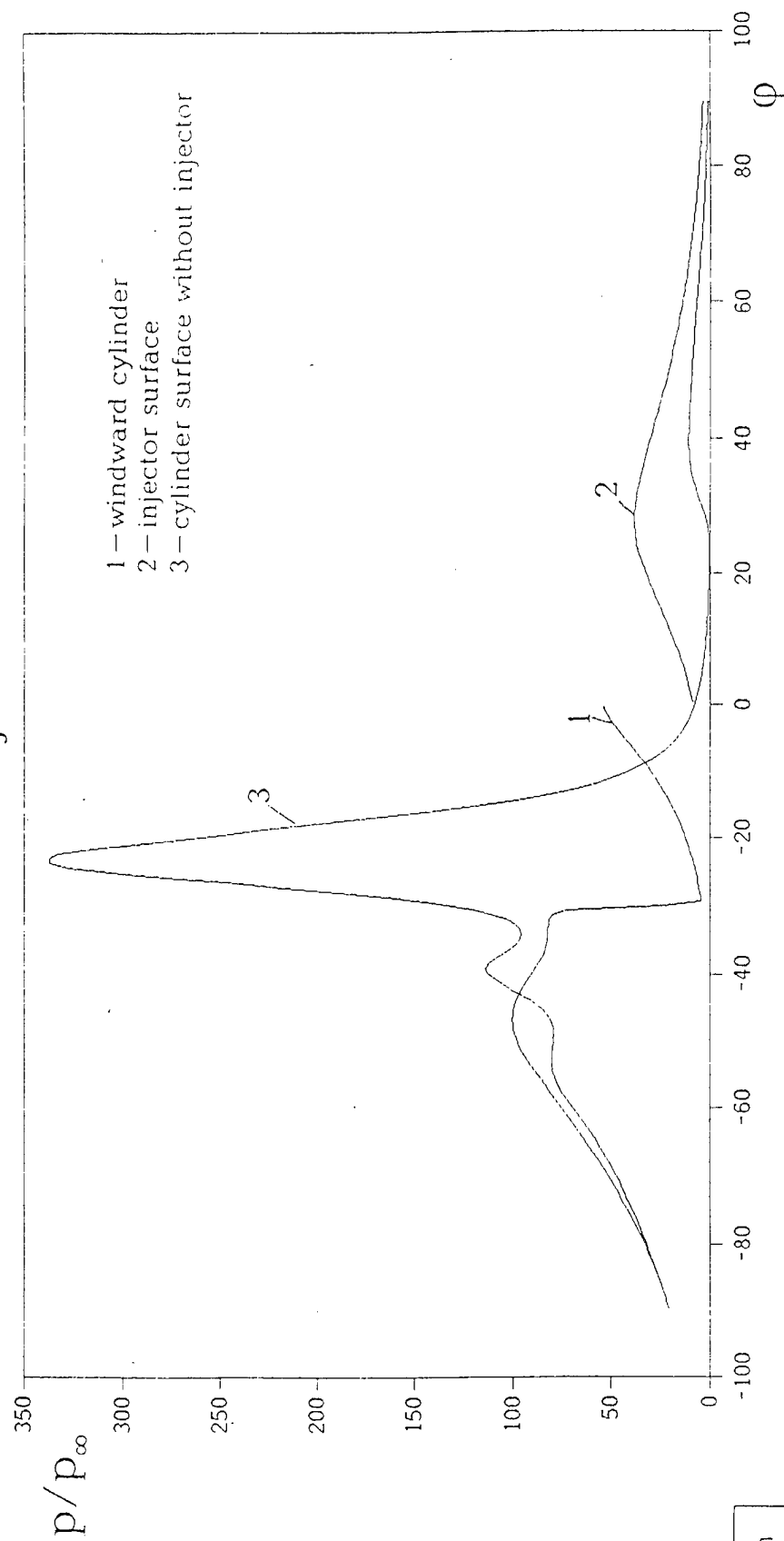
Fig. 101

Model 1

Fig. 102

Model 1

Fig. 103

Model 1

Fig. 104

Model 1

Legend:
△ X*=0,53
□ X*=0,33
- X*=0,38 calculatio[n]

Axis labels: $\bar{X}$ (vertical), I^*_j (horizontal)

Fig. 105

Model 1

Fig. 106

Model 1

Legend:
- △ X*=0,53
- □ X*=0,33
- - X*=0,38 calculation

Axis labels: I_j^* (horizontal), L_j (vertical)

Fig. 107